From Block Copolymers to Crosslinked Networks: Anionic Polymerization Affords Functional Macromolecules for Advanced Technologies

Alison R. Schultz

Dissertation submitted to the faculty of the

Virginia Polytechnic Institute and State University in partial fulfillment of the requirements for the degree of

Doctor of Philosophy

In

Chemistry

Timothy E. Long (Chair)
Robert Moore (Member)
John B. Matson (Member)
Louis A. Madsen (Member)

May 3, 2016
Blacksburg, Virginia

Keywords: phosphonium, block copolymers, additive manufacturing, photopolymerization, anionic polymerization, Michael addition

ABSTRACT

Ion-containing macromolecules continue to stimulate new opportunities for emerging electro-active applications ranging from high performance energy devices to water purification membranes. Progress in polymer synthesis and engineering now permit well-defined, ion-containing macromolecules with tunable morphologies, mechanical performance, ion conductivity, and 3D structure in order to address these globally challenged technologies. Achieving tailored chemical compositions with high degrees of phase separation for optimizing conductivity and water adsorption remains a constant synthetic challenge and presents an exciting opportunity for engineering sophisticated macromolecular architectures. This dissertation will introduce unprecedented charged polymers using conventional free radical and anionic polymerization to incorporate ionic functionalities based on phosphonium cations. This new class of copolymers offers unique properties with ionic functionality for tailorable electro-active performance.

Concurrent advances in synthesis and precise manufacturing of advanced polymeric materials are also required to meet these diverse technologies. Herein, we will reveal the synergy between polymer chemistry and additive manufacturing (also known as 3D Printing), introducing the advantage of this rapidly emerging manufacturing technology and its application in the layer-by-layer fabrication of tailored phosphonium polymerized ionic liquids (PILs) with high architectural precision and reproducibility. Varying phosphonium monomer concentration, diacrylate crosslinking comonomer, and display images enabled precise 3D design and polymeric properties. The resulting crosslinked phosphonium PIL objects exhibited a synergy of high thermal stability, tunable glass transition temperature, and optical clarity. Ion conductivity measurements on printed objects revealed a systematic progression in conductivity with ionic liquid monomer

content, and thermal properties and solvent extraction demonstrated the formation of a polymerized ionic liquid network with gel fractions exceeding 95%. The advanced electromechanical properties of phosphonium-containing macromolecules continue to provide new polymerization strategies for phosphorus-containing monomers.

For the first time, we also reveal anionic polymerization as an unprecedented and efficient strategy for achieving well-defined phosphorus-containing macromolecules. The polymerization of 4-diphenylphosphino styrene (DPPS) afforded the controlled synthesis of phosphorus-containing homopolymers, poly(DPPS-*b*-S) and poly(I-*b*-DPPS) diblock copolymers, and poly(S-*b*-I-*b*-DPPS) ABC triblock copolymers. These well-defined block copolymer architectures exhibited predictable molecular weights and narrow polydispersities, as well as ordered phase separated morphologies and tunable mechanical properties. *In situ* Fourier transform infrared (FTIR) spectroscopy was employed to monitor the anionic polymerization in real time, using the vinyl CH_2 out-of-plane wag vibration for each polymerizing monomer to generate a 2D waterfall plot for peak absorbance *vs.* time (min). Pseudo-first-order kinetic analysis determined observed rate constants, k_{obs}, for each propagation step. Sized exclusion chromatography revealed the living polymerization process, depicting molecular weight shifts in the SEC traces upon sequential monomer addition. Post-alkylation enabled controlled placement of phosphonium functionality in within the block copolymer compositions, producing well-defined phosphonium-containing block copolymers with low degrees of compositional heterogeneity.

In order to advance this polymerization strategy further, we also report synthetic efforts for enabling living anionic polymerization with an unprecedented piperazine-containing difunctional organolithium initiator, 1,4-bis[4-(1-phenylethenyl)benzyl] piperazine (DPHPL). Current literature reveals a synthetic gap for dilithium initiators suitable with anionic polymerization

conditions involving nonpolar solvents. The appeal remains high for the opportunity to synthesize well-defined thermoplastic elastomers with low degrees of compositional heterogeneity in the rubbery midblock microstructure and with diverse external block sequences with varying levels of polarity. Piperazine provided a polar unit within the difunctional initiator design, promoting ion dissociation and miscibility with hydrocarbon solvents and enabling the initiation and propagation of isoprene. This novel initiator facilitates the synthesis of thermoplastic elastomers with desired cis-1,4 microstructure in polydienes.

Enabling the green synthesis of sophisticated polymer architectures is also a major concern for these emerging technologies and Michael addition chemistry provides a synthetic approach for designing novel macromolecular compositions with ambient and solvent-free conditions and high tolerance to an abundance of polymerizable monomers with diverse functionality. Our final chapter will describe this synthetic method and its application in developing 2-component acetoacetate curing systems for solvent-free adhesive technologies. These efforts focus on functionalizing hydroxyl-terminated, hydrogenated polybutadiene oligomers to achieve novel bisacetoacetate Michael donors and diacrylate Michael acceptors. Analytical methods involving *In situ* FTIR spectroscopy and rheology were used to investigate these novel, 2-component Michael adhesives and elucidate the effects of catalyst concentration, temperature, and Michael acceptor composition on gel times and crosslinked network moduli. The Michael addition reaction permits the green synthesis of hyperbranched polydiene networks with ambient and solvent-free conditions and high tolerance to diverse monomers. Exploring novel macromolecular compositions using a vast array of polymerizable Michael donors and acceptors will further facilitate solvent-free adhesive technologies.

ACKNOWLEDGEMENTS

I would like to thank my advisor, Prof. Timothy Long, for his guidance, encouragement, and support during my time in graduate school. His passion for scientific discovery and consistent strive for excellence helped me accomplish my scientific goals and strengthen my development as a polymer scientist. He is an excellent scientist and professional role model, and I am grateful for the influence of his advisement and leadership throughout my scientific pursuits. I would also like to extend my gratitude to my committee members for their participation and support: Prof. Robert Moore, Prof. John Matson, and Prof. Louis Madsen. I would like to acknowledge Dr. Renlong Gao for his mentorship during my first year of graduate school and teaching me the importance of working aggressively toward achieving my research goals. Special thanks also to Dr. Chainika Jangu, Dr. Phil Lambert, Nicholas Chartrain, and Gregory Fahs for their friendship and collaboration throughout my graduate program. I will always cherish the successful research endeavors and fun moments we shared together in Blacksburg. I would like to thank all my senior group members, previous and present, for their encouragement, discussions, and support: Mana Tamami, Shijing Cheng, Mike Allen, Sean Hemp, Nancy Zhang, Tianyu Wu, Matthew Green, Steve June, David Inglefield, Daniel Buckwalter. I am also thankful to our post-docs, previous and present, for their advisement: Asem Abdulahad, Maruti Hegde, Nick Moon, and Sachin Bobade. Additionally, I would like to thank the rest of the Long group members who I interacted with who were pivotal during my graduate career: Philip Scott, Mingtao Chen, Ashley Nelson, Evan Margaretta, Keren Zhang, Joe Dennis, Dan Buckwalter, David Inglefield, Renlong Gao, Matt Green, Steve June, Mana Tamami, and all of my undergraduates (David Ruohoniemi, Niki Camateros-Mann, James Reese).

I would also like to extend my thanks to collaborators and funders in our research: Dr. Frederick Beyer and the Army Research Laboratory; Dr. Carl Willis and Kraton Polymers; Mike Scanish, Bill Schneider, Dan Cotsakis, Anil Shenoy and Carlisle Construction and Materials. I would like to thank our funding source from the U.S. Army Research Laboratory and the U.S. Army Research Office under contract/grant number W911NF-07-1-0452 Ionic Liquids in Electro-Active Devices Multidisciplinary University Research Initiative (ILEAD MURI). Finally, I am forever grateful to my family for their continued love and support in my life endeavors. I am thankful for both my older sisters, Samantha Robinson and Dr. Danielle Schultz, for their love and friendship which continues to motivate me in pursuing my goals. I would like to thank Danielle for being a strong role model throughout my graduate career in chemistry and inspiring me to pursue my own endeavors for a PhD. I am deeply thankful to my parents, Leon and Joan Schultz. Words cannot quantify how much I love them. Their love and support throughout my life has strengthened me to pursue all my life goals.

TABLE OF CONTENTS

Chapter 1. Charged Block Copolymers for Energy Harvesting and Water Purification Technologies 1

1.1 Abstract 1

1.2 Introduction 2

1.3 Morphological benefits of charged block copolymers 3

1.4 Sulfonated styrenic block copolymers 7

1.5 New directions for charged block copolymers 11

1.6 Conclusions 16

1.7 References 16

Chapter 2. 3D Printing Ionic Liquid Networks with Mask Projection Micro-Stereolithography 21

2.1 Abstract 21

2.2 Introduction 22

2.3 Experimental 25

2.3.1 Materials 25

2.3.2 Instrumentation 25

2.3.3 Anion exchange reaction of phosphonium IL 27

2.3.4 MPuSL working curves for photocuring phosphonium PIL networks 28

2.3.5 MPuSL fabrication process for 3D printing phosphonium PIL networks 29

2.4 Results and Discussion 30

2.5 Conclusions 41

2.6 Acknowledgements 42

2.7 References 42

Chapter 3. 3D Printing Hierarchical Polymeric Structures for Tissue-Engineered Scaffolds 45

3.1 Abstract 45

3.2 Introduction 46

3.3 Experimental 48

3.3.1 Materials 48

3.3.2 Instrumentation 48

3.3.3 Synthesis of PPG and Pluronic diacrylate 49
3.3.4 MPuSL fabrication process for 3D printing pluronic networks 49
3.4 Results and Discussion 50
3.5 Conclusions 60
3.6 Acknowledgements 60
3.7 References 61
Chapter 4. Phosphonium-Containing Diblock Copolymers from Living Anionic Polymerization of Diphenylphosphino Styrene 63
4.1 Abstract 63
4.2 Introduction 64
4.3 Experimental 66
4.3.1 Materials 66
4.3.2 Instrumentation 66
4.3.3 *In situ* FTIR monitoring of the anionic polymerization of 4-diphenylphosphino styrene 67
4.3.4 Anionic polymerization of poly(4-diphenylphosphino styrene-*b*-styrene) 68
4.3.5 Anionic polymerization of poly(isoprene-*b*-4-diphenylphosphino styrene) 69
4.3.6 Alkylation of poly(I-b-DPPS) diblock copolymers 69
4.3.7 Film casting 70
4.4 Results and Discussion 71
4.5 Conclusions 80
4.6 Acknowledgements 80
4.7 References 81
Chapter 5. Phosphorus-Containing ABC Triblock Copolymers from Living Anionic Polymerization of 4-Diphenylphosphino Styrene 83
5.1 Abstract 83
5.2 Introduction 84
5.3 Experimental 86
5.3.1 Materials 86
5.3.2 Instrumentation 86
5.3.3 *In situ* FTIR monitoring of the anionic polymerization of poly(S-*b*-I-*b*-DPPS) 87
5.3.4 Anionic polymerization of poly(S-*b*-I-*b*-DPPS) 88

5.3.5 Film casting 89
5.4 Results and Discussion 89
5.5 Conclusions 98
5.6 Acknowledgements 99
5.7 References 99
Chapter 6. Piperazine-Containing Dilithium Anionic Initiators Based of 1,1-Diphenylethylene Compounds 102
6.1 Abstract 102
6.2 Introduction 103
6.3 Experimental Section 105
6.3.1 Materials 105
6.3.2 Instrumentation 105
6.3.3 Synthesis of 1,4-*bis*[4-(1-phenylethenyl)benzyl] piperazine (*bis*-DPEP) 105
6.3.4 *In Situ* FTIR spectroscopy monitors *bis*-DPEP dilithium initiator production 108
6.3.5 *In Situ* FTIR spectroscopy monitors the anionic polymerization of isoprene using *bis*-DPEP dilithium initiator production 108
6.3.6 Anionic polymerization with *bis*-DPEP dilithium initiator achieves high molecular weight, polyisoprene homopolymers 109
6.4 Results and Discussion 109
6.5 Conclusions 113
6.6 Acknowledgements 114
6.7 References 114
Chapter 7. Acetoacetate Curing Systems for Solvent-Free Based Roofing Adhesives 116
7.1 Abstract 116
7.2 Introduction 117
7.3 Experimental 119
7.3.1 Materials 119
7.3.2 Instrumentation 119
7.3.3 Synthesis of Krasol diacrylate, Michael acceptors 120
7.3.3 Synthesis of Krasol bisAcAc, Michael donors 121
7.3.4 Network formation 121

7.3.5 In situ FTIR reactions for model studies 122
7.3.5 Preparing EPDM, PVC, and TPO tensile samples with Michael adhesives 122
7.4 Results and Discussion 123
7.5 Conclusions 141
7.6 Acknowledgements 142
7.7 References 142
Chapter 8. Suggested Work 144
8.1 Phosphonium-containing polyurethanes for mask projection microstereolithography 144
8.2 Phosphonium-containing diblocks for 3D printing with thiol-ene “click” chemistry 146
8.3 Phosphonium-containing ABC triblock copolymers for ion-transport studies 147
8.4 Living anionic polymerization with a piperazine-containing dilithium initiator achieves liquid polyisoprene diols 148
8.5 Living anionic polymerization with a piperazine-containing dilithium initiator achieves phosphorus-containing ABA triblock copolymers 151
8.6 4-Dichlorophosphino styrene enables the production of diverse phosphorus-containing styrenic monomers 153
8.7 References 154

LIST OF FIGURES

FIGURE 1.1. SCHEMATIC OF BLOCK COPOLYELECTROLYTES AND DISCUSSION OF NEUTRAL BLOCK COPOLYMERS AND CHARGE SOLUBILITY EFFECTS. (A), SCHEMATIC OF A NEUTRAL DIBLOCK COPOLYMER (TOP) OF LENGTH *N* WITH BLOCKS A AND B THAT INTERACT VIA AN INTERACTION PARAMETER X. A DIBLOCK COPOLYELECTROLYTE (BOTTOM) INCLUDES CHARGED MONOMERS ALONG THE A-BLOCK OF LENGTH $f_A N$, WITH MOBILE AND OPPOSITELY CHARGED COUNTERIONS NEARBY TO MAINTAIN OVERALL CHARGE NEUTRALITY. **(B)** CANONICAL PHASE DIAGRAM OF NEUTRAL BLOCK COPOLYMERS, WHICH FORM A DISORDERED PHASE (D) AS WELL AS HEXAGONAL (H), LAMELLAR (L), AND INVERSE-HEXAGONAL (H) NANOSTRUCTURES DEPENDING ON THE RELATIVE LENGTH OF THE A-BLOCK (IF THE IMMISCIBILITY X IS SUFFICIENTLY HIGH). **(C, D)** THE INFLUENCE OF CHARGE DUE TO ION ENTROPY AND SOLUBILITY EFFECTS BUT IGNORING THE (IMPORTANT) PRESENCE OF ELECTROSTATIC COHESION, WHEN Γ_A = 17.1 AND Γ_B = 27.8. ($E_{R,A}$ = 6.5 AND $E_{R,B}$ = 4.0, RESPECTIVELY, FOR ION RADII *A* = 0.25 NM). THE EFFECTS CAN BE CAPTURED BY SHIFTING X IN A MANNER PROPORTIONAL TO THE CHARGE FRACTION, AS SHOWN IN **(D)**, WHERE THE ORIGINAL PHASE BOUNDARIES (SHOWN IN **C**) COLLAPSE ONTO THE UNCHARGED PHASE BOUNDARIES FOR THE SHIFTED VALUE X_{EFF}, USING C = -160.0.[22] 4

FIGURE 1.2. EFFECT OF CHARGE COHESION ON NANOSTRUCTURE PHASE BEHAVIOUR. (**A)** ELECTROSTATIC COHESION BETWEEN THE CHARGED A-BLOCKS AND THE COUNTERIONS. IF THE COUPLING PARAMETER Γ >1, THE COMPONENTS ARE ELECTROSTATICALLY CORRELATED IN A LIQUID-LIKE ORDERED STRUCTURE, HAVING PROFOUND CONSEQUENCES FOR THE PHASE DIAGRAM. WE NOTE THAT THIS IS ASYMMETRIC; COULOMBIC COHESION MANIFESTS ONLY IN THE CHARGED A-BLOCK AND NOT IN THE UNCHARGED B-BLOCK. (**B)** NANOSTRUCTURE PHASE BEHAVIOR FOR A NUMBER OF COULOMBIC INTERACTION STRENGTHS Γ (BLACK AND RED CURVES DENOTE PHASE BOUNDARIES). AT LOW VALUES OF Γ, NANOSTRUCTURE FORMATION IS SUPPRESSED BY THE ENTROPY OF THE COUNTERIONS THAT SUPPRESS DEMIXING, WHEREAS NANOSTRUCTURE FORMATION IS ENHANCED AT HIGHER VALUES OF Γ OWING TO COULOMBIC COHESION IN THE A-RICH PHASES. WE NOTE THAT ORDERED STATES ARE OBSERVED EVEN AT A = 0 FOR Γ = 17.1.[22] 6

FIGURE 1.3. CHARGE CONTROL OF PERCOLATING NANOSTRUCTURES. COMPARISON BETWEEN TWO INVERSE-HEXAGONAL NANOSTRUCTURES IN THE X, f_A-PLANE. ELECTROSTATIC COHESION OPENS THE PATHWAY TO A DIFFERENT TYPE OF INVERSE-HEXAGONAL STRUCTURE, WHERE THE CONTINUOUS PHASE IS FORMED BY THE CHARGED MINORITY COMPONENT—SHOWN HERE FOR Γ = 17.1 AND A CHARGE FRACTION OF THE A-BLOCK OF 15% (GREEN CROSS). THE CHEMICAL AND DIELECTRIC PROPERTIES OF BCPS CAN ONLY ALLOW FOR THOSE HEXAGONAL PHASES WHERE THE CONTINUOUS PHASE IS FORMED BY THE MAJORITY COMPONENT (BLACK CROSS). THESE ARE SCHEMATICALLY SHOWN AT THE BOTTOM, ALONG WITH EXAMPLE PATHS FOR ION TRANSPORT THROUGH THE CHARGED A PHASE (ORANGE). TRANSPORT IN CHARGED SYSTEMS IS THROUGH A PERCOLATING MINORITY PHASE THAT MAY POSSESS TRANSPORT PROPERTIES ASSOCIATED WITH THE A/B INTERFACE, WHEREAS THE UNCHARGED SYSTEM IS PRIMARILY A BULK MAJORITY PHASE PERCOLATING AROUND MINORITY OBSTRUCTIONS.[22] 6

FIGURE 1.4. (A) THROUGH-PLANE AND (B) IN-PLANE 1D SMALL-ANGLE X-RAY SCATTERING INTENSITY VERSUS SCATTERING VECTOR AS A FUNCTION OF IEC. THE INSETS SHOW THROUGH-PLANE (A) AND IN-PLANE (B) 2D SMALL-ANGLE X-RAY SCATTERING PATTERNS OF

P-2.0 PENTABLOCK COPOLYMER MEMBRANE. THE ANGLE BETWEEN TWO DASHED LINES IN THE 2D IN-PLANE SCATTERING PATTERN (B) INDICATES THE INTEGRATED AZIMUTHAL ANGLE. THE EXCESS SCATTERING IN THE VERTICAL DIRECTION IN THE 2D IN-PLANE SCATTERING ARISES FROM THE SURFACE REFLECTION, BECAUSE THE X-RAY BEAM IS WIDER THAN THE FILM THICKNESS. (C) SCHEMATIC ILLUSTRATION OF MORPHOLOGICAL CHANGES WHEN MEMBRANES ARE CAST FROM SOLUTION. THE PENTABLOCK COPOLYMERS FORM MONODISPERSE SPHERICAL MICELLES WITH DENSE SS CORES AND HI-TBS CORONAE SWOLLEN BY SOLVENT IN CYCLOHEXANE/HEPTANE SOLUTIONS. IN MEMBRANES THE SS DOMAINS ARE DISCRETE WHEN2R < D AND INTERCONNECTED WHEN 2R > D, WHERE R INDICATES THE CORE RADIUS IN SOLUTION AND D REPRESENTS THE CENTER-TO-CENTER DISTANCE OF THE SS MICRODOMAINS IN THE MEMBRANE. THESE TWO DIMENSIONAL REPRESENTATIONS ARE NECESSARILY HIGHLY IDEALIZED RENDITIONS OF COMPLEX THREE-DIMENSIONAL MORPHOLOGIES.[1] 8

FIGURE 1.5. GRAPHICAL REPRESENTATION OF SODIUM CHLORIDE PERMEABILITY VERSUS DONOR CELL SALT CONCENTRATION FOR SULFONATED BLOCK COPOLYMERS AND NAFION® 111. IEC VALUES IN UNITS OF MEQ/G.[30] 9

FIGURE 1.6. (A) CHEMICAL STRUCTURES AND SMALL-ANGLE X-RAY SCATTERING PROFILES SHOWING A HIGHER DEGEE OF SELF-ASSEMBLY FOR MORE FLEXIBLE ALKYL ENDBLOCKS AS EVIDNENCED BY THE HIGHER ORDER CORRELATION PEAK IN THE SCATTERING PROFILE. (B) CONDUCTIVITY OF (LEFT) 29 MOL% SULFONATED AND (RIGHT) 100 MOL% SULFONATED PHMA AND PFMA TRIBLOCK COPOLYMERS AS A FUNCTION OF RELATIVE HUMIDITY.[31] 10

FIGURE 1.7. SULFONIMIDE-CONTAINING TRIBLOCK COPOLYMERS FOR IMPROVED CONDUCTIVITY AND MECHANICAL PERFORMANCE.[37] 11

FIGURE 1.8. (A) TEMPERATURE-DEPENDENT IONIC CONDUCTIVITY (Σ) OF TRIBLOCK COPOLYMERS WITH VARYING COMPOSITIONS OBTAINED USING NMR (OPEN SYMBOLS) AND ELECTROCHEMICAL IMPEDANCE SPECTROSCOPY (EIS) (CLOSED SYMBOLS) **(B)** TEMPERATURE-DEPENDENT IONIC CONDUCTIVITY NORMALIZED WITH TG OF THE CENTRAL BLOCK. **(C)** SAXS ANALYSIS OF A−BC−A TRIBLOCK COPOLYMERS CONFIRMING MICROPHASE SEPARATION WITH DIFFERING ION CONTENT AS COMPARED TO A HOMOGENEOUS MORPHOLOGY OBSERVED IN THE RANDOM COPOLYMER (IN GREEN).[37] 12

FIGURE 1.9. TEMPERATURE-DEPENDENT IONIC CONDUCTIVITY OF POLY(STY-*B*-[EVBIM][TF_2N]-*B*-STY) WITH 0, 20, AND 40 WT% [EMIM][TFO] PLOTTED VERSUS 1000/T.[43] 13

FIGURE 1.10. IONIC CONDUCTIVITY OF AMMONIUM- AND PHOSPHONIUM-CONTAINING PILS. PHOSPHONIUM PILS EXHIBITED HIGHER IONIC CONDUCTIVITIES THAN AMMONIUM ANALOGS. IMPEDANCE SPECTROSCOPY PERFORMED FROM 135 °C TO 95 °C IN 10 °C/STEP USING A FOUR-POINT IN-PLANE CELL.[70] 14

FIGURE 1.11. SMALL ANGLE X-RAY SCATTERING PROFILES REVEAL ORIENTED BULK MORPHOLOGIES FOR POLY(I-*B*-DPPS), POLY(I-*B*-C_6DPPS)$^+BR^-$, AND POLY(I-*B*-C_{12}DPPS)$^+BR^-$ DIBLOCK COPOLYMERS. APPEARANCE OF BROAD PEAK IN POLY(I-*B*-C_{12}DPPS)$^+BR^-$ SCATTERING PROFILE CORRESPONDS TO INTERDIGITATED BILAYERS.[76] 15

FIGURE SI 2.1. WORKING CURVES FOR POLY(PEGDNMA), POLY(PEGDMA_{90}-*CO*-TOPTF_2N_{10}), AND POLY(PEGDMA_{75}-*CO*-TOPTF_2N_{25}) WITH 2 WT. % PHOTOINITIATOR 28

FIGURE SI 2.2. TGA CHARACTERIZATION OF POLY(PEGDMA-*CO*-TOPTF_2N) 3D PRINTED RECTANGULAR TEST SPECIMENS CONTAINING 0 MOL%, 5 MOL%, 10 MOL%, 25 MOL%, AND 40 MOL% TOPTF_2N. 30

FIGURE 2.1. PHOTORHEOLOGY CHARACTERIZATION OF (A) POLY(BDA) AND (B) POLY(PEGDMA) AT VARIOUS LIGHT INTENSITY EXPOSURE. (C) PHOTORHEOLOGY CHARACTERIZATION COMPARING STRUCTURE-PROCESSING RELATIONSHIPS BETWEEN POLY(BDA),

POLY(PEGDMA), POLY(BDA_{90}-*CO*-$TOPTF_2N_{10}$), AND POLY($PEGDMA_{90}$-*CO*-$TOPTF_2N_{10}$) AT 5 MW/CM^2 LIGHT INTENSITY EXPOSURE. 35
FIGURE 2.2. MASK PROJECTION MICRO-STEREOLITHOGRAPHY SUCCESSFULLY 3D PRINTS POLY(PEGDMA-*CO*-$TOPTF_2N$) 33 MM TALL RECTANGULAR TEST SPECIMENS, 8 MM TALL CONES, 8 MM TALL HYPERBOLOID, AND 8 MM TALL FIGURINE. 36
FIGURE 2.3. X-RAY MICROCT IMAGE OF 3D PRINTED POLY($PEGDMA_{90}$-*CO*-$TOPTF_2N_{10}$) CONES IN COMPARISON TO ORIGINAL CAD DESIGN. 37
FIGURE 2.4. DETAILED IMAGES OF 3D PRINTED POLY($PEGDMA_{90}$-*CO*-$TOPTF_2N_{10}$) HYPERBOLOID WITH OPTICAL MICROSCOPY AND SCATTERING ELECTRON MICROSCOPY 37
FIGURE 2.5. DSC CHARACTERIZATION FOR POLY(PEGDMA-*CO*-$TOPTF_2N$) 3D PRINTED RECTANGLULAR TEST SPECIMENS CONTAINING 0 MOL%, 5 MOL%, 10 MOL%, 25 MOL%, AND 40 MOL% $TOPTF_2N$. 39
FIGURE 2.6. IONIC CONDUCTIVITY FOR POLY(PEGDMA-*CO*-$TOPTF_2N$) 3D PRINTED RECTANGULAR FILMS WITH 10 MOL%, 25 MOL%, AND 40 MOL% $TOPTF_2N$. THE RELATIVE HUMIDITY WAS MAINTAINED AT 10% OVER THE 60 TO 150 °C. 41
FIGURE 3.1. (A) PHOTORHEOLOGY OF PLURONIC L-31 DIACRYLATE AT VARIOUS LIGHT INTENSITY EXPOSURE. (C) PHOTORHEOLOGY COMPARISON BETWEEN PLURONIC L-31, L-61, AND 10RS AT 5 MW/CM^2 LIGHT INTENSITY EXPOSURE. 53
FIGURE 3.2. MASK PROJECTION MICRO-STEREOLITHOGRAPHY SUCCESSFULLY 3D PRINTS DIACRYLATE FUNCTIONALIZED PPG, PLURONIC L-31, L-61, AND 10RS 33 MM TALL RECTANGULAR TEST SPECIMENS, AND PLURONIC L-61 8 MM TALL SCAFFOLD. 55
FIGURE 3.3. DETAILED IMAGES OF 3D PRINTED PLURONIC L-61, SCAFFOLD WITH OPOTICAL MICROSCOPY. 55
FIGURE 3.4. DETAILED IMAGES OF 3D PRINTED PLURONIC L-61, SCAFFOLD WITH SCATTERING ELECTRON MICROSCOPY. 56
FIGURE 3.5. X-RAY MICROCT IMAGE OF 3D PRINTED POLURONIC L-61 SCAFFOLD IN COMPARISON TO ORIGINAL CAD IMAGE. 56
FIGURE 3.6. PHOTO-POLYMERIZATION AND 3D PRINTING ENABLES (A) 3D PRINTED TEST BARS WITH HORIZONTAL LAYERS, (B) PHOTO-CROSSLINKED BARS, AND (C) 3D TEST BARS WITH VERTICAL LAYERS. 57
FIGURE 3.7. DMA CHARACTERIZATION OF 3D PPG PRINTED TEST BARS WITH HORIZONTAL LAYERS, PHOTO-CROSSLINKED PPG BARS, AND 3D PRINTED PPG BARS WITH VERTICAL LAYERS.. 58
FIGURE 3.8. TENSILE ANALYSIS OF (A) 3D PPG PRINTED TEST BARS WITH HORIZONTAL LAYERS, (B) PHOTO-CROSSLINKED PPG BARS, AND (C) 3D PRINTED PPG BARS WITH VERTICAL LAYERS. 50 MM/MIN, AVERAGE OF 5 SAMPLES 59
FIGURE 3.9. TENSILE ANALYSIS OF (A) 3D PLURONIC® 10R5, (B) 3D PLURONIC® L-31, AND (C) 3D PLURONIC® L-61 PRINTED TEST BARS WITH VERTICAL LAYERS. 50 MM/MIN, AVERAGE OF 5 SAMPLES 59
FIGURE SI 4.1. *IN SITU* FTIR MONTIORING OF DPPS VINYL DISAPPEARANCE AT 918 CM^{-1} OVER TIME IN A 3D WATERFALL PLOT AND 2D NORMALIZED PLOT. 68
FIGURE SI 4.2. ^1H NMR REVEALS P^+PH^3-CH_2- PROTONS AND ^{31}P NMR REVEALS PRODUCTION OF THE POHOSPHONIUM CATION, POST-ALKYLATION. 70
FIGURE 4.1. SEC CHARACTERIZATION FOR POLY(DPPS), POLY(DPPS-*B*-S) AFTER SEQUENTIAL ADDITION OF STYRENE, AND POLY(I-*B*-DPPS). 74
FIGURE 4.2. DMA CHARCTARIZATION OF POLY(I-*B*-DPPS), POLY(I-*B*-$C_6DPPS)^+BR^-$, AND POLY(I-*B*-$C_{12}DPPS)^+BR^-$ 76

FIGURE 4.3. SMALL ANGLE X-RAY SCATTERING PROFILES REVEAL BULK MORPHOLOGIES FOR POLY(I-*B*-DPPS). SCATTERING MAXIMA ARE OBSERVED AT Q*, 2Q*, 3Q*, 4Q*, INDICATING A LAMELLAR MORPHOLOGY.....78
FIGURE 4.4. SMALL ANGLE X-RAY SCATTERING PROFILES REVEAL BULK MORPHOLOGIES FOR POLY(I-*B*-C_6DPPS)$^+$BR$^-$. SCATTERING MAXIMA ARE OBSERVED AT Q*, 2Q*, 3Q*, 4Q*, INDICATING A LAMELLAR MORPHOLOGY.. 78
FIGURE 4.5. SMALL ANGLE X-RAY SCATTERING PROFILES REVEAL BULK MORPHOLOGIES FOR POLY(I-*B*-C_{12}DPPS)$^+$BR$^-$. SCATTERING MAXIMA ARE OBSERVED AT Q*, AND 2Q*, SUGESSTING A LESS ORDERED LAMELLAR MORPHOLOGY. A BROAD SCATTERING PEAK AT APPROXIMATELY Q = 2.1 NM^{-1} CORRESPONDS TO THE INTERDIGITATED PACKING OF DODECYL CHAINS ON THE PHOSPHONIUM CATION.....79
FIGURE 4.6. SMALL ANGLE X-RAY SCATTERING PROFILES REVEAL ORIENTED BULK MORPHOLOGIES FOR POLY(I-*B*-DPPS), POLY(I-*B*-C_6DPPS)$^+$BR$^-$, AND POLY(I-*B*-C_{12}DPPS)$^+$BR$^-$ DIBLOCK COPOLYMERS. APPEARANCE OF BROAD PEAK IN POLY(I-*B*-C_{12}DPPS)$^+$BR$^-$ SCATTERING PROFILE CORRESPONDS TO INTERDIGITATED BILAYERS 79
FIGURE 5.1. *IN SITU* FTIR SPECTROSCOPY MONITORS THE ANIONIC POLYMERIZATION OF POLY(S-*B*-I-*B*-DPPS), TRACKING THE C=C VINYL VIBRATIONAL FREQUENCY PEAKS FOR EACH PROPAGATING MONOMER (STYRENE, 908 CM^{-1}; ISOPRENE, 912 CM^{-1}; DPPS, 918 CM^{-1}).....91
FIGURE 5.2. PSEUDO-FIRST-ORDER KINETIC ANALYSIS OF POLY(S-*B*-I-*B*-DPPS) ABC TRIBLOCK COPOLYMERS.....92
FIGURE 5.3. SEC RESULTS FOR POLY(S-*B*-I-*B*-DPPS) ABC TRIBLOCK COPOLYMERS.....93
FIGURE 5.4. DMA CHARACTERIZATION FOR POLY(S_{25}-*B*-I_{50}-*B*-$DPPS_{25}$), POLY(S_{50}-*B*-I_{50}-*B*-$DPPS_{25}$), AND POLY(S_{20}-*B*-I_{120}-*B*-$DPPS_{50}$) 94
FIGURE 5.5. TENSILE STRESS-STRAIN CURVES FOR POLY(S_{25}-*B*-I_{50}-*B*-$DPPS_{25}$), POLY(S_{50}-*B*-I_{50}-*B*-$DPPS_{25}$), AND POLY(S_{20}-*B*-I_{120}-*B*-$DPPS_{50}$) 95
FIGURE 5.6. ATOMIC FORCE MICROSCOPY IMAGES REVEAL SURFACE MORPHOLOGIES FOR (A) POLY(S_{25}-*B*-I_{50}-*B*-$DPPS_{25}$), (B) POLY(S_{50}-*B*-I_{50}-*B*-$DPPS_{25}$), AND (C) POLY(S_{20}-*B*-I_{120}-*B*-$DPPS_{50}$) 97
FIGURE 5.7. SMALL ANGLE X-RAY SCATTERING PROFILES REVEAL ORIENTED BULK MORPHOLOGIES FOR POLY(S_{25}-*B*-I_{50}-*B*-$DPPS_{25}$), POLY(S_{50}-*B*-I_{50}-*B*-$DPPS_{25}$), AND POLY(S_{20}-*B*-I_{120}-*B*-$DPPS_{50}$) ABC TRIBLOCK COPOLYMERS. 98
FIGURE 6.1. COMMON DIFUNCTIONAL INITIATORS BASED ON DOUBLE 1,1-DPE COMPOUNDS. 104
FIGURE SI 6.1. GC-MS CONFIRMS THE TARGET MOLECULAR WEIGHT OF THE ISOLATED 1,4-BIS[4-(1-PHENYLETHENYL)BENZYL] PIPERAZINE.....107
FIGURE SI 6.2. (A) ^{1}H AND (B) ^{13}C NMR SPECTROSCOPY CONFIRMS STRUCTURE AND PURITY 1,4-BIS[4-(1-PHENYLETHENYL)BENZYL] PIPERAZINE 107
FIGURE 6.2 *IN SITU* FTIR MONITORS THE VINYL CONCENTRATION DISAPPEARANCE VERSUS TIME FOR (A) 1,4-BIS[4-(1-PHENYLETHENYL)BENZYL] PIPERAZINE (967 CM^{-1}) AND (B) ISOPRENE (912 CM^{-1}).....111
FIGURE 6.3. SEC CHARACTERIZATION OF POLYISOPRENES WITH VARIOUS MOLECULAR WEIGHTS 113
FIGURE 7.1. SHEAR VISCOSITIES FOR KRASOL® OLIGOMERS, GENERATED USING SHEAR SWEEPS AT A CONSTANT 1 HZ FREQUENCY AND CONSTANT TEMPERATURE. FILLED DOTS CORRESPOND TO SHEAR VISCOSITY AT 25 ^{O}C AND EMPTY DOTS CORRESPOND TO 50 ^{O}C. 125
FIGURE 7.2. CONTACT ANGLE MEASUREMENTS FOR KRASOL® OLIGOMERS WITH VARIABLE END GROUP FUNCTIONALITY. MODIFICATIONS FROM A DIOL TO A DIACRYLATE AND BISACETOACETATE INFLUENCES THE DEGREE OF WETTING. 125
FIGURE 7.3. *IN SITU* FTIR SPECTROSCOPY MONITORS THE MICHAEL CROSSLINKING REACTION AS A FUNCTION OF MICHAEL ACCEPTOR COMPOSITIONS, TRACKING THE C=C VINYL

VIBRATIONAL FREQUENCY PEAKS FOR EACH ACCEPTOR (KRASOL® DA, 890 CM^{-1}; 1,4-BDA, 0810 CM^{-1}; AND TMPTA, 815 CM^{-1}). 128
FIGURE 7.4. *IN SITU* FTIR SPECTROSCOPY MONITORS THE MICHAEL CROSSLINKING REACTION WITH 1.0:1.4 MOLAR RATIOS OF KRASOL BISACAC TO MICHAEL ACCEPTOR, WHERE THE MICHAEL ACCEPTOR = KRASOL DA (BLUE), OR A 95:5 MOL% RATIO OF KRASOL DA: TMPTA (PURPLE). TRACKING THE C=C VINYL VIBRATIONAL FREQUENCY PEAKS FOR KRASOL® DA (890 CM^{-1}) GENERATED THE 2D WATERFALL PLOT. 128
FIGURE 7.5. PSEUDO-FIRST-ORDER KINETIC ANALYSIS CALCULATES THE OBSERVED RATES, K_{OBS} (S^{-1}), OF MICHAEL CROSSLINKING REACTIONS AS A FUNCTION OF MICHAEL ACCEPTOR COMPOSITIONS. 129
FIGURE 7.6. *IN SITU* FTIR SPECTROSCOPY MONITORS THE MICHAEL CROSSLINKING WITH THE PRESENCE OF 10 WT. % TACKIFIER, INDOPOLE H-100 OR WINGTACK 10, TRACKING THE C=C VINYL VIBRATIONAL FREQUENCY PEAKS FOR KRASOL® DA AT 890 CM^{-1}. 131
FIGURE 7.7. PSEUDO-FIRST-ORDER KINETIC ANALYSIS CALCULATES THE OBSERVED RATES, K_{OBS} (S^{-1}), OF MICHAEL CROSSLINKING REACTIONS WITH THE PRESENCE OF 10 WT. % TACKIFIER, INDOPOLE H-100 OR WINGTACK 10. 131
FIGURE 7.8. RHEOLOGICAL CHARACTERIZATION OF MICHAEL NETWORK FORMATION AS FUNCTION OF WT. % DBU CATALYST. (A) GRAPHICAL SUMMARY OF GEL TIME (MIN) VS. WT. % DBU. (B) REPRESENTATIVE RHEOLOGICAL PLOT OF G' AND G" (PA) VS. TIME (MIN) FOR NETWORK CROSSLINKING WITH 2 WT. % DBU. 133
FIGURE 7.9. RHEOLOGICAL CHARACTERIZATION OF MICHAEL NETWORK FORMATION AS FUNCTION OF TEMPERATURE. (A) GRAPHICAL SUMMARY OF GEL TIME (MIN) VS. TEMPERATURE (^{O}C). (B) REPRESENTATIVE RHEOLOGICAL PLOT OF G' AND G" (PA) VS. TIME (MIN) FOR NETWORK CROSSLINKING WITH 1 WT. % DBU AT 25 ^{O}C. 134
FIGURE 7.10. RHEOLOGICAL CHARACTERIZATION OF MICHAEL NETWORK FORMATION AS FUNCTION OF MICHAEL ACCEPTOR COMPOSITIONS: KRASOL® DA, 1,4-BDA, AND TMPTA. (A) GRAPHICAL SUMMARY OF GEL TIME (MIN) VS. TEMPERATURE (^{O}C). (B) REPRESENTATIVE RHEOLOGICAL PLOT OF G' AND G" (PA) VS. TIME (MIN) FOR CROSSLINKING 1,4-BDA WITH 1 WT. % DBU AT 25 ^{O}C. 135
FIGURE 7.11. RHEOLOGICAL CHARACTERIZATION OF ACETOACETATE CURING SYSTEMS INVOLVING KRASOL® BISACAC AND 1,4-BDA WITH VARIABLE TEMPERATURE (^{O}C). (A) GRAPHICAL SUMMARY OF GEL TIME (MIN) VS. TEMPERATURE (^{O}C). (B) REPRESENTATIVE RHEOLOGICAL PLOT OF G' AND G" (PA) VS. TEMPERATURE (^{O}C) FOR NETWORK CROSSLINKING WITH 1 WT. % DBU AT 50 ^{O}C. 136
FIGURE 7.12. RHEOLOGICAL CHARACTERIZATION OF KRASOL® NETWORK FORMATION AS WITH THE PRESENCE OF 10 WT. % TACKIFIER, INDOPOLE H-100 OR WINGTACK 10. (A) GRAPHICAL SUMMARY OF GEL TIME (MIN) VS. TEMPERATURE (^{O}C). (B) REPRESENTATIVE RHEOLOGICAL PLOT OF G' AND G" (PA) VS. TIME (MIN) FOR CROSSLINKING 1,4-BDA WITH 1 WT. % DBU AT 25 ^{O}C. 137
FIGURE 7.13. INSTRON 180 PEEL TESTS OF ACETOACETATE CURING SYSTEMS INVOLVING 2000 G/MOL KRASOL® BISACETOACETATE AND DIACRYLATE (2K KRASOL®), AND 2000 G/MOL KRASOL® BISACETOACETATE AND THE COMMERCIALLY AVAILABLE 1,4-BUTANEDIOL DIACRYLATE (2K KRASOL®: 1,4 BDA), NEOPRENE AND TPO BASED BONDING ADHESIVES, AND LOW VOC BONDING ADHESIVES. REPRESENTATIVE PLOTS OF AVERAGE DATA OF 3 ADHERED ROOFING SAMPLES: (A) EPDM TO EPDM, (B) PVC TO PVC, AND (C) TPO TO TPO. 139
FIGURE 7.14. INSTRON 180 PEEL TESTS OF ACETOACETATE CURING SYSTEMS INVOLVING 2000 G/MOL KRASOL® BISACETOACETATE AND DIACRYLATE (2K KRASOL®) WITH 10 WT. % INCORPORATED TACKIFIERS WINGTACK-10 OR INDOPOLE H-100. REPRESENTATIVE PLOTS OF

AVERAGE DATA OF 3 ADHERED ROOFING SAMPLES: (A) EPDM TO EPDM, (B) PVC TO PVC, AND (C) TPO TO TPO.....140

LIST OF TABLES

Table 2.1. Thermal properties, % gel fraction, and VFT fitting and alaysis of PIL conductivity data for poly(PEGDMA-co-TOPTf2N) 3D printed rectangular test specimens 39
Table 3.1. Compositional details for Pluronic diols 51
Table 4.1. Small angle x-ray scattering tabulated peak postiions 77
Table 5.1. SEC results for poly(S-b-I-b-DPPS) triblock copolymers. 93
Table 5.2. Summary of Tensile Properties for poly(S_{25}-*b*-I_{50}-*b*-$DPPS_{25}$), poly(S_{50}-*b*-I_{50}-*b*-$DPPS_{25}$), poly(S_{20}-*b*-I_{120}-*b*-$DPPS_{20}$) 96
Table 7.1. Instron 180^{o} peel tests results 141

LIST OF SCHEMES

SCHEME 2.1. (A) ANION EXCHANGE OF PHOSPHONIUM 4-VINYLBENZYL TRIOCTYL PHOSPHONIUM CHLORIDE. (B) SYNTHESIS OF POLY(PEGDMA-*CO*-TOPTF$_2$N) AND POLY(BDA-*CO*-TOPTF$_2$N) CROSSLINKED 3D NETWORKS. 32
SCHEME 3.1. GENERAL REACTION SCHEME FOR SYNTHESIZING AND PHOTOPOLYMERIZING PPG AND PLURONIC® DIACRYLATES. 51
SCHEME 4.1. ANIONIC POLYMERIZATION ACHIEVES POLY(DPPS). 71
SCHEME 4.2. SEQUENTIAL MONOMER ADDITION ACHIEVES COPOLYMERIZATION OF DIBLOCKS (**A**) POLY(DPPS-*B*-S) IN POLAR SOLVENT CONDITIONS AND (**B**) POLY(I-*B*-DPPS) IN NONPOLAR SOLVENT CONDITIONS. 73
S**CHEME 4.3.** POST-ALKYLATION PRODUCES PHOSPHONIUM CONTAINING DIBLOCK COPOLYMERS, POLY(I-*B*-C_6DPPS)$^+$BR$^-$ AND POLY(I-*B*-C_{12}DPPS)$^+$BR$^-$ 74
S**CHEME 5.1.** SEQUENTIAL MONOMER ADDITION ACHIEVES POLY(S-B-I-B-DPPS) TRIBLOCK COPOLYMERS. 9074
SCHEME 6.1. SYNTHETIC METHOD FOR PREPARATION OF 1,4-BIS[4-(1-PHENYLETHENYL)BENZYL] PIPERAZINE AND DILITHIUM DERIVATIVE. 111
SCHEME 6.2. 1,4-BIS[4-(1-PHENYLETHENYL)BENZYL] PIPERAZINE DILITHIUM INITIATOR IN THE SYNTHESIS OF POLYISOPRENES. 112
SCHEME 7.1. GENERAL REACTION SCHEME SYNTHESIZING KRASOL® A) MICHAEL ACCEPTOR AND B) MICHAEL DONOR. 123
SCHEME 7.2. MICHAEL ADDITION REACTION FOR SYNTHESIS OF KRASOL® CROSSLINKED MICHAEL NETWORKS. 126
SCHEME 7.3. MODEL REACTION KINETIC STUDIES FOR MICHAEL ADDITION REACTIONS AS A FUNCTION OF MICHAEL ACCEPTOR COMPOSITIONS: KRASOL® DA, 1,4-BDA, AND TMPTA. 127
SCHEME 7.4. MODEL REACTION KINETIC STUDIES FOR MICHAEL ADDITION REACTIONS WITH THE PRESENCE OF 10 WT. % TACKIFIER, INDOPOLE H-100 OR WINGTACK 10. 130
SCHEME 7.5. MICHAEL ADDITION CURING REACTION OF KRASOL® DIACRYLATE AND BISACETOACETATE AS A FUNCTION OF DBU CONCENTRATION. 132
SCHEME 7.6. MICHAEL ADDITION CURING REACTION AS A FUNCTION OF TEMPERATURE. 133
SCHEME 7.7. MICHAEL ADDITION CURING REACTION OF 2-COMPONENTS INVOLVING 2000 G/MOL KRASOL® BISACETOACETATE AND THE COMMERCIALLY AVAILABLE 1,4-BUTANEDIOL DIACRYLATE AS FUNCTION OF TEMPERATURE (^{O}C). 136
SCHEME 8.1.1. PROPOSED TRANSESTERIFICATION REACTION BETWEEN DIMETHYL 5-BENZYL TRIOCTYLPHOSPHONIUM BIS(TRIFLUOROMETHANE) SULFONAMIDE SALT AND PTMO 145
SCHEME 8.1.2. TWO-STEP SYNTHESIS OF PTMO-BASED URETHANE DIACRYLATES 146
SCHEME 8.2.1. THIOL-ENE "CLICK" CHEMISTRY AFFORDS EFFICIENT UV-CURING OF POLYOLEFINS 147
SCHEME 8.3.1. ALKYLATING PHOSPHORUS-CONTAINING ABC TRIBLOCK COPOLYMERS ENABLE CATION-CONTAINING STYRENIC BLOCK COPOLYMERS TO COMPLEMENT SULFONATED ANALOGUES 148
SCHEME 8.4.1. SYNTHETIC METHOD FOR PRODUCING AND INITIATING 1,4-BIS[4-(1PHENYLETHENYL)BENZYL] PIPERAZINE. 150
SCHEME 8.4.2. SYNTHETIC ROUTE FOR ACHIEVING HYDROGENATED POLYISOPRENE DIOLS. 150
SCHEME 8.5.1. ANIONIC POLYMERIZATION WITH A PIPERAZINE-CONTAINING DILITHIUM INITIATOR AFFORDS POLY(DPPS-*B*-I-*B*-DPPS). 152

SCHEME 8.6.1. ALKYLATION REACTION WITH DICHLOROPHOSPHINO STYRENE AFFORDS DIVERSE PHOSPHINO STYRENIC MONOMERS WITH ALKYL OR PHENYL SUBSTITUENTS. 153

Chapter 1: Charged Block Copolymers for Energy Harvesting and Water Purification Technologies

Alison R. Schultz and Timothy E. Long

Macromolecules Innovation Institute, Department of Chemistry, Virginia Tech, Blacksburg

VA 24061

*To whom correspondence should be addressed. E-mail: telong@vt.edu TEL: (540) 231-2480

FAX: (540) 231-8517

Keywords: Ion-containing block copolymers, water purification, energy storage, sulfonated block copolymers, sulfonamide, phosphonium

1.1 *Abstract*

Ion-containing block copolymers afford well-defined structural compositions with diverse morphologies for tunable mechanical and ion transport properties, suitable for electro-active membrane applications in energy harvesting and water purification. This review features current accomplishments in polymer science, pertaining to ion-containing block copolymers and their unique physical properties. New theoretical studies provide more precise representation of phase behavior in ion-containing block copolymers, enabling more accurate evaluations of morphological influences on enhanced ion transport properties in block copolymer membranes. Compositional changes to sulfonated styrenic block copolymers achieve tunable water and ion transport properties, and novel functionalized styrenic monomers enable new directions for sulfonamide- and phosphonium- containing block copolymer analogues. Collectively, these

interdisciplinary accomplishments reveal the potential role of ion-containing block copolymers in addressing modern day global challenges in energy and clean water.

1.2 *Introduction*

Pursuing versatile ion-containing block copolymer compositions continues to stimulate new opportunities for addressing global concerns involving energy and clean water. Synthetic advances in polymer science now permit well-defined, ion-containing block copolymers with tunable morphologies, mechanical performance, and ion conductivity for emerging electro-active applications ranging from high performance energy devices to water purification membranes. Achieving tailored chemical compositions with high degrees of phase separation for optimizing conductivity and water adsorption remains a synthetic challenge and presents an exciting opportunity for engineering sophisticated macromolecular architectures. Sulfonated block copolymers[1-8] represent exemplary ion-containing compositions, abundantly appearing in the literature as promising membranes for fuel cell and water purification technologies and inspiring new synthetic directions for cation-containing polymeric derivatives.

Previous investigations involving sulfonated polymers predominately involved segmented block compositions containing sulfonated poly(imide)[9], poly(phenylene)[10], poly(ketone)[11,12], and poly(sulfone) units.[13] Diverse electro-active applications for these charged polymers enabled fundamental insight into the effects of sulfonation levels on morphology, water adsorption, and ion transport properties, facilitating innovative discoveries in the dynamics of water-polymer and ion-polymer interactions. Theoretical development with simulated models, coupled with experimental investigations involving nuclear magnetic resonance[14,15], dielectric[16,17], fluorescence[18,19], and infrared[20] spectroscopy provided multiple length scales for measuring Brownian diffusion of water and ions through polymeric membranes, revealing tunable transport

mechanisms as a function of sulfonation levels and morphology. Lack of controlled charge placement remains a synthetic limitation for sulfonated segmented block compositions and restricts commercialization for water purification technologies. These synthetic concerns inspire alternative directions for controlled free radical and anionic polymerization strategies, enabling sophisticated block copolymer architectures with low degrees of compositional heterogeneity for tunable physical and mechanical properties.

This review features an ensemble of theoretical and synthetic accomplishments in polymer science, pertaining to ion-containing block copolymers and their unique physical properties. Recent physical studies provide more precise representation of phase behavior in ion-containing block copolymers, enabling new theoretical evaluations for morphological influences on enhanced ion transport properties in block copolymer membranes. Compositional changes to sulfonated styrenic block copolymers achieve tunable water and ion transport properties, and novel functionalized styrenic monomers enable new directions for sulfonimide-, imidazolium-, ammonium-, and phosphonium- containing block copolymer analogues. Collectively, these interdisciplinary accomplishments enable a new perspective on ion-containing block copolymers and their potential role in facilitating technologies for energy harvesting and water purification.

1.3 *Morphological benefits of charged block copolymers*

Ion-containing block copolymers self-assemble into well-defined nanostructures, enabling thermally stable compositions with tunable electromechanical properties for customized ion exchange membranes. Successful optimization in ion exchange capacity requires a physical representation for the synergistic relationship of morphology and ion conductivity, which reveals the profound effects of ion concentration on nanostructure. Until recently, phenomenological

understanding for the phase behavior in block copolymers depended on the classic Flory-Huggins model and failed to provide a precise representation of ionic concentration effects on microphase separation.[1,21] The conventional model is capable of accounting for long-range Coulombic interactions between charged species, including charges along polymer backbones as well as mobile counterions, considering only counterion solubility effects on suppressing or enhancing phase separation (Fig. 1). For both cases, adjusting the phase behavior shifts phase diagrams and, with a correction for immiscibility, collapses the phase diagrams onto a single, universal curve that maps directly to traditional phase diagrams for uncharged block copolymers.

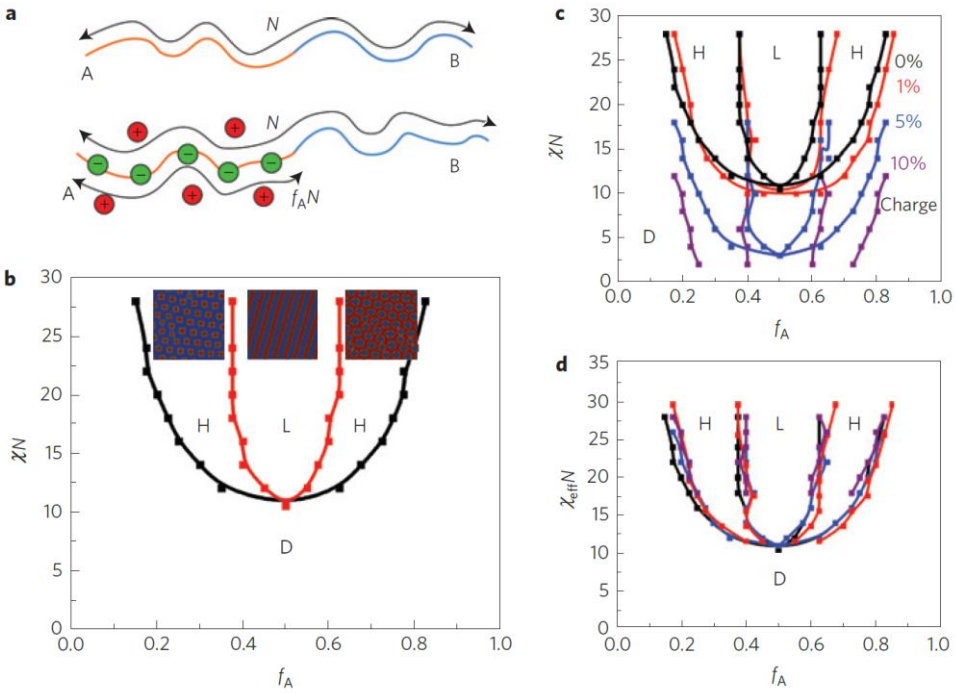

Figure 1.1. Schematic of block copolyelectrolytes and discussion of neutral block copolymers and charge solubility effects. (a), Schematic of a neutral diblock copolymer (top) of length N with blocks A and B that interact via an interaction parameter χ. A diblock copolyelectrolyte (bottom) includes charged monomers along the A-block of length $f_A N$, with mobile and oppositely charged counterions nearby to maintain overall charge neutrality. **(b)** Canonical phase diagram of neutral block copolymers, which form a disordered phase (D) as well as hexagonal (H), lamellar (L), and inverse-hexagonal (H) nanostructures depending on the relative length of the A-block (if the immiscibility χ is sufficiently high). **(c, d)** The influence of charge due to ion entropy and solubility effects but ignoring the (important) presence of electrostatic cohesion, when $\Gamma_A = 17.1$ and $\Gamma_B = 27.8$. ($\varepsilon_{r,A} = 6.5$ and $\varepsilon_{r,B} = 4.0$, respectively, for ion radii $a = 0.25$ nm). The effects can

be captured by shifting χ in a manner proportional to the charge fraction, as shown in **(d)**, where the original phase boundaries (shown in **c**) collapse onto the uncharged phase boundaries for the shifted value χ_{eff}, using C = -160.0.[22]

Olvera de la Cruz *et al.* proposed a new model to address local charge-level effects that arise from the presence of long-range electrostatic forces, which manifest as short-range charge ordering, and contribute to a large cohesion among charged monomers and ions.[22] The new model combines self-consistent field theory and liquid state theory[23] to capture and relate both length scales and establish an accurate thermodynamic representation of charged block copolymers (Fig. 1.2). The Coulombic strength, Γ, of electrostatic cohesion drastically alters the phase diagram shape and enables electrostatic manipulation for achieving new nanostructures that are inaccessible to conventional uncharged block copolymers, including percolated phases for ion transport. Nanostructures such as the inverse hexagonal and lamellar phases are in principle "percolating" structures, owing to the possibility of an ion transporting along an uninterrupted pathway through the material.[24] In this context, electrostatic cohesion facilitates new phases, inaccessible to traditional uncharged block compositions, enabling phase separation into percolating structures even when the charged block sequence is the minority phase (Fig. 1.3). This provides beneficial ramifications in battery and water purification membrane applications, affording ion transport channels without resorting to more elaborate chain architectures typically required to form similar structures.

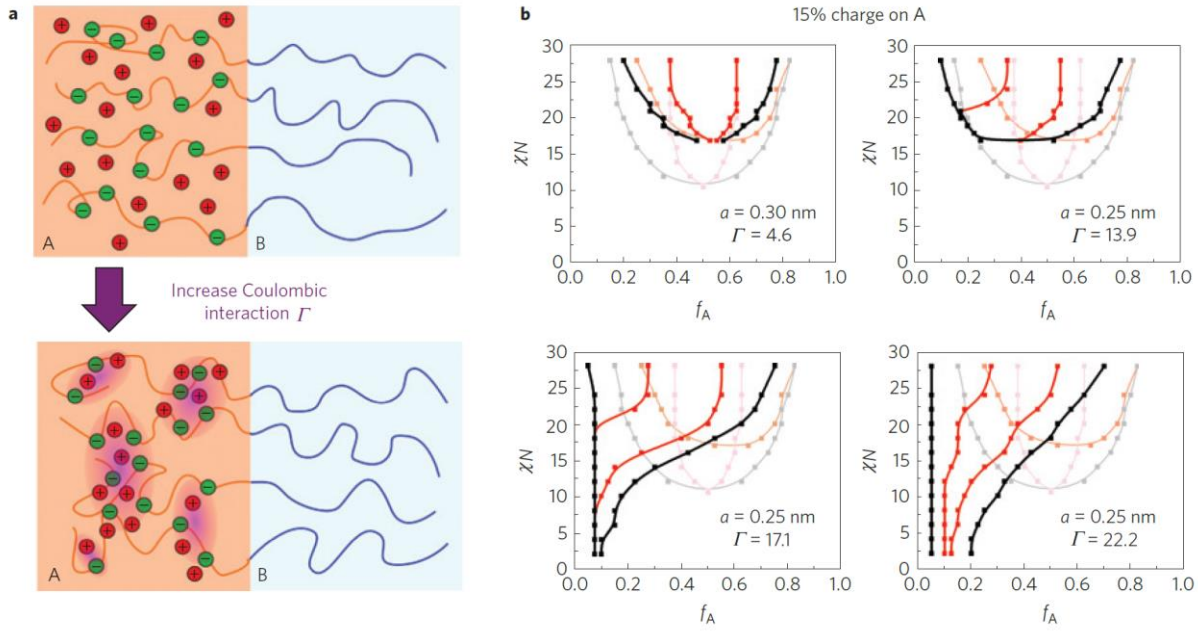

Figure 1.2. Effect of charge cohesion on nanostructure phase behavior. (**a)** Electrostatic cohesion between the charged A-blocks and the counterions. If the coupling parameter Γ >1, the components are electrostatically correlated in a liquid-like ordered structure, having profound consequences for the phase diagram. We note that this is asymmetric; Coulombic cohesion manifests only in the charged A-block and not in the uncharged B-block. (**b)** Nanostructure phase behavior for a number of Coulombic interaction strengths Γ (black and red curves denote phase boundaries). At low values of Γ, nanostructure formation is suppressed by the entropy of the counterions that suppress demixing, whereas nanostructure formation is enhanced at higher values of Γ owing to Coulombic cohesion in the A-rich phases. We note that ordered states are observed even at α = 0 for Γ = 17.1.[22]

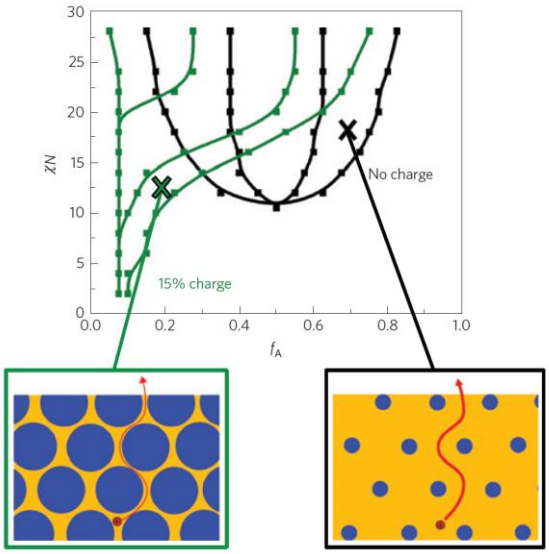

Figure 1.3. Charge control of percolating nanostructures. Comparison between two inverse-hexagonal nanostructures in the χ, f_A-plane. Electrostatic cohesion opens the pathway to a different type of inverse-hexagonal structure, where the continuous phase is formed by the charged minority

component—shown here for $\Gamma = 17.1$ and a charge fraction of the A-block of 15% (green cross). The chemical and dielectric properties of BCPs can only allow for those hexagonal phases where the continuous phase is formed by the majority component (black cross). These are schematically shown at the bottom, along with example paths for ion transport through the charged A phase (orange). Transport in charged systems is through a percolating minority phase that may possess transport properties associated with the A/B interface, whereas the uncharged system is primarily a bulk majority phase percolating around minority obstructions.[22]

1.4 *Sulfonated Styrenic Block Copolymers*

Sulfonated styrenic block copolymers represent exemplary ion-containing compositions, possessing fortified viscoelastic behavior and enhanced microphase separation for improved ion-transport. Literature examples typically reveal phase separation within a modified Flory-Huggins diagram, where ionic association strength within these block compositions are accounted for with an increased interaction parameter χ, allowing for lower block molecular weights and improved microphase separation. Previous investigations involving sulfonated block copolymers elucidated effects of sulfonation level on morphologies and electro-active properties, predominately focusing on Kraton® sulfonated poly(styrene-*b*-hydrogenated butadiene-*b*-styrene) [poly(SS-*b*-HB-*b*-SS)] and sulfonated poly(styrene-*b*-hydrogenated isoprene-*b*-styrene) [poly(SS-*b*-HI-*b*-SS)] triblock copolymers.[25,26] High sulfonation content in the external block sequences, however, afforded highly hydrophilic membranes unsuitable for water purification applications due to high water uptake and poor mechanical properties. Kraton® sulfonated poly(tert-butyl styrene-*b*-hydrogenated isoprene-*b*-sulfonated styrene-*b*-hydrogenated isoprene-*b*-*tert*-butyl styrene) [poly(tBS-*b*-HI-*b*-SS-*b*-HI-*b*-tBS)] pentablock copolymers provide selectively sulfonated mid-blocks with 0-50 mol% sulfonation for tunable water uptake and ion-transport properties, and poly(HI-*b*-tBS) external blocks for tailored mechanical and elastomeric perfomance.[1,27-29] Increasing sulfonation content along the pentablock copolymer in a nonpolar solvent environment promotes micelle formation, where the SS midblock aggregates into a charged core surrounded by

a nonpolar corona composed of a poly(HI-*b*-tBS) matrix.[1] These electrostatic interactions enable new phase transitions for the charged block copolymer, where short-range electrostatic cohesion promotes percolated, interconnected microdomains with increasing charge content for improved ion-transport. Winey *et al.* observed this morphological phenomenon, observing transitions in SAXS profiles from discrete microdomains to an interconnected orientation as sulfonation levels increased to 50 mol% (2.0 IEC).[1]

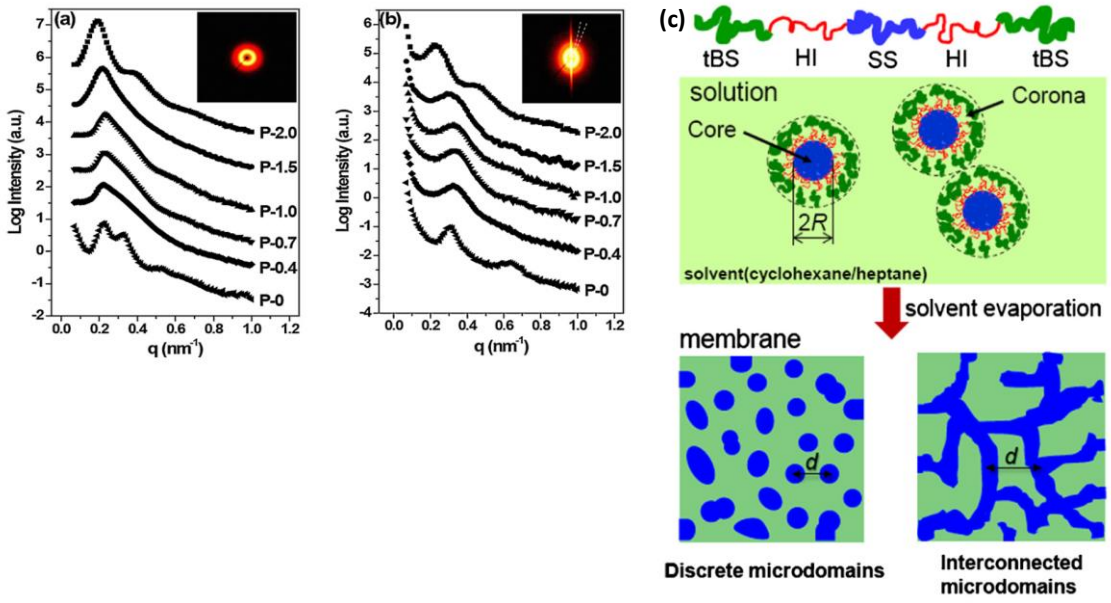

Figure 1.4. (a) Through-plane and (b) in-plane 1D small-angle X-ray scattering intensity versus scattering vector as a function of IEC. The insets show through-plane (a) and in-plane (b) 2D small-angle X-ray scattering patterns of P-2.0 pentablock copolymer membrane. The angle between two dashed lines in the 2D in-plane scattering pattern (b) indicates the integrated azimuthal angle. The excess scattering in the vertical direction in the 2D in-plane scattering arises from the surface reflection, because the X-ray beam is wider than the film thickness. (c) Schematic illustration of morphological changes when membranes are cast from solution. The pentablock copolymers form monodisperse spherical micelles with dense SS cores and HI-tBS coronae swollen by solvent in cyclohexane/heptane solutions. In membranes the SS domains are discrete when2R < d and interconnected when 2R > d, where R indicates the core radius in solution and d represents the center-to-center distance of the SS microdomains in the membrane. These two dimensional representations are necessarily highly idealized renditions of complex three-dimensional morphologies.[1]

Taking these morphological properties into account, Freeman *et al.* employed water permeability, salt permeability, and surface charge (zeta potential) experiments to characterize the copolymers.[30] Water uptake analysis revealed a directly proportional relationship between water permeability and sulfonation levels. It also showed that water uptake reduced when *tert*-butyl styrene content increased.[30] Salt permeability analysis produced similar results, showing a directly proportional relationship between sodium chloride uptake and sulfonation fraction. Likewise, increasing hydrophobic content along the copolymer reduced salt uptake. In addition to these factors, Freeman *et al.* also noticed comparable behavior between salt uptake and the donor cell sodium concentration levels, suggesting that these membranes operate under Donnan exclusion effects.[31] Overall, these trends seemed to compare and even exceed salt permeability measurements for Nafion® 111 (Fig. 1.5).[30]

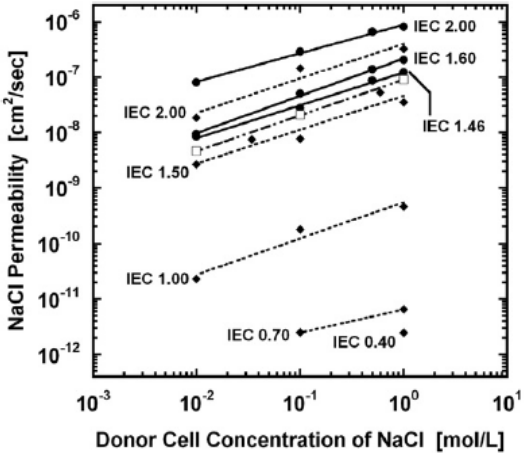

Figure 1.5. Graphical representation of sodium chloride permeability vs. donor cell salt concentration for block copolymers A (●) and B (♦) and Nafion® 111 (□). IEC values in units of meq/g.[30]

Many of these investigations focus on tuning the chemical composition, sulfonation level, and molecular weight of the hydrophilic phase for optimizing the composition and size of the ionic block where transport occurs. However, a few studies also reveal the influence of the non-ionic unit on ion transport. Hickner *et al.*, for example, prepared two triblock copolymers with identical sulfonated midblock segments and differing hydrophobic external blocks to demonstrate the effects of hydrophobicity on physical properties and morphologies.[32] Small-angle X-ray scattering profiles failed to reveal high ordered peaks for samples with more rigid, higher T_g fluorinated

external blocks, indicating a disordered morphology. Alternatively, triblock copolymer samples with more flexible alkyl external blocks promoted self-assembled nanostructures and two well-defined peaks in the X-ray scattering profile confirmed the ordered morphology (Fig. 1.6).[32] As expected, membranes with higher degrees of order exhibited increased ion conductivity than the unordered samples. In another study, Lovell *et al.* tuned the polarity of the non-ionic unit to achieve tailored graft copolymer architectures with predictable ion conductivity. Replacing poly(styrene) or poly(vinylidene fluoride) backbones with poly(acrylonitrile) graft copolymers with sulfonated grafts enabled membranes with increased water interactions along the poly(acrylonitrile) non-ionic main chain and resulted in lower conductivities.[33]

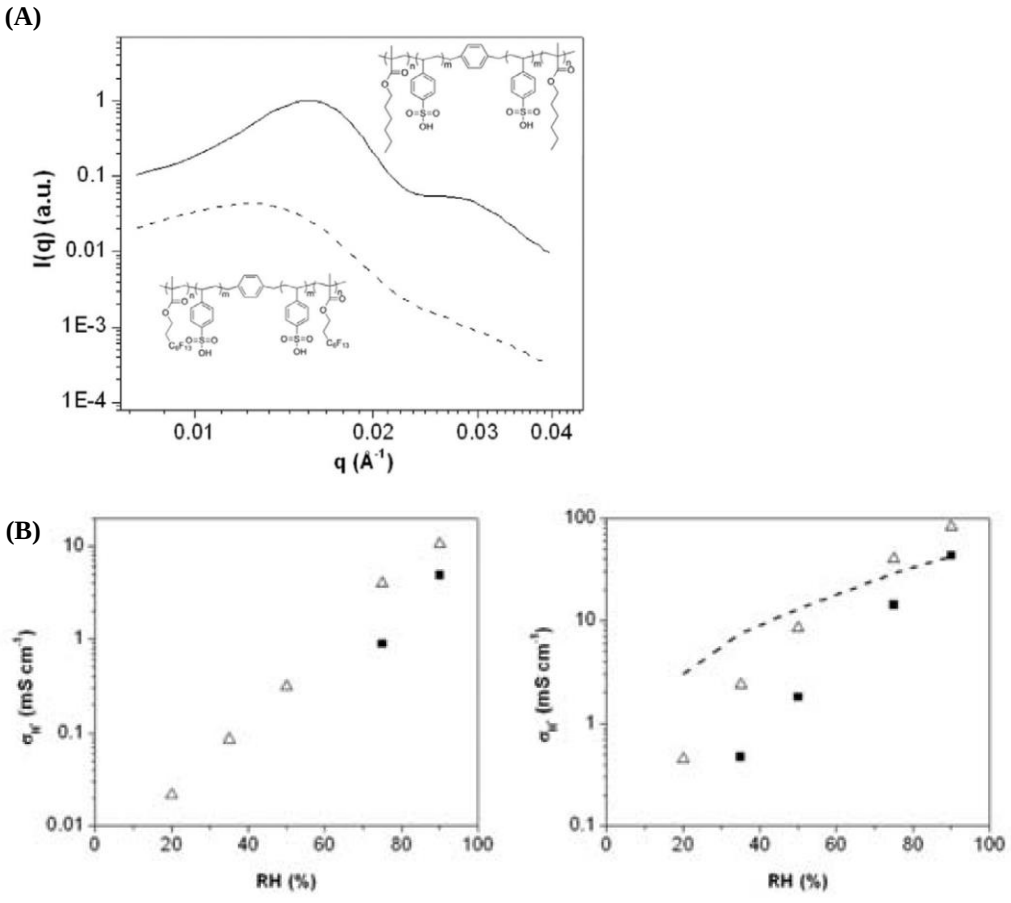

Figure 1.6. (A) Chemical structures and small-angle X-ray scattering profiles showing a higher degree of self-assembly for more flexible alkyl endblocks as evidenced by the higher order

correlation peak in the scattering profile. (B) Conductivity of (left) 29 mol% sulfonated and (right) 100 mol% sulfonated PHMA and PFMA triblock copolymers as a function of relative humidity; (■) PHMA, (▵) PHMA, (---) Nafion.[32]

1.5 *New directions for charged block copolymers*

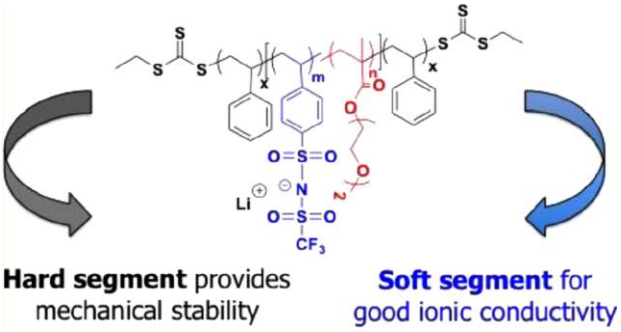

Figure 1.7. Sulfonimide-Containing Triblock Copolymers for Improved Conductivity and Mechanical Performance.[38]

Although literature reports extensively reveal sulfonated block copolymers as promising membranes for technologies ranging from fuel cells and water purification[34] to actuators[35] and nanofabrication[36], concern for thermal and charge stability due to low temperature degradation reactions poses an architectural design flaw and inspires new directions in polymerizing alternative charged monomers.[29,37] Our group recently demonstrated the reversible addition−fragmentation chain transfer (RAFT) polymerization of a 4-styrenesulfonyl-(trifluoromethylsulfonyl)imide monomer for the synthesis of well-defined ionomeric A−BC−A triblock copolymers, featuring a microphase-separated morphology and a combination of excellent mechanical properties and high ion transport (Fig 1.7 and 1.8).[38] The soft central "BC" block is composed of poly(4-styrenesulfonyl-(trifluoromethylsulfonyl)imide) (poly(Sty-Tf_2N)) with $-SO_2-N^--SO_2-CF_3$ anionic groups associated with a mobile lithium cation and low-T_g di(ethylene glycol)methyl ether methacrylate (DEGMEMA) units. External polystyrene A blocks provide mechanical strength with nanoscale morphology even at high ion content. In the central block, the Sty-Tf_2N monomer enables an important delocalization of the negative charge. Li+ ions are not strongly associated with the polymer chain, thus enabling fast transport and high ion conductivity.[39]

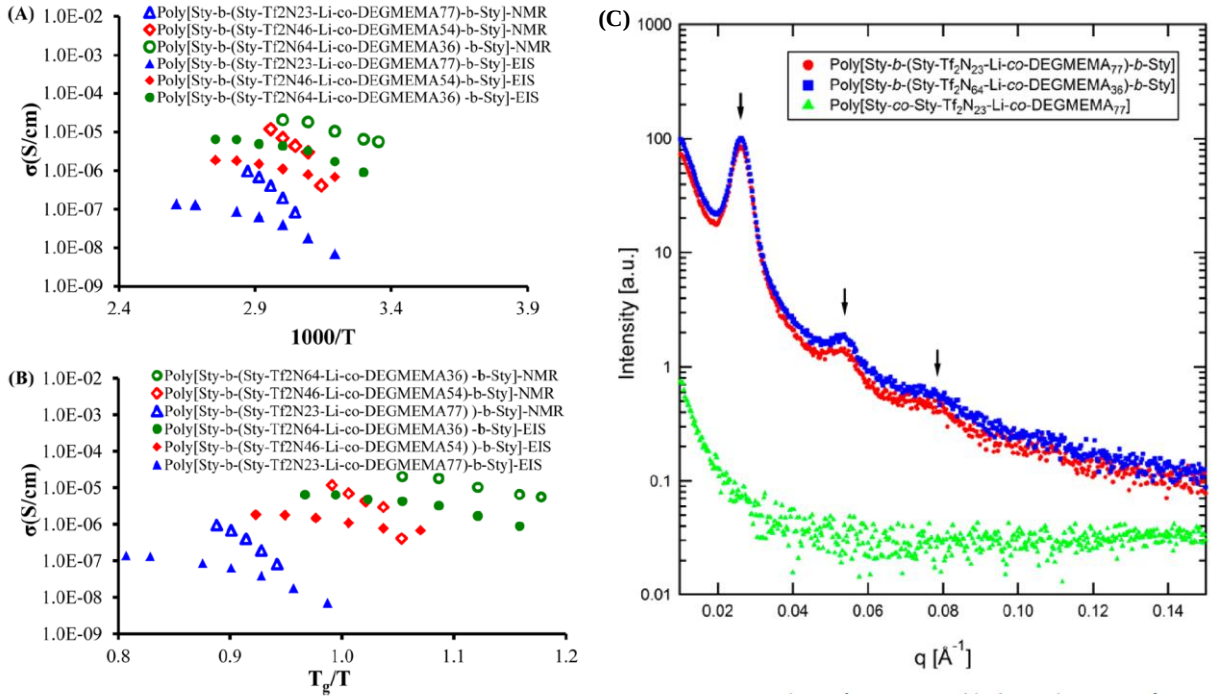

Figure 1.8. (A) Temperature-dependent ionic conductivity (σ) of triblock copolymers with varying compositions obtained using NMR (open symbols) and electrochemical impedance spectroscopy (EIS) (closed symbols) **(B)** Temperature-dependent ionic conductivity normalized with Tg of the central block. **(C)** SAXS analysis of A−BC−A triblock copolymers confirming microphase separation with differing ion content as compared to a homogeneous morphology observed in the random copolymer (in green).[38]

Watanabe and DesMarteau first addressed the idea of charge delocalization on perfluorinated sulfonimide,[40,41] and Armand *et al.* demonstrated the synthesis of poly(Sty-Tf_2N)$^-$ Li^+ blends with PEO and producing single-ion polymer electrolytes for lithium batteries. Ion conductivities were approximately 10 times higher for a membrane with poly(Sty-Tf_2N) ($\sim 10^{-6}$ S/cm at 70 °C) compared to a membrane with lithium poly-(styrene sulfonate).[39] Incorporating ethylene oxide units into the perfluorinated polysulfonimide afforded crown ether-like complexes to promote solvation and dissociation of ionic aggregates. Ethylene oxide also lowers the T_g of the charged block copolymers, thereby increasing segmental mobility and ionic conductivity. Feng *et al.* synthesized copolymers of poly(Sty-Tf_2N)$^-Li^+$ and methoxypoly(ethylene glycol) acrylate, which had an ion conductivity of $\sim 10^{-6}$ S/cm at 25 °C and 10^{-4} S/cm at 60 °C.[39]

Polymerization of imidazolium-based styrenic monomers is another common method for achieving single-ion conductors suitable for electo-active membrane applications for energy harvesting and ion exchange membranes. Numerous studies focus on optimizing polyelectrolyte homopolymer properties to maximize their impact on block copolymer functionality upon copolymerization. Mahanthappa *et al.* probed ionic conductivities of poly(vinylbenzyl imidazolium)s with different alkyl substituent lengths and counterions.[42] They also examined the influence of morphology on ionic conductivity of well-defined poly(styrene-*b*-vinylbenzyl imidazolium) diblock copolymers, revealing an increase of ionic conductivity over two orders of magnitude with increasing imidazolium block lengths.[42] Long *et al.* further investigated poly(styrene-*b*-vinylbenzyl imidazolium-*b*-styrene) ABA triblock copolymers, revealing compositional effects on mechanical properties, water uptake, and ion conductivity.[43] These studies also revealed ionic liquid incorporation as a systematic approach for increasing ion conductivity, complementing previous ionic liquid swell studies from Lodge, Frisbie *et al.* with poly(styrene-*b*-ethylene oxide-*b*-styrene) and poly(styrene-*b*-methyl methacrylate-*b*-styrene) triblock copolymers, poly(styrene-b-ethylene oxide-b-styrene) and poly(styreneb-methyl methacrylate-b-styrene).[44]

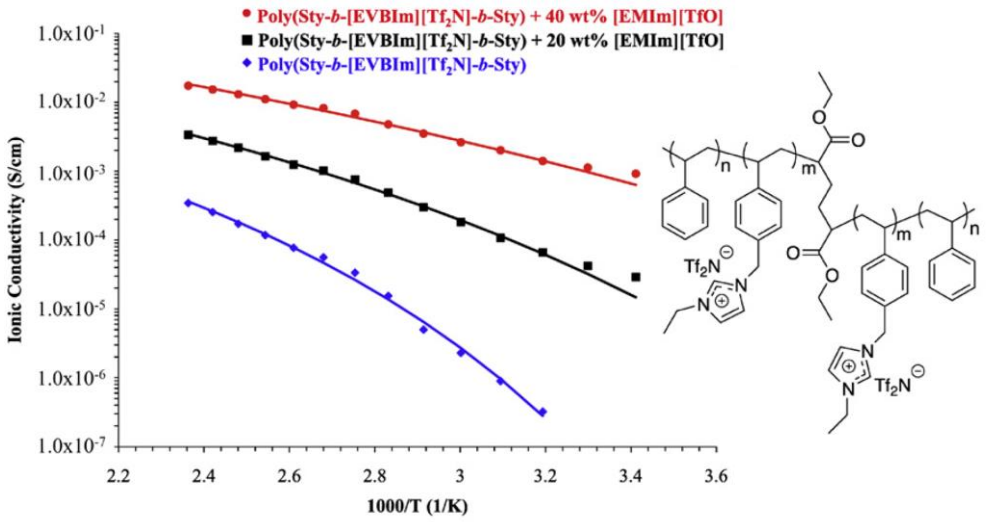

Figure 1.9. Temperature-dependent ionic conductivity of poly(Sty-*b*-[EVBIm][Tf_2N]-*b*-Sty) with 0, 20, and 40 wt% [EMIm][TfO] plotted versus 1000/T.[43]

Commonly investigated ammonium poly(ionic liquids) (PILs) include quaternized poly(2-dimethylaminoethyl methacrylate),[45] poly(vinylbenzyl ammonium)s,[46] and poly(diallyldimethylammonium chloride).[47] Similar to ammonium ILs, they typically exhibit poor thermal stabilities with basic counterions due to a Hoffman elimination mechanism, where the counterion abstracts a β-hydrogen, in the first step of an elimination reaction.[48] Recent studies reveal phosphonium PILs as superior analogues to ammonium PILs, exhibiting enhanced thermal and chemical stability, and improved ion conductivity.[47,49-58] Increasing the atomic radii from a cationic nitrogen to cationic phosphorus affords phosphonium-containing compositions with enhanced cationic strength in comparison to ammonium-analogues, attributing to their improved physical and chemical properties.[50,59-69] Long *et al.* reported a detailed structure–property relationship study of ammonium and phosphonium PILs, examining the influence of cation selection, alkyl substituent length and phosphonium PILs on thermal properties, ionic conductivities, and morphologies.[70] These investigations revealed ionic conductivity values an order of magnitude higher for phosphonium PILs in comparison to ammonium analogues (Fig. 1.10).[70]

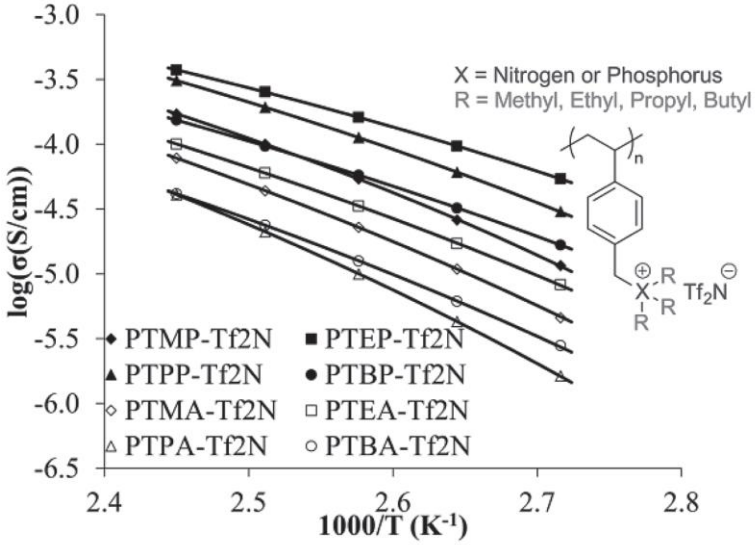

Figure 1.10. Ionic conductivity of ammonium- and phosphonium-containing PILs. Phosphonium PILs exhibited higher ionic conductivities than ammonium analogs. Impedance spectroscopy performed from 135 °C to 95 °C in 10 °C/step using a four-point in-plane cell.[70]

As widely documented in the literature, substitution reactions involving 4-vinylbenzyl chloride and nucleophilic phosphines produce styrenic monomers bearing phosphonium functionality at the *para*-benzylic site.[71] While benzylic substitution affords facile monomer synthesis, thermal and chemical instability also results due to the acidity of benzylic hydrogens and susceptibility to undergo Hoffman elimination degradation.[71] 4-Diphenylphosphino styrene (DPPS) is a commercially available monomer without benzylic protons, eliminating the possibility of the Hoffman elimination mechanism. In a previous communication, Long et al. demonstrated for the first time the unique ability of DPPS to polymerize under harsh anionic polymerization conditions and produce unprecedented phosphonium-containing diblock copolymers.[72] Post-alkylation enabled controlled placement of phosphonium functionality in poly(I-*b*-DPPS) diblock copolymers, producing well-defined phosphonium-containing block copolymers with low degrees of compositional heterogeneity. Incorporating phosphonium charge disrupted the highly ordered lamellar bulk morphology of the neutral diblock precursor and gave rise to new morphologies involving interdigitated packing of alkyl chains on the phosphonium cation, for tuning ion-transport properties.

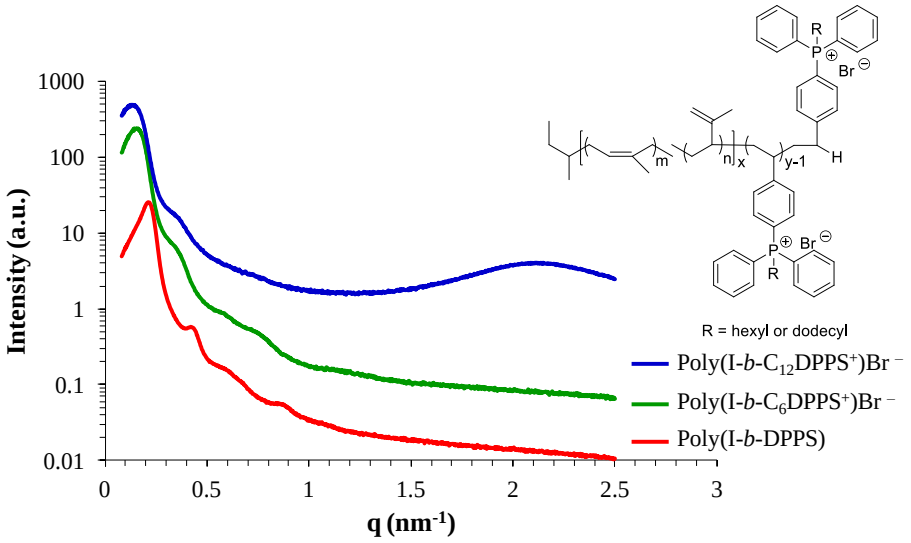

Figure 1.11. Small Angle X-Ray Scattering profiles reveal oriented bulk morphologies for poly(I-*b*-DPPS), poly(I-*b*-C_6DPPS)$^+Br^-$, and poly(I-*b*-C_{12}DPPS)$^+Br^-$ diblock copolymers. Appearance of broad peak in poly(I-*b*-C_{12}DPPS)$^+Br^-$ scattering profile corresponds to interdigitated bilayers.[72]

1.6 *Conclusions*

This review features current accomplishments in polymer science, pertaining to ion-containing block copolymers and their unique physical properties. Ion-containing block copolymers for achieving well-defined structural compositions with diverse morphologies for tunable mechanical and ion transport properties, suitable for electro-active membrane applications in energy harvesting and water purification. New theoretical studies provide more precise representation of phase behavior in ion-containing block copolymers, enabling more accurate evaluations of morphological influences on enhanced ion transport properties in block copolymer membranes. Compositional changes to sulfonated styrenic block copolymers achieve tunable water and ion transport properties, and novel functionalized styrenic monomers enable new directions for sulfonimide-, imidazolium-, ammonium-, and phosphonium- containing block copolymer analogues. Collectively, these interdisciplinary accomplishments reveal the potential role of ion-containing block copolymers in addressing modern day global challenges in energy and clean water.

1.7 *References*

(1) Choi, J.-H.; Willis, C. L.; Winey, K. I. *J. membr. sci.* **2012**, *394*, 169.

(2) Harrison, W. L.; Hickner, M. A.; Kim, Y. S.; McGrath, J. E. *Fuel Cells* **2005**, *5*, 201.

(3) Hickner, M. A.; Ghassemi, H.; Kim, Y. S.; Einsla, B. R.; McGrath, J. E. *Chem. Rev.* **2004**, *104*, 4587.

(4) Park, H. B.; Freeman, B. D.; Zhang, Z.-B.; Sankir, M.; McGrath, J. E. *Angewandte Chemie International Edition* **2008**, *47*, 6019.

(5) Sumner, M. J.; Harrison, W. L.; Weyers, R. M.; Kim, Y. S.; McGrath, J. E.; Riffle, J. S.; Brink, A.; Brink, M. H. *J. Membr. Sci.* **2004**, *239*, 199.

(6) Wang, S. M., J. E. In *Synthetic Methods In Step-Growth Polymers*; Rogers, M. E. L., Timothy E., Ed.; Wiley: New York, 2003, p 327.

(7) Xie, W.; Cook, J.; Park, H. B.; Freeman, B. D.; Lee, C. H.; McGrath, J. E. *Polymer* **2011**, *52*, 2032.

(8) Xie, W.; Park, H.-B.; Cook, J.; Lee, C. H.; Byun, G.; Freeman, B. D.; McGrath, J. E. *Water Sci. Technol.* **2010**, *61*, 619.

(9) Asano, N.; Aoki, M.; Suzuki, S.; Miyatake, K.; Uchida, H.; Watanabe, M. *Journal of the American Chemical Society* **2006**, *128*, 1762.

(10) Kobayashi, T.; Rikukawa, M.; Sanui, K.; Ogata, N. *Solid State Ionics* **1998**, *106*, 219.

(11) Xing, P.; Robertson, G. P.; Guiver, M. D.; Mikhailenko, S. D.; Wang, K.; Kaliaguine, S. *J. membr. sci.* **2004**, *229*, 95.

(12) Kerres, J.; Tang, C.-M.; Graf, C. *Industrial & engineering chemistry research* **2004**, *43*, 4571.

(13) Schuster, M.; Kreuer, K.-D.; Andersen, H. T.; Maier, J. *Macromolecules* **2007**, *40*, 598.

(14) Zawodzinski, T. A.; Derouin, C.; Radzinski, S.; Sherman, R. J.; Smith, V. T.; Springer, T. E.; Gottesfeld, S. *Journal of the electrochemical society* **1993**, *140*, 1041.

(15) Fontanella, J. J.; Edmondson, C. A.; Wintersgill, M. C.; Wu, Y.; Greenbaum, S. G. *Macromolecules* **1996**, *29*, 4944.

(16) Paddison, S. *Annual Review of Materials Research* **2003**, *33*, 289.

(17) Lu, Z.; Polizos, G.; Macdonald, D. D.; Manias, E. *Journal of The Electrochemical Society* **2008**, *155*, B163.

(18) Moilanen, D. E.; Spry, D.; Fayer, M. *Langmuir* **2008**, *24*, 3690.

(19) Spry, D.; Goun, A.; Glusac, K.; Moilanen, D. E.; Fayer, M. *Journal of the American Chemical Society* **2007**, *129*, 8122.

(20) Laporta, M.; Pegoraro, M.; Zanderighi, L. *Phys. Chem. Chem. Phys.* **1999**, *1*, 4619.

(21) Sariban, A.; Binder, K. *The Journal of chemical physics* **1987**, *86*, 5859.

(22) Sing, C. E.; Zwanikken, J. W.; de la Cruz, M. O. *Nature materials* **2014**, *13*, 694.

(23) Sing, C. E.; Zwanikken, J. W.; de la Cruz, M. O. *Physical review letters* **2013**, *111*, 168303.

(24) Sax, J.; Ottino, J. *Polymer Engineering & Science* **1983**, *23*, 165.

(25) Choi, J.-H.; Ye, Y.; Elabd, Y. A.; Winey, K. I. *Macromolecules* **2013**, *46*, 5290.

(26) Elabd, Y. A.; Napadensky, E.; Walker, C. W.; Winey, K. I. *Macromolecules* **2006**, *39*, 399.

(27) Elabd, Y. A.; Walker, C. W.; Beyer, F. L. *J. membr. sci.* **2004**, *231*, 181.

(28) Kim, J.; Kim, B.; Jung, B. *J J. membr. sci.* **2002**, *207*, 129.

(29) Kim, B.; Kim, J.; Jung, B. *J. membr. sci.* **2005**, *250*, 175.

(30) Geise, G. M.; Freeman, B. D.; Paul, D. R. *Polymer* **2010**, *51*, 5815.

(31) Krasemann, L.; Tieke, B. *Langmuir* **2000**, *16*, 287.

(32) Moore, H. D.; Saito, T.; Hickner, M. A. *Journal of Materials Chemistry* **2010**, *20*, 6316.

(33) Chuy, C.; Ding, J.; Swanson, E.; Holdcroft, S.; Horsfall, J.; Lovell, K. V. *Journal of the Electrochemical Society* **2003**, *150*, E271.

(34) Wang, X.; Goswami, M.; Kumar, R.; Sumpter, B. G.; Mays, J. *Soft Matter* **2012**, *8*, 3036.

(35) Shahinpoor, M.; Bar-Cohen, Y.; Simpson, J.; Smith, J. *Smart materials and structures* **1998**, *7*, R15.

(36) Bocharova, V.; Agapov, A. L.; Tselev, A.; Collins, L.; Kumar, R.; Berdzinski, S.; Strehmel, V.; Kisliuk, A.; Kravchenko, I. I.; Sumpter, B. G. *Advanced Functional Materials* **2015**, *25*, 805.

(37) Gao, R.; Zhang, M.; Dixit, N.; Moore, R. B.; Long, T. E. *Polymer* **2012**, *53*, 1203.

(38) Jangu, C.; Savage, A. M.; Zhang, Z.; Schultz, A. R.; Madsen, L. A.; Beyer, F. L.; Long, T. E. *Macromolecules* **2015**, *48*, 4520.

(39) Feng, S.; Shi, D.; Liu, F.; Zheng, L.; Nie, J.; Feng, W.; Huang, X.; Armand, M.; Zhou, Z. *Electrochimica Acta* **2013**, *93*, 254.

(40) Borodin, O.; Smith, G.; Geiculescu, O.; Creager, S. E.; Hallac, B.; DesMarteau, D. *The Journal of Physical Chemistry B* **2006**, *110*, 24266.

(41) Matsui, K.; Kikuchi, Y.; Hiyama, T.; Tobita, E.; Kondo, K.; Akimoto, A.; Seita, T.; Watanabe, H.; Google Patents: 1987.

(42) Weber, R. L.; Ye, Y.; Banik, S. M.; Elabd, Y. A.; Hickner, M. A.; Mahanthappa, M. K. *Journal of Polymer Science Part B: Polymer Physics* **2011**, *49*, 1287.

(43) Green, M. D.; Wang, D.; Hemp, S. T.; Choi, J.-H.; Winey, K. I.; Heflin, J. R.; Long, T. E. *Polymer* **2012**, *53*, 3677.

(44) Zhang, S.; Lee, K. H.; Frisbie, C. D.; Lodge, T. P. *Macromolecules* **2011**, *44*, 940.

(45) Hunley, M. T.; England, J. P.; Long, T. E. *Macromolecules* **2010**, *43*, 9998.

(46) Blasig, A.; Tang, J.; Hu, X.; Shen, Y.; Radosz, M. *Fluid phase equilibria* **2007**, *256*, 75.

(47) Valade, D.; Boschet, F.; Roualdes, S.; Ameduri, B. *Journal of Polymer Science Part A: Polymer Chemistry* **2009**, *47*, 2043.

(48) Scammells, P. J.; Scott, J. L.; Singer, R. D. *Australian Journal of Chemistry* **2005**, *58*, 155.

(49) Jangu, C.; Long, T. E. *Polymer* **2014**.

(50) Hemp, S. T.; Zhang, M.; Allen, M. H.; Cheng, S.; Moore, R. B.; Long, T. E. *Macromolecular Chemistry and Physics* **2013**.

(51) Tsunashima, K.; Yonekawa, F.; Sugiya, M. *Chemistry letters* **2008**, *37*, 314.

(52) Tsunashima, K.; Yonekawa, F.; Sugiya, M. *Electrochemical and Solid-State Letters* **2009**, *12*, A54.

(53) van Schalkwijk, W.; Scrosati, B. *Advances in lithium-ion batteries*; Springer, 2002.

(54) Bauer, B.; Strathmann, H.; Effenberger, F. *Desalination* **1990**, *79*, 125.

(55) Papageorgiou, N.; Athanassov, Y.; Armand, M.; Bonho, P.; Pettersson, H.; Azam, A.; Grätzel, M. *Journal of The Electrochemical Society* **1996**, *143*, 3099.

(56) Cheng, S.; Zhang, M.; Wu, T.; Hemp, S. T.; Mather, B. D.; Moore, R. B.; Long, T. E. *Journal of Polymer Science Part A: Polymer Chemistry* **2012**, *50*, 166.

(57) Wasserscheid, P.; Keim, W. *Angewandte Chemie* **2000**, *39*, 3772.

(58) Wasserscheid, P.; Welton, T. *Ionic liquids in synthesis*; Wiley Online Library, 2008; Vol. 1.

(59) Hemp, S. T.; Zhang, M.; Tamami, M.; Long, T. E. *Polym. Chem.* **2013**, *4*, 3582.

(60) Abdulahad, A. I.; Jangu, C.; Hemp, S. T.; Long, T. E. In *Macromolecular Symposia* 2014; Vol. 342, p 56.

(61) HEMP, S.; ALLEN, M.; SMITH, A.; LONG, T.; WO Patent 2,012,174,543: 2012.

(62) Hemp, S. T.; Allen Jr, M. H.; Green, M. D.; Long, T. E. *Biomacromolecules* **2011**, *13*, 231.

(63) Hemp, S. T.; Smith, A. E.; Bryson, J. M.; Allen Jr, M. H.; Long, T. E. *Biomacromolecules* **2012**, *13*, 2439.

(64) Smith, A. E.; Hemp, S. T.; Allen, M. H.; Bryson, J. M.; Long, T. E. In *MOLECULAR THERAPY*; NATURE PUBLISHING GROUP 75 VARICK ST, 9TH FLR, NEW YORK, NY 10013-1917 USA: 2012; Vol. 20, p S246.

(65) Earle, M. J.; Seddon, K. R. *Pure and Applied Chemistry* **2000**, *72*, 1391.

(66) Kenawy, E.-R.; Abdel-Hay, F. I.; El-Magd, A. A.; Mahmoud, Y. *Reactive and Functional Polymers* **2006**, *66*, 419.

(67) Kenawy, E. R.; Mahmoud, Y. A. G. *Macromolecular Bioscience* **2003**, *3*, 107.

(68) Kanazawa, A.; Ikeda, T.; Endo, T. *Journal of applied polymer science* **1994**, *53*, 1245.

(69) Kanazawa, A.; Ikeda, T.; Endo, T. *Journal of Polymer Science Part A: Polymer Chemistry* **1993**, *31*, 335.

(70) Hemp, S. T.; Zhang, M.; Allen, M. H.; Cheng, S.; Moore, R. B.; Long, T. E. *Macromolecular Chemistry and Physics* **2013**, *214*, 2099.

(71) Ye, Y.; Elabd, Y. A. *Macromolecules* **2011**, *44*, 8494.

(72) Schultz, A. R.; Fahs, G. B.; Jangu, C.; Chen, M.; Moore, R. B.; Long, T. E. *Chemical Communications* **2016**, *52*, 950.

Chapter 2: 3D Printing Phosphonium Ionic Liquid Networks with Mask Projection Micro-stereolithography

(Published in *ACS Macro Letters*)

*Alison R. Schultz, Philip M. Lambert, Nicholas A. Chartrain, David M. Ruohoniemi, Zhiyang Zhang, Chainika Jangu, Musan Zhang, Christopher B. Williams[1], and Timothy E. Long[2]**

[1]Department of Mechanical Engineering, Virginia Tech, Blacksburg, VA 24061, USA. E-mail: cbwilliams@vt.edu.

[2]Macromolecule Innovation Institute, Department of Chemistry, Virginia Tech, Blacksburg, VA 24061, USA. E-mail: telong@vt.edu.

*To whom correspondence should be addressed. E-mail: telong@vt.edu. TEL: (540)231-2480. FAX: (540)231-8517.

Keywords: Ionic Liquids, Additive Manufacturing, Photopolymerization, Rheology

2.1 *Abstract*

Photopolymerization coupled with mask projection micro-stereolithography successfully generated various 3D printed phosphonium polymerized ionic liquids (PILs) with low UV light intensity requirements and high digital resolution. Varying phosphonium monomer concentration, diacrylate crosslinking comonomer, and display images enabled precise 3D design and polymeric properties. The resulting crosslinked phosphonium PIL objects exhibited a synergy of high thermal stability, tunable glass transition temperature, optical clarity, and ion conductivity, which are collectively well-suited for emerging electro-active membrane technologies. Ion conductivity measurements on printed objects revealed a systematic progression in conductivity with ionic liquid monomer content, and thermal properties and solvent extraction demonstrated the formation of a polymerized ionic liquid network with gel fractions exceeding 95%.

2.2 *Introduction*

Ionic liquid monomers provide unique macromolecules that incorporate cationic sites either pendant to or within the polymer backbone with an accompanying mobile counteranion. These charged polymers provide beneficial properties such as a complement of ionic conductivity, thermal and chemical stability, and anion exchange capability. Most studies describe polymers containing ammonium, imidazolium, and 1,2,3-triazolium cations with mobile counteranions such as halides, tetrafluoroborate (BF_4), hexafluorophosphate (PF_6), and bis(trifluoromethanesulfonyl)imide (Tf_2N).[1-3] Our current research has demonstrated advantages of phosphonium polymerized ionic liquids (PILs) with improved thermal stability, enhanced ion conductivity, and more efficient nucleic acid delivery compared to ammonium and imidazolium analogues. Limited commercial availability of phosphonium monomers impeded the design of phosphonium PILs and favored the development of ammonium and imidazolium PIL derivatives. However, an expanded commercial phosphine library has recently enabled the synthesis of low viscosity, high conductivity phosphonium monomers, and resulted in the production of diverse phosphonium-containing macromolecules, including homopolymers,[4] random copolymers,[5] and block copolymers.[6] Current research efforts reveal phosphonium PILs as candidates for ion conducting membranes due to the cationic functionality within each polymeric repeat unit, and the earlier literature suggests impact on technologies ranging from electromechanical actuators[7-9] and gas separation membranes[10-12] to ion exchange membranes.[13-17] The simultaneous enhancement in thermal stability and ion conductivity for phosphonium PILs promises opportunities to enable higher temperature applications, which is critical for demanding aerospace, electronics, and transportation industries.

Enhanced thermal stability of phosphonium PILs stems from a preferred degradation process involving a high temperature nucleophilic substitution mechanism, unlike ammonium derivatives that generally favor Hofmann elimination with a counteranion abstraction of a β-hydrogen. Long *et al.* recently described these mechanisms in a systematic comparison between ammonium and phosphonium PILs, which examined structure-property relationships and elucidated the influence of cation selection, alkyl substituent length, and counteranion on thermal properties, ionic conductivities, and morphologies.[18] Elabd and Winey *et al.* also extensively examined structure-property relationships of imidazolium PILs and reported the impact of counteranion selection and functional substituents on tailoring PIL glass transition temperature (T_g) and electrochemical properties for enhancing ionic conductivity.[19] These studies systematically confirmed that reduced T_g values favored increased ionic conductivity. Other precedent literature supports these claims and specifically describes trifluoromethanesulfonate (TfO) and bis-(trifluoromethanesulfonate)imide (Tf_2N) counteranions to tune T_g and ionic conductivity.[20,21] Various polymerization and post-polymerization strategies for synthesizing phosphonium PILs exist in the literature. McGrath *et al.* reported the synthesis of poly(arylene ether) main chain phosphonium-containing ionomers for high-performance applications, such as ion exchange membranes.[22] Long *et al*. studied structure-property relationships of random and block copolymers involving phosphonium styrenic salts containing either methyl, ethyl, propyl, butyl, or octyl chains.[5,6,18,23] Other synthetic studies disclose atom transfer (ATRP),[24] and reversible addition-fragmentation transfer (RAFT)[25,26] polymerization methods for achieving well-defined phosphonium PILs.

Concurrent advances in fabricating devices from novel monomers and polymers are also needed to meet these technologies. Additive manufacturing, often referred to as 3D printing, where

objects are constructed in a layer-by-layer fashion, enables the design and creation of geometrically complex objects with tailored topology, and thus, functionality. Stereolithography (SL), a well-established additive manufacturing technology, is used to create objects with features < 100 μm by selectively scanning an ultraviolet (UV) laser beam across a reservoir of photopolymer resin. In mask projection micro-stereolithography (MPμSL), a modification of the SL process, an entire cross-sectional layer of photopolymer is cured upon projecting digitally patterned UV light with a dynamic mask (e.g., a digital micromirror device, commonly found in digital projectors).[27] Unlike traditional SL processes, the laser beam radius or scan speed do not limit MPμSL, and thus enables the fabrication of feature sizes smaller than 10 μm, while also reducing build-times by an order-of-magnitude.[28-30] MPμSL's ability to selectively pattern UV light in a layer-by-layer fabrication process provides the opportunity for tailoring polymer architecture and material properties across multiple length scales in 3D space. The goal of this work is therefore to develop photocrosslinkable ionic liquids for this process to enable the production of complex micron-scale electromechanical objects. Herein, we report photopolymerization strategies coupled with additive manufacturing to achieve 3D printed phosphonium PILs in order to demonstrate the first example of 3D printing of an ion-conducting polymer. Conventional strategies for printing ion-conducting materials are limited to conductive composites, which require additional production cost and energy, and often results in printed objects with potential composite leaching. We introduce the potential synergy between MPμSL technology and ionic liquids to form crosslinked networks with chemically bound charged species for enhanced charge stability and extended ion-conductivity.

2.3 *Experimental Section*

2.3.1 Materials

Bis(trifluoromethane)sulfonimide lithium salt (99%), 4-vinylbenzyl chloride (≥90%), trioctyl phosphine (99%), 1,4-butanediol diacrylate (90%), 2, 2-dimethoxy-1, 2-diphenylethan-1-one (≥90%), and poly(ethylene glycol) dimethacrylate (M_n 550 g/mol) were purchased from Sigma Aldrich and used as received unless otherwise noted. 4-Vinylbenzyl trioctyl phosphonium chloride (TOPCl)[1] was synthesized according to the previous literature.

2.3.2 Instrumentation

The MPμSL machine consists of a UV light source, conditioning optics, a mirror, a dynamic mask connected to a computer, imaging optics, and a prepolymer container with a stage mounted on a linear actuator.[2] A LightningCure LC-L1V3 UV LED system by Hamamatsu was chosen as a source of ultraviolet light. The conditioning optics (Edmund Optics) ensure that the entire dynamic mask is illuminated by UV light while the imaging optics focus the patterned light onto the prepolymer surface and reduce the image dimensions by a factor of two. The dynamic mask, a FlexLight X1 DLP Development System (Keynote Photonics) consists of a DLP 0.95 1080p DMD from Texas Instruments and a developer board. The DMD is a 1920 x 1080 array of aluminum micromirrors that measures 0.95-inch along the diagonal. Each square micromirror has a side length of 10.8 μm. The imaging optics reduce the image dimensions by a factor of 2 so the effective projection area of each micromirror on the surface of the photopolymer surface is 5.4 μm x 5.4 μm. Due to the optics of the system, the maximum part size in the XY plane is 6mm by 8mm. The Z direction is currently limited to 36mm. A linear actuator (Zaber NA11B60) was used to control the movement of a custom stage made by Fused Deposition Modeling (FDM).

Thermogravimetric analysis (TGA) was performed using a TA Instruments TGA 2950 at a 10 °C/min heating ramp. Differential scanning calorimetry (DSC) was performed using a TA Instruments Q1000. Scans were obtained under N_2 with heating at 10 °C/min and cooling at 100 °C/min; T_g's were recorded on the second heating cycle. Vapor sorption thermogravimetric analysis (TGASA) was conducted with a TA Instruments Q5000 in the isotherm mode for 120 minutes at 30 ^oC followed by a 5% relative humidity ramp for 19 cycles. Photorheology was performed using a TA Instruments DHR-2 rheometer with a 20 mm parallel plate geometry and Smart Swap^{TM} UV geometry. The samples were subjected to oscillatory strain experiments at increasing UV light intensity (UHP, 500 um gap, 10 Hz, 0.05% oscillatory strain). The resulting storage and loss moduli for each polymer were plotted using the TA Instruments TRIOS software package. A SkyScan 1172 X-Ray MicroCT performed a 180° scan on 3D printed PIL cones using a 0.4° step increment. The 3D cones were reconstructed as a stl file and were digitally modeled using NetFabb software for 3D modeling. A NEO Scope JCM 5000 scanning electron microscope (SEM) imaged complex 3D objects for analyzing architectural features and build reproducibility. 3D objects were mounted on a SEM disc, and required no additional sputter-coating to reduce electron charging effects.

Impedance spectroscopy was obtained using a Metrohm Autolab 302N with a 4-point in-plane cell (BekkTech, Inc., Loveland, CO, USA) and an ESPEC BTL-433 environmental chamber, which controlled the temperature from 60 °C to 150 °C at 10% relative humidity. 3D printed, 33 mm x 6 mm x 2 mm, ionic liquid containing blocks were soaked in THF for 12 h, dried at 90 ^oC under reduced pressure (0.5 mmHg) for 4 h and then subsequently annealed at 60 °C in the environmental chamber for 24 h before measurements. The alternating voltage set point was 0.2 V and the frequency was varied from 0.1 Hz to 1 MHz. Each measurement was the average of 5

measurements and measurements were performed in 10 °C/step from 60 °C to 150 °C. The sample was equilibrated at each temperature for at least 2 h before measurement. The resistance was calculated from the x-intercept of the Nyquist plot in the Autolab Nova software suite and subsequently converted to conductivity using $\sigma = L / AR$ where L is the length between the inner electrodes, A is the area between the electrodes, and R is the measured resistance.

The Vogel–Fulcher–Tamman (VFT) equation is a three-parameter equation with the variables infinite conductivity (σ_0), the Vogel temperature (T_0) where ion motion stops, and a constant related to the activation temperature or Arrhenius activation energy (B). The 3-parameter VFT equation is as follows:

$$\boldsymbol{\sigma(T) = \sigma_0 exp\left(\frac{-B}{T - T_0}\right)}$$

The Origin Lab 7 software suite was utilized to fit phosphonium PIL conductivity data using the three-parameter VFT equation.

2.3.3 Anion exchange reaction of phosphonium IL

A typical synthesis of 4-vinylbenzyl trioctyl phosphonium bis(trifluoromethane)sulfonimide ($TOPTf_2N$) was performed as follows: A solution of 150 g of $LiTf_2N$ in 500 mL of anhydrous dichloromethane and a solution of 50 g of OPCl in 100 mL of anhydrous dichloromethane was mixed in a 1 L beaker. After stirring overnight at room temperature, the resulting cloudy solution was filtered, and the filtrate was vacuum stripped and redissolved in 100 mL of dichloromethane and washed with DI H_2O (3 x 100 mL). The obtained IL was evaluated with silver nitrate, and a silver chloride precipitate was not observed, indicating the absence of chloride anions. The product was dried at 30 ^oC under reduced pressure (0.5 mmHg) for 2 days until constant weight. (Yield of $TOPTf_2N$: 92%).

2.3.4 MPμSL working curves for photocuring phosphonium PIL networks

A MPμSL working curve for each 3D sample was achieved using the Beer-Lambert law of absorption, which is defined as: $C_d = D_p \ln(E/E_c)$. The working curve relates the exposure of light provided at the photocurable ionic liquid sample surface (E) and the depth to which the sample is crosslinked into a polymer network (cure depth, C_d). The minimum exposure required to begin polymer crosslinking is the critical exposure (E_c). It is essential to determine the working curve for each fabricated 3D network to ensure complete exposure with UV energy for polymer curing. To determine the working curve, the photocurable sample undergoes a series of varied UV exposures and the resulting thin films are measured for thickness. The thickness at each exposure is plotted on a semilog plot; the working curve typically shows a linear relationship between the cure depth and the natural log of exposure. The critical exposure is located at the resultant curve's x-intercept and depth of penetration is determined by analyzing the slope of the curve.

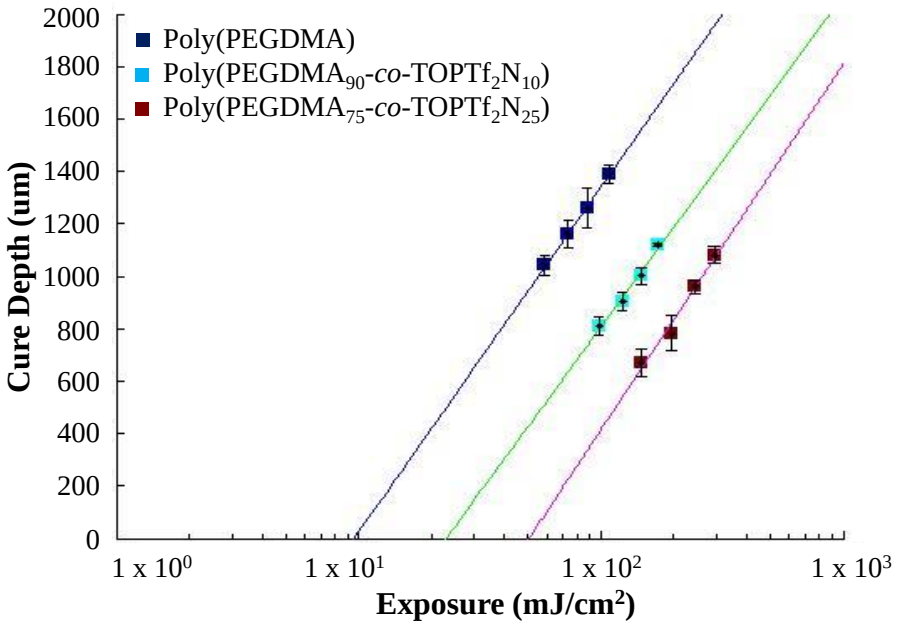

Figure SI 2.1. Working curves for poly(PEGDMA), poly(PEGDMA$_{90}$-*co*-TOPTf$_2$N$_{10}$), and poly(PEGDMA$_{75}$-*co*-TOPTf$_2$N$_{25}$) with 2 wt.% photoinitiator.

2.3.5 MPμSL fabrication process for 3D printing phosphonium PIL networks.

All of the 3D printed phosphonium ionic liquid networks were fabricated following a similar procedure and the construction of a 33 mm x 6 mm x 2 mm, poly(PEGDMA$_{90}$-*co*-TOPTf$_2$N$_{10}$) 3D test specimen with 10 mol% TOPTf$_2$N ionic liquid follows as an example. Micro-stereolithography fabrication begins first by slicing a 3D computer aided design (CAD) model into individual images for projecting onto the photocurable sample. An additive manufacturing software, NetFabb, created slices (saved as bitmap images) of a desired thickness (100 μm was used). A LabView program was used to control the projection of these images by the DMD and the movement of the stage. A 30 mL beaker was filled with poly(ethylene glycol) dimethacrylate (24.75 g, 50.0 mmol), 4-vinylbenzyl trioctyl phosphonium bis(trifluoromethane)sulfonimide salt (3.85 g, 50.0 mmol), and 2, 2-dimethoxy-1, 2-diphenylethan-1-one (572.0 mg), and a stage was lowered into the beaker until slightly submerged. The LabView program then turned individual mirrors "on" or "off" to represent the first image. The UV light passed from the LED lamp through the conditioning optics and mirror to the DMD. This resulted in the image being projected from the DMD onto the thin layer of prepolymer directly above the stage. Each layer was cured with 25.57 mJ/cm^2 exposure energy, as determined from the working curve of the test specimen. After this set time, the DMD mirrors were turned "off" so that no light was projected into the photocurable ionic liquid sample and the stage was lowered into the container. The stage was completely submerged and then returned to one layer thickness below the surface. The LabView software loaded the next layer's image and the process was repeated until the object was completely fabricated. After each object was fabricated, the object was isolated and washed with a few drops of isopropyl alcohol (IPA) to remove any uncured photocurable ionic liquid sample. The networks were then dried at 90 ^{o}C under reduced pressure (0.5 mmHg) overnight.

Thermogravimetric analysis (TGA) probed the thermal properties for the various poly(PEGDMA-*co*-$TOPTf_2N$) rectangular test specimens and confirmed corresponding target wt.% incorporation of $TOPTf_2N$.

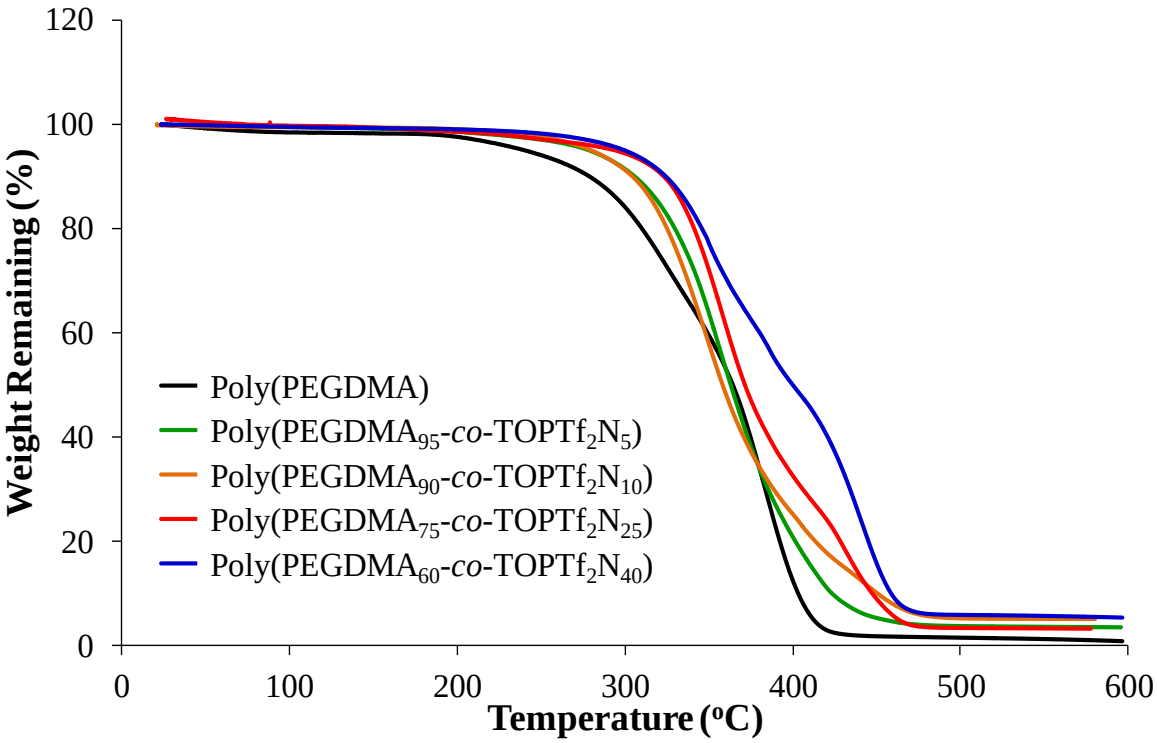

Figure SI 2.2. TGA characterization for poly(PEGDMA-*co*-$TOPTf_2N$) 3D printed rectangular test specimens containing 0 mol%, 5 mol%, 10 mol%, 25 mol%, and 40 mol% mol% $TOPTf_2N$.

2.4 *Results and Discussion*

Scheme 2.1(a) depicts the synthetic strategy for achieving the phosphonium ionic liquid monomer, 4-vinylbenzyl trioctyl phosphonium bis(trifluoromethanesulfonate)imide ($TOPTf_2N$). Subsequent quantitative anion exchange of the phosphonium chloride salt precursor (TOPCl) with Tf_2N resulted in the $TOPTf_2N$ liquid monomer at room temperature, which exhibited a melting temperature (T_m) below -90 °C and an onset of degradation temperature (T_d) of 420 °C. The notably low T_m for $TOPTf_2N$ classifies the monomer as a polymerizable room temperature ionic

liquid, while the high T_d value suggests the potential for poly(TOPTf$_2$N) in high-temperature electro-active devices. The anion exchanged monomer did not dissolve in nonpolar solvents such as hexanes in contrast to the precursor TOPCl. This counteranion dependent solubility suggested that the association between the phosphonium cation and the bulky Tf$_2$N anion was relatively weak.

Scheme 2.1. (**A**) Anion exchange of phosphonium 4-vinylbenzyl trioctyl phosphonium chloride. (**B**) Synthesis of poly(PEGDMA-*co*-TOPTf$_2$N) and poly(BDA-*co*-TOPTf$_2$N) crosslinked 3D networks.

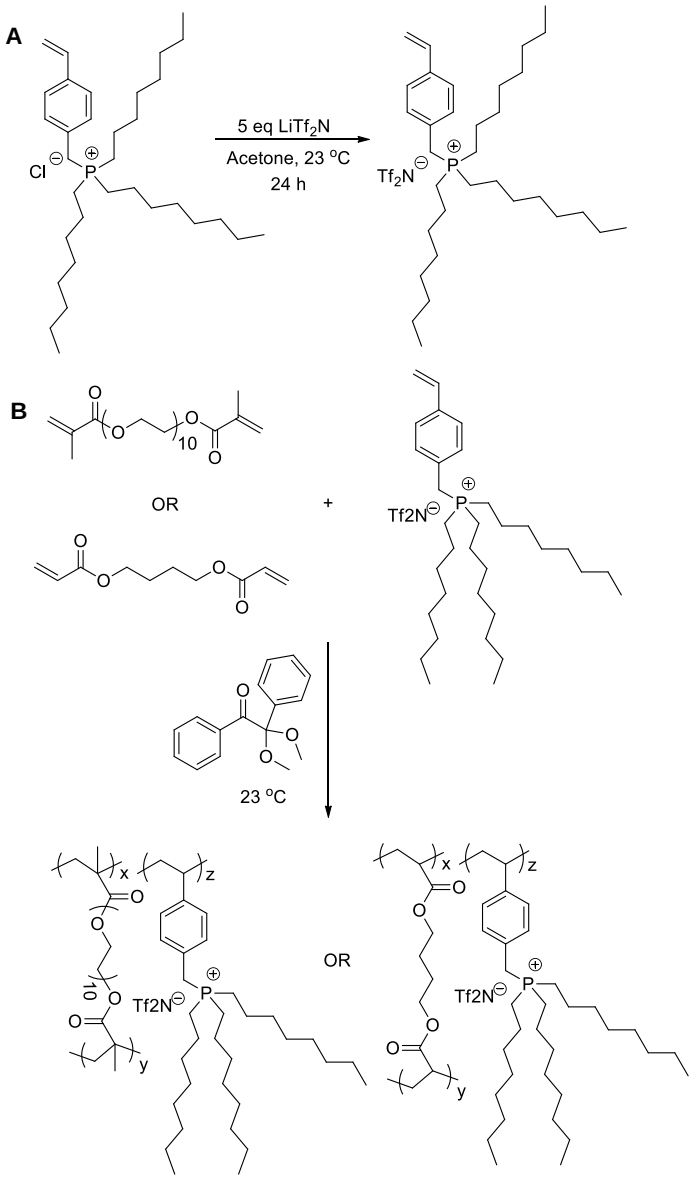

TOPTf$_2$N unexpectedly revealed improved miscibility with polar reagents including UV-curable diacryclic monomers such as 1,4-butanediol diacrylate (BDA) and poly(ethylene glycol) dimethacrylate (PEGDMA). This enabled diverse photocured poly(BDA-*co*-TOPTf$_2$N) and poly(PEGDMA-*co*-TOPTf$_2$N) crosslinked networks with increasing mol% incorporation of

TOPTf$_2$N phosphonium ionic liquid monomer. UV-curing TOPTf$_2$N ionic liquid monomer into traditional poly(BDA) and poly(PEGDMA) crosslinked networks offers an opportunity to impart thermally stable charged sites for improving ion mobility, gas diffusion, and salt permeability. Tuning these properties with phosphonium ionic liquid concentration will tailor resulting electro-active membranes for advanced applications in batteries,[31,32] gas separation,[33,34] and water desalination.[35,36]

Scheme 2.1(b) depicts the photopolymerization of poly(BDA-*co*-TOPTf$_2$N) and poly(PEGDMA-*co*-TOPTf$_2$N) crosslinked networks, including 2 wt.% of the photoinitiator 2, 2-dimethoxy-1, 2-diphenylethan-1-one and exposure to a 365 nm UV light source. Photorheology investigations evaluated the effects of UV light intensity on cure time and storage modulus (G') of the crosslinked networks, which enabled a comparison in structure-processing relationships between poly(PEGDMA), poly(BDA), poly(PEGDMA$_{90}$-*co*-TOPTf$_2$N$_{10}$), and poly(BDA$_{90}$-*co*-TOPTf$_2$N$_{10}$) networks (Figure 2.1). Increasing UV light intensity of 5 mW/cm^2, 10 mW/cm^2, and 20 mW/cm^2 revealed faster cure times for all samples while maintaining a two step G' transition, corresponding to the approximate gel point transition from a viscous to solid state during photopolymerization. Overlaying the photorheology data for the crosslinked networks at 5 mW/cm^2 elucidated the photoprocessing differences between PEGDMA- and BDA-containing networks, revealing slower crosslinking of PEGDMA chains in comparison to the BDA monomer. The extended photocuring time correlated to the ethylene oxide spacer within the PEGDMA crosslinking agent, which also advantageously reduces the T_g and imparts network flexibility during photocuring at room temperature.

Photopolymerization strategies for UV-curing poly(PEGDMA-*co*-TOPTf$_2$N) crosslinked networks coupled with MPμSL technology achieved layer-by-layer fabrication of poly(PEGDMA-

co-TOPTf$_2$N) crosslinked 3D objects. Literature reports thoroughly detail the MPμSL operating system apparatus.[27] The process involves a light emitting diode (LED) that projects light into a series of conditioning optics, which includes collimating lenses, wavelength filters, and homogenizing rods. A mirror reflects the conditioned light onto a dynamic pattern generator (dynamic mask) parallel to the projection surface, which then digitally patterns and projects the incident light as an image. Finally, an optical lens resizes the patterned light in order to focus the final image on the surface of photocurable viscous monomers or oligomers. The projected pattern initiates the crosslinking of monomer or oligomers, causing a change in phases from a liquid to a solid state during photopolymerization. During a layer-by-layer process, the first layer of photocurable monomer or oligomer is cured on a build platform under an UV intensity of 4.9 mW/cm^2 (Figure E2.1). The build platform repositions such that additional viscous monomer or oligomer recoats the previously cured polymer to provide material for creating a subsequent layer. An image of the next cross-sectional layer projects onto the subsequent layer and the photocuring process repeats until achieving a final 3D object.

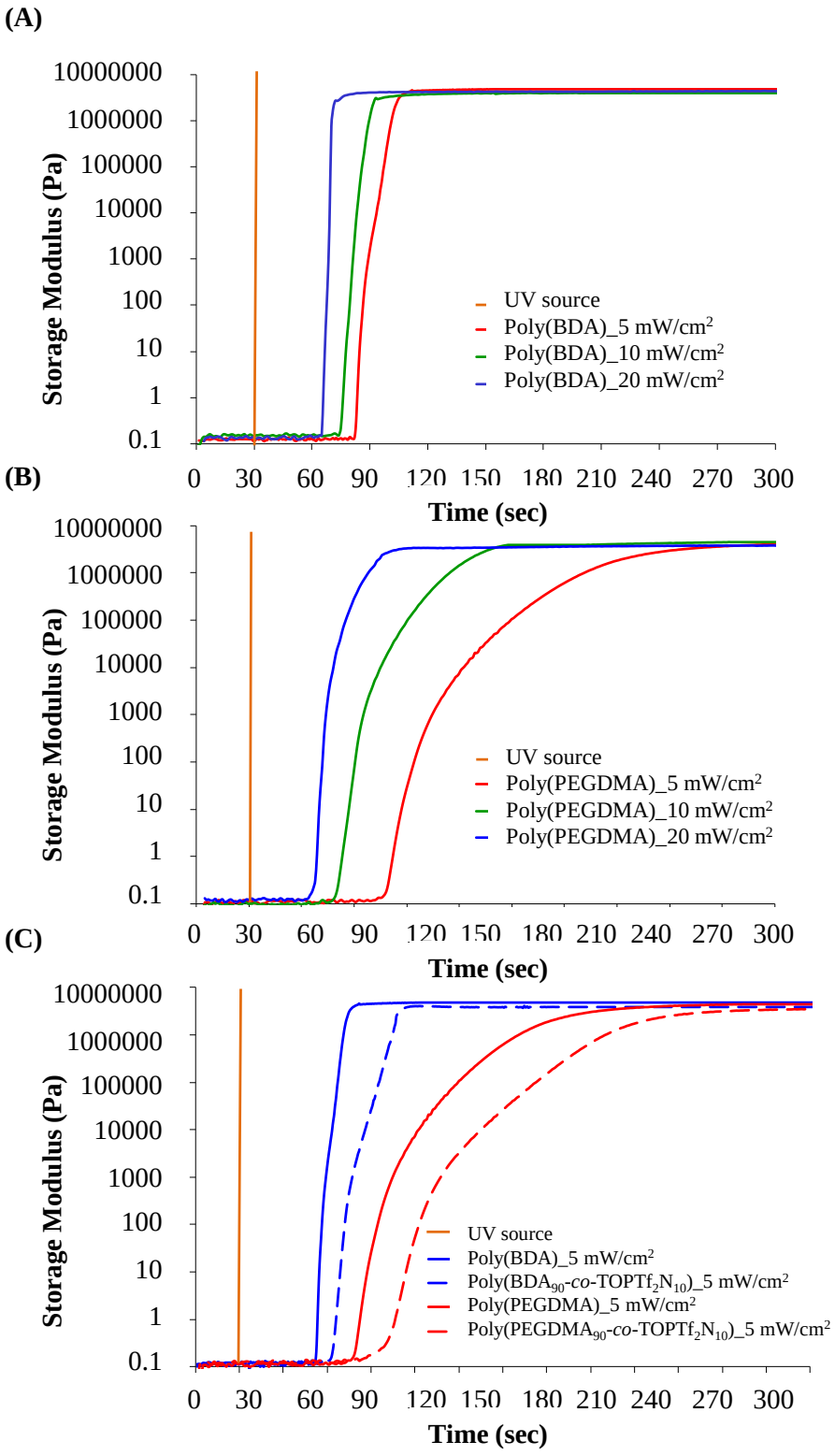

Figure 2.1. Photorheology characterization of (**A**) poly(BDA) and (**B**) poly(PEGDMA) at various light intensity exposure. (**C**) Photorheology characterization comparing structure-processing

relationships between poly(BDA), poly(PEGDMA), poly(BDA$_{90}$-*co*-TOPTf$_2$N$_{10}$), and poly(PEGDMA$_{90}$-*co*-TOPTf$_2$N$_{10}$) at 5 mW/cm^2 light intensity exposure.

A diverse range of computer-aided design (CAD) files enable the additive manufacturing of diverse 3D printed poly(PEGDMA-*co*-TOPTf$_2$N) objects, ranging from 33 mm tall rectangular test specimens to 8 mm tall 3D cones, hyperboloids, and figurines (Figure 2.2). X-Ray microCT scanning reconstructed a CAD image of the poly(PEGDMA$_{90}$-*co*-TOPTf$_2$N$_{10}$) 3D cones, demonstrating systematic efficiency in reproducing CAD designs (Figure 2.3). Scanning electron microscopy (SEM) images of the poly(PEGDMA$_{90}$-*co*-TOPTf$_2$N$_{10}$) 3D hyperboloid depicts well-defined architecture and build reproducibility in the complex object (Figure 2.4). The surface roughness depicted in both X-Ray microCT and SEM images is consistent for all printed objects and is attributed to the micro-stereolithography build process.

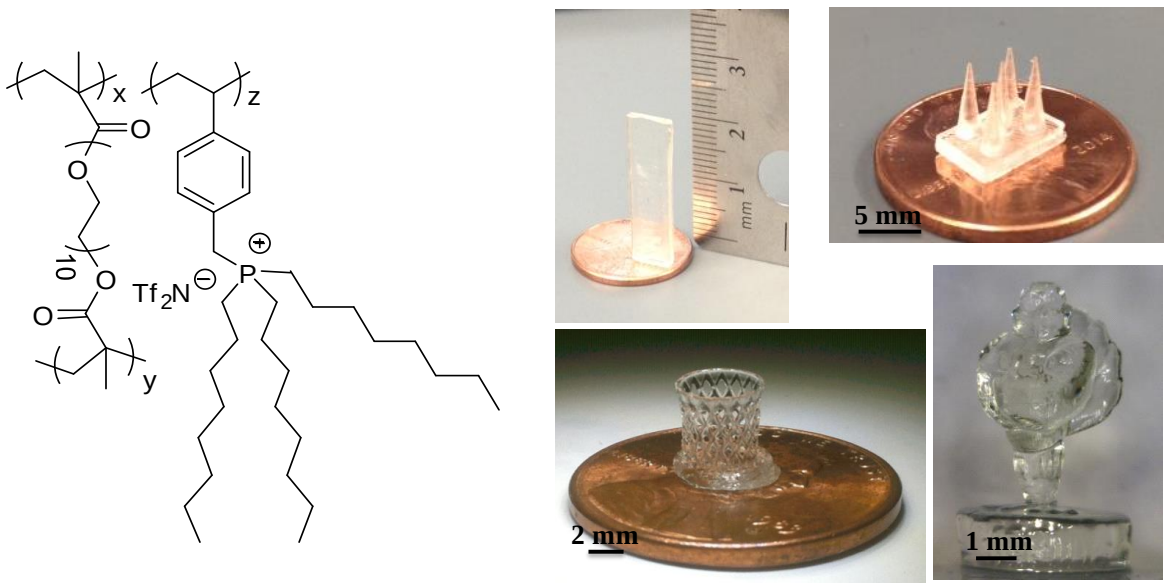

Figure 2.2. Mask projection micro-stereolithography successfully 3D prints poly(PEGDMA-*co*-TOPTf$_2$N) 33 mm tall rectangular test specimens, 8 mm tall cones, 8 mm tall hyperboloid, and 8 mm tall figurine.

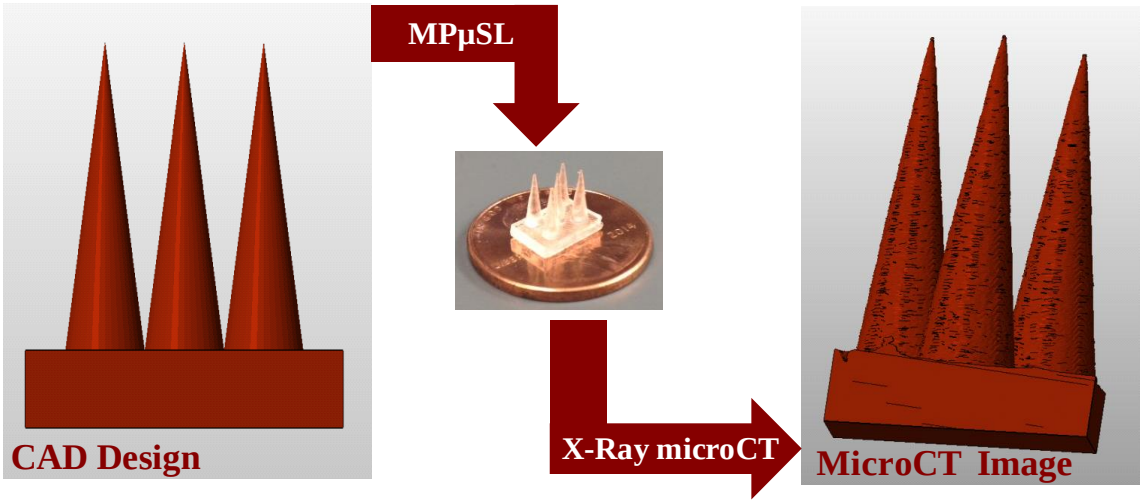

Figure 2.3. X-Ray microCT image of 3D printed poly(PEGDMA90-*co*-TOPTf2N10) cones in comparison to original CAD design.

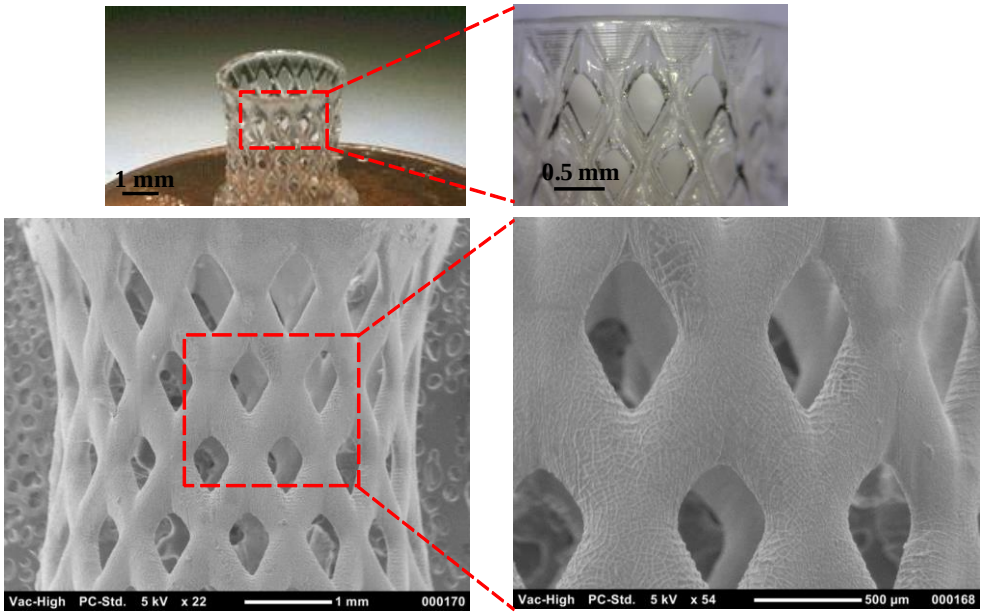

Figure 2.4. Detailed images of 3D printed poly(PEGDMA90-*co*-TOPTf2N10) hyperboloid with optical microscopy and scattering electron microscopy.

Varying the mol% incorporation of $TOPTf_2N$ achieved a series of 3D, 33 mm x 6 mm x 2 mm test specimens including: poly(PEGDMA), poly($PEGDMA_{95}$-*co*-$TOPTf_2N_5$),

poly(PEGDMA$_{90}$-*co*-TOPTf$_2$N$_{10}$), poly(PEGDMA$_{75}$-*co*-TOPTf$_2$N$_{25}$), and poly(PEGDMA$_{60}$-*co*-TOPTf$_2$N$_{40}$). Soxhlet extraction with THF at reflux for 24 h determined wt.% gel fraction for all test specimens, revealing gel fractions of 90-97 wt.% and confirming high UV-curing efficiency (Table 2.1). Thermogravimetric analysis (TGA) probed the thermal properties for the various poly(PEGDMA-*co*-TOPTf$_2$N) samples and confirmed corresponding target wt.% incorporation of TOPTf$_2$N (Table 2.1 and Figure E2.2). The TGA transitions for the poly(PEGDMA-*co*-TOPTf$_2$N) samples exhibited a two-step thermal degradation profile with the initial step ($T_{d,\ 5\%\ wt.\ loss}$) occurring at approximately 320 ^{o}C, corresponding to PEGDMA degradation, and the second step occurring at approximately 420 ^{o}C, correlating with the T_d of TOPTf$_2$N. Increasing mol% incorporation of TOPTf$_2$N resulted in two-step weight loss profiles that varied in wt.% remaining. For poly(PEGDMA-*co*-TOPTf$_2$N) test specimens with 5 mol%, 10 mol%, 25 mol%, and 40 mol% TOPTf$_2$N, second step TGA transitions revealed an increase in wt.% remaining values that corresponded to 7 wt.%, 13 wt.%, 30 wt.%, and 46 wt.% TOPTf$_2$N. The observed increase in wt.% TOPTf$_2$N compared well to the mol% values and confirmed the incorporation of the TOPTf$_2$N. Differential scanning calorimetry (DSC) elucidated the effects of increasing TOPTf$_2$N content on T_g values for the 3D fabricated poly(PEGDMA-*co*-TOPTf$_2$N) test specimens (Table 2.1). As anticipated for crosslinked networks, increasing mol% content of TOPTf$_2$N resulted in an observable slight depression in T_g. The control poly(PEGDMA) sample revealed a T_g of -10 ^{o}C, which gradually decreased to -18 ^{o}C for 40 mol% TOPTf$_2$N. The observed trend in decreasing T_g correlated to the increasing content of polymerized phosphonium ionic liquid within the photocrosslinked PEGDMA matrix.

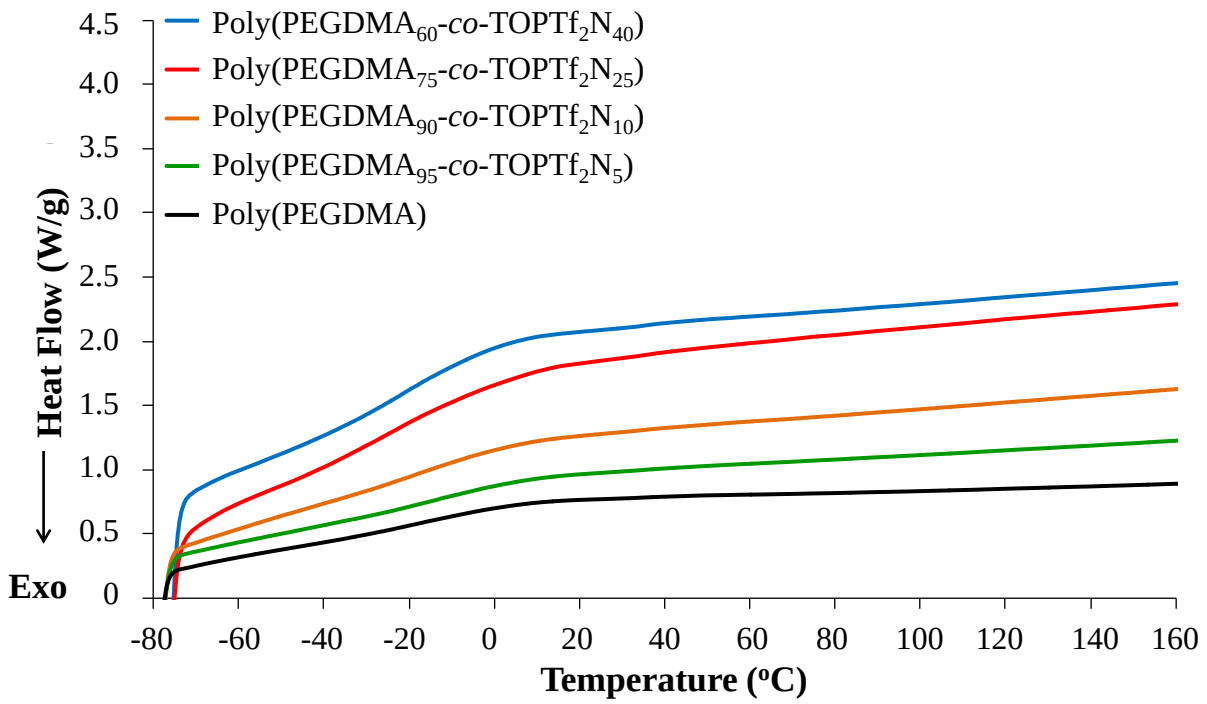

Figure 2.5. DSC characterization for poly(PEGDMA-*co*-TOPTf$_2$N) 3D printed rectangular test specimens containing 0 mol%, 5 mol%, 10 mol%, 25 mol%, and 40 mol% mol% TOPTf$_2$N.

Table 2.1. Thermal properties, % gel fraction, and VFT fitting and analysis of PIL conductivity data for poly(PEGDMA-*co*-TOPTf2N) 3D printed rectangular test specimens.

Sample	% gel fraction	$T_{d,1}$ (ºC)	$T_{d,1}$ wt.%	$T_{d,2}$ (ºC)	$T_{d,2}$ wt.%	T_g (ºC)	σ_{inf} [S cm^{-1}]	B [K]	T_0 [K]
Crosslinked PEGDMA	94	320	100	NA	NA	-10	-5.75	411	292
Poly(PEGDMA$_{95}$-*co*-TOPTf$_2$N$_5$)	95	320	91	420	9	-10	NA	NA	NA
Poly(PEGDMA$_{90}$-*co*-TOPTf$_2$N$_{10}$)	97	320	83	420	15	-14	-2.34	1376	193
Poly(PEGDMA$_{75}$-*co*-TOPTf$_2$N$_{25}$)	95	330	68	420	35	-16	-2.15	1085	217
Poly(PEGDMA$_{60}$-*co*-TOPTf$_2$N$_{40}$)	93	330	60	420	40	-18	-1.04	2034	127

* **% gel fraction:** wt.% remaining after reflux in THF for 24 h
* **$T_{d,1}$:** First step thermal degradation
* **$T_{d,2}$:** Second step thermal degradation

Consistent with previous literature reports, a lower T_g increased ionic conductivity for the 3D fabricated poly(PEGDMA-*co*-TOPTf$_2$N) test specimens (Figure 2.5). Ionic conductivity in single-ion conductors strongly depends on frequency and temperature.[37] The value of DC conductivity is defined as the in-phase component of the conductivity, which is independent of frequency over a 3-decade frequency range. Poly(PEGDMA$_{60}$-*co*-TOPTf$_2$N$_{40}$), which has the highest mol% of the phosphonium ion-conducting units, exhibited the highest ionic conductivity and the lowest T_g. Ionic conductivity decreased with increasing mol% of PEGDMA and correlated closely with the phosphonium-containing charge concentration, where the poly(PEGDMA) revealed the lowest ionic conductivity. These results agreed with our previous studies that compared conductivity of phosphonium and ammonium PILs, revealing a comparable conductivity range at the operating temperature for the crosslinked networks with increasing phosphonium PIL content. All specimens for conductivity measurements were performed at 10% relative humidity, and the control poly(PEGDMA) agree with earlier reports.[38] While the effects of a lowered T_g optimized ionic conductivity, TGA-sorption analysis also confirmed negligible effects of water adsorption of poly(PEGDMA-*co*-TOPTf$_2$N) test specimens. While increasing mol% of TOPTf$_2$N revealed increasing water uptake with time, the hydrophobic Tf$_2$N counteranion in a PEGDMA matrix limited water uptake to less than 0.5 wt.%.

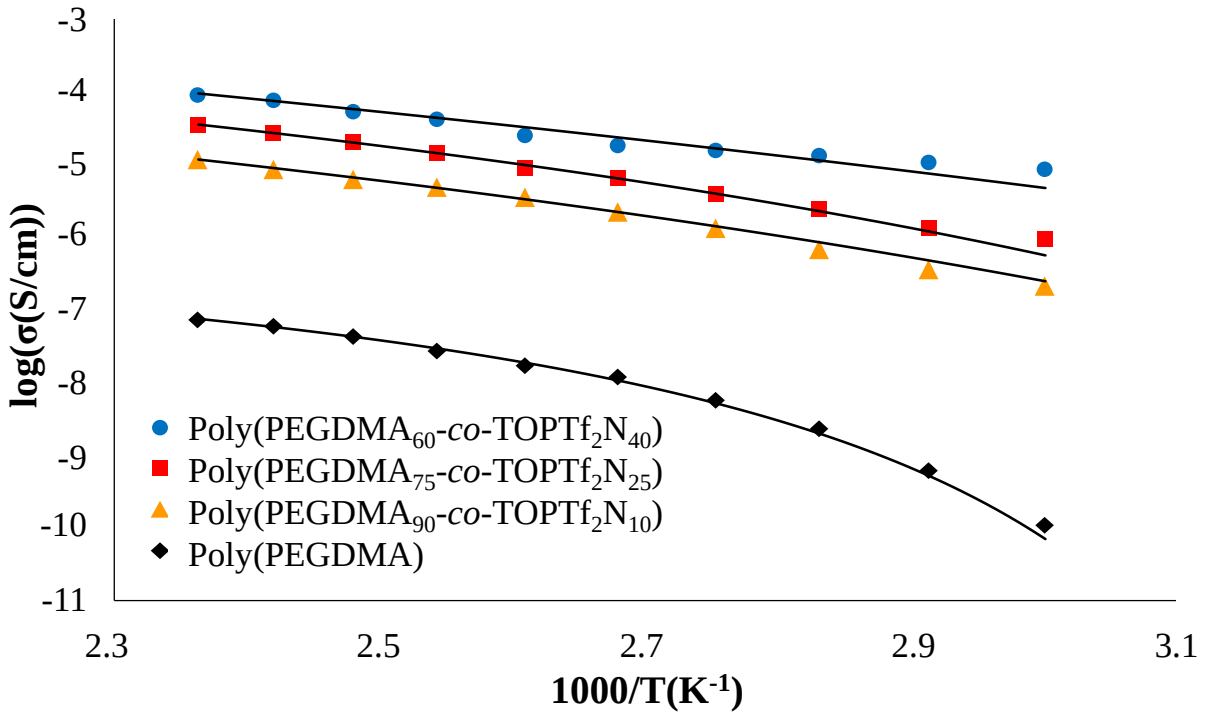

Figure 2.6. Ionic conductivity for poly(PEGDMA-*co*-TOPTf2N) 3D printed rectangular films with 10 mol%, 25 mol%, and 40 mol% $TOPTf_2N$. The relative humidity was maintained at 10% over the 60 to 150 °C.

2.5 *CONCLUSIONS*

Future studies will focus on expanding phosphonium PILs into more complex and well-defined conductive objects for emerging electro-active membrane technologies. Varying phosphonium charge concentration, crosslinking monomers, and digital images will enable the construction of diverse 3D printed phosphonium PILs with tunable nanoscale structures, 3D designs, and conductive properties. MPμSL advantageously offers control in customizing 3D objects and, in combination with novel polymer compositions, provides an exciting approach for designing and optimizing additive manufacturing technologies.

2.6 *ACKNOWLEDGMENTS*

We acknowledge the Institute for Critical Technology and Applied Science (ICTAS) and the Design, Research, and Education for Additive Manufacturing Systems (DREAMS) laboratory at Virginia Tech for instrument support. We also thank Dr. Rolf Mueller in the Department of Mechanical Engineering for access to the microCT instrumentation.

2.7 *REFERENCES*

(1) Allen, M. H.; Hemp, S. T.; Zhang, M.; Zhang, M.; Smith, A. E.; Moore, R. B.; Long, T. E. *Polym. Chem.* 2013, *4*, 2333.

(2) Lu, J.; Yan, F.; Texter, J. *Prog. Polym. Sci.* 2009, *34*, 431.

(3) Obadia, M. M.; Mudraboyina, B. P.; Serghei, A.; Phan, T. N.; Gigmes, D.; Drockenmuller, E. *ACS Macro Letters* 2014, *3*, 658.

(4) Godeau, G.; Navailles, L.; Nallet, F.; Lin, X.; McIntosh, T. J.; Grinstaff, M. W. *Macromolecules* 2012, *45*, 2509.

(5) Cheng, S.; Zhang, M.; Wu, T.; Hemp, S. T.; Mather, B. D.; Moore, R. B.; Long, T. E. *Journal of Polymer Science Part A: Polymer Chemistry* 2012, *50*, 166.

(6) Hemp, S. T.; Smith, A. E.; Bryson, J. M.; Allen, M. H.; Long, T. E. *Biomacromolecules* 2012, *13*, 2439.

(7) Jangu, C.; Wang, J. H. H.; Wang, D.; Sharick, S.; Heflin, J. R.; Winey, K. I.; Colby, R. H.; Long, T. E. *Macromolecular Chemistry and Physics* 2014.

(8) Gao, R.; Wang, D.; Heflin, J. R.; Long, T. E. *J. Mater. Chem.* 2012, *22*, 13473.

(9) Wu, T.; Wang, D.; Zhang, M.; Heflin, J. R.; Moore, R. B.; Long, T. E. *ACS Appl. Mater. Interfaces* 2012, *4*, 6552.

(10) Freeman, B. D. *Macromolecules* 1999, *32*, 375.

(11) Zhang, Y.; Zhang, S.; Lu, X.; Zhou, Q.; Fan, W.; Zhang, X. P. *Chem.--Eur. J.* 2009, *15*, 3003.

(12) Lin, H.; Wagner, E. V.; Swinnea, J. S.; Freeman, B. D.; Pas, S. J.; Hill, A. J.; Kalakkunnath, S.; Kalika, D. S. *J. Membr. Sci.* 2006, *276*, 145.

(13) Wang, S.-W.; Liu, W.; Colby, R. H. *Chemistry of Materials* 2011, *23*, 1862.

(14) Gu, S.; Cai, R.; Yan, Y. *Chem. Commun.* 2011, *47*, 2856.

(15) Noonan, K. J. T.; Hugar, K. M.; Kostalik, H. A.; Lobkovsky, E. B.; Abruna, H. D.; Coates, G. W. *J. Am. Chem. Soc.* 2012, *134*, 18161.

(16) Moore, C. M.; Hackman, S.; Brennan, T.; Minteer, S. D. *J. Membr. Sci.* 2005, *254*, 63.

(17) Yan, X.; He, G.; Gu, S.; Wu, X.; Du, L.; Wang, Y. *Int. J. Hydrogen Energy* 2012, *37*, 5216.

(18) Hemp, S. T.; Zhang, M.; Allen, M. H., Jr.; Cheng, S.; Moore, R. B.; Long, T. E. *Macromol. Chem. Phys.* 2013, *214*, 2099.

(19) Chen, H.; Choi, J.-H.; Salas-de la Cruz, D.; Winey, K. I.; Elabd, Y. A. *Macromolecules* 2009, *42*, 4809.

(20) Ohno, H.; Yoshizawa, M.; Ogihara, W. *Electrochim. Acta* 2004, *50*, 255.

(21) Armand, M.; Endres, F.; MacFarlane, D. R.; Ohno, H.; Scrosati, B. *Nat. Mater.* 2009, *8*, 621.

(22) Ghassemi, H.; Riley, D. J.; Curtis, M.; Bonaplata, E.; McGrath, J. E. *Appl. Organomet. Chem.* 1998, *12*, 781.

(23) Hemp, S. T.; Zhang, M.; Tamami, M.; Long, T. E. *Polym. Chem.* 2013, *4*, 3582.

(24) Borguet, Y. P.; Tsarevsky, N. V. *Polym. Chem.* 2012, *3*, 2487.

(25) Wang, R.; Lowe, A. B. *J. Polym. Sci., Part A: Polym. Chem.* 2007, *45*, 2468.

(26) Stokes, K. K.; Orlicki, J. A.; Beyer, F. L. *Polym. Chem.* 2011, *2*, 80.

(27) Lambert, P. M.; III, E. A. C.; Williams, C. B. In *Solid Freeform Fabrication Symposium* Austin, Texas, 2013, p 111.

(28) Bertsch, A.; Lorenz, H.; Renaud, P. *Sensors and Actuators A: Physical* 1999, *73*, 14.

(29) Zheng, X.; Deotte, J.; Alonso, M. P.; Farquar, G. R.; Weisgraber, T. H.; Gemberling, S.; Lee, H.; Fang, N.; Spadaccini, C. M. *Review of Scientific Instruments* 2012, *83*.

(30) Bertsch, A.; Zissi, S.; Jezequel, J.; Corbel, S.; Andre, J. *Microsystem Technologies* 1997, *3*, 42.

(31) Kuo, P.-L.; Wu, C.-A.; Lu, C.-Y.; Tsao, C.-H.; Hsu, C.-H.; Hou, S.-S. *ACS Appl. Mater. Interfaces* 2014, *6*, 3156.

(32) Green, M. D.; Choi, J.-H.; Winey, K. I.; Long, T. E. *Macromolecules* 2012, *45*, 4749.

(33) Bara, J. E.; Gabriel, C. J.; Lessmann, S.; Carlisle, T. K.; Finotello, A.; Gin, D. L.; Noble, R. D. *Industrial & engineering chemistry research* 2007, *46*, 5380.

(34) Sanders, D. F.; Smith, Z. P.; Guo, R.; Robeson, L. M.; McGrath, J. E.; Paul, D. R.; Freeman, B. D. *Polymer* 2013, *54*, 4729.

(35) Hatakeyama, E. S.; Ju, H.; Gabriel, C. J.; Lohr, J. L.; Bara, J. E.; Noble, R. D.; Freeman, B. D.; Gin, D. L. *J. Membr. Sci.* 2009, *330*, 104.

(36) Sagle, A. C.; Ju, H.; Freeman, B. D.; Sharma, M. M. *Polymer* 2009, *50*, 756.

(37) Lee, M.; Choi, U. H.; Colby, R. H.; Gibson, H. W. *Chemistry of Materials* 2010, *22*, 5814.

(38) Walker, C. N.; Versek, C.; Touminen, M.; Tew, G. N. *ACS Macro Letters* 2012, *1*, 737.

Chapter 3: 3D printing hierarchical polymeric structures for tissue-engineered scaffolds

Alison R. Schultz[1], Nicholas Chartrian[2], Phil Lambert[2], Musan Zhang[1], Justin Sirrine[1], Niki Camateros-Mann[1], Courtney P. Long[1], Victoria Christopher B. Williams[2], and Timothy E. Long[1]

[1]Macromolecules Innovation Institute, Department of Mechanical Engineering, Virginia Tech, Blacksburg, VA 24061, USA. E-mail: cbwilliams@vt.edu.

[2]Macromolecules Innovation Institute, Department of Chemistry, Virginia Tech, Blacksburg, VA 24061, USA. E-mail: telong@vt.edu.

*To whom correspondence should be addressed. E-mail: telong@vt.edu. TEL: (540)231-2480. FAX: (540)231-8517

Keywords: 3D printing, photorheology, Pluronic® diols, tissue-engineered scaffolds

3.1 *Abstract*

End group functionalization provides a facile synthetic approach for converting commercially available PPG and Pluronic® diols into photo-curable polyether diacrylates for generating photo-crosslinked, 3D printed networks. This synthetic process afforded a series of Pluronic® diols including: Pluronic L-31®, Pluronic® L-61, and Pluronic® 10RS, for evaluating compositional effects on photo-curing behavior. Photo-polymerization methods coupled with mask projection micro-stereolithography (MPμSL) enabled 3D PPG and Pluronic® crosslinked networks in a layer-by-layer fashion, with features smaller than 10 μm, and constructed well-defined, 33 mm tall 3D test bar specimen and 8 mm tall porous scaffolds. Dynamic mechanical analysis and tensile studies elucidated the effects of printed layer directions on the mechanical performance of 3D printed test bars. Optical microscopy, scanning electron microscopy (SEM), and X-Ray MicroCT enabled complimentary methods for imaging preliminary scaffolds, revealing high precision in the printing process and capturing structural details and reproducibility within the 3D object. The goal of these

investigations is to evaluate novel photo-curable oligomers for 3D printing technologies and for potential applications in 3D printing tissue-engineered scaffolds with well-defined geometric precision and mechanical properties.

3.2 *Introduction*

Advancing synthetic strategies and precise manufacturing of novel biopolymers provides opportunities for pioneering tissue-engineered scaffolds. The role of the scaffold is to restore morphological and biological function to a damaged tissue and, therefore, must provide both mechanical support and a biocompatible environment for cellular recognition and adhesion, while providing sufficient porosity for diffusing essential nutrients to the damaged site.[1-4] Conventional fabrication techniques such as particulate leeching[5,6], gas foaming[7,8], and electrospinning[9,10] disadvantageously fail to control precise placement of a material within a scaffold.[11,12] In addition, the resulting scaffolds tend to have inadequate pore interconnectivity, random pore sizes, and low mechanical strength.[13] Polymer chemistry and additive manufacturing (also known as 3D Printing) are synergistically revolutionizing the design and fabrication of tissue-engineered scaffolds, enabling the layer-by-layer manufacturing of tailored synthetic biopolymers into 3D printed scaffolds with high architectural precision and reproducibility. Customized 3D printed scaffolds provide tunable properties such as pore size, interconnectivity, and mechanical strength to govern cell adhesion and growth.

The biocompatibility and biodegradability of oligoethers and oligoesters is well-documented and utilized for many biomedical applications ranging from engineered extracellular matrices[14,15], targeted drug delivery[16,17], and highly selective molecular sensors.[18,19] Polycaprolactone[20,21] (PCL) and Pluronics®[22,23], a series of ABA triblock copolymers containing polyethylene glycol (PEG) and polypropylene glycol (PPG), are FDA approved and promoted in the biomedical industry for

various devices and implants.[24] These paradigmatic biopolymers are commercially available and easy to process, qualifying them as attractive compositions for 3D printing. Literature precedence exists for printing PCL into porous scaffolds for bone tissue repair and regeneration. Additional studies report the UV irradiation of acrylate modified Pluronics® that produced covalently crosslinked hydrogels comparable in strength to human tissue.[22]

This chapter introduces the synthesis of photocurable, diacrylate functionalized PPG and Pluronics® L-31, L-61, and 10R5 for potential applications in 3D printing tissue-engineering scaffolds (Scheme 1 and Table I). Photorheology probed photo-crosslinking behavior of the PPG and Pluronic® diacrylate compositions, elucidating the influence of intensity and diacrylate composition on cure time. Mask projection micro-stereolithography (MPμSL), a well-established additive manufacturing technology, photo-crosslinked the diacrylate oligomers in a layer-by-layer fashion, with features smaller than 10 μm, and constructed well-defined, 33 mm tall 3D test bar specimen and 8 mm tall porous scaffolds. Dynamic mechanical analysis and tensile studies elucidated the effects of printed layer directions on the mechanical performance of 3D printed test bars. Optical microscopy, scanning electron microscopy (SEM), and X-Ray MicroCT enabled complimentary methods for imaging preliminary scaffolds, revealing high precision in the printing process and capturing structural details and reproducibility within the 3D object. As biomedical applications for 3D printing tissue-engineered scaffolds emerge, expanding the selection of biocompatible, photo-curable polymers and establishing structure-property-processing relationships suitable for 3D printing will facilitate these technologies.

3.3 *Experimental Section*

3.3.1 Materials

Bis(trifluoromethane)sulfonimide lithium salt (99%), 2, 2-dimethoxy-1, 2-diphenylethan-1-one (≥90%), acryoyl chloride, Pluronic L-31, Pluronic L-61, and Pluronic 10RS were purchased from Sigma Aldrich and used without any further purification.

3.3.2 Instrumentation

The MPμSL machine consists of a UV light source (Hamamatsu LightningCure LC-L1V3 UV LED), conditioning optics (Edmund Optics), a mirror, a dynamic mask connected to a computer, imaging optics, and a 50 mL beaker with a stage mounted on a linear actuator (Zaber NA11B60).[25] The dynamic mask, a FlexLight X1 DLP Development System (Keynote Photonics) consists of a DLP 0.95 1080p DMD from Texas Instruments and a developer board. The DMD is a 1920 x 1080 array of aluminum micromirrors that measures 0.95-inch along the diagonal. Each square micromirror has a side length of 10.8 μm. The imaging optics reduce the image dimensions by a factor of 2 so the effective projection area of each micromirror on the surface of the photopolymer surface is 5.4 μm x 5.4 μm.

Photorheology was performed using a TA Instruments DHR-2 rheometer with a 20 mm parallel plate geometry and Smart Swap™ UV geometry. Pluronic® samples were subjected to oscillatory strain experiments at increasing UV light intensity (UHP, 500 um gap, 10 Hz, 0.05% oscillatory strain). The resulting storage and loss moduli for each composition were plotted using the TA Instruments TRIOS software package. A SkyScan 1172 X-Ray MicroCT performed a 180° scan on 3D printed Pluronic® L-61 tissue-engineered scaffold using a 0.4° step increment. An stl file provided a reconstructed image of the Pluronic® scaffold, digitally modeled using NetFabb

software for 3D modeling. A NEO Scope JCM 5000 scanning electron microscope (SEM) imaged complex 3D objects for analyzing architectural features and build reproducibility. 3D objects were mounted on a SEM disc, and required no additional sputter-coating to reduce electron charging effects. Dynamic mechanical analysis (DMA) was conducted on a TA Instruments Q800 Dynamic Mechanical Analyzer in tension mode at a frequency of 1 Hz, an oscillatory amplitude of 15 μm, and a static force of 0.01 N. The temperature ramp was 3 ^{o}C/min. The glass-transition temperature (T_g) was determined at the peak maximum of the tan δ curve. Tensile experiments employed an Instron at 50 mm/min strain rate.

3.3.3 Synthesis of PPG and Pluronic Diacrylates

In a representative reaction, a 100-mL round-bottomed flask in an ice bath equipped with an addition funnel and a nitrogen inlet was charged with Pluronic L-31 (55 mmol, 60 g), K_2CO_3 (17 mmol, 23 g), and DCM (250 mL). Acryloyl chloride (17 mmol, 15 g) was added dropwise and the reaction was allowed to stir overnight at 0°C. Upon completion, the resulting cloudy solution was filtered through celite twice to remove salt by-product and the filtrate was vacuum stripped. The obtained Pluronic L-31 diacrylate was dried at 30 ^{o}C under reduced pressure (0.5 mmHg) for 24 h until constant weight. (Yield: 92%).

3.3.4 MPμSL Fabrication Process for 3D Printing Pluronic Networks.

All of the 3D printed Pluronic® networks follow a similar procedure and the construction of a 4 mm x 4 mm x 8 mm 3D Pluronic® L-61 scaffold represents an example. NetFabb created slices (saved as bitmap images) of a 3D computer aided design (CAD) model into individual images at desired thickness (100 μm) for projecting onto the photocurable Pluronic® L-61. A LabView program projected each image with control using the DMD and the movement of the

stage. Pluronic® L-61 (30 g, 27.5 mmol) with 2, 2-dimethoxy-1, 2-diphenylethan-1-one (572.0 mg) were mixed in a 30 mL beaker and a stage was lowered and slightly submerged into the beaker. The LabView program directed individual mirrors "on" or "off" to display the first image. The UV light passed from the LED lamp through the conditioning optics and mirror to the DMD, which projected the image onto the thin layer of Pluronic® directly above the stage. Each layer required 25.57 mJ/cm^2 of exposure energy, as determined from the working curve of the test specimen. After complete exposure, the DMD mirrors turned "off" and prohibited light from projecting into the photo-curable Pluronic® L-61 sample. The stage moved until it was completely submerged and then returned to one layer thickness below the surface. The LabView software loaded the next layer's image and the process repeated until the scaffold was completely fabricated. Upon fabrication, the scaffold was isolated and rinsed with isopropyl alcohol (IPA) to remove any uncured Pluronic® L-61.

3.4 *Results and Discussion*

Scheme 3.1 reveals end group functionalization as a facile synthetic approach for converting commercially available PPG and Pluronic® diols into photo-curable polyether diacrylates for generating photo-crosslinked, 3D printed networks. The synthetic strategy follows earlier literature protocols detailing PPG diol functionalization with acryloyl chloride, and extends the modification approach with a series of Pluronic® diols including: Pluronic L-31®, Pluronic® L-61, and Pluronic® 10RS. Table 3.1 provides compositional details for the selected series, reveling variation in molecular weight and block sequence. These unique features enable new opportunities for diversifying the architectural complexity of photo-curable oligomers with block designs and subsequently elucidating compositional effects on photo-curing behavior. ^{1}H NMR revealed a

shift in -CH_2- protons upon modifying the diol to a diacrylate, revealing quantitative functionalization as the -CH_2- protons for the diol derivative disappeared.

Scheme 3.1. General reaction scheme for synthesizing and photopolymerizing PPG and Pluronic® diacrylates.

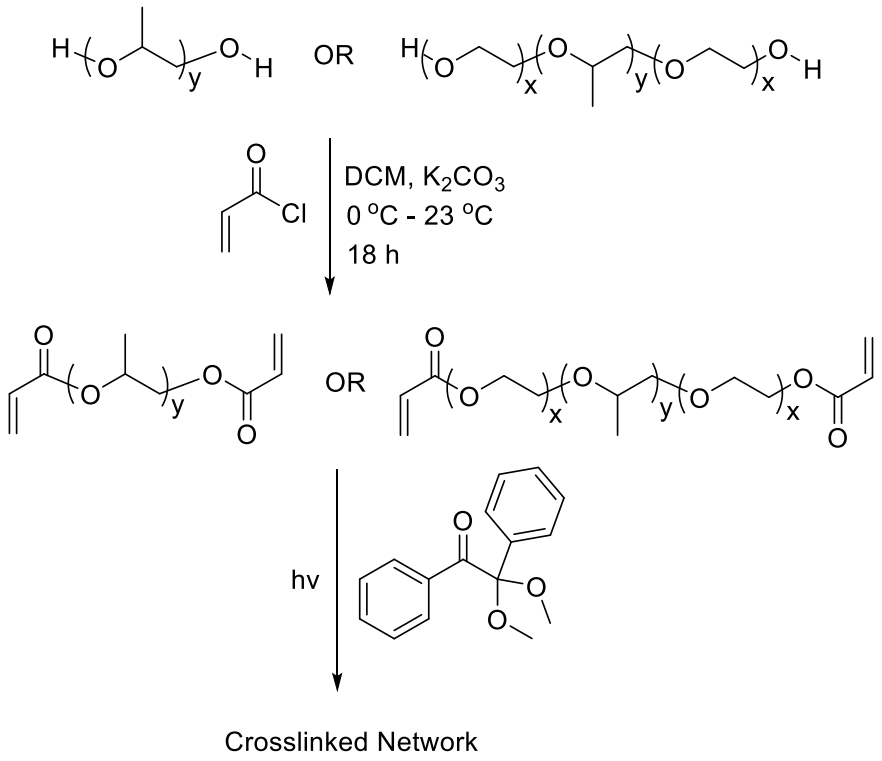

Table 3.1 Compositional details for Pluronic® diols

Composition	M_n* (g/mol)	PEG DP (M_n)	PEG wt %	PPG DP (M_n)
Pluronic L-31 (PEG-PPG-PEG)	1,100	1x2 (110)	10	17 (900)
Pluronic L-61 (PEG-PPG-PEG)	2,000	2x2 (200)	10	31 (1,800)
Pluronic 10RS (PPG-PEG-PPG)	2,000	22-23 RU (1,100)	50	8x2 (900)

*Reported from Sigma-Aldrich

Photorheology evaluated the effects of UV light intensity on cure time and storage modulus (G') of the crosslinked networks, which enabled a comparison in structure-processing relationships between all pluronic diacrylate samples with PPG control samples (Fig. 3.1). Increasing UV light intensity of 5 mW/cm^2, 10 mW/cm^2, and 20 mW/cm^2 revealed faster cure times for all samples while maintaining a two step G' transition, corresponding to the approximate gel point transition from a viscous to solid state during photopolymerization. Overlaying the photorheology data for the crosslinked networks at 5 mW/cm^2 elucidated the photoprocessing differences between all pluronic networks, revealing the fastest crosslinking for the low molecular weight Pluronic L-31 and the slowest crosslinking for the highly PEG incorporated Pluronic 10RS.

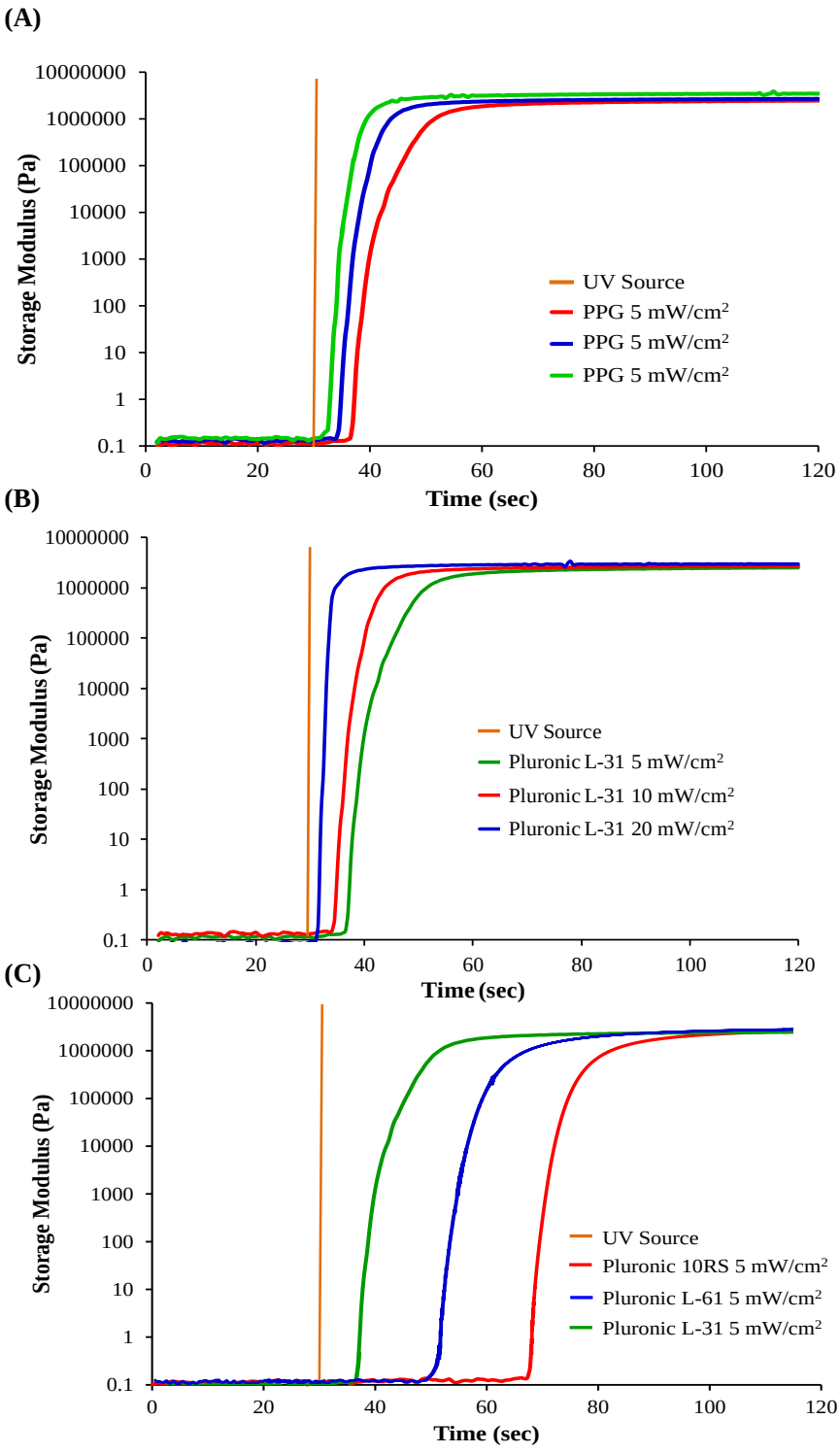

Figure 3.1. (A) Photorheology of pluronic L-31 diacrylate at various light intensity exposure. (C) Photorheology comparison between Pluronic L-31, L-61, and 10RS at 5 mW/cm^2 light intensity exposure.

Photopolymerization strategies coupled with MPμSL achieved layer-by-layer fabrication of PPG and Pluronic crosslinked 3D objects. Literature reports thoroughly detail the MPμSL operating system apparatus.[25] A diverse range of computer-aided design (CAD) files enabled the additive manufacturing of diverse 3D printed objects, ranging from 33 mm tall rectangular test specimens to an 8 mm tall tissue-engineered scaffold (Fig. 3.2). Optical microscopy reveals a representative image of a Pluronic L-61 3D scaffold, capturing the fine detailed layering within the printed architecture in comparison to the original CAD image (Fig. 3.3). Scanning electron microscopy (SEM) images of the representative Pluronic L-61 3D scaffold reveals the layered features down to a 500 um scale, and further displays the well-defined architecture and build reproducibility in the complex object (Fig. 3.4). X-Ray microCT scanning reconstructed a CAD image of the Pluronic L-61 3D scaffold, demonstrating systematic efficiency in reproducing CAD designs (Fig. 3.5). The surface roughness depicted in both X-Ray microCT and SEM images is consistent for all printed objects and is attributed to the micro-stereolithography build process. Soxhlet extraction with THF at reflux for 24 h determined wt.% gel fraction for all test specimens, revealing gel fractions of 92-98 wt.% and confirming high UV-curing efficiency.

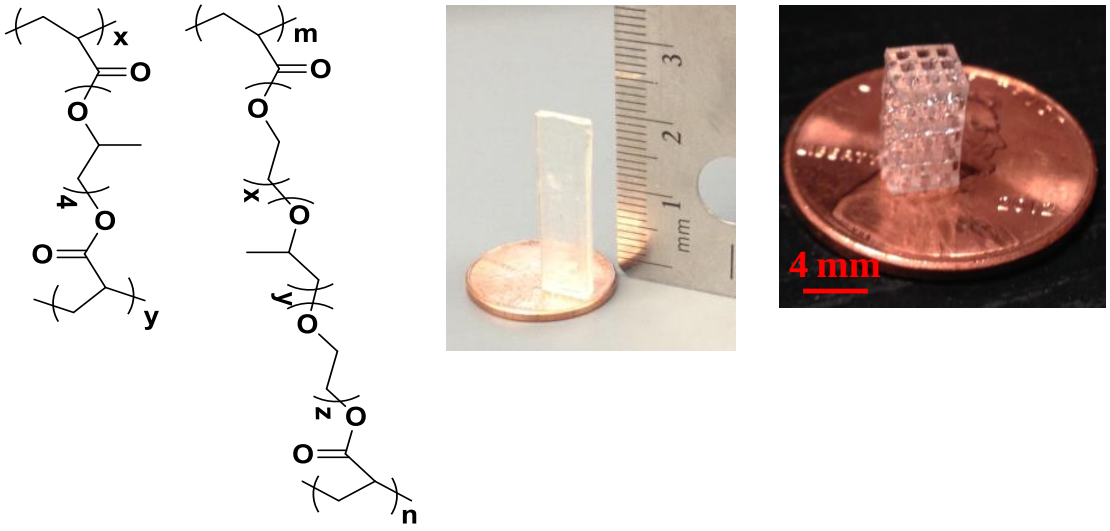

Figure 3.2. Mask projection micro-stereolithography successfully 3D prints diacrylate functionalized PPG, Pluronic L-31, L-61, and 10RS 33 mm tall rectangular test specimens, and Pluronic L-61 8 mm tall scaffold.

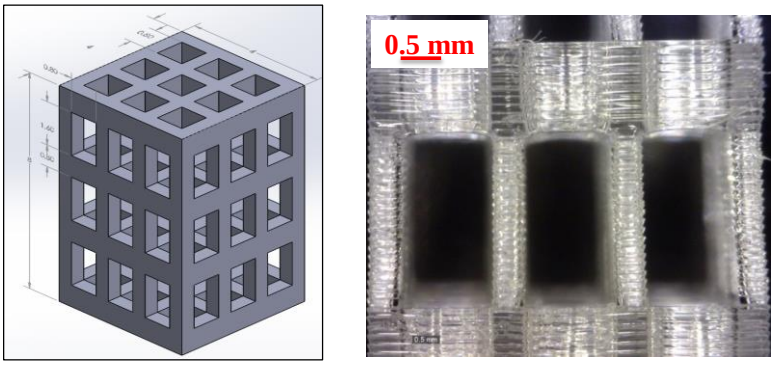

Figure 3.3. Detailed images of 3D printed Pluronic L-61 scaffold with optical microscopy.

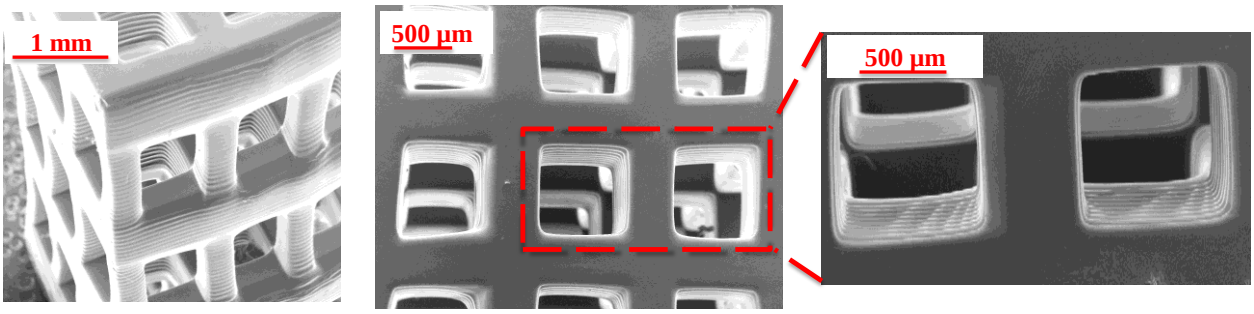

Figure 3.4. Detailed images of 3D printed Pluronic L-61, scaffold with scattering electron microscopy.

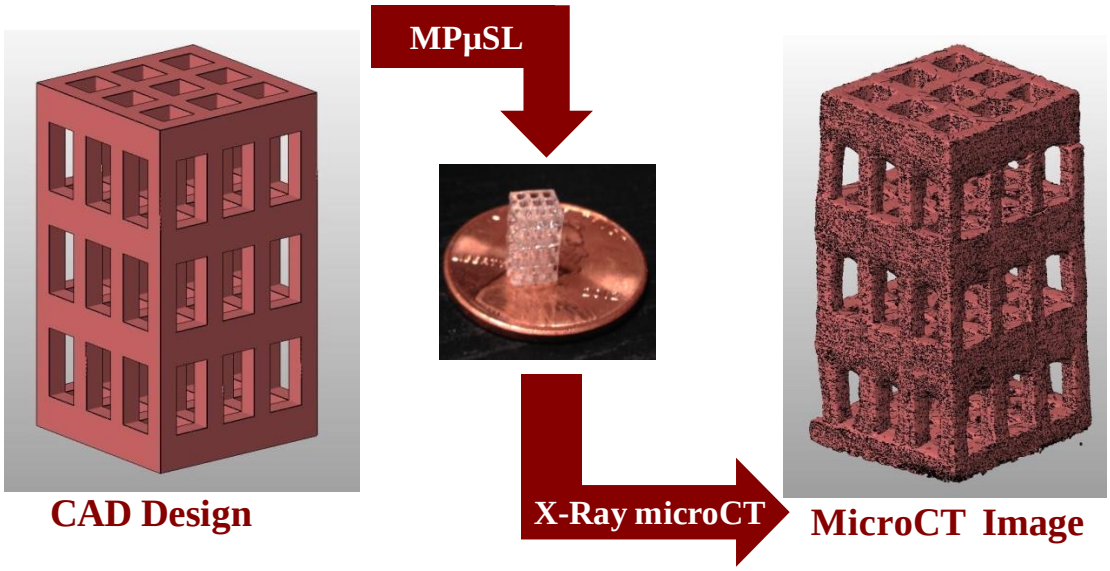

Figure 3.5. X-Ray microCT image of 3D printed Pluronic L-61 scaffold in comparison to original CAD design.

Varying the wt. % incorporation of PPG in the Pluronic compositions, achieved a series of 3D, 33 mm × 6 mm × 2 mm test specimens for mechanical analysis in comparison to 3D printed poly(PPG) control samples. Soxhlet extraction with THF at reflux for 24 h determined wt % gel fraction for all test specimens, revealing gel fractions of 93−97 wt % and confirming high UV-curing efficiency. Fig. 3.6 reveals the 3 samples catergories for the printed bars: (A) 3D printed with horizontal layers, (B) photo-crosslinked, and (C) 3D printed with vertical layers. DMA and tensile studies evaluated the thermomechanical behavior for all PPG thermoset polymer bars, revealing a constant G' values for the glassy state of all samples, constant Tg values, and constant G' values in the equilibrium region (Fig. 3.7). All of these features confirmed curing consistency for all sample bars.

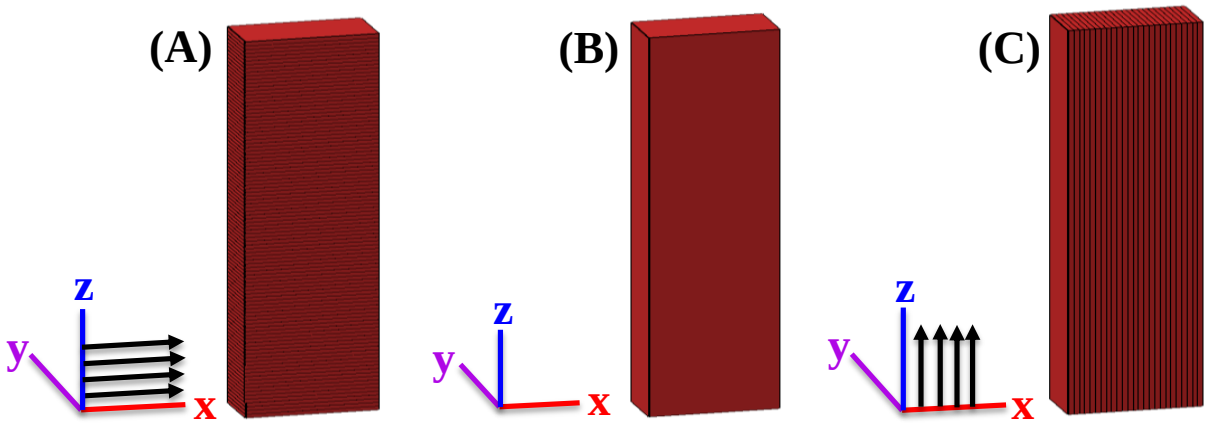

Figure 3.6. Photo-polymerization and 3D printing enables (A) 3D printed test bars with horizontal layers, (B) photo-crosslinked bars, and (C) 3D test bar specimen with vertical layers.

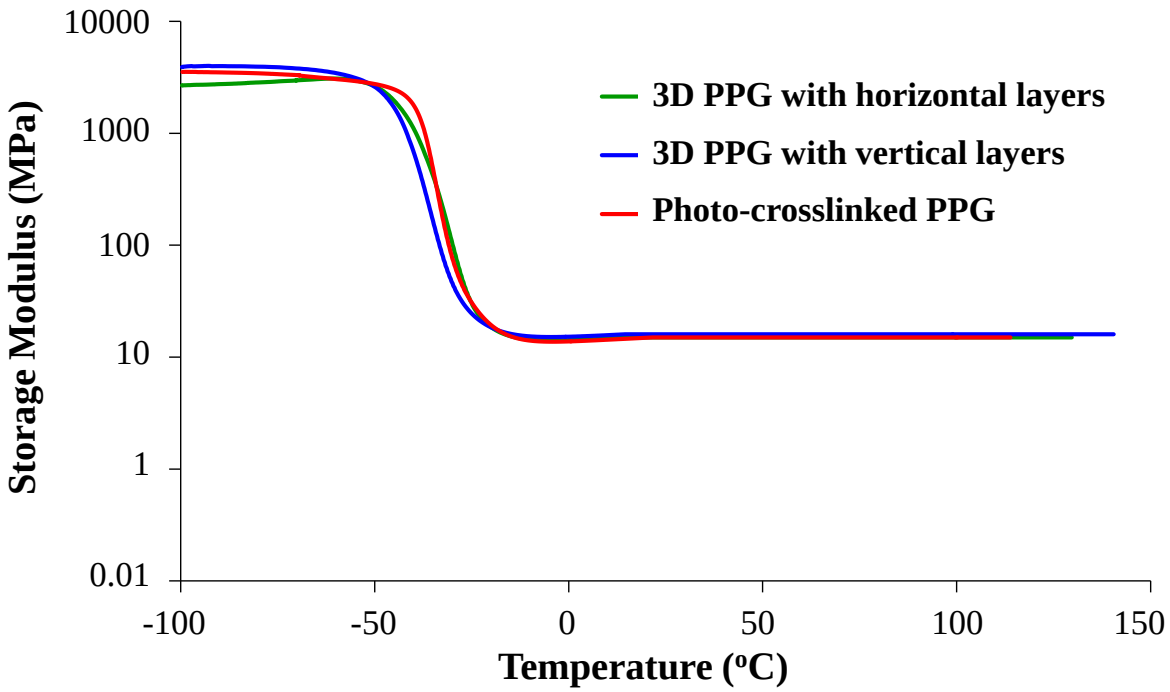

Figure 3.7. DMA characterization of 3D PPG printed test bars with horizontal layers, photo-crosslinked PPG bars, and 3D PPG test bar specimen with vertical layers. Tension mode 3 ºC/min, 1 Hz.

Tensile experiments revealed the effects of the printing process on the mechanical performance, revealing the increasing strain % break values in the order of: bars printed with horizontal layers < photo-crosslinked bars < bars printed with vertical layers. The vertical layered bar exhibited the highest mechanical performance, revealing mechanical reinforcement in the layered orientation. Comparing 3D printed bars with vertical layers for the Pluronic series enabled an evaluation compositional effects on mechanical performance, revealing increasing strain % break values in the order of: 10R5 < L-31 < L-61. This trend revealed increased mechanical performance or compositions with increasing PPG content and with increasing M_n.

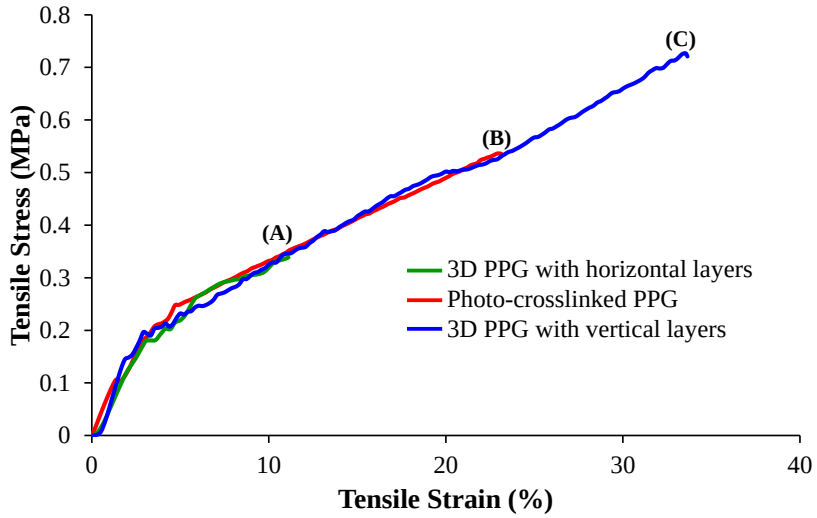

Figure 3.8. Tensile analysis of (A) 3D PPG printed test bars with horizontal layers, (B) photo-crosslinked PPG bars, and (C) 3D PPG test bar specimen with vertical layers. 50 mm/min, average of 5 samples.

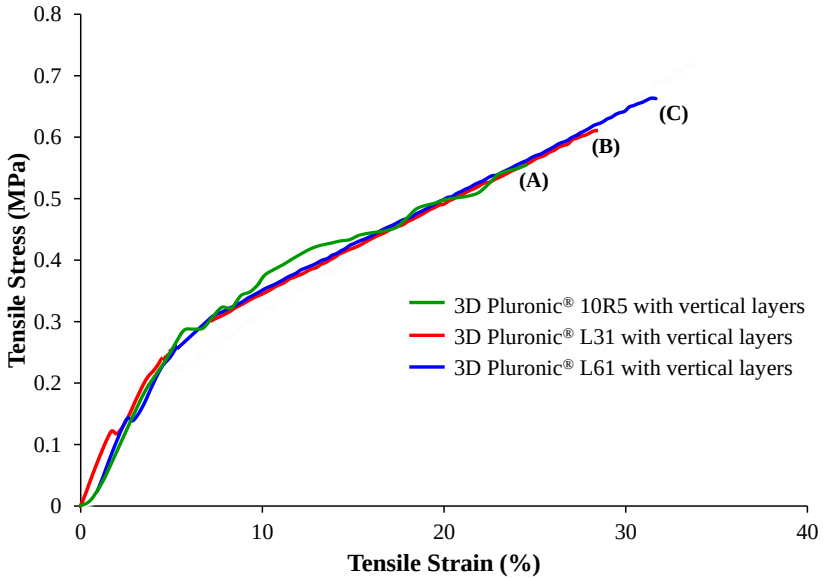

Figure 3.9. Tensile analysis of (A) 3D Pluronic® 10R5 (B) 3D Pluronic® L31 bars, and (C) 3D Pluronic® L61 test bar specimen with vertical layers. 50 mm/min, average of 5 samples.

3.5 *Conclusions*

This chapter reveals for the first time 3D printed Pluronic® networks, in order to demonstrate the synergy between MPμSL technology and printing a complex biocompatible polymeric material. We achieved an efficient method for producing tissue-engineered scaffolds, with well-defined architectures and build reproducibility. Mechanical testing with tensile experiments reveal the mechanical enhancement properties of PPG segments within the Pluronic® compositions. Future studies will focus on expanding this research toward more complex scaffold designs with multi-component materials for tunable cell adhesion.

3.6 *Acknowledgements*

This material is based upon work supported in part by the Howard Hughes Medical Institute through the Scieneering Program and through Objet. We would also like to thank the Williams group for the collaboration of 3D printing. We acknowledge the Institute for Critical Technology and Applied Science (ICTAS) and the Design, Research, and Education for Additive Manufacturing Systems (DREAMS) laboratory at Virginia Tech for instrument support. We also thank Dr. Rolf Mueller in the Department of Mechanical Engineering for access to the microCT instrumentation.

3.7 *References*

(1) Cooper, J. A.; Lu, H. H.; Ko, F. K.; Freeman, J. W.; Laurencin, C. T. *Biomaterials* **2005**, *26*, 1523.

(2) Yu, X.; Bellamkonda, R. V. *Tissue engineering* **2003**, *9*, 421.

(3) Hutmacher, D. W. *Biomaterials* **2000**, *21*, 2529.

(4) Hollister, S. J. *Nature materials* **2005**, *4*, 518.

(5) Liu, X.; Ma, P. X. *Annals of biomedical engineering* **2004**, *32*, 477.

(6) Kim, S.-S.; Park, M. S.; Jeon, O.; Choi, C. Y.; Kim, B.-S. *Biomaterials* **2006**, *27*, 1399.

(7) Agrawal, C.; Ray, R. B. *Journal of biomedical materials research* **2001**, *55*, 141.

(8) Mikos, A. G.; Temenoff, J. S. *Electronic Journal of Biotechnology* **2000**, *3*, 23.

(9) Li, W. J.; Laurencin, C. T.; Caterson, E. J.; Tuan, R. S.; Ko, F. K. *Journal of biomedical materials research* **2002**, *60*, 613.

(10) Yoshimoto, H.; Shin, Y.; Terai, H.; Vacanti, J. *Biomaterials* **2003**, *24*, 2077.

(11) Gauvin, R.; Chen, Y.-C.; Lee, J. W.; Soman, P.; Zorlutuna, P.; Nichol, J. W.; Bae, H.; Chen, S.; Khademhosseini, A. *Biomaterials* **2012**, *33*, 3824.

(12) Lee, J. W.; Ahn, G.; Kim, J. Y.; Cho, D.-W. *Journal of Materials Science: Materials in Medicine* **2010**, *21*, 3195.

(13) Cho, D.-W.; Kang, H.-W. In *Computer-Aided Tissue Engineering*; Springer: 2012, p 341.

14) Fedorovich, N. E.; Alblas, J.; de Wijn, J. R.; Hennink, W. E.; Verbout, A. J.; Dhert, W. J. *Tissue engineering* **2007**, *13*, 1905.

(15) Freyman, T.; Naimark, W.; Palasis, M.; Google Patents: 2003.

(16) Veronese, F. M.; Pasut, G. *Drug discovery today* **2005**, *10*, 1451.

(17) Buirge, A. W.; Google Patents: 1998.

(18) Gokel, G. W.; Leevy, W. M.; Weber, M. E. *Chemical reviews* **2004**, *104*, 2723.

(19) Ushakov, E. N.; Alfimov, M. V.; Gromov, S. P. *Russian Chemical Reviews* **2008**, *77*, 39.

(20) Lim Soo, P.; Luo, L.; Maysinger, D.; Eisenberg, A. *Langmuir* **2002**, *18*, 9996.

(21) Kweon, H.; Yoo, M. K.; Park, I. K.; Kim, T. H.; Lee, H. C.; Lee, H.-S.; Oh, J.-S.; Akaike, T.; Cho, C.-S. *Biomaterials* **2003**, *24*, 801.

(22) Oshiro, A.; da Silva, D. C.; de Mello, J. C.; de Moraes, V. W.; Cavalcanti, L. P.; Franco, M. K.; Alkschbirs, M. I.; Fraceto, L. F.; Yokaichiya, F.; Rodrigues, T. *Langmuir* **2014**, *30*, 13689.

(23) Escobar-Chávez, J. J.; López-Cervantes, M.; Naik, A.; Kalia, Y.; Quintanar-Guerrero, D.; Ganem-Quintanar, A. *Journal of Pharmacy & Pharmaceutical Sciences* **2006**, *9*, 339.

(24) Tay, B. Y.; Zhang, S. X.; Myint, M. H.; Ng, F. L.; Chandrasekaran, M.; Tan, L. K. A. *Journal of Materials Processing Technology* **2007**, *182*, 117.

(25) Lambert, P. M.; III, E. A. C.; Williams, C. B. In *Solid Freeform Fabrication Symposium* Austin, Texas, 2013, p 111.

Chapter 4: Phosphonium-Containing Diblock Copolymers from Living Anionic Polymerization of Diphenylphosphino Styrene

(Published in *Chemical Communications*)

*Alison R. Schultz, Chainika Jangu, Mingtao Chen, Gregory Fahs, Robert B. Moore, and Timothy E. Long**

Macromolecules Innovation Institute, Department of Chemistry, Virginia Tech, Blacksburg, VA 24061, USA. E-mail: telong@vt.edu.

*To whom correspondence should be addressed. E-mail: telong@vt.edu. TEL: (540)231-2480. FAX: (540)231-8517.

Keywords: Anionic polymerization, phosphonium, *in situ* FTIR spectroscopy, SAXS

4.1 *Abstract*

Anionic polymerization of 4-diphenyl phosphino styrene (DPPS) achieved homopolymers, poly(DPPS-*b*-S) and poly(I-*b*-DPPS) diblock copolymers with predictable molecular weights and narrow polydispersities. *In situ* FTIR spectroscopy monitored the anionic polymerization of DPPS and tracked monomer consumption. Sized exclusion chromatography revealed the living polymerization poly(DPPS-*b*-S), revealing molecular weight shifts in the SEC traces upon sequential monomer addition with styrene. Sequential monomer addition also enabled a poly(I-*b*-DPPS) diblock copolymer, revealing the versatility of the DPPS monomer and its compatibility with nonpolar solvent conditions. Post-alkylation enabled controlled placement of phosphonium functionality in poly(I-*b*-DPPS) diblock copolymers, producing well-defined phosphonium-containing block copolymers with low degrees of compositional heterogeneity. Incorporating phosphonium charge disrupted the highly ordered lamellar bulk morphology of the neutral diblock

precursor and gave rise to new morphologies involving interdigitated packing of alkyl chains on the phosphonium cation.

4.2 *Introduction*

Styrenic block copolymers receive continued attention for the production of thermally stable compositions with tunable physical and mechanical properties, impacting technologies ranging from high performance adhesives[1,2] and durable coatings[3,4] to biomaterials[5,6] and medical devices.[7-10] Immiscible block sequences promote microphase separation, facilitating self-assembly into various nanostructured compositions with tailored sequence lengths and volume fractions, molecular weight distribution, and chemical compositions. Tuning structural composition and nanostructured morphologies engineers a vast array of styrenic block copolymers and enables predictable viscoelastic properties for targeted applications. Incorporating ion-containing extended sequences imparts electrostatic interactions for enhancing microphase separation and thermomechanical properties, and provides electromechanical properties suitable for additional technologies involving electro-active[11,12] and ion exchange membranes.[13-15]

Sulfonated styrenic block copolymers represent exemplary ion-containing compositions, possessing fortified viscoelastic behavior and enhanced microphase separation due to synergistic properties of ionomers[16,17] and block copolymers.[18] Ionic association within these block compositions increases the Flory-Huggins interaction parameter χ for microphase separation, allowing for lower block molecular weights and improved microphase separation.[19] Previous investigations involving sulfonated block copolymers[20,21] elucidated effects of sulfonation level, molecular weight, and relative humidity on morphologies and electro-active properties, and earlier work predominately focused on Kraton® sulfonated poly(styrene-*b*-hydrogenated butadiene-*b*-styrene) [poly(SS-*b*-HB-*b*-SS)] and sulfonated poly(styrene-*b*-hydrogenated isoprene-*b*-styrene)

[poly(SS-*b*-HI-*b*-SS)] triblock copolymers,[22,23] and Kraton® sulfonated poly(tert-butyl styrene-*b*-hydrogenated isoprene-*b*-sulfonated styrene-*b*-hydrogenated isoprene-*b*-tert-butyl styrene) [poly(tBS-*b*-HI-*b*-SS-*b*-HI-*b*-tBS)] pentablock copolymers (0-50 mol% sulfonated polystyrene).[24-27] Although these reports revealed sulfonated block copolymers as promising membranes for technologies ranging from fuel cells and water purification[28] to actuators[29] and nanofabrication[30], concern for thermal and charge stability due to low temperature degradation reactions poses an architectural design flaw and inspires new directions in polymerizing alternative charged monomers.[27,31]

Recent studies reveal phosphorus-containing macromolecules as promising analogues to sulfonated polymers, revealing tunable oxidation states (phosphates, phosphines, phosphine oxides, and phosphoniums), high alkylation efficiency,[32,33] thermal and base stability,[32,33] high ionic conductivity,[11,34] tailored structures and morphologies,[35] and ionic aggregation.[36] Phosphorus-containing monomers exhibiting vinylbenzyl-, acrylate-, and methacrylate-polymerizable units achieves a wide range of phosphorus-containing macromolecules including homopolymers,[37] random copolymers,[38] and block copolymers.[39,40] Although many of these synthetic methods involve controlled free radical strategies, anionic polymerization remains a commercially viable process for producing block copolymers with architectural precision and low degrees of compositional heterogeneity. Herein, we report the controlled anionic polymerization of 4-diphenylphosphino styrene (DPPS) as an unprecedented method for achieving novel phosphorus-containing styrenic block copolymers. DPPS does not contain β-hydrogens to the phosphorus atom that are susceptible for low temperature Hoffman elimination degradation pathways and, consequently, is structurally advantageous for achieving phosphonium-containing block copolymers with enhanced thermal and base stability in comparison to sulfonated styrenic

block copolymers. Sequential monomer addition strategies enabled poly(I-*b*-DPPS) block copolymers for elucidating post-alkylation effects on structure-morphology behavior. As ion-containing polymers emerge for electro-active membranes, designing novel phosphonium-containing block copolymers with predictable structure-morphology-property relationships will facilitate commercial technologies.

4.3 *Experimental Section*

4.3.1 Materials

4-diphenylphosphino styrene (99%), styrene (99%), isoprene (99%), and 1.4 M *sec*-butyllithium solution in cyclohexane were purchased from Sigma Aldrich and used as received unless otherwise noted. Styrene and isoprene, containing 10-15 ppm of *t*-butyl catechol, were distilled from calcium hydride and dibutyl magnesium.

4.3.2 Instrumentation

In situ FTIR analysis employed a Mettler Toledo ReactIR 45M attenuated total reflectance reaction apparatus equipped with a light conduit and DiComp (diamond composite) insertion probe. Size-exclusion chromatography (SEC) was used to determine the molecular weights of phosphino-containing polymers at 40 ^{o}C in THF at 1 mL/min. THF SEC was performed on a Waters SEC equipped with two Waters Styragel HR5E (THF) columns, a Waters 717 plus autosampler, a Wyatt MiniDAWN, and a Waters 2414 differential refractive index detector. An Optilab T-rEX refractometer ($\lambda = 658$) was used to measure d*n*/d*c* values offline for determination of absolute weight-average molecular weights. ^{1}H and ^{31}P NMR spectroscopy (Varian Inova, 400 MHz) determined polymer composition and degree of alkylation. SAXS experiments were performed using a Rigaku S-Max 3000 3 pinhole SAXS system, equipped with a rotating anode

emitting X-ray with a wavelength of 0.154 nm (Cu Kα). The sample-to-detector distance was 1604 mm, and q-range was calibrated using a silver behenate standard. Two-dimensional SAXS patterns were obtained using a fully integrated 2D multiwire, proportional counting, gas-filled detector, with an exposure time of 2 hours. All the SAXS data were analyzed using the SAXSGUI software package to obtain radially integrated SAXS intensity versus scattering vector q, where $q = (4\pi/\lambda)\sin(\theta)$, θ is one half of the scattering angle and λ is the wavelength of X-ray. SAXS profiles were vertically shifted to facilitate a comparison of the peak positions.

4.3.3 *In situ* FTIR monitoring of the anionic polymerization of 4-diphenylphosphino styrene

2.0 g 4-diphenylphosphino styrene and 8 mL of dry THF were added to a two-necked, 25-mL, flame-dried, round-bottomed flask with a magnetic stir bar. One neck was sealed with a rubber septum, and the DiComp probe was inserted into the second neck and sealed. The probe tip was submerged below the monomer surface, and the ReactIR spectrometer was programmed to collect a spectrum every 1 min for 5 h (SI Figure 1). The flask was purged with nitrogen for 15 min and placed in an isopropanol/dry ice bath at -78 ºC. *Sec*-butyllithium (0.02 mL) initiated growth of a 10,000 g/mol polymer. After 1 h with FTIR analysis, the product was diluted with THF or chloroform and precipitated into methanol.

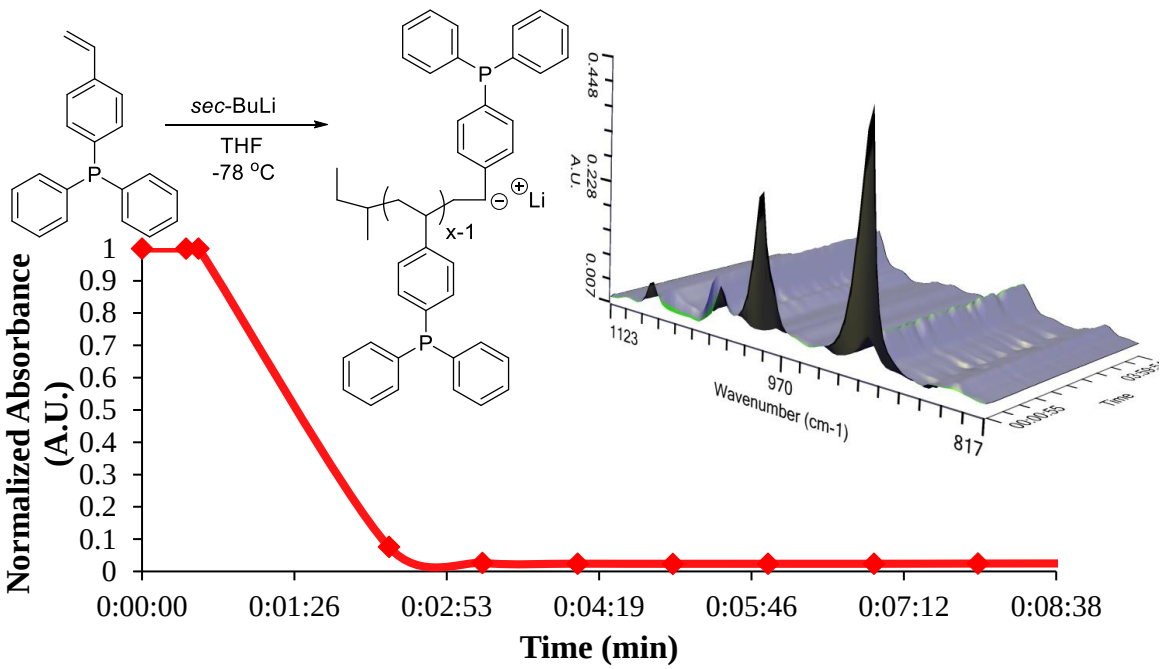

Figure SI 4.1 *In situ* FTIR monitoring of DPPS vinyl concentration disappearance at 918 cm^{1} over time in a 3D waterfall plot and 2D normalized plot.

4.3.4 Anionic polymerization of poly(4-diphenylphosphino styrene-*b*-styrene)

To a 100-mL flame dried, nitrogen purged, and sealed round bottom flask with stir bar, (3.00 g) DPPS and 50 mL of THF were added. The reaction flask was cooled to -78 °C for 10 min and *sec*-butyl lithium (0.07 mL, 0.1 mmol) was then added to the solution to initiate growth of a 30,000 g/mol polymer. The first reaction was allowed to proceed for 5 min and the second monomer, 2.97 mL styrene (3.00 g) was sequentially added to the reaction mixture. The polymerization was terminated after 5 min with degassed methanol (0.2 mL), and the resulting poly(DPPS-*b*-S) diblock copolymer solution was precipitated into methanol and dried at 23 °C under reduced pressure (0.5 mmHg) for 24 h to obtain a white powder (90-95% isolated yield).

4.3.5 Anionic polymerization of poly(isoprene-*b*-4-diphenylphosphino styrene)

To a 100-mL flame dried, nitrogen purged, and sealed round bottom flask with stir bar, (15 mL, 10.2 g) isoprene and 50 mL of cyclohexane were added. The reaction flask was heated to 50 ^{o}C for 10 min and *sec*-butyl lithium (0.24 mL, 0.2 mmol) was then added to the solution to initiate growth of a 30,000 g/mol polymer. The first reaction was allowed to proceed for 2 h and 4-diphenylphosphino styrene (5.1 g) was sequentially added to the reaction mixture. The polymerization was terminated after 30 min with degassed methanol (1.0 mL), and the resulting AB diblock copolymer was precipitated into methanol and dried at 23 ^{o}C under reduced pressure (0.5 mmHg) for 24 h to obtain a white powder (95% isolated yield).

4.3.6 Alkylation of poly(I-*b*-DPPS) diblock copolymers

The following protocol describes a typical alkylation on DPPS-containing polymers. 2.00 g poly(I-*b*-DPPS) and 2.00 molar ratio of 1-bromohexane was dissolved in 25 mL tetrahydrofuran and the reaction refluxed at 70 ^{o}C for 48 h. The resulting phosphonium-containing diblock copolymer precipitated from the reaction solution. The final product was isolated and re-precipitated into diethyl ether. ^{1}H-NMR and ^{31}P-NMR tracked the appearance of alkyl substituents to confirm functionalization and production of a phosphonium cation. The final polymer was allowed to dry at 30 ^{o}C under reduced pressure (0.5 mmHg) for 48 h to obtain a white powder (98% isolated yield).

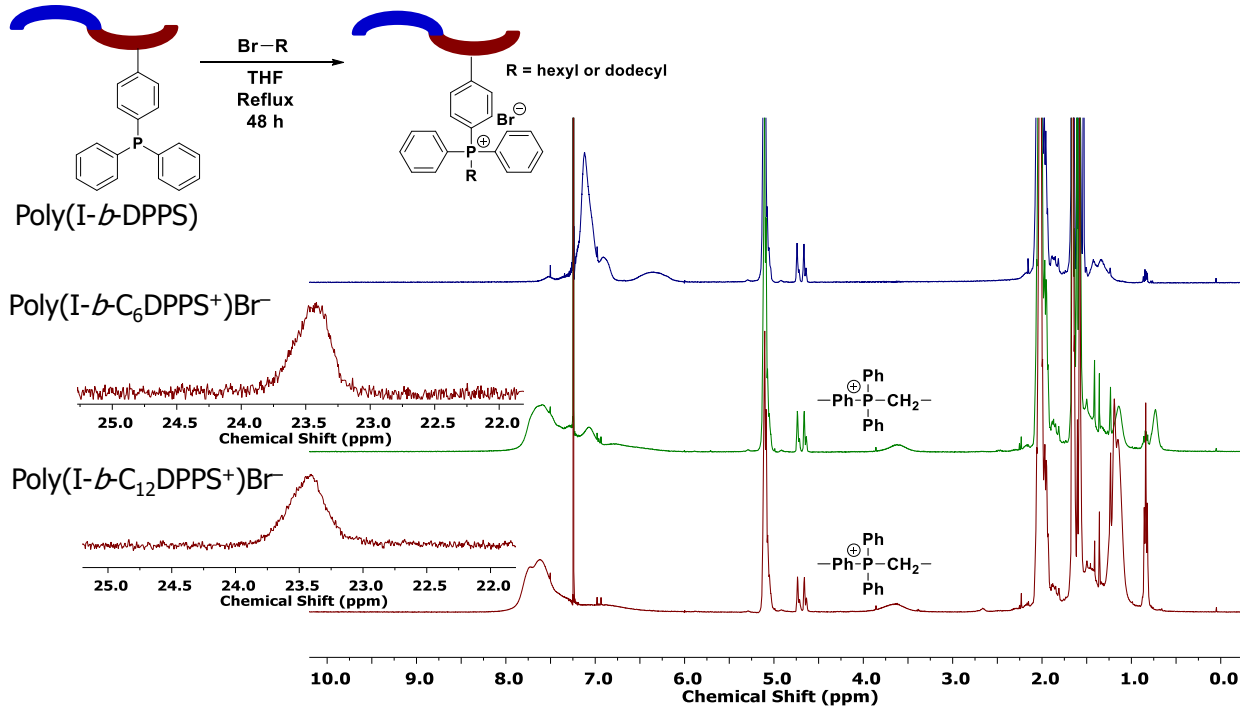

Figure SI 4.2. ^{1}H-NMR reveals $P^{+}Ph_3$-CH_2- protons and ^{31}P-NMR reveals production of the phosphonium cation, post-alkylation.

4.3.7 Film Casting

All phosphonium-containing diblock copolymers and their neutral analogue were dissolved in toluene and cast from a 30 wt% solution. Films were slowly dried at ambient conditions for 2 d followed with 2 d of drying at room temperature under reduced pressure (5 mmHg). Annealing occurred for 2 d at 120 ^{o}C under reduced pressure (5 mmHg) before characterization studies. Films were stored in a nitrogen-purged dry box to prevent undesirable oxidative reactions with the polyisoprene and poly(DPPS) sequences.

4.4 *Results and Discussion*

Scheme 4.1 depicts anionic polymerization as a facile and controlled approach for achieving poly(DPPS) homopolymers in THF using *sec*-butyllithium as the initiator. The reaction proceeded at -78 ^{o}C to maintain stereochemical control of the propagating, deep red poly(styryl)lithium chains under the polar, aprotic solvent conditions. *In situ* FTIR spectroscopy monitored DPPS propagation, using the C=C vinyl vibrational frequency peak at 918 cm^{-1} and generating a normalized waterfall plot for peak absorbance vs. time (min). Tracking vinyl concentration disappearance over time indicated that complete monomer consumption occurred within 5 min (S1). Size exclusion chromatography (SEC) confirmed a 30,000 g/mol target M_n value for the homopolymer, and revealed monomodality in the chromatogram and a narrow polydispersity of 1.05 (Figure 4.1).

Scheme 4.1. Anionic polymerization achieves poly(DPPS).

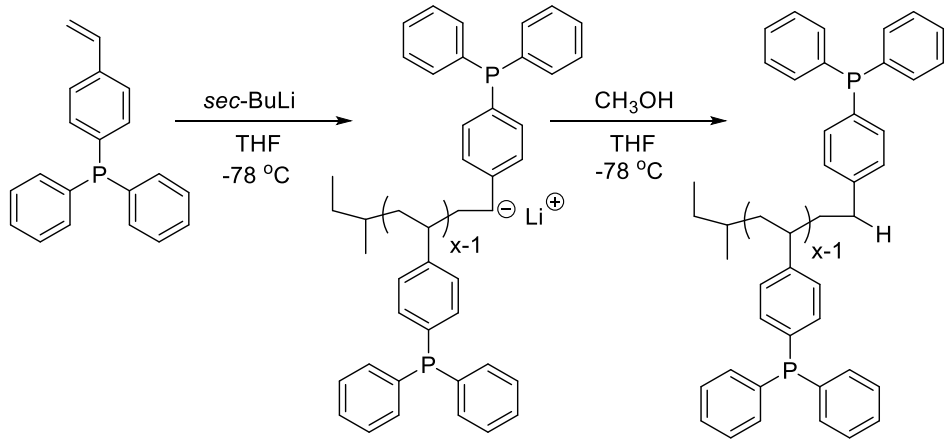

Sequential monomer addition studies with styrene further verified the controlled polymerization of DPPS, revealing characteristics of a truly "living" polymerization (Scheme 4.2A). In these studies, *sec*-butyllithium initiated the anionic polymerization of DPPS and produced living propagating chains with target M_n of 30,000 g/mol. Sequential monomer addition

enabled the anionic copolymerization with styrene, resulting in a poly(DPPS-*b*-S) block copolymer with final M_n of 60,000 g/mol (PDI = 1.06). SEC chromatograms in Figure 1 show the molecular weight shift during the sequential addition from poly(DPPS) to poly(DPPS-*b*-S) with narrow molecular weight distributions, which is indicative of living polymerization.

Living anionic polymerization with sequential monomer addition also produced a novel poly(I-*b*-DPPS) diblock copolymer in order to demonstrate the versatility in block composition and architecture (Scheme 4.2B). Moreover, this experiment elucidated DPPS propagation behavior in nonpolar solvent conditions suitable for targeting 1, 4-configuration cis-isomer diene microstructure. For this study, sec-butyllithium first initiated a living poly(isoprene) (M_n = 30,000 g/mol) due to the insoluble properties of poly(DPPS) in nonpolar solvents. After 2 h, isoprene monomer was completely consumed and DPPS was sequentially added to the living chain in order to produce a second block sequence (M_n = 15,000 g/mol) compatible with the polymer solution. The homogeneous, orange reaction mixture stirred for 30 min to complete DPPS propagation before quenching with acidic methanol. SEC analysis confirmed the total M_n = 45,000 g/mol value for poly(I-b-DPPS) and revealed a narrow polydispersity of 1.04 (Figure 4.1).

Scheme 4.2. Sequential monomer addition achieves copolymerization of diblocks (**A**) poly(DPPS-*b*-S) in polar solvent conditions and (**B**) poly(I-*b*-DPPS) in nonpolar solvent conditions.

A)

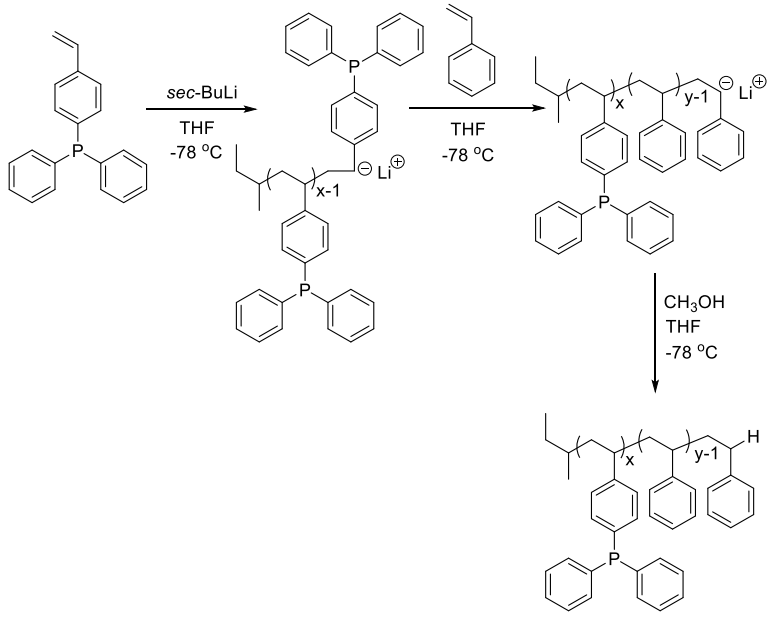

B)

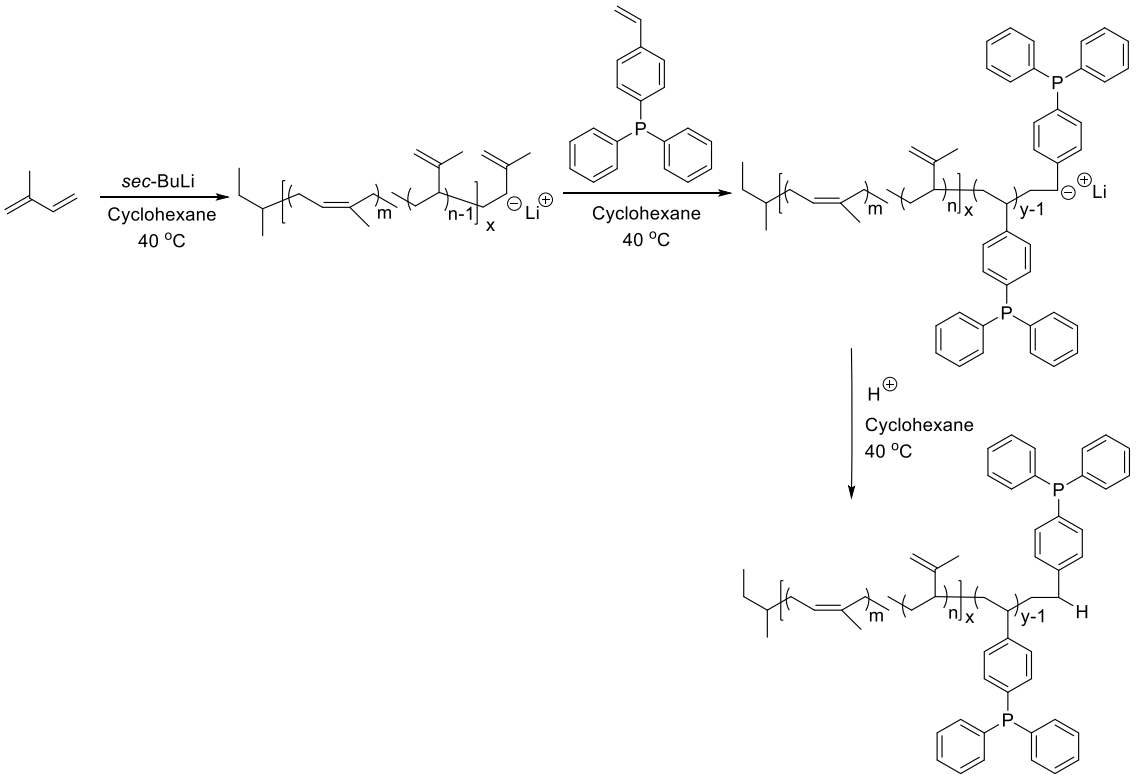

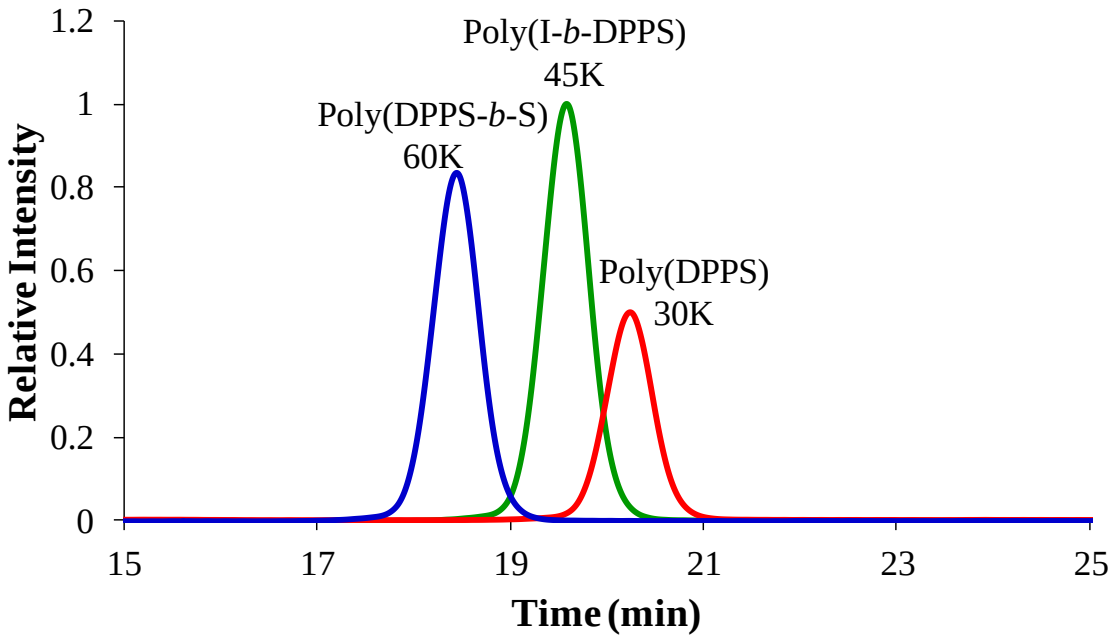

Figure 4.1. SEC characterization for poly(DPPS), poly(DPPS-*b*-S) after sequential addition of styrene, and poly(I-*b*-DPPS).

Scheme 4.3. Post-alkylation produces phosphonium containing diblock copolymers, poly(I-*b*-C_6DPPS)$^+Br^-$ and poly(I-*b*-C_{12}DPPS)$^+Br^-$.

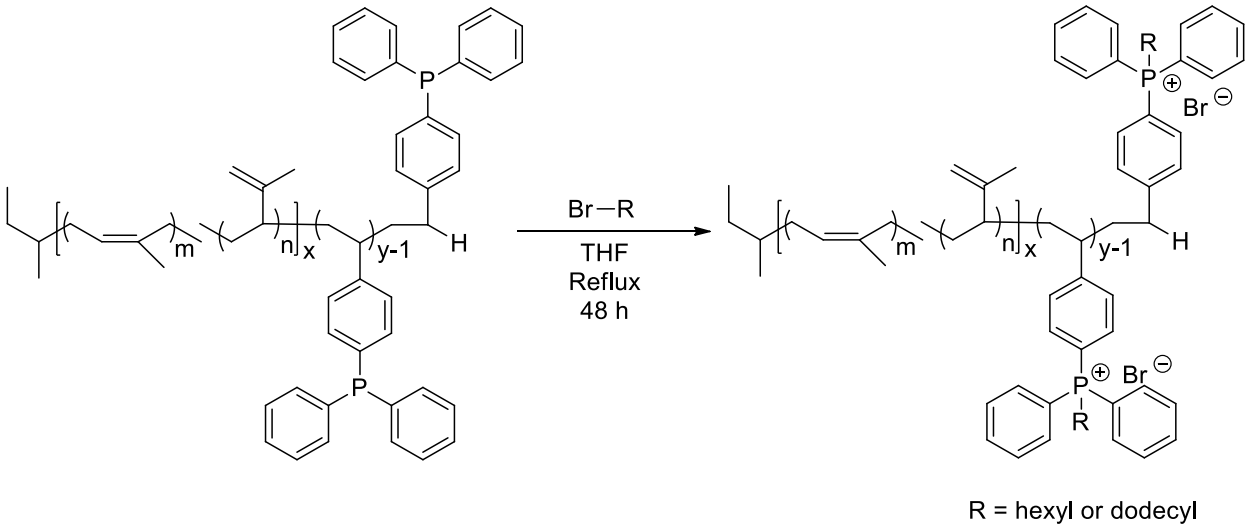

Poly(I-*b*-DPPS) diblock copolymer provided a balance of hard (DPPS, high T_g = 120 ^oC) and soft (I, low T_g = -50 ^oC) block sequences to fabricate a mechanically robust, free-standing film. Post-alkylation with bromohexane and bromododecane achieved phosphonium based derivatives (Scheme 3), poly(I-*b*-C_6DPPS)$^+Br^-$ and poly(I-*b*-C_{12}DPPS)$^+Br^-$ and DMA was employed to confirm the presence of microphase separation and elucidated the corresponding effects on thermomechanical properties (Fig. 4.2). Storage modulus (G') vs. temperature (^oC) plots revealed two distinctive transitions, corresponding to the glass transition temperature (T_g) for the soft, polyisoprene block at -55 ^oC and the various T_g values poly(DPPS), poly(I-*b*-C_6DPPS)$^+Br^-$ and poly(I-*b*-C_{12}DPPS)$^+Br^-$. Increasing the alkyl length dramatically depressed the rubbery plateau storage modulus, enabling tailored viscoelastic properties. The rubbery plateau extended for approximately 110 ^oC with a flow temperature above 100 ^oC, allowing a wide, operational temperature range for the novel diblock copolymers in diverse technologies. Previous literature on traditional poly(S-*b*-I) diblocks detail comparable thermomechanical properties and operational temperature windows.[41,42] The miscibility of DPPS and isoprene components in the poly(I-*b*-DPPS) diblock copolymer advantageously affords viscoelastic properties in agreement with conventional AB-type thermoplastic elastomers. However, post-modification reactions with DPPS provides opportunities for extending these properties beyond current industrial applications.

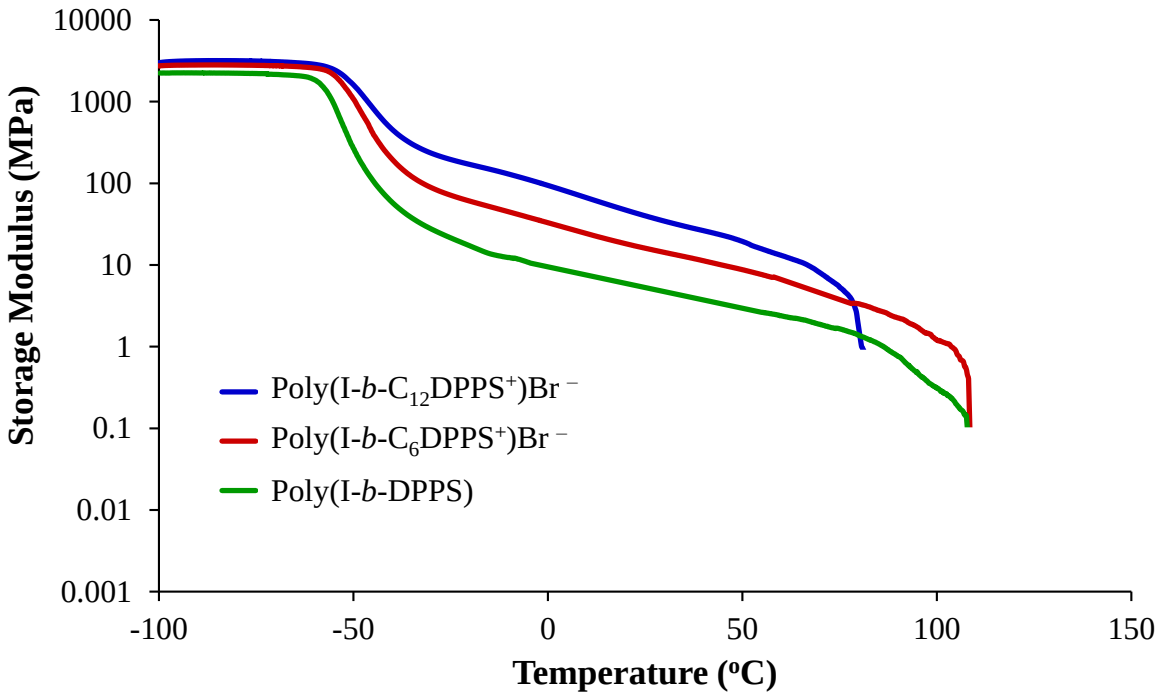

Figure 4.2. DMA characterization for poly(I-b-DPPS), poly(I-*b*-C_6DPPS)$^+$Br$^-$ and poly(I-*b*-C_{12}DPPS)$^+$Br$^-$.

Small angle X-ray scattering analysis (SAXS) probed and compared the microphase-separated bulk morphologies of the neutral and charged samples (Table 4.1 and Figure 4.6). All SAXS measurements were performed at room temperature, and all films were slowly cast from toluene and annealed at 120 °C under reduced pressure (5 mmHg) to facilitate phase separation of the blocks. The neutral poly(I-*b*-DPPS) block copolymer sample exhibited an ordered scattering profile with peak maxima at q^*, $2q^*$, $3q^*$, and $4q^*$, indicating a lamellar morphology (Figure 4.3). Bragg's law was used to approximate lamellar spacing from the primary scattering maximum at q*, revealing a Bragg distance of 28 nm. The scattering profile for both poly(I-*b*-C_6DPPS)$^+$Br$^-$ and poly(I-*b*-C_{12}DPPS)$^+$Br$^-$ exhibit broader scattering maxima compared to the neutral copolymer, presumably due to the incorporated ion associations that prohibit sufficient thermal annealing in these samples. Scattering maxima are observed at q*, 2q*, 3q*, 4q* for poly(I-*b*-C_6DPPS)$^+$Br$^-$ and

q*, 2q* for poly(I-*b*-C_{12}DPPS)$^{+}Br^{-}$, suggesting a less ordered lamellar morphology for both samples compared to the neutral copolymer (Figure 4.4 and 4.5). The lamellar spacing for both poly(I-*b*-C_6DPPS)$^{+}Br^{-}$ and poly(I-*b*-C_{12}DPPS)$^{+}Br^{-}$ is calculated to be 38 nm. Increasing the alkyl length also gave rise to a broad scattering peak at approximately q = 2.1 nm^{-1}, corresponding to the interdigitated packing of dodecyl chains on the phosphonium cation. A similar phenomenon was observed in earlier reports involving random copolymers containing trioctyl phosphonium styrenic ionic liquids.[38] Tuning film casting conditions and applying transmission electron microscopy (TEM) will further elucidate the morphology of phosphonium-containing diblock copolymers.

Table 4.1. Small angle x-ray scattering tabulated peak positions.

Peak Number	poly(I-*b*-DPPS)	poly(I-*b*-C_{12}DPPS)$^{+}Br^{-}$	poly(I-*b*-C_{12}DPPS)$^{+}Br^{-}$
q_1	0.223 nm^{-1}	0.171 nm^{-1}	0.157 nm^{-1}
q_2	0.443 nm^{-1}	0.346 nm^{-1}	0.339 nm^{-1}
q_3	0.654 nm^{-1}	0.536 nm^{-1}	_
q_4	0.874 nm^{-1}	0.734 nm^{-1}	_

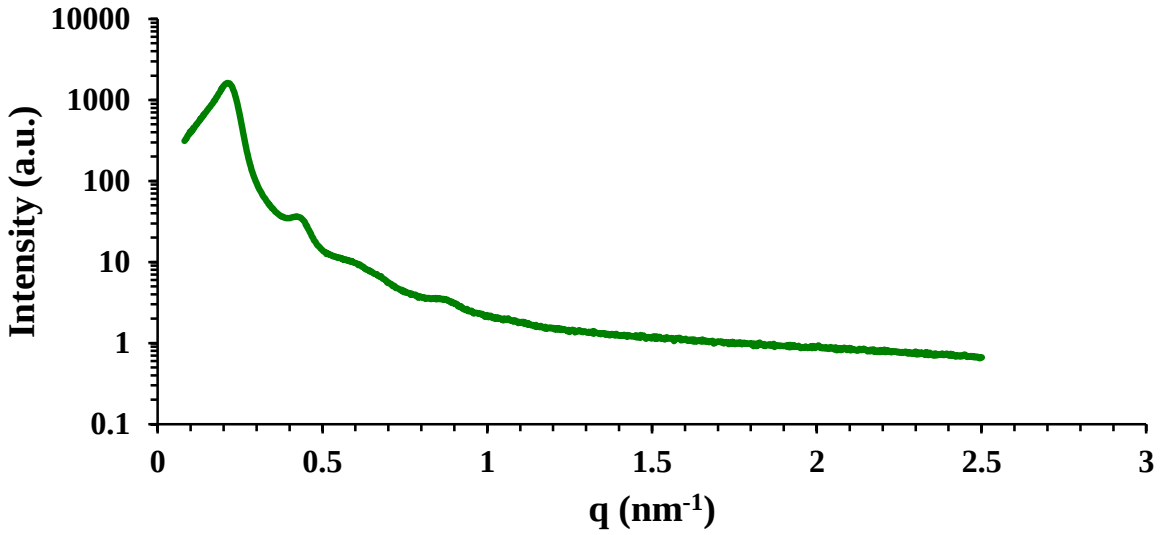

Figure 4.3. Small Angle X-Ray Scattering profiles reveal bulk morphologies for poly(I-*b*-DPPS). Scattering maxima are observed at q*, 2q*, 3q*, 4q*, indicating a lamellar morphology.

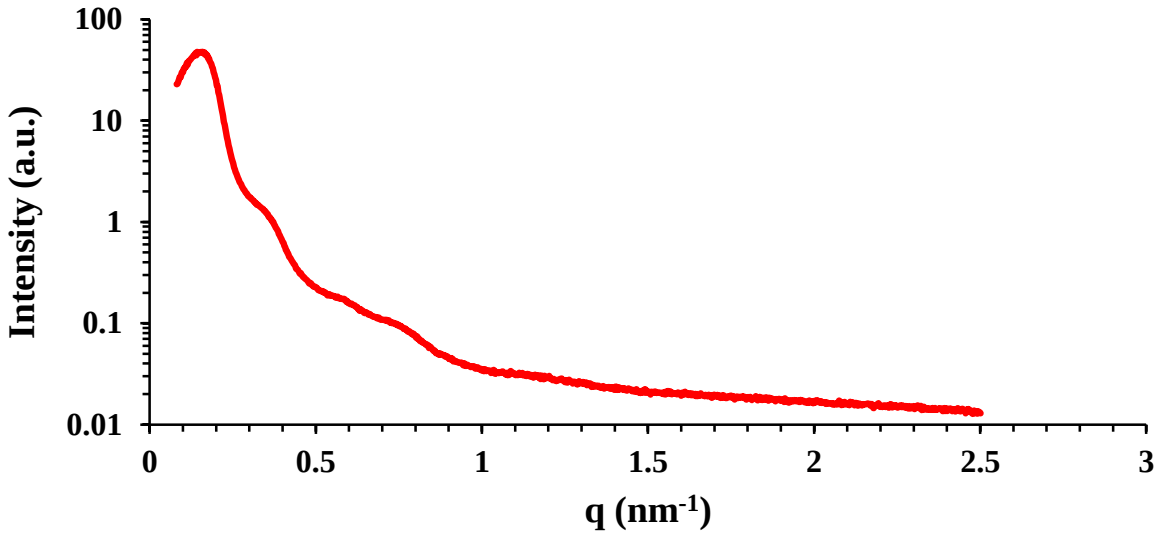

Figure 4.4. Small Angle X-Ray Scattering profiles reveal bulk morphologies for poly(I-*b*-C_6DPPS)$^+$Br$^-$. Scattering maxima are observed at q*, 2q*, 3q*, 4q*, indicating a lamellar morphology.

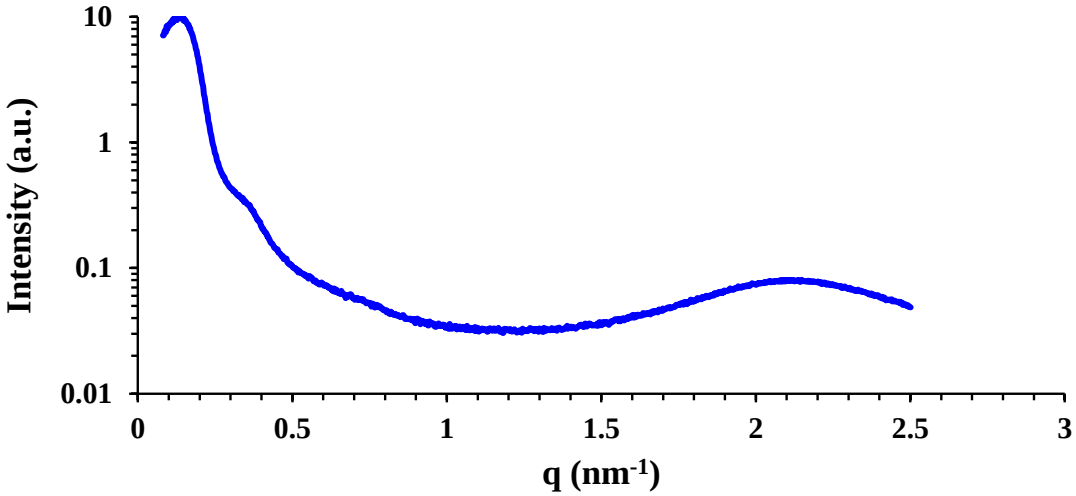

Figure 4.5. Small Angle X-Ray Scattering profiles reveal bulk morphologies for poly(I-*b*-C_{12}DPPS)$^{+}$Br^{-}. Scattering maxima are observed at q*, 2q*, suggesting a less ordered lamellar morphology. A broad scattering peak at approximately q = 2.1 nm^{-1} corresponds to the interdigitated packing of dodecyl chains on the phosphonium cation.

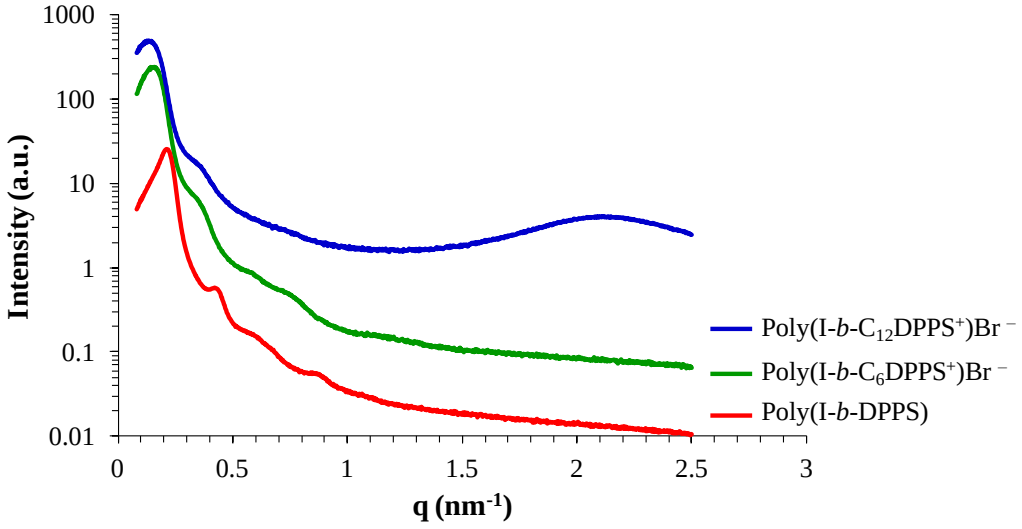

Figure 4.6. Small Angle X-Ray Scattering profiles reveal oriented bulk morphologies for poly(I-*b*-DPPS), poly(I-*b*-C_6DPPS)$^{+}$Br^{-}, and poly(I-*b*-C_{12}DPPS)$^{+}$Br^{-} diblock copolymers. Appearance of broad peak in poly(I-*b*-C_{12}DPPS)$^{+}$Br^{-} scattering profile corresponds to interdigitated bilayers.

4.5 *Conclusions*

Living anionic polymerization afforded novel phosphine-containing homopolymers and diblock copolymers with targetable molecular weights and narrow polydispersities. Sequential monomer addition strategies enabled poly(DPPS-*b*-S) and poly(I-*b*-DPPS) block copolymers for suitable polar and nonpolar solvent conditions. A balance of soft-hard volume fractions for poly(I-*b*-DPPS) block copolymers promoted self-assembly into lamellar microphase separated morphologies. Post-alkylation efficiently converted the phosphine backbone to a phosphonium cation, achieving poly(I-*b*-C_6DPPS)$^+Br^-$ and poly(I-*b*-C_{12}DPPS)$^+Br^-$, which disrupted the bulk morphology of the traditional neutral composition. Increasing the alkyl chain length gave rise to a new phase, corresponding to interdigitated packing of dodecyl chains on the phosphonium cation. Future studies will extend these novel phosphonium diblock compositions to ABA- and ABC- type triblock architectures, in order to evaluate these phosphonium-containing styrenic block copolymers as ion-containing thermoplastic elastomers.

4.6 *Acknowledgements*

We acknowledge the Institute for Critical Technology Applied Science (ICTAS) for laboratory support and we thank Dr. Carl Willis of Kraton Polymers for insightful discussions. This material is partially based upon work supported by the National Science Foundation under Grant No. DMR-0923107.

4.7 *References*

(1) Tse, M. F. *Journal of Adhesion Science and Technology* **1989**, *3*, 551.

(2) Mauritz, K. A.; Blackwell, R. I.; Beyer, F. L. *Polymer* **2004**, *45*, 3001.

(3) Hashimoto, T.; Tsutsumi, K.; Funaki, Y. *Langmuir* **1997**, *13*, 6869.

(4) Ma, M.; Hill, R. M.; Lowery, J. L.; Fridrikh, S. V.; Rutledge, G. C. *Langmuir* **2005**, *21*, 5549.

(5) Kazunori, K.; Masayuki, Y.; Teruo, O.; Yasuhisa, S. *Journal of Controlled Release* **1993**, *24*, 119.

(6) Kwon, G. S.; Kataoka, K. *Advanced drug delivery reviews* **1995**, *16*, 295.

(7) Ranade, S. V.; Richard, R. E.; Helmus, M. N. *Acta Biomaterialia* **2005**, *1*, 137.

(8) Weiss, R. *Department of Polymer Engineering* **1992**, *67*, 127.

(9) Park, H. B.; Freeman, B. D.; Zhang, Z.-B.; Sankir, M.; McGrath, J. E. *Angew. Chem., Int. Ed.* **2008**, *47*, 6019.

(10) Brown, K.; Hooker, J. C.; Creton, C. *Macromolecular Materials and Engineering* **2002**, *287*, 163.

(11) Schultz, A. R.; Lambert, P. M.; Chartrain, N. A.; Ruohoniemi, D. M.; Zhang, Z.; Jangu, C.; Zhang, M.; Williams, C. B.; Long, T. E. *ACS Macro Letters* **2014**, *3*, 1205.

(12) Gao, R.; Zhang, M.; Dixit, N.; Moore, R. B.; Long, T. E. *Polymer* **2012**, *53*, 1203.

(13) Gao, R.; Wang, D.; Heflin, J. R.; Long, T. E. *Journal of Materials Chemistry* **2012**, *22*, 13473.

(14) Allen, M. H.; Green, M. D.; Getaneh, H. K.; Miller, K. M.; Long, T. E. *Biomacromolecules* **2011**, *12*, 2243.

(15) Allen, M. H., Jr.; Wang, S.; Hemp, S. T.; Chen, Y.; Madsen, L. A.; Winey, K. I.; Long, T. E. *Macromolecules*, Ahead of Print.

(16) Page, K. A.; Cable, K. M.; Moore, R. B. *Macromolecules* **2005**, *38*, 6472.

(17) MacKnight, W.; DeMejo, L.; Vogl, O. *Acta Polymerica* **1980**, *31*, 617.

(18) Weiss, R.; Sen, A.; Pottick, L.; Willis, C. *Polymer* **1991**, *32*, 2785.

(19) Choi, J.-H.; Willis, C. L.; Winey, K. I. *Journal of Membrane Science* **2012**, *394–395*, 169.

(20) Jackson, A.; Beers, K. M.; Chen, X. C.; Hexemer, A.; Pople, J. A.; Kerr, J. B.; Balsara, N. P. *Review of Scientific Instruments* **2013**, *84*, 075114.

(21) Park, M. J.; Balsara, N. P. *Macromolecules* **2008**, *41*, 3678.

(22) Choi, J.-H.; Ye, Y.; Elabd, Y. A.; Winey, K. I. *Macromolecules* **2013**, *46*, 5290.

(23) Elabd, Y. A.; Napadensky, E.; Walker, C. W.; Winey, K. I. *Macromolecules* **2006**, *39*, 399.

(24) Choi, J.-H.; Willis, C. L.; Winey, K. I. *Journal of membrane science* **2012**, *394*, 169.

(25) Elabd, Y. A.; Walker, C. W.; Beyer, F. L. *Journal of membrane science* **2004**, *231*, 181.

(26) Kim, J.; Kim, B.; Jung, B. *Journal of membrane science* **2002**, *207*, 129.

(27) Kim, B.; Kim, J.; Jung, B. *Journal of membrane science* **2005**, *250*, 175.

(28) Wang, X.; Goswami, M.; Kumar, R.; Sumpter, B. G.; Mays, J. *Soft Matter* **2012**, *8*, 3036.

(29) Shahinpoor, M.; Bar-Cohen, Y.; Simpson, J.; Smith, J. *Smart materials and structures* **1998**, *7*, R15.

(30) Bocharova, V.; Agapov, A. L.; Tselev, A.; Collins, L.; Kumar, R.; Berdzinski, S.; Strehmel, V.; Kisliuk, A.; Kravchenko, I. I.; Sumpter, B. G. *Advanced Functional Materials* **2015**, *25*, 805.

(31) Gao, R.; Zhang, M.; Dixit, N.; Moore, R. B.; Long, T. E. *Polymer* **2012**, *53*, 1203.

(32) Ren, H.; Sun, J.; Wu, B.; Zhou, Q. *Polym. Degrad. Stab.* **2007**, *92*, 956.

(33) Rana, U. A.; Vijayaraghavan, R.; Walther, M.; Sun, J.; Torriero, A. A. J.; Forsyth, M.; MacFarlane, D. R. *Chem Commun* **2011**, *47*, 11612.

(34) Hemp, S. T.; Zhang, M.; Allen, M. H., Jr.; Cheng, S.; Moore, R. B.; Long, T. E. *Macromol. Chem. Phys.* **2013**, *214*, 2099.

(35) Gu, Y.-Y.; Lodge, T. P. *Macromolecules* **2011**, *44*, 1732.

(36) Cheng, S.; Zhang, M.; Wu, T.; Hemp, S. T.; Mather, B. D.; Moore, R. B.; Long, T. E. *J. Polym. Sci., Part A: Polym. Chem.* **2012**, *50*, 166.

(37) Wang, K.; Zeng, Y.; He, L.; Yao, J.; Suresh, A. K.; Bellare, J.; Sridhar, T.; Wang, H. *Desalination* **2012**, *292*, 119.

(38) Cheng, S.; Zhang, M.; Wu, T.; Hemp, S. T.; Mather, B. D.; Moore, R. B.; Long, T. E. *Journal of Polymer Science Part A: Polymer Chemistry* **2012**, *50*, 166.

(39) Borguet, Y. P.; Tsarevsky, N. V. *Polym. Chem.* **2012**, *3*, 2487.

(40) Terashima, T.; Kamigaito, M.; Baek, K.-Y.; Ando, T.; Sawamoto, M. *J. Am. Chem. Soc.* **2003**, *125*, 5288.

(41) Bailey, T. S.; Pham, H. D.; Bates, F. S. *Macromolecules* **2001**, *34*, 6994.

(42) Wu, C.; Wu, G.; Wu, C. *Journal of applied polymer science* **2006**, *102*, 4157.

Chapter 5: Living Anionic Polymerization of 4-Diphenylphosphino Styrene for ABC Triblock Copolymers

(Submitted to *Polymer International*)

*Alison R. Schultz, Mingtao Chen, Gregory B. Fahs, Robert B. Moore, and Timothy E. Long**

Macromolecules Innovation Institute, Department of Chemistry, Virginia Tech, Blacksburg, VA 24061, USA. E-mail: telong@vt.edu.

*To whom correspondence should be addressed. E-mail: telong@vt.edu. TEL: (540)231-2480. FAX: (540)231-8517.

Keywords: Anionic polymerization, phosphonium, thermoplastic elastomer, *in situ* FTIR spectroscopy, thermomechanical, morphology

5.1 *Abstract*

Living anionic polymerization of 4-diphenylphosphino styrene (DPPS) achieved unprecedented poly(S-*b*-I-*b*-DPPS) ABC triblock copolymers with predictable molecular weights and narrow polydispersities. *In situ* FTIR spectroscopy probed the anionic polymerization, monitoring vinyl disappearance during sequential monomer addition for kinetic analysis. Varying the concentration of reinforcing, polystyrenic external blocks enabled diverse compositions with tunable thermomechanical properties and tailored morphology. Dynamic mechanical analysis (DMA) confirmed the presence of microphase separation in the triblock copolymers and revealed a broad temperature range (~100 ^{o}C) for a plateau region and onset of flow temperatures above 100 ^{o}C. Small-angle X-ray scattering (SAXS) and atomic force microscopy (AFM) collectively revealed solid state morphologies of the triblock copolymers and probed phase separation at the nanoscale. Well-defined poly(S-*b*-I-*b*-DPPS) ABC triblock copolymers with tunable structure-

property relationships now permit phosphorus-containing thermoplastic elastomers for emerging applications.

5.2 *Introduction*

ABC triblock copolymers often exhibit unique nanostructured morphologies in comparison to conventional AB and ABA analogues, eliciting interest for both modeling phase behavior and studying morphological transitions.[1-8] The Flory-Huggins interaction parameter, χ, governs the phase behavior for block copolymers and enables self-assembly into well-defined nanostructures with tailored sequence lengths and volume fractions, molecular weight distribution, and chemical compositions.[9,10] Morphological structure ranges from basic lamellae[2,11] to core-shell gyroids[3,6] and unique knitting patterns.[12,13] Blending with conventional copolymer analogues,[14] or incorporating noncovalent interactions[4,15,16] within the polymer composition provides additional opportunities for engineering novel morphological structures and broadening structure-morphology-property relationships.

Earlier literature extensively describes ABC triblock copolymers containing diene-,[17,18] styrene-,[19,20] methacrylate-,[15,18] or pyridine-based monomers,[21,22] revealing synthetic methods involving anionic,[23] atom transfer radical,[15] and radical addition transfer polymerizations.[24] Among these various mechanisms, living anionic polymerization provides the only route for producing diene-containing block copolymers with the desirable high *cis*-1,4-configuration and the associated low glass transition temperature. The benefits of living anionic polymerization also include commercial viability, rapid reaction times, ambient temperatures, and quantitative yields. Functional group tolerance with organolithium initiators remains a challenge, encouraging alternative controlled free radical polymerization methods and inspiring novel non-electrophilic monomers suitable for anionic polymerization.

In our previous communication, living anionic polymerization of 4-diphenylphosphino styrene (DPPS) was reported for the first time as an unprecedented method for achieving novel phosphorus-containing diblock copolymers.[25] Incorporating phosphorus-containing sequences into macromolecular architectures advantageously provides diverse oxidation states (phosphates, phosphines, phosphine oxides, and phosphoniums), high alkylation and metal catalysis efficiency,[26,27] thermal and base stability,[26-28] and tailored structures and morphologies.[29] Literature precedence exists for phosphorus-containing monomers exhibiting vinylbenzyl-,[30,31] acrylate-,[32] and methacrylate polymerizable units,[33] facilitating synthetic methods involving conventional and controlled free radical polymerizations.[29] However, DPPS does not contain a benzylic carbon adjacent to the phosphorus atom, thus eliminating the low temperature reverse Menschutkin (nucleophilic) degradation pathways. Consequently, DPPS is structurally advantageous for achieving phosphonium-containing block copolymers with enhanced thermal and base stability in comparison to benzylic phosphorus-containing monomers. Moreover, compatibility with organolithium initiators and anionic polymerization conditions distinguishes DPPS as an ideal monomer for novel phosphorus-containing block copolymer architectures.

In this manuscript, we extend living anionic polymerization methods further and demonstrate the unprecedented synthesis of poly(styrene-*b*-isoprene-*b*-diphenylphosphino styrene) [poly(S-*b*-I-*b*-DPPS)] ABC triblock copolymers. These compositions represent a new class of styrenic block copolymers, featuring advantages of a phosphorus-containing sequence for the production of high performance thermoplastic elastomers. Poly(S-*b*-I-*b*-DPPS) ABC triblocks exhibit high thermal stability with tunable physical and mechanical properties for targeted technologies ranging from high performance adhesives[34,35] and durable coatings,[36,37] to biomaterials[38,39] and medical devices.[40,41] *In situ* Fourier transform infrared (FTIR) spectroscopy

monitored the anionic polymerization, revealing vinyl disappearance during sequential monomer addition and invoking pseudo-first-order kinetics to determine observed rate constants, k_{obs}, for propagation. Size exclusion chromatography (SEC) confirmed the well-defined synthesis of poly(S-*b*-I-*b*-DPPS) triblock copolymers, and tailored compositions enabled diverse architectures for tunable mechanical performance and morphology. Dynamic mechanical analysis (DMA) elucidated microphase separation effects on thermomechanical properties, and SAXS and AFM provided complementary techniques for characterizing the microphase separated morphologies. As ABC triblock copolymers emerge as versatile thermoplastic elastomers, investigating novel phosphorus-based macromolecular with predictable structure–morphology–property relationships will facilitate industrial applications.

5.3 *Experimental Section*

5.3.1 Materials

4-diphenylphosphino styrene (99%), styrene (99%), isoprene (99%), and 1.4 M sec-butyllithium solution in cyclohexane were purchased from Sigma Aldrich and used as received unless otherwise noted. Styrene and isoprene, containing 10-15 ppm of t-butyl catechol, were distilled at reduced pressure from calcium hydride and dibutyl magnesium.

5.3.2 Instrumentation

In situ FTIR spectroscopic analysis employed a Mettler Toledo ReactIR 45M attenuated total reflectance reaction apparatus equipped with a light conduit and DiComp (diamond composite) insertion probe. Size exclusion chromatography (SEC) was used to determine the molecular weights of phosphorus-containing polymers at 40 ^{o}C in THF at 1 mL/min. THF SEC was performed on a Waters SEC equipped with two Waters Styragel HR5E (THF) columns, a Waters 717 plus autosampler, a Wyatt MiniDAWN, and a Waters 2414 differential refractive index

detector. An Optilab T-rEX refractometer ($\lambda = 658$) was used to measure dn/dc values offline for determination of absolute weight-average molecular weights. Atomic force microscopy (AFM) was conducted on a Veeco MultiMode AFM using a tapping mode under ambient conditions.

Small angle x-ray scattering (SAXS) experiments were performed using a Rigaku S-Max 3000 3 pinhole SAXS system, equipped with a rotating anode emitting X-ray with a wavelength of 0.154 nm (Cu Kα). The sample-to-detector distance was 1604 mm, and q-range was calibrated using a silver behenate standard. Absolute intensity calibration was performed using a glassy carbon standard. Two-dimensional SAXS patterns were obtained using a fully integrated 2D multiwire, proportional counting, gas-filled detector, with an exposure time of 2 h. All the SAXS data were analyzed using the SAXSGUI software package to obtain radially integrated SAXS intensity versus scattering vector q, where $q = (4\pi/\lambda)\sin(\theta)$, θ is one half of the scattering angle and λ is the wavelength of X-ray. SAXS profiles have been corrected for background and vertically shifted to facilitate a comparison of the peak positions. Dynamic mechanical analysis (DMA) was conducted on a TA Instruments Q800 Dynamic Mechanical Analyzer in tension mode at a frequency of 1 Hz, an oscillatory amplitude of 15 μm, and a static force of 0.01 N. The temperature ramp was 3 ^{o}C/min. The glass-transition temperature (T_g) was determined at the peak maximum of the tan δ curve. Tensile experiments employed an Instron at 50 mm/min strain rate.

5.3.3 *In situ* FTIR spectroscopy monitors the anionic polymerization of poly(S-*b*-I-*b*-DPPS)

A 25-mL, flame-dried, round-bottomed flask contained (2.0 mL, 1.8 g) styrene and 8 mL of dry cyclohexane. A rubber septum sealed a neck of the flask, and the DiComp probe was inserted into a second neck and sealed. The probe tip was submerged below the monomer surface, and the ReactIR spectrometer programmed spectrum collection every 1 min for 5 h (SI Figure 1). Nitrogen purged the reaction flask for 15 min and then the reaction flask submerged into 50 ^{o}C heated oil bath. *Sec*-butyllithium (0.02 mL) initiated polymerization of a 10,000 g/mol polymer.

After 1 h, (2.65 mL, 1.8 g) isoprene sequentially added to the reaction mixture and propagation occurred for 2 h. At this time, 4-diphenylphosphino styrene (1.81 g) was sequentially added and polymerized for 30 min. Degassed methanol (0.5 mL) terminated the polymerization and the resulting ABC block copolymer was precipitated into methanol and dried at 23 ^{o}C under reduced pressure (0.5 mmHg) for 24 h to obtain a white powder (98% isolated yield).

5.3.4 Anionic polymerization of poly(styrene-*b*-isoprene-*b*-4-diphenylphosphino styrene) ABC triblock copolymers

In a representative polymerization, a 250-mL flame dried, nitrogen purged, and sealed round-bottomed flask contained 8 mL (7.27 g) styrene and 125 mL cyclohexane at 50 °C. Sec-butyllithium (0.29 mmol) initiated the orange poly(styryl)lithium living chain of 25,000 g mol^{-1} and propagation was complete within 45 min. Sequential monomer addition with 21 mL isoprene (14.54 g) achieved poly(isoprenyl)lithium of 50,000 g mol^{-1}. After 2 h, 4-diphenylphosphino styrene (5.1 g) was sequentially added to produce a deep red phosphorus-containing poly(styryl)lithium chain of 25,000 g mol^{-1}. The polymerization was terminated after 30 min with degassed methanol (1.0 mL), and the resulting ABC triblock copolymer was precipitated into methanol and dried at 23 ^{o}C under reduced pressure (0.5 mmHg) for 24 h to obtain a white powder (poly(S_{50k}-*b*-I_{50k}-*b*-$DPPS_{25k}$), 97% isolated yield). ^{1}H NMR (400 MHz, $CDCl_3$, 25 °C, δ): 0.8 – 0.9 ppm (br, $CH_3CH_2CH(CH_3)$-), 1.1 – 1.2 ppm (br, -CH_3 in 1,2-polyisoprene units), 1.2 – 1.5 ppm (br, -CH_2CH-, -CH_2CH- in 1,2-polyisoprene and 3,4-polyisoprene units), 1.61 ppm (br, -CH3 in *trans*-1,4-polyisoprene units), 1.64 ppm (br, -CH_3 in 3,4-polyisoprene units), 1.68 ppm (br, -CH_3 in *cis*-1,4-polyisoprene units), 1.8 – 2.2 ppm (br, -CH_2CH=, -$CH_2C(CH_3)$= in 1,4-polyisoprene units), 4.6 – 4.8 ppm (br, -$C(CH_3)=CH_2$ 3,4-polyisoprene units and -$CH=CH_2$ 1,2-polyisoprene units), 4.8 – 5.4 ppm (br, -$CH=C(CH_3)$- 1,4-polyisoprene units). 1.5 (–CH_2– polymer backbone, –

CH– polymer backbone), 6.2 – 7.3 (aromatic protons). ^{31}P NMR (400 MHz, $CDCl_3$, 25 °C, δ): -10.0 (phosphine).

5.3.5 Film casting

All ABC triblock copolymers were dissolved in toluene and cast from a 30 wt% solution. Films were slowly dried at ambient conditions for 2 d followed with 2 d of drying at room temperature under reduced pressure (5 mmHg). Annealing occurred for 2 d at 150 ^{o}C under reduced pressure (5 mmHg) before characterization studies. Films were stored in a nitrogen-purged dry box to prevent undesirable oxidative reactions.

5.4 *Results and Discussion*

Scheme 5.1 depicts living anionic polymerization for achieving unprecedented poly(S-*b*-I-*b*-DPPS) triblock copolymers with molecular weight precision and narrow polydispersities. Sequential monomer addition in cyclohexane at 50 ^{o}C enabled microstructural control of the polyisoprene soft segment and afforded homogeneous reaction mixtures suitable for polymerizing DPPS in the nonpolar solvent. *In situ* FTIR spectroscopy monitored the sequential addition process, i.e., the vinyl CH_2 out-of-plane wag mode for each monomer (styrene, 908 cm^{-1}; isoprene, 912 cm^{-1}; DPPS, 918 cm^{-1}) and generated a normalized 2D waterfall plot for absorbance vs. time (sec) (Fig. 5.1). Vinyl concentration disappearance as a function of time elucidated monomer propagation, revealing approximately 20 min reaction times for styrene and DPPS and 40 min for isoprene to ensure complete conversion. The styrenic monomers exhibited faster propagation times in comparison to isoprene, presumably due to the lower activation energies required for producing the more delocalized carbanion. Although the isoprene monomer absorption decreased

substantially, a small percentage of the band remained after complete conversion. The residual vinyl absorption was due to the typical 8% 3, 4-addition that occurs under these reaction conditions. Pseudo-first order kinetic analysis of monomer concentration (M/M_0) versus time (sec) provided additional insight into the polymerization kinetics, revealing a similar observed rate constant, k_{obs}, for DPPS (2.9×10^{-2} s^{-1}) compared to styrene (2.4×10^{-1} s^{-1}) and isoprene (1.1×10^{-2} s^{-1}). FTIR spectroscopy also defined suitable anionic polymerization conditions for the synthesis of novel phosphorus-containing ABC triblock copolymers (Fig. 5.2).

Scheme 5.1. Sequential monomer addition achieves poly(S-*b*-I-*b*-DPPS) triblock copolymers.

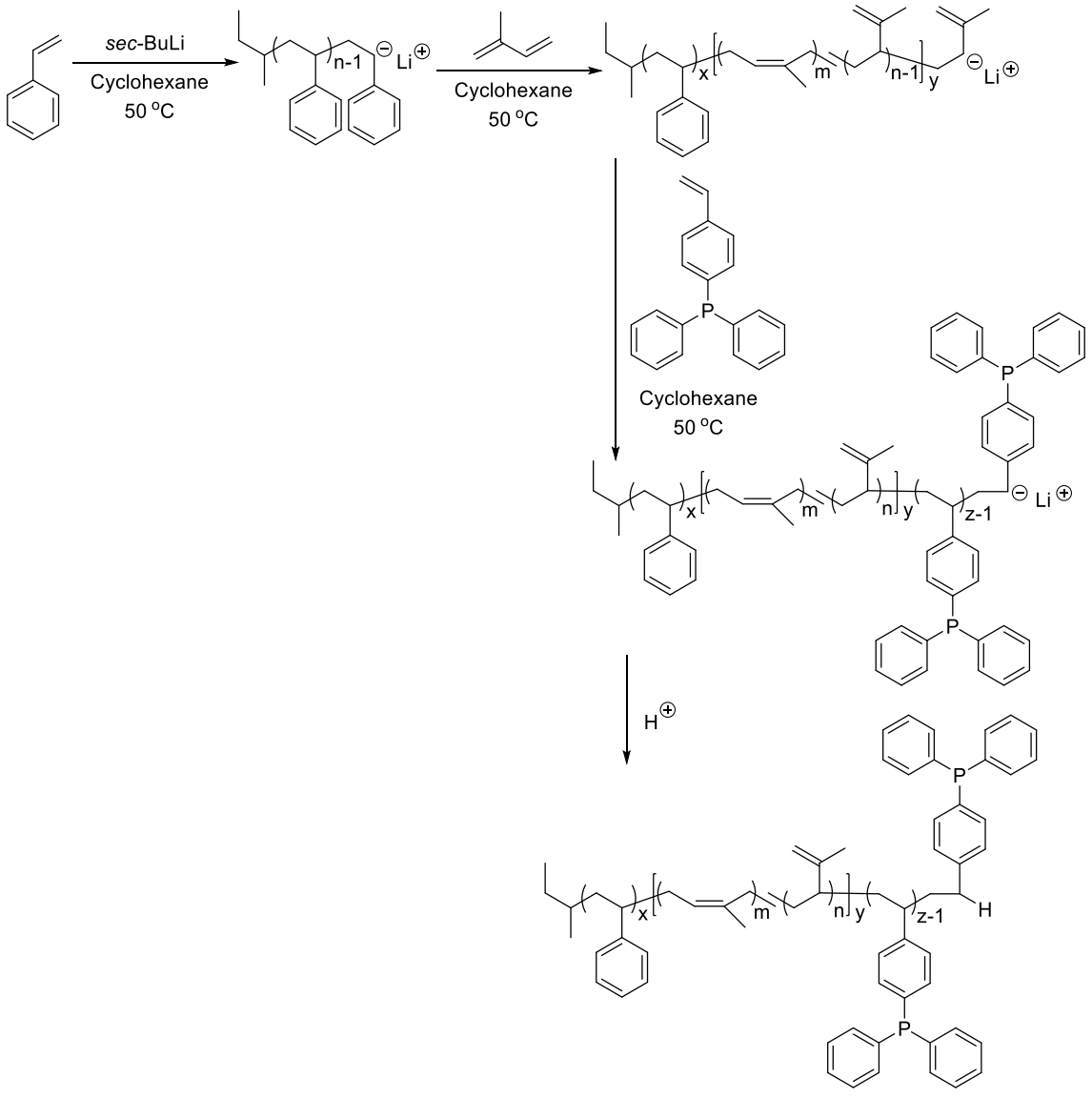

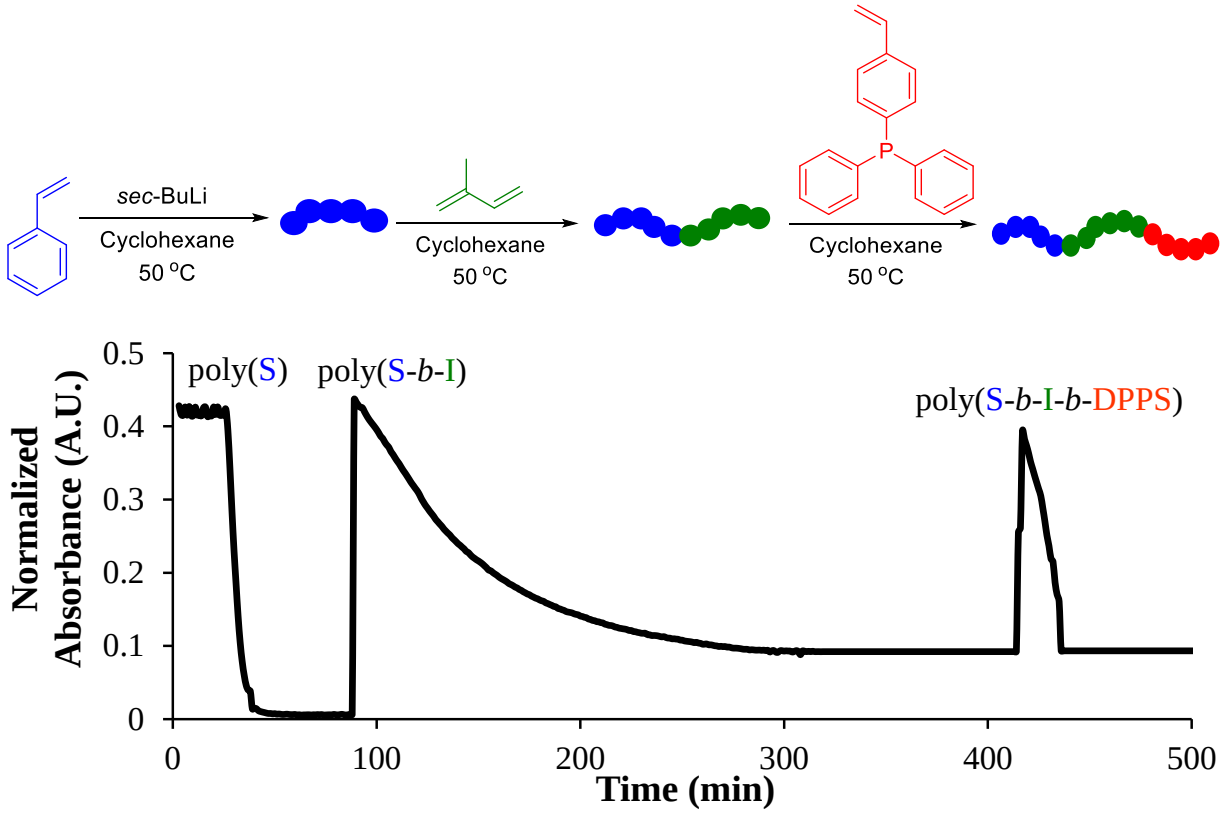

Figure 5.1. *In situ* FTIR spectroscopy monitors the anionic polymerization of poly(S-*b*-I-*b*-DPPS), tracking the C=C vinyl vibrational frequency peaks for each propagating monomer (styrene, 908 cm^{-1}; isoprene, 912 cm^{-1}; DPPS, 918 cm^{-1}). Monomers were added in a sequential fashion.

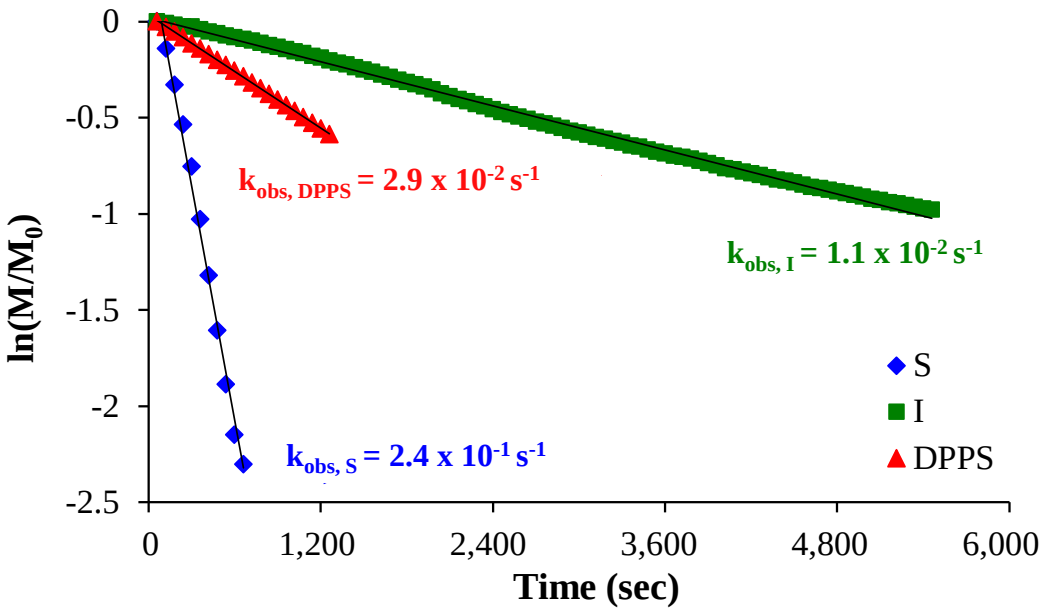

Figure 5.2. Pseudo-first-order kinetic analysis of poly(S-*b*-I-*b*-DPPS) triblock copolymerization.

Variations in the poly(S-*b*-I-*b*-DPPS) composition afforded diverse block copolymer architectures with tailored sequence lengths and molecular weights. Increasing the concentration of the reinforcing, polystyrene and poly(DPPS) external segments from 25 wt. %, 50 wt. %, to 60 wt. % achieved an exemplary series of poly(S-*b*-I-*b*-DPPS) triblock copolymers for evaluating structure-property relationships. SEC confirmed anionic polymerization as a controlled method for tailoring the triblock copolymer structure, revealing predictable number-average molecular weight (M_n) values, unimodal chromatograms, and narrow polydispersities (PDIs < 1.10) (Fig. 5.3). Table 5.1 summarizes the compositional details for the triblock copolymers with favorable agreement between the targeted and absolute M_n values.

Table 5.1. SEC results for poly(S-*b*-I-*b*-DPPS) triblock copolymers.

Sample	External Blocks wt. %	Central Block wt. %	Target M_n (kg/mol)	SEC M_n (kg/mol)	M_w/M_n
Poly(S_{50k}-*b*-I_{50k}-*b*-$DPPS_{25k}$)	60 %	40%	125	122	1.07
Poly(S_{25k}-*b*-I_{50k}-*b*-$DPPS_{25k}$)	50 %	50 %	100	103	1.07
Poly(S_{20k}-*b*-I_{120k}-*b*-$DPPS_{20k}$)	25 %	75 %	160	155	1.08

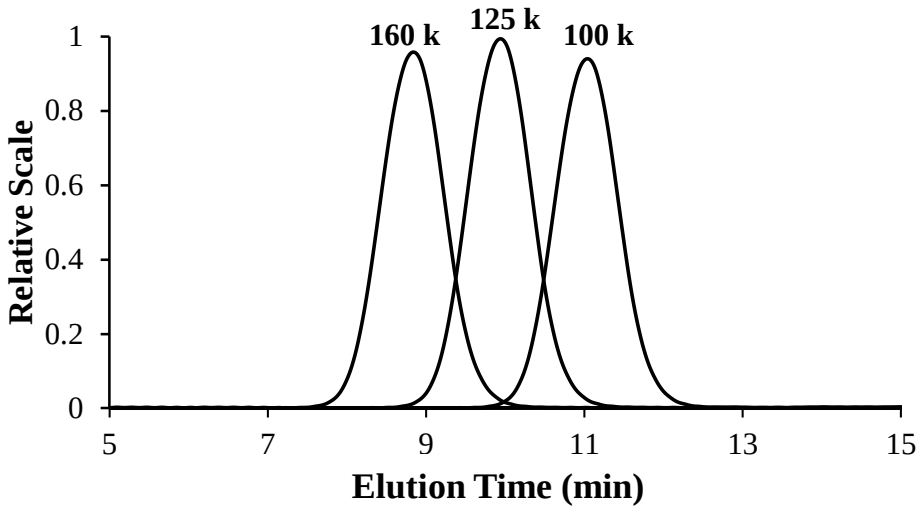

Figure 5.3. SEC characterization of poly(S-*b*-I-*b*-DPPS) triblock copolymers.

Altering the weight fractions of the soft, polyisoprene central block (I, T_g = - 50 °C) and the hard polystyrenic external blocks (S, T_g = 100 °C and DPPS, T_g = 120 °C) promoted microphase separation in the poly(S-*b*-I-*b*-DPPS) triblock copolymers and enabled free-standing films for DMA and tensile experiments. All films were slowly cast from toluene and annealed at 150 °C under reduced pressure to facilitate phase separation. DMA confirmed the presence of microphase separation and elucidated the corresponding effects on thermomechanical properties. Storage modulus (G') vs. temperature plots revealed two distinctive transitions, corresponding to the glass

transition temperature (T_g) for the soft, polyisoprene central block at -55 °C and the T_g for the phase-mixed, polystyrenic external blocks at 110 °C (Fig. 5.4). Increasing the concentration of the external, reinforcing blocks dramatically increased the rubbery plateau storage modulus, enabling tailored viscoelastic properties. The rubbery plateau extended for approximately 120 °C with a flow temperature above 100 °C, allowing a wide modulus-invariant temperature range for the novel triblock copolymers. Previous literature on traditional poly(S-*b*-I-*b*-S) thermoplastic elastomers detail comparable thermomechanical properties and operational temperature windows.[42,43] The miscibility of styrenic components in poly(S-*b*-I-*b*-DPPS) triblock copolymers advantageously affords viscoelastic properties in agreement with conventional ABA-type thermoplastic elastomers. However, post-alkylation or oxidation reactions with DPPS provides opportunities for extending these properties for emerging industrial applications.

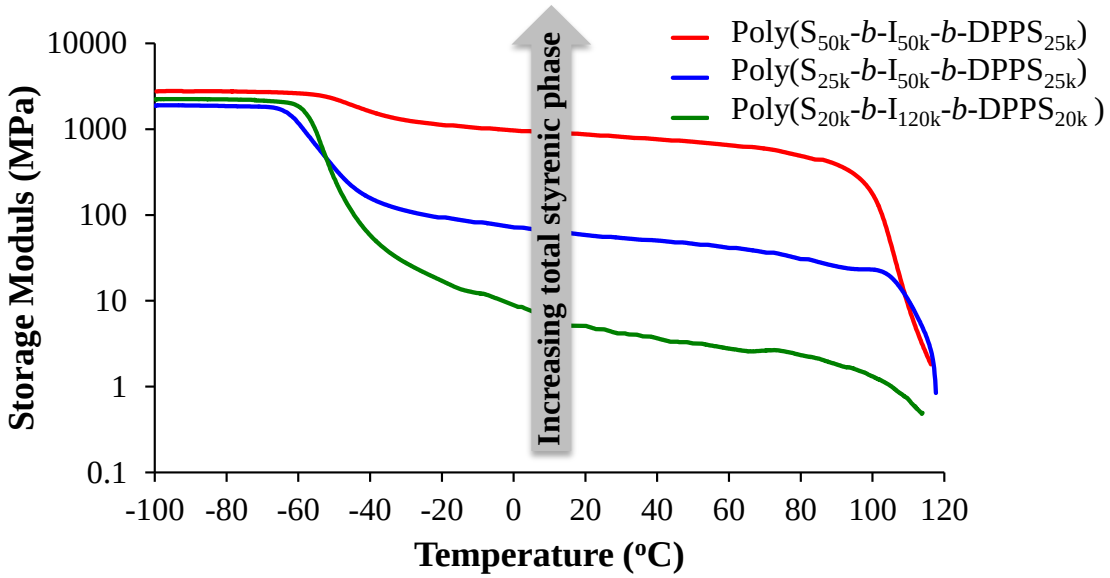

Figure 5.4. DMA characterization for poly(S_{25k}-*b*-I_{50k}-*b*-$DPPS_{25k}$), poly(S_{50k}-*b*-I_{50k}-*b*-$DPPS_{25k}$), and poly(S_{20k}-*b*-I_{120k}-*b*-$DPPS_{20k}$).

Uniaxial stress-strain tensile analysis evaluated the influence of polystyrenic, external block concentrations on ultimate properties of poly(S-*b*-I-*b*-DPPS) films at ambient conditions. Fig. 5.5 shows representative stress *vs.* strain curves for the triblock copolymers with external blocks containing 25 wt. %, 50 wt. %, and 60 wt. % polystyrene and poly(DPPS). Increasing the concentration of reinforcing, external blocks systematically altered the triblock mechanical properties, leading to increased Young's modulus and tensile stress and decreased tensile strain (Table 5.2). The external block concentration and microphase-separated structure accounted for the observed mechanical differences. The high T_g polystyrenic segments form hard domains within the phase separated triblock copolymer, imparting physical crosslinks associated with a high modulus. Increasing the concentration of hard domains enhanced physical reinforcement and increased the corresponding Young's moduli and stress at break. These trending mechanical properties agree with previous literature studies involving conventional poly(S-*b*-I-*b*-S) thermoplastic elastomers.[42-44]

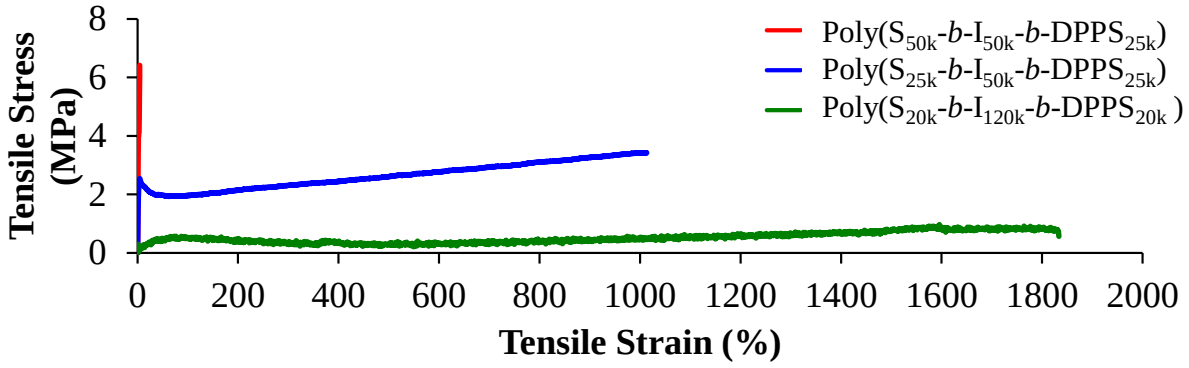

Figure 5.5. Tensile stress-strain curves for poly(S_{25k}-*b*-I_{50k}-*b*-$DPPS_{25k}$), poly(S_{50k}-*b*-I_{50k}-*b*-$DPPS_{25k}$), and poly(S_{20k}-*b*-I_{120k}-*b*-$DPPS_{20k}$).

Table 5.2. Summary of tensile properties for poly(S_{25k}-*b*-I_{50k}-*b*-$DPPS_{25k}$), poly(S_{50k}-*b*-I_{50k}-*b*-$DPPS_{25k}$), and poly(S_{20k}-*b*-I_{120k}-*b*-$DPPS_{20k}$).

Sample	Stress at Break (MPa)	Strain at Break (%)	Young's Modulus (MPa)
Poly(S_{50k}-*b*-I_{50k}-*b*-$DPPS_{25k}$)	6.0 ± 1.0	10 ± 2.0	640 ± 48
Poly(S_{25k}-*b*-I_{50k}-*b*-$DPPS_{25k}$)	4.0 ± 0.3	1100 ± 100	580 ± 2.2
Poly(S_{20k}-*b*-I_{120k}-*b*-$DPPS_{20k}$)	1.5 ± 0.2	1800 ± 200	30 ± 0.8

AFM and SAXS provided complementary techniques for characterizing the surface and bulk morphological features of the poly(S-*b*-I-*b*-DPPS) triblock copolymers. In a typical AFM phase image of a microphase separated block copolymer, the hard domains appear as lighter regions and the soft phase appears as darker regions. Fig. 5.6 shows the AFM tapping mode phase images for the triblock copolymers with 25 wt. %, 50 wt. %, and 60 wt. % polystyrenic external blocks, revealing tunable microphase separated morphologies for each composition. SAXS experiments revealed the microphase-separated bulk morphologies of the ABC triblock copolymer samples as a complement to the AFM surface morphology analysis (Fig. 5.7). Poly(S_{25k}-*b*-I_{50k}-*b*-$DPPS_{25k}$) exhibited an ordered scattering profile with peak maxima at q*, 2q*, 3q*, and 4q*, which is indicative of one-dimensional packing symmetry corresponding to a lamellar morphology. Bragg's law was used to approximate lamellar spacing from the primary scattering maximum at q*, revealing a Bragg distance of 27 nm. The scattering profile for both poly(S_{50k}-*b*-I_{50k}-*b*-$DPPS_{25k}$) and poly(S_{20k}-*b*-I_{120k}-*b*-$DPPS_{20k}$) revealed significantly less ordered bulk morphologies with a lack of long range periodicity. Poly(S_{50k}-*b*-I_{50k}-*b*-$DPPS_{25k}$) exhibits peak maxima at q*, 2q*, and 3q*, which could be indicative of a disordered lamellar morphology with a Bragg spacing of

29 nm. Based on the weak, broad SAXS scattering maxima, the morphological structure for poly(S_{20k}-*b*-I_{120k}-*b*-$DPPS_{20k}$) is less clear. For this sample, it is reasonable to consider the two peaks present at 0.4 nm^{-1} and 0.7 nm^{-1} as the symmetry elements q* and $\sqrt{3}$q*, indicative of either spherical domains or bicontinuous phase separation with close packed liquid-like ordering on the scale of approximately 17 nm. Earlier literature involving poly(S-*b*-I)[45] and poly(I-*b*-DPPS)[25] block copolymers reveal a similar morphology. The observation of phase separation from AFM and SAXS correlated well with observations in DMA experiments, which indicated a microphase-separated morphology for all compositions.

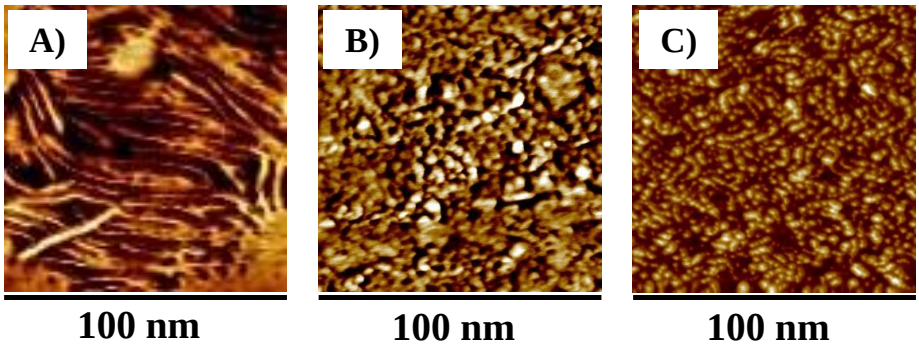

Figure 5.6. Atomic force microscopy images reveal surface morphologies for (A) poly(S_{25k}-*b*-I_{50k}-*b*-$DPPS_{25k}$), (B) poly(S_{50k}-*b*-I_{50k}-*b*-$DPPS_{25k}$) and (C) poly(S_{20k}-*b*-I_{120k}-*b*-$DPPS_{20k}$).

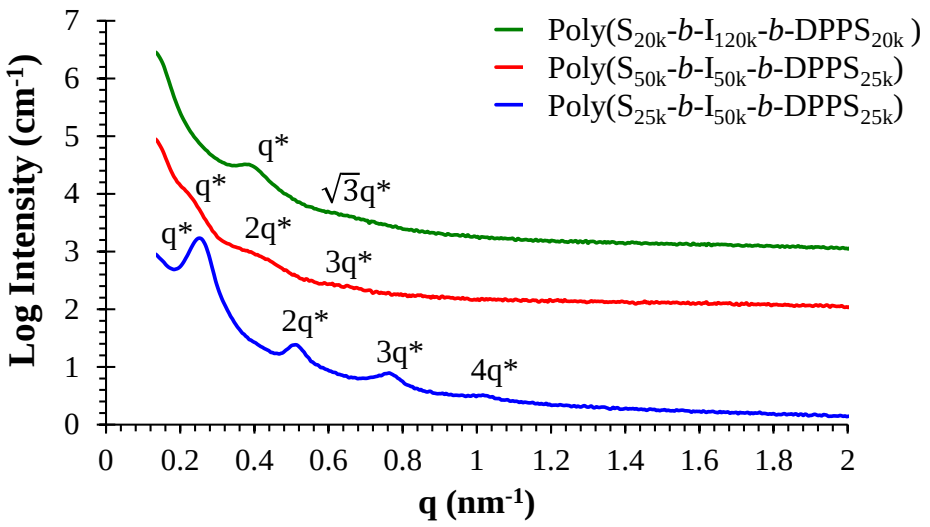

Figure 5.7. Small Angle X-Ray Scattering profiles reveal oriented bulk morphologies for poly(S_{25k}-*b*-I_{50k}-*b*-$DPPS_{25k}$), poly(S_{50k}-*b*-I_{50k}-*b*-$DPPS_{25k}$), and poly(S_{20k}-*b*-I_{120k}-*b*-$DPPS_{20k}$).

5.5 *Conclusions*

Living anionic polymerization now permits a new class of phosphorus-containing styrenic ABC triblock copolymers, featuring tunable physical and mechanical properties for the production of high performance thermoplastic elastomers. Sequential monomer addition afforded poly(S-*b*-I-*b*-DPPS) ABC triblock copolymers with targetable molecular weights and narrow polydispersities. *In situ* FTIR spectroscopy confirmed the living synthesis of poly(S-*b*-I-*b*-DPPS) and provided kinetic insight for each propagation step. A balance of soft-hard volume fractions for poly(S-*b*-I-*b*-DPPS) block copolymers promoted self-assembly into diverse microphase separated morphologies and afforded tunable mechanical performance. Future studies will continue to extend the living anionic polymerization of 4-diphenylphosphino styrene for the production of diverse block copolymer architectures, and post-alkylation studies will enable phosphonium-containing derivatives for electro-active membrane applications.

5.6 *Acknowledgements*

We acknowledge the Institute for Critical Technology Applied Science (ICTAS) for laboratory support. This material is partially based upon work supported by the National Science Foundation under Grant No. DMR-0923107.

5.7 *References*

(1) Arai, K.; Kotaka, T.; Kitano, Y.; Yoshimura, K. *Macromolecules* **1980**, *13*, 455.

(2) Mogi, Y.; Kotsuji, H.; Kaneko, Y.; Mori, K.; Matsushita, Y.; Noda, I. *Macromolecules* **1992**, *25*, 5408.

(3) Breiner, U.; Krappe, U.; Stadler, R. *Macromolecular rapid communications* **1996**, *17*, 567.

(4) Schultz, A. R.; Lambert, P. M.; Chartrain, N. A.; Ruohoniemi, D. M.; Zhang, Z.; Jangu, C.; Zhang, M.; Williams, C. B.; Long, T. E. *ACS Macro Letters* **2014**, *3*, 1205.

(5) Elbs, H.; Fukunaga, K.; Stadler, R.; Sauer, G.; Magerle, R.; Krausch, G. *Macromolecules* **1999**, *32*, 1204.

(6) Zheng, W.; Wang, Z.-G. *Macromolecules* **1995**, *28*, 7215.

(7) Chatterjee, J.; Jain, S.; Bates, F. S. *Macromolecules* **2007**, *40*, 2882.

(8) Phan, S.; Fredrickson, G. *Macromolecules* **1998**, *31*, 59.

(9) Choi, J.-H.; Willis, C. L.; Winey, K. I. *Journal of Membrane Science* **2012**, *394*, 169.

(10) Sariban, A.; Binder, K. *The Journal of chemical physics* **1987**, *86*, 5859.

(11) Breiner, U.; Krappe, U.; Abetz, V.; Stadler, R. *Macromolecular Chemistry and Physics* **1997**, *198*, 1051.

(12) Shefelbine, T.; Vigild, M.; Matsen, M.; Hajduk, D.; Hillmyer, M.; Cussler, E.; Bates, F. *Journal of the American Chemical Society* **1999**, *121*, 8457.

(13) Ott, H.; Abetz, V.; Altstädt, V. *Macromolecules* **2001**, *34*, 2121.

(14) Abetz, V.; Goldacker, T. *Macromolecular rapid communications* **2000**, *21*, 16.

(15) Guerlain, C.; Piogé, S.; Detrembleur, C.; Fustin, C. A.; Gohy, J. F. *Journal of Polymer Science Part A: Polymer Chemistry* **2015**, *53*, 459.

(16) Sing, C. E.; Zwanikken, J. W.; Olvera de la Cruz, M. *Nat Mater* **2014**, *13*, 694.

(17) Shibayama, M.; Hasegawa, H.; Hashimoto, T.; Kawai, H. *Macromolecules* **1982**, *15*, 274.

(18) Löbling, T. I.; Hiekkataipale, P.; Hanisch, A.; Bennet, F.; Schmalz, H.; Ikkala, O.; Gröschel, A. H.; Müller, A. H. *Polymer* **2015**, *72*, 479.
(19) Lodge, T. P. *Macromolecular chemistry and physics* **2003**, *204*, 265.
(20) Fielding-Russell, G.; Pillai, P. *Polymer* **1974**, *15*, 97.
(21) Arai, K.; Kotaka, T.; Kitano, Y.; Yoshimura, K. *Macromolecules* **1980**, *13*, 1670.
(22) Kudose, I.; Kotaka, T. *Macromolecules* **1984**, *17*, 2325.
(23) Theodosopoulos, G.; Pitsikalis, M. In *Anionic Polymerization*; Springer: 2015, p 541.
(24) Germack, D. S.; Wooley, K. L. *Macromolecular Chemistry and Physics* **2007**, *208*, 2481.
(25) Schultz, A. R.; Fahs, G. B.; Jangu, C.; Chen, M.; Moore, R. B.; Long, T. E. *Chemical Communications* **2016**, *52*, 950.
(26) Yang, S.; Wang, J.; Huo, S.; Cheng, L.; Wang, M. *Polymer Degradation and Stability* **2015**, *115*, 63.
(27) Terashima, T.; Kamigaito, M.; Baek, K.-Y.; Ando, T.; Sawamoto, M. *Journal of the American Chemical Society* **2003**, *125*, 5288.
(28) Hemp, S. T.; Zhang, M.; Allen, M. H.; Cheng, S.; Moore, R. B.; Long, T. E. *Macromolecular Chemistry and Physics* **2013**, *214*, 2099.
(29) Hemp, S. T.; Smith, A. E.; Bryson, J. M.; Allen, M. H.; Long, T. E. *Biomacromolecules* **2012**, *13*, 2439.
(30) Womble, C. T.; Coates, G. W.; Matyjaszewski, K.; Noonan, K. J. *ACS Macro Letters* **2016**, *5*, 253.
(31) Xue, Y.; Xiao, H. *Journal of Biomedical Materials Research Part A* **2015**.
(32) Liao, H.; Ma, D.; Jiao, Z.; Xie, Y.; Tan, S.; Cai, X.; Huang, L. *Journal of Adhesion Science and Technology* **2015**, *29*, 171.
(33) Guterman, R.; Gillies, E. R.; Ragogna, P. J. *Langmuir* **2015**, *31*, 5181.
(34) Tse, M. F. *Journal of Adhesion Science and Technology* **1989**, *3*, 551.
(35) Mauritz, K. A.; Blackwell, R. I.; Beyer, F. L. *Polymer* **2004**, *45*, 3001.
(36) Hashimoto, T.; Tsutsumi, K.; Funaki, Y. *Langmuir* **1997**, *13*, 6869.
(37) Ma, M.; Hill, R. M.; Lowery, J. L.; Fridrikh, S. V.; Rutledge, G. C. *Langmuir* **2005**, *21*, 5549.
(38) Kazunori, K.; Masayuki, Y.; Teruo, O.; Yasuhisa, S. *Journal of Controlled Release* **1993**, *24*, 119.

(39) Kwon, G. S.; Kataoka, K. *Advanced drug delivery reviews* **1995**, *16*, 295.

(40) Ranade, S. V.; Richard, R. E.; Helmus, M. N. *Acta Biomaterialia* **2005**, *1*, 137.

(41) Weiss, R.; Fitzgerald, J.; Kim, D. *Macromolecules* **1991**, *24*, 1071.

(42) Wu, C.; Wu, G.; Wu, C. *Journal of applied polymer science* **2006**, *102*, 4157.

(43) Ferrer, G. G.; Sánchez, M. S.; Sánchez, E. V.; Colomer, F. R.; Ribelles, J. L. G. *Polymer international* **2000**, *49*, 853.

(44) Fetters, L. J.; Morton, M. *Macromolecules* **1969**, *2*, 453.

(45) Ouarti, N.; Viville, P.; Lazzaroni, R.; Minatti, E.; Schappacher, M.; Deffieux, A.; Putaux, J.-L.; Borsali, R. *Langmuir* **2005**, *21*, 9085.

Chapter 6: Piperazine-containing dilithium anionic initiators based on 1,1-diphenylethylene compounds

Alison R. Schultz, Sachin Bobade, and Timothy E. Long

(Ready to submit in *Chemical Communications*)

*Alison R. Schultz, Chainika Jangu, Mingtao Chen, Gregory Fahs, Robert B. Moore, and Timothy E. Long**

Macromolecules Innovation Institute, Department of Chemistry, Virginia Tech, Blacksburg, VA 24061, USA. E-mail: telong@vt.edu.

*To whom correspondence should be addressed. E-mail: telong@vt.edu. TEL: (540)231-2480. FAX: (540)231-8517.

Keywords: Anionic polymerization, polyisoprene, piperazine, *in situ* FTIR spectroscopy

6.1 *Abstract*

Living anionic polymerization of isoprene with an unprecedented piperazine-containing difunctional organolithium initiator, 1,4-bis[4-(1-phenylethenyl)benzyl] piperazine (bis-DPEP), achieved well-defined polyisoprene homopolymers with predictable molecular weights and controlled microstructures. Piperazine provided a polar component within the difunctional initiator design, promoting ion dissociation and miscibility with hydrocarbon solvents and enabling the initiation and propagation of isoprene. *In situ* FTIR spectroscopy monitored the dilithium initiator formation and the anionic polymerization of isoprene, tracking vinyl consumption for kinetic analysis. These investigations provide fundamental insight into difunctional organolithium initiators, aiming to guide future research and applications involving sophisticated, diene-containing macromolecules.

6.2 *Introduction*

Synthetic efforts for developing ideal difunctional organolithium initiators, suitable for the anionic polymerization of 1,3-diene monomers in nonpolar solvents, originated in the late 1960s and receives continued interest due to industrial applications involving microelectronics,[1-3] coatings,[4-7] and adhesives.[8-11] Living anionic polymerization of 1,3-diene monomers in nonpolar solvents advantageously constructs macromolecular compositions with the desirable 1,4-configuration and the associated viscoelastic properties of the cis-isomer. However, these conditions prevent copolymerization of 1,3-diene monomers with polar monomers and, consequently, limit compositional possibilities for diene-containing macromolecules. Designing compatible difunctional organolithium initiators provides opportunities for polymerizing 1,3-dienes with microstructural control and enables sequential monomer addition strategies with polar monomers and additives.

1,1-Diphenylethylene (1,1-DPE) represents an exemplary precursor to difunctional organolithium initiators, exhibiting high reactivity with butyllithium initiators and solubility in nonpolar solvents.[12,13] Charged 1,1-DPE readily propagates styrene-,[14-16] diene-,[17-19] and methacrylate-based monomers,[20-23] yet fails to undergo homopolymerization due to its bulky diphenyl substituents. Difunctional initiators containing double 1,1-DPE compounds first appeared in the literature with 1,3-bis(1-phenylethyenyl) benzene and 1,3-bis[1-(methylphenyl)ethenyl)] benzene,[24] and continued with compositions ranging from 1,4-bis(1-phenylethenyl) benzene[25,26] and 4,4'-bis(1-phenylethenyl)-1,1'-biphenyl[27] to 2,2-bis[4-(1-phenylethenyl)phenyl]propane[28] and 4,4'bis[(1-phenylethenyl)phenyl] ether (Fig. 6.1).[25,29] These earlier reports detailed addition reactions with sec-butyllithium in nonpolar solvents, revealing decreased solubility for the charged difunctional initiators as ion associations increased. Heat,

polar additives, and polar solvents facilitate solubility and ion dissociations, though typically avoided due to potential deleterious effects on the resulting polydiene microstructure.

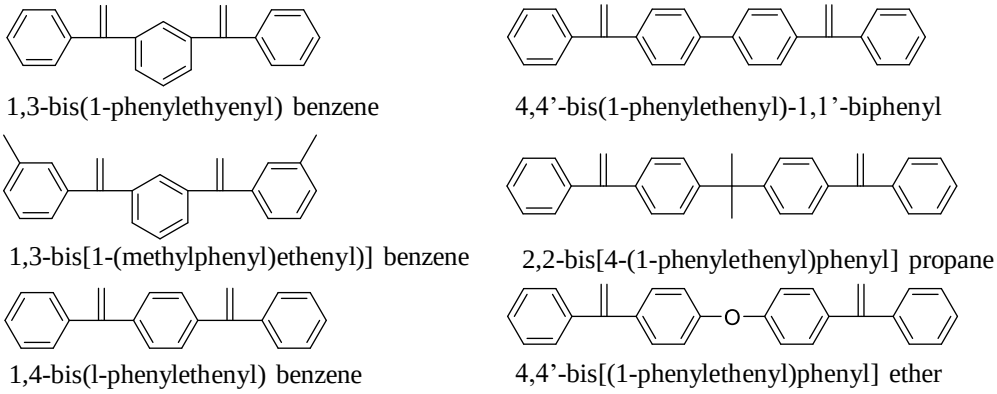

Figure 6.1. Common difunctional initiators based on double 1,1-DPE compounds.

Herein we report 1,4-bis[4-(1-phenylethenyl)benzyl] piperazine (bis-DPEP) as an unprecedented difunctional organolithium initiator based on double 1,1-DPE compounds for polymerizing isoprene with architectural precision and improved solubility in nonpolar solvents. Earlier literature extensively describes amine-containing monomers for living anionic polymerization mechanisms, revealing beneficial polarity enhancements to macromolecular designs and applications.[30-32] Incorporating a polar, piperazine component within the difunctional initiator reduces unfavorable ion associations, enables miscibility with hydrocarbon solvents, and maintains nonpolar solvent conditions required for achieving polyisoprene homopolymers with microstructural control. As industrial applications for diene-containing macromolecules continuously emerge, designing difunctional organolithium initiators will enable novel compositional possibilities to meet these technologies.

6.3 *Experimental Section*

6.3.1 Materials:

Phenyl(p-tolyl)methanone (99%), methyllithium solution (1.6 M in diethyl ether), methyl iodide (97%), potassium carbonate (97%) piperazine, and *sec*-butyl lithium solution (1.4 M in hexanes) were purchased from Sigma Aldrich and used as received.

6.3.2 Instrumentation

In situ FTIR analysis employed a Mettler Toledo ReactIR 45M attenuated total reflectance reaction apparatus equipped with a light conduit and DiComp (diamond composite) insertion probe. Size exclusion chromatography (SEC) was used to determine the molecular weights of phosphorus-containing polymers at 40 ^{o}C in THF at 1 mL/min. THF SEC was performed on a Waters SEC equipped with two Waters Styragel HR5E (THF) columns, a Waters 717 plus autosampler, a Wyatt MiniDAWN, and a Waters 2414 differential refractive index detector. An Optilab T-rEX refractometer ($\lambda = 658$) was used to measure dn/dc values offline for determination of absolute weight-average molecular weights. ^{1}H and ^{13}C NMR spectroscopy (Varian Inova, 400 MHz) determined the structural confirmation of the dilithium initiator and polymer composition.

6.3.3 Synthesis of 1,4-bis[4-(1-phenylethenyl)benzyl] piperazine (bis-DPEP)

Phenyl(p-tolyl)methanone (20 g, 0.10 mol) and 50 mL dichloromethane was added to a 125 mL, flame-dried, round-bottomed flask. The reaction contents were purged with nitrogen and 1.2 molar equivalence of methyl iodide and methyllithium solution was added to the mixture. The reaction proceeded for overnight quantitatively reduce the carbonyl and produce 1-(1-methoxy-1-phenylethyl)-4-methylbenzene. The reaction mixture was washed with water 3xs and the organic layer was vacuum stripped to isolate the methoxy- analogue, white solid (97% yield). 1-(1-methoxy-1-phenylethyl)-4-methylbenzene (10 g, 0.045 mol) and N-bromosuccinimide (11.8 g,

0.066 mol) was charged to a clean, 125 mL, round-bottomed flask with 50 mL of carbon tetrachloride. The reaction flask was sealed with a rubber septum and the mixture was allowed to stir under an IR lamp for overnight. The reaction mixture was distilled under high vacuum to isolate 1-(bromomethyl)-4-(1-phenylvinyl)benzene. Recrystallization in acetone achieved the purified product as a white solid, (96% yield). 1-(Bromomethyl)-4-(1-phenylvinyl)benzene (5 g, 0.018 mol) was then added to a clean 125 mL, round-bottomed flask with piperazine (0.78 g, 0.009 mol), potassium carbonate (2.53 g, 0.018 mol), and 50 mL acetone. The was equipped and sealed off with a condenser, and the reaction was allowed to proceed at reflux for 24 h. Residual salt byproduct was filtered from the reaction mixture, and distillation under high vacuum isolated the final product, 1,4-bis[4-(1-phenylethenyl)benzyl] piperazine. Recrystallization in acetone achieved the purified product as a white solid, (94% yield). GC-MS (Target molecular weight 470.7 g/mol, Observed molecular weight: 470.2 g/mol. ^{1}H NMR (400 MHz, $CDCl_3$, 25 °C, δ): 2.5 ppm (-N-CH_2-CH_2-N-, piperazine protons), 3.5 ppm (-N-CH_2-, methylene protons), 5.5 ppm (-CH_2-, ethylene protons), 7.0-7.5 ppm (aromatic protons). ^{13}C NMR (400 MHz, $CDCl_3$, 25 °C, δ): 52 ppm (-N-CH_2-CH_2-N-, piperazine carbons), 62 ppm (-N-CH_2-, methylene carbons), 116 ppm (-CH_2-, ethylene carbons), 128-145 ppm (aromatic carbons).

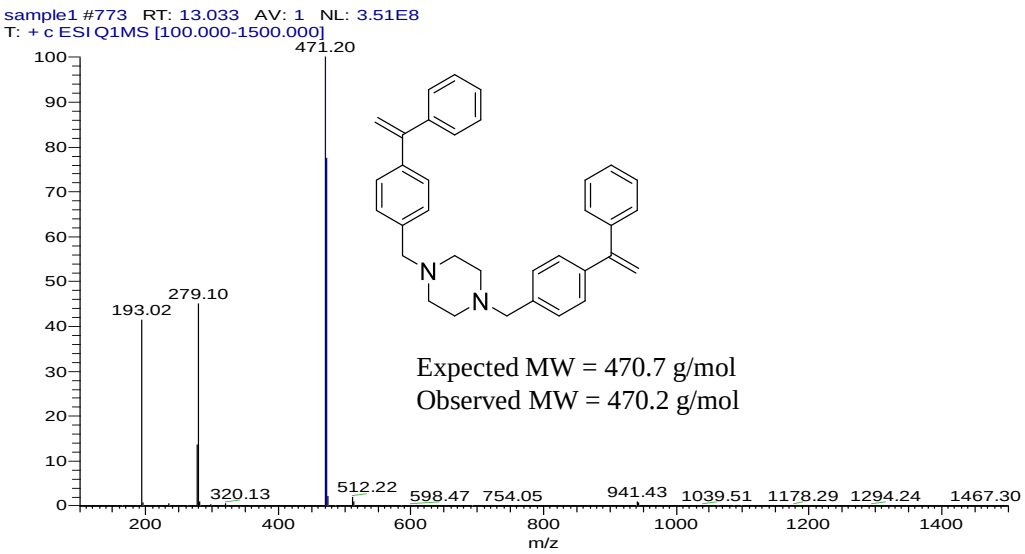

Figure SI 6.1. GC-MS confirms the target molecular weight of the isolated 1,4-bis[4-(1-phenylethenyl)benzyl] piperazine.

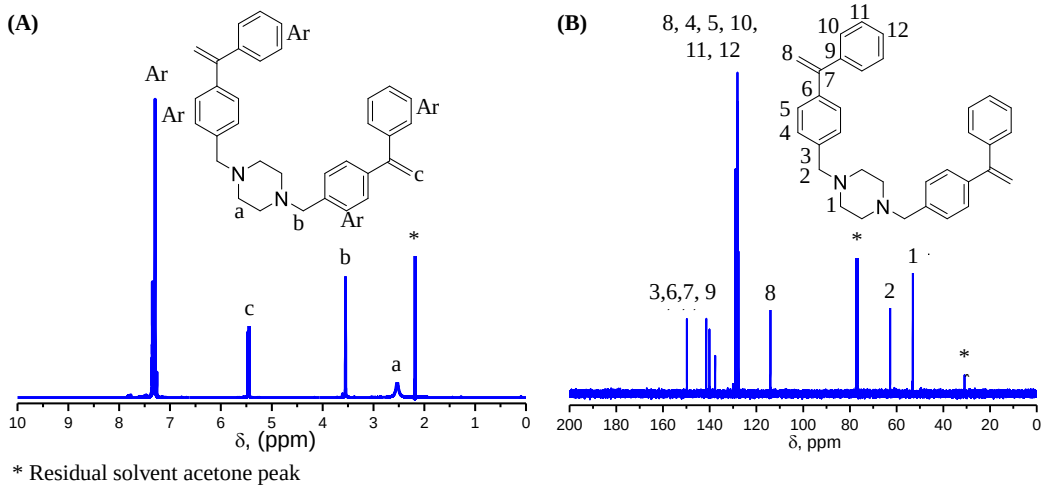

Figure SI 6.2. (A) ^{1}H NMR and (B) ^{13}C NMR spectroscopy confirm structure and purity of 1,4-Bis[4-(1-phenylethenyl)benzyl] piperazine.

6.3.4 *In situ* FTIR monitors the production of the bis[4-(1-phenylethenyl)benzyl] piperazine dilithium initiator

A 25-mL, flame-dried, round-bottomed flask contained (0.50 mg, 0.10 mmol) bis[4-(1-phenylethenyl)benzyl] piperazine and 8 mL of dry cyclohexane. A rubber septum sealed one neck of the flask, and the DiComp probe was inserted into the second neck and sealed. The probe tip submerged below the monomer surface, and the ReactIR spectrometer programmed a spectrum collection every 1 min for 5 h (Fig. 6.2). Nitrogen purged the reaction flask for 15 min and then reaction flask submerged into 50 ^{o}C heated oil bath. *Sec*-butyllithium (0.006 mL, 0.05 mmol) enabled the production of the bis[4-(1-phenylethenyl)benzyl] piperazine dilithium initiator. Tracking the absorption disappearance for the C=C vinyl vibrational frequency peak at 967 cm^{-1} over time revealed a complete vinyl conversion to the dilithium product within 3 h.

6.3.5 *In situ* FTIR monitors the anionic polymerization of isoprene using bis[4-(1-phenylethenyl)benzyl] piperazine dilithium initiator

A 25-mL, flame-dried, round-bottomed flask contained (0.50 mg, 0.10 mmol) bis[4-(1-phenylethenyl)benzyl] piperazine and 8 mL of dry cyclohexane. A rubber septum sealed one neck of the flask, and the DiComp probe was inserted into the second neck and sealed. The probe tip submerged below the monomer surface, and the ReactIR spectrometer programmed a spectrum collection every 1 min for 5 h (Fig. 6.2). Nitrogen purged the reaction flask for 15 min and then reaction flask submerged into 50 ^{o}C heated oil bath. *Sec*-butyllithium (0.006 mL, 0.05 mmol) enabled the production of a deep red, bis[4-(1-phenylethenyl)benzyl] piperazine dilithium initiator. After 3 h (2.65 mL, 1.8 g) isoprene sequentially added to the initiator propagation occurred for 1 h. Tracking the absorption disappearance for the C=C vinyl vibration peak at 912 cm^{-1} over time revealed complete vinyl consumption within 1.5 h.

6.3.6 Anionic polymerization with a bis[4-(1-phenylethenyl)benzyl] piperazine dilithium initiator achieves high molecular weight, polyisoprene homopolymers

In a representative polymerization, a 125-mL flame dried, nitrogen purged, and sealed round bottom flask contained (0.50 mg, 0.20 mmol) bis[4-(1-phenylethenyl)benzyl] piperazine and 50 mL of dry cyclohexane at 50 °C. Sec-butyllithium (0.10 mmol) initiated the deep red bis[4-(1-phenylethenyl)benzyl] piperazine dilithium initiator was allowed 3 h to reach full initiation. Sequential monomer addition with 21 mL isoprene (14.54 g) achieved a clear poly(isoprenyl)lithium living chain of 75,000 g mol^{-1}. After 2 h, the polymerization was terminated with degassed methanol (1.0 mL), and the resulting polyisoprene homopolymer was precipitated into methanol and dried at 23 °C under reduced pressure (0.5 mmHg) for 24 h to obtain a clear, viscous liquid (97% isolated yield). ^{1}H NMR (400 MHz, $CDCl_3$, 25 °C, δ): 0.8 – 0.9 ppm (br, $CH_3CH_2CH(CH_3)$-), 1.1 – 1.2 ppm (br, -CH_3 in 1,2-polyisoprene units), 1.2 – 1.5 ppm (br, -CH_2CH-, -CH_2CH- in 1,2-polyisoprene and 3,4-polyisoprene units), 1.61 ppm (br, -CH3 in *trans*-1,4-polyisoprene units), 1.64 ppm (br, -CH_3 in 3,4-polyisoprene units), 1.68 ppm (br, -CH_3 in *cis*-1,4-polyisoprene units), 1.8 – 2.2 ppm (br, -CH_2CH=, -CH_2C(CH_3)= in 1,4-polyisoprene units), 4.6 – 4.8 ppm (br, -C(CH_3)=CH_2 3,4-polyisoprene units and -CH=CH_2 1,2-polyisoprene units), 4.8 – 5.4 ppm (br, -CH=C(CH_3)- 1,4-polyisoprene units). 1.5 (–CH_2– polymer backbone, –CH– polymer backbone).

6.4 *Results and Discussion*

Scheme 6.1 depicts nucleophilic substitution as a facile approach for synthesizing bis-DPEP, in accordance to literature protocols for previous difunctional initiators based on double 1,1-DPE compounds.[29] ^{1}H and ^{13}C NMR and GC-Mass spectroscopy characterized the final white solid product, confirming its chemical structure and ensuring its high purity (SI Fig. 6.1 and 6.2).

Subsequent addition with sec-butyllithium at 50 ^{o}C in cyclohexane produced the deep red bis-DPEP dilithium initiator (Scheme 6.1). *In situ* FTIR spectroscopy monitored bis-DPEP dilithium formation, using the C=C vinyl vibrational frequency peak at 967 cm^{-1} and generated a 2D normalized waterfall plot for peak absorbance vs. time (min). Tracking vinyl concentration disappearance over time revealed a complete vinyl conversion to the dilithium product within 3 h (Fig. 6.2). *In situ* FTIR spectroscopy then monitored sequential isoprene addition, pinning the isoprene C=C vinyl vibration peak at 912 cm^{-1} and producing a second 2D normalized waterfall plot. Tracking the isoprene vinyl concentration disappearance revealed complete vinyl consumption within 1.5 h, confirming the anionic polymerization of isoprene with the bis-DPEP dilithium initiator (Fig. 6.2). Size exclusion chromatography (SEC) confirmed a 35,000 g mol^{-1} target M_n value for the homopolymer, and revealed monomodality in the chromatogram and a narrow polydispersity (PDI) of 1.09 (Fig. 6.3). ^{1}H NMR spectroscopy elucidated the microstructure for the polyisoprene homopolymer, revealing a 90% yield for the favorable 1,4-configuration with 75% of the *cis*-isomer (SI 6.2).

Scheme 6.1. Synthetic method for preparation of 1,4-bis[4-(1-phenylethenyl)benzyl] piperazine and dilithium derivative.

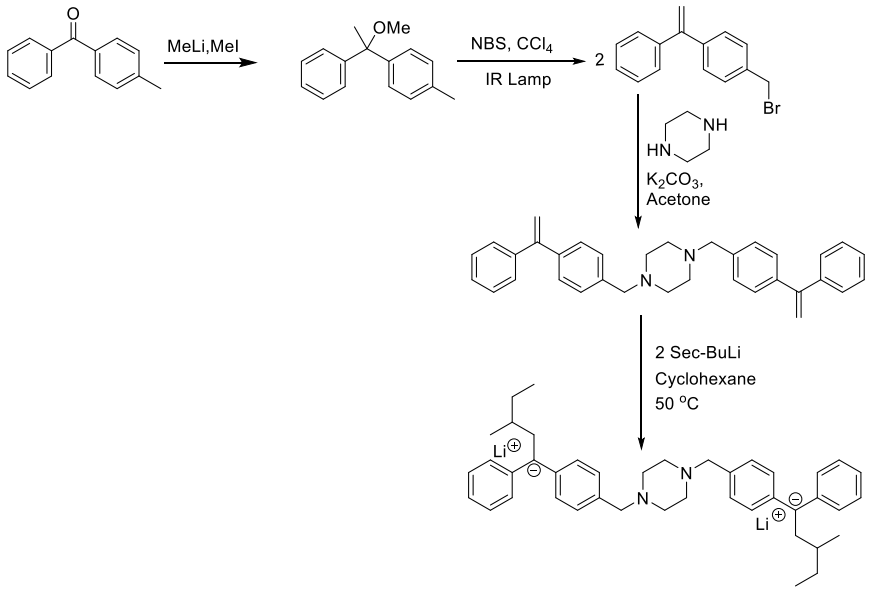

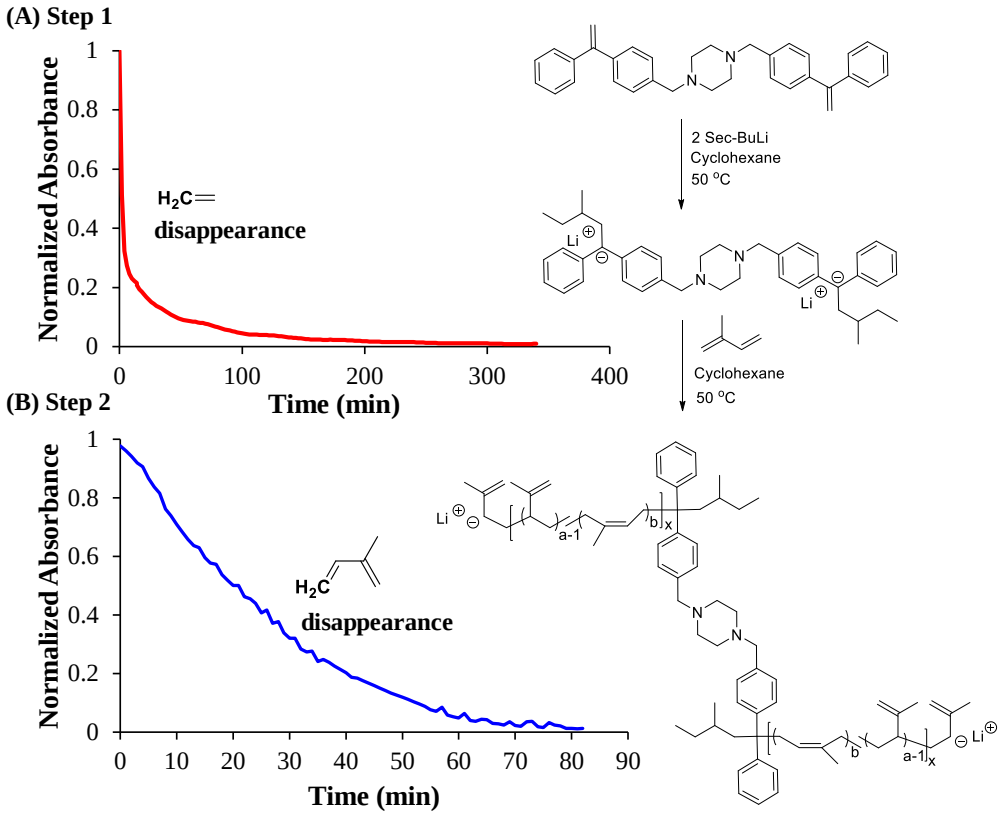

Figure 6.2. *In situ* FTIR spectroscopy monitors vinyl disappearance versus time for (A) 1,4-Bis[4-(1-phenylethenyl)benzyl] piperazine (967 cm-1) and (B) Isoprene (912 cm-1).

In situ FTIR studies elucidated the anionic polymerization mechanisms involving isoprene and the bis-DPEP dilithium initiator, and derived an unprecedented synthetic method for preparing polyisoprenes with controlled molecular weights. Scheme 6.2 reveals the new synthetic procedure, including the initial 3 h time requirement for the dilithium initiator production. Seeding techniques with small quantities of isoprene facilitated the carbanion crossover mechanism from the dilithium initiator and promoted homogeneity for the reaction mixture.[33] Sequential addition with the remaining isoprene quantities enabled polyisoprenes with increasing molecular weights, targeting M_n values of 70,000 g mol^{-1} (PDI = 1.06) and 150,000 g mol^{-1} (PDI = 1.08). SEC revealed the controlled shift in increasing target M_n values, monomodality in the chromatograms, and narrow polydispersity for the homopolymers (Fig. 6.3).

Scheme 6.2. 1,4-Bis[4-(1-phenylethenyl)benzyl] piperazine dilithium initiator in the synthesis of polyisoprenes.

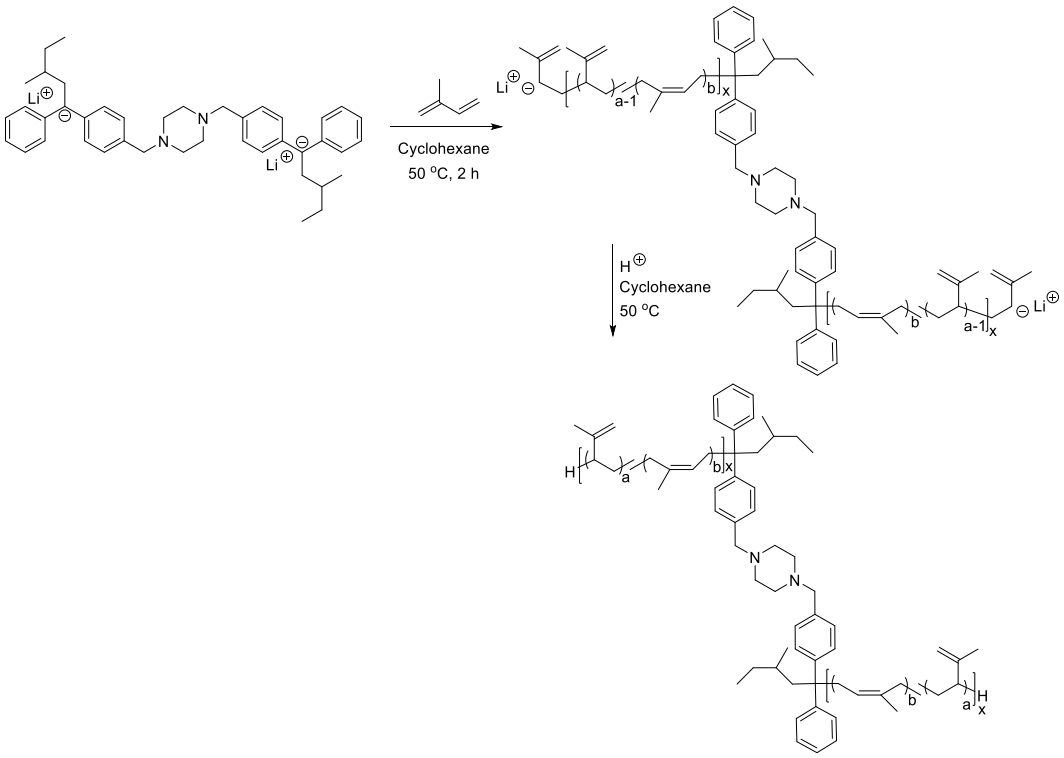

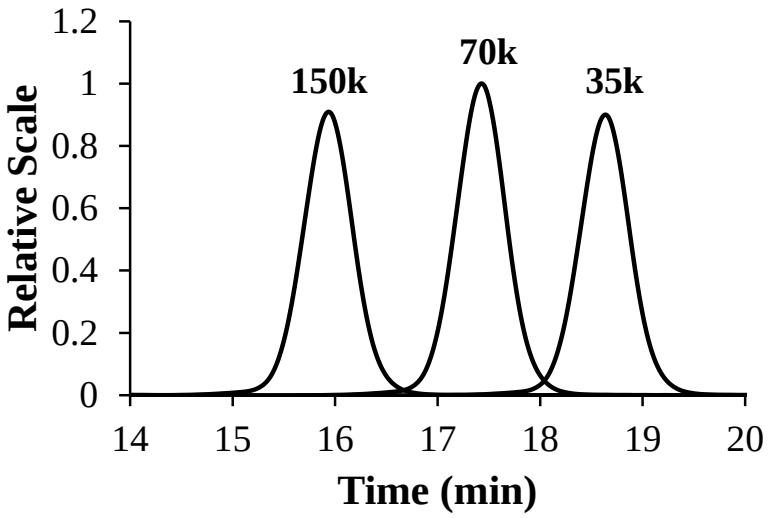

Figure 6.3. SEC characterization of polyisoprenes with various molecular weights.

6.5 *Conclusions*

A piperazine-inspired compositional design afforded the novel difunctional organolithium initiator, 1,4-bis[4-(1-phenylethenyl)benzyl] piperazine, suitable for the living anionic polymerization of isoprene. The unprecedented synthetic method achieved polyisoprene homopolymers with well-defined microstructures, controlled molecular weights, and narrow polydispersities. Piperazine served as a polar additive within the difunctional initiator composition, promoting ion dissociation and solubility with the nonpolar solvent, cyclohexane. The controlled anionic polymerization of isoprene with 1,4-bis[4-(1-phenylethenyl)benzyl] piperazine provides opportunities to engineer unique ABA-type triblock copolymers with diverse functional monomers, and also enables post-polymerization reactions with electrophilic agents for producing novel difunctional polyisoprene compositions. Future studies will extend these diene-containing macromolecular architectures, in order to evaluate 1,4-bis[4-(1-phenylethenyl)benzyl] piperazine as a versatile and robust dilithium initiator.

6.6 *Acknowledgements*

We acknowledge the Institute for Critical Technology Applied Science (ICTAS) for laboratory support. This material is partially based upon work supported by the National Science Foundation under Grant No. DMR-0923107.

6.7 *References*

(1) Luxton, A. R. *Rubber Chemistry and Technology* **1981**, *54*, 596.

(2) So, Y. H.; Foster, P.; Im, J. H.; Garrou, P.; Hetzner, J.; Stark, E.; Baranek, K. *Journal of Polymer Science Part A: Polymer Chemistry* **2006**, *44*, 1591.

(3) Dai, L.; Griesser, H. J.; Hong, X.; Mau, A. W.; Spurling, T. H.; Yang, Y.; White, J. W. *Macromolecules* **1996**, *29*, 282.

(4) Hashimoto, T.; Tsutsumi, K.; Funaki, Y. *Langmuir* **1997**, *13*, 6869.

(5) Woodward, I.; Schofield, W.; Roucoules, V.; Badyal, J. *Langmuir* **2003**, *19*, 3432.

(6) Malucelli, G.; Bongiovanni, R.; Sangermano, M.; Ronchetti, S.; Priola, A. *Polymer* **2007**, *48*, 7000.

(7) Xiang, Y.; Yan, B.; Yue, B.; McNeff, C. V.; Carr, P. W.; Lee, M. L. *Journal of Chromatography A* **2003**, *983*, 83.

(8) Rosser, R. W.; Neville, R. G. *Journal of Applied Polymer Science* **1969**, *13*, 215.

(9) Phillips, J. P.; Deng, X.; Todd, M. L.; Heaps, D. T.; Stevenson, S.; Zhou, H.; Hoyle, C. E. *Journal of applied polymer science* **2008**, *109*, 2895.

(10) Tse, M. F. *Journal of Adhesion Science and Technology* **1989**, *3*, 551.

(11) Barcia, F. L.; Soares, B. G.; Sampaio, E. *Journal of applied polymer science* **2004**, *93*, 2370.

(12) Evans, A. G.; George, D. B. *Journal of the Chemical Society (Resumed)* **1961**, 4653.

(13) Casling, R.; Evans, A. G.; Rees, N. *Journal of the Chemical Society B: Physical Organic* **1966**, 519.

(14) Yuki, H.; Hotta, J.; Okamoto, Y.; Murahashi, S. *Bulletin of the Chemical Society of Japan* **1967**, *40*, 2659.

(15) Ureta, E.; Smid, J.; Szwarc, M. *Journal of Polymer Science Part A-1: Polymer Chemistry* **1966**, *4*, 2219.
(16) Bywater, S.; Worsfold, D. *Canadian Journal of Chemistry* **1962**, *40*, 1564.
(17) Yuki, H.; Okamoto, Y. *Bulletin of the Chemical Society of Japan* **1970**, *43*, 148.
(18) Yuki, H.; Okamoto, Y. *Bulletin of the Chemical Society of Japan* **1969**, *42*, 1644.
(19) Trepka, W. J. *Journal of Polymer Science Part B: Polymer Letters* **1970**, *8*, 499.
(20) Deporter, C. D.; Long, T. E.; McGrath, J. E. *Polymer international* **1994**, *33*, 205.
(21) Creutz, S.; Teyssié, P.; Jérôme, R. *Macromolecules* **1997**, *30*, 6.
(22) Gupta, P.; Elkins, C.; Long, T. E.; Wilkes, G. L. *Polymer* **2005**, *46*, 4799.
(23) Han, S.; Hagiwara, M.; Ishizone, T. *Macromolecules* **2003**, *36*, 8312.
(24) Tung, L. H.; Lo, G. Y.; Beyer, D. E.; Google Patents: 1979.
(25) Tung, L.; Lo, G. Y.; Beyer, D. *Macromolecules* **1978**, *11*, 616.
(26) Quirk, R. P.; Yoo, T. *Polymer Bulletin* **1993**, *31*, 29.
(27) Tung, L. H.; Lo, G. Y.; Rakshys, J. W.; Beyer, D. E.; Google Patents: 1980.
(28) Bae, Y. C.; Faust, R. *Macromolecules* **1998**, *31*, 2480.
(29) Tung, L.; Lo, G.-S. *Macromolecules* **1994**, *27*, 1680.
(30) Schultz, A. R.; Jangu, C.; Long, T. E. *Polymer Chemistry* **2014**, *5*, 6003.
(31) Couture, G.; Alaaeddine, A.; Boschet, F.; Ameduri, B. *Progress in Polymer Science* **2011**, *36*, 1521.
(32) Arai, K.; Kotaka, T.; Kitano, Y.; Yoshimura, K. *Macromolecules* **1980**, *13*, 1670.
(33) Lo, G.-S.; Otterbacher, E.; Gatzke, A.; Tung, L. *Macromolecules* **1994**, *27*, 2233.

Chapter 7: Acetoacetate Curing Systems for Solvent-Free Based Roofing Adhesives

(Submitted as provisional patent, VTIP 16-155)

Alison R. Schultz, Mingtao Chen, James E. Reese, S. Richard Turner, Timothy E. Long

Macromolecules Innovation Institute, Department of Chemistry, Virginia Tech, Blacksburg

VA 24061

*To whom correspondence should be addressed. E-mail: telong@vt.edu TEL: (540) 231-2480

FAX: (540) 231-8517

Keywords: Michael addition; Adhesives; Solvent-free; Low VOC; EPDM; PVC; TPO; *In situ* FTIR spectroscopy; Rheology; Peel test; solvent-free

7.1 *Abstract*

The elimination of solvents in numerous adhesive formulations and applications remains a long sought after goal. In particular, rooftop adhesion for many membranes to a substrate generally requires the use of environmentally unfriendly solvents and the design of new solvent-free adhesives remains an unmet approach for advancing roofing adhesive technology. This chapter describes novel, hydrogenated polybutadiene Michael adhesives and their unprecedented solvent-free adhesion to roofing membranes. *In situ* FTIR spectroscopy and rheology elucidated the effects of catalyst concentration, temperature, and the molecular weight of Michael donors and acceptors on gel times and crosslinked network moduli. 180° peel tests provided insight into the adhesive strength for bonded EPDM, PVC, and TPO roofing membranes, revealing the universal adhesive

property of Michael adhesives. The Michael addition reaction permits the green synthesis of sophisticated hyperbranched networks with ambient and solvent-free conditions and high tolerance to diverse monomers. Exploring novel macromolecular compositions using a vast array of polymerizable Michael donors and acceptors fosters solvent-free adhesive technologies.

7.2 *Introduction*

The Michael addition reaction, coined after Arthur Michael and its discovery in the 1800s, provides an efficient synthetic route for the conjugate addition of electron poor olefins (Michael acceptors) to a vast array of nucleophiles (Michael donors). The synthetic strategy advantageously requires ambient and solvent-free conditions and offers high tolerance to an abundance of polymerizable monomers with diverse functionality, permitting the green synthesis of sophisticated polymer architectures ranging from linear thermoplastics to hyperbranched networks.[1-4] Exploring novel macromolecular compositions with diverse polymerizable Michael donors and acceptors fosters diverse technologies including biomedical,[5-7] pharmaceutical,[8,9] coatings,[10,11] and adhesives.[11,12]

Some potential chemistry for consideration involves diacrylate based Michael acceptors and bisacetoacetate Michael donors composed of nonvolatile small molecules and oligomers (hydrocarbon-, glycerol-, phenyl-, ethylene oxide-, silyl-, ester-, amide-, maleimide-, nitrile-, cyano-, sulfone-, and alkyl methacrylate- based compositions).[13-18] Less common, but equally applicable, vinyl ketones, nitro ethylenes, α,β-unsaturated aldehydes, vinyl phosphonates, acrylonitrile, vinyl pyridines, azo compounds and even β-keto acetylenes and acetylene esters also serve as Michael acceptors.[3,19,20] Donor selection may also extend to non-enolate nucleophiles such as amines, thiols, and phosphines, and these reactions are typically referred to as 'Michael-type additions'.[3] A weak base catalyst is required to activate bisacrylate Michael donors and enable

the addition reaction across a carbon-carbon multiple bond of Michael acceptors, achieving a solvent-free, 2-component adhesive network with high conversions and tunable reaction rates. Catalysts range from organic bases such as tetramethylguanidine (TMG), triethylamine, 1,8-diazabicyclo[5.4.0]undec-7-ene (DBU), and 1,5-diazabicyclo[4.3.0]non-5-ene (DBN) to inorganic bases such as potassium carbonate, boron trifluoride, aluminum trichloride, and zinc chloride.[3,21]

Rooftop adhesion involving EPDM, PVC, and TPO based membranes represents an appealing new technical application for the Michael addition reaction, providing an opportunity to revolutionize commercially available roofing adhesives with 2-component and solvent-free Michael adhesives. EPA regulations restrict solvent based adhesives to a narrow supply of approved low volatile organic components (low VOC), rendering various commercially available roofing adhesives less viable. Solvents such as toluene, heptane, and xylene, for example, enabled high performance bonding adhesives for several decades and no longer suit EPA low VOC standards.[22] Substitution with approved low VOCs including acetone, *tert*-butyl acetate, *para*-chlorobenzotrifluoride, and methyl ethyl ketone achieves compatibility with EPA regulations, yet fails to provide comparable adhesive performance to conventional formulations.[22-24] In this chapter, we report poly(hydrogenated butadiene) as novel, 2-component, and solvent-free Michael adhesives and reveal their green application in roofing adhesion. Experimental studies involving *in situ* FTIR spectroscopy, rheology, and 180 peel tests elucidated crosslinking reaction kinetics, gel times, and adhesive performance. As EPA regulations continue to limit solvent selection in adhesive technologies, investigating novel macromolecular compositions with diverse polymerizable Michael donors and acceptors will facilitate solvent-free industrial applications.

7.3 *Experimental Section*

7.3.1 Materials

Poly(hydrogenated butadiene) diols (Krasol® HLBH-P 2000, 2,000 g/mol) (97-99 %) was purchased from Cray Valley and used as received. Acryloyl chloride (99%), anhydrous dichloromethane (99%), potassium carbonate (97%), and *tert*-butyl acetoacetate (99%), and 1,8-diazabicyclo-[5.4.0]-undec-7-ene (99%) were purchased from Sigma Aldrich and used as received. EPDM, PVC, and TPO roofing membranes were provided by Carlisle Construction.

7.3.2 Instrumentation

In situ FTIR analysis employed a Mettler Toledo ReactIR 45M attenuated total reflectance reaction apparatus equipped with a light conduit and DiComp (diamond composite) insertion probe. Rheological experiments were conducted on a TA Instruments AR2000 Rheometer at a frequency of 1Hz and a temperature of 10 ^{o}C, 25 ^{o}C, and 50 ^{o}C. The gel time was recorded when the storage modulus (G0) and loss modulus (G00) were equal. ^{1}H NMR spectroscopy (Varian Inova, 400 MHz) determined polymer composition and degree of modification. FTA 200 contact angle analyzer (First Ten Angstroms, Portsmouth, VA) measured all contact angles using a sessile drop technique. Polymer-coated EPDM, PVC, and TPO samples were placed on an adjustable platform and ≈ 5 μL of Milli-Q water (Millipore Gradient A10) was placed on the surface using a 3 mL 22 gauge syringe. A video CCD camera captured single frame movies for all contact angles, the resulting drop shapes were fit to a mathematical expression. Calculating the slope of the tangent to the drop at the liquid-solid-vapor interface determined final contact angle values (FTA Operator's and Installation Manuals, revision 2.0, May 30, 1997). Four replicates were performed to determine the average contact angle.

TA Instruments thermogravimetric analyzer (TGAQ50) enabled thermogravimetric analysis with a heating rate of 10 °C/min to 600 °C under a N_2. TA Instruments Q1000 differential scanning calorimeter (DSC) elucidated thermal transitions with a heating rate of 10 °C/min utilizing a heat/cool/heat cycle. T_g was determined from the second heat cycle. Dynamic mechanical analysis (DMA) was conducted on a TA Instruments Q800 Dynamic Mechanical Analyzer in tension mode at a frequency of 1 Hz, an oscillatory amplitude of 15 μm, and a static force of 0.01 N. The temperature ramp was 3 ^oC/min. The glass-transition temperature (T_g) was determined at the peak maximum of the tan δ curve. Tensile, 180^o peel experiments employed an Instron at 50 mm/min strain rate.

7.3.3 Synthesis of Krasol® diacrylate, Michael acceptors

In a representative reaction, a two-neck 500 mL round-bottomed flask, equipped with a 50 mL addition funnel containing acryloyl chloride (5.2 g, 0.055 mol) in anhydrous dichloromethane (20 mL), was charged with 2,000 g/mol Krasol® diol (50 g, 0.025 mol) and anhydrous potassium carbonate (10.37 g, 0.075 mol) and was sealed with a rubber septum. Anhydrous dichlormethane (110 mL) cannulated into the reaction flask and an ice bath was assembled to cool the reaction contents to 0 ^oC. Acryloyl chloride was added dropwise overnight and the reaction was allowed to warm to 23 ^oC. Salt by-product was filtered through Celite® and the organic solute was washed 3x with H_2O. Dichloromethane was removed under reduced pressure (5 mmHg) and the product was isolated as a clear liquid and was dried in vacuo at 23 ^oC (48.23 g, 96 % yield). ^1H NMR (400 MHz, $CDCl_3$): 6.47 (d, 2H), 6.22 (dd, 2H), 5.77 (d, 2H), 4.13 (m, 4H), 0.75-1.5 (polymer backbone).

7.3.4 Synthesis of Krasol® bisAcAc, Michael donors

In a typical procedure, 2,000 g/mol Krasol® diol (10.0 g, 10 mmol), *tert*-butyl acetoacetate (tBuAcAc) (6.3 g, 40 mmol, 4 equiv.), and toluene (50 mL) were charged to a two-necked 100-ml flask, equipped with a short-path distillation head, receiving flask, and magnetic stirrer. The mixture was maintained at 110 ^{o}C for 4 h and vacuum (0.1 mmHg) was applied to remove the tert-butanol by-product and excess tBuAcAc. An additional 6.3 g tBuAcAc was added and heating continued for 3 h at 130 ^{o}C in order to ensure quantitative functionalization. Vacuum (0.1 mmHg) at 130 ^{o}C was applied to remove volatile starting reagents and reaction by-products and the product was quantitatively isolated as a clear pale-yellow liquid. ^{1}H NMR (400MHz, CDCl3) of the 2000 g/mol Krasol bisAcAc: 0.75-1.5 (polymer backbone), 1.24 ppm (dd, 6H, $CHCH_3OAcAc$), 2.26 ppm (s, 6H, $COCH_2COCH_3$), 5.08 ppm (m, 4H, CH_2CHCH_3OAcAc), 5.29 ppm (s, enol C=CH-C=O).

7.3.5 Network Formation

In a representative reaction, Krasol® bisAcAc (2.5 g, 1.25 mmol), and Krasol diacrylate (3.0 g, 1.5 mmol, 1.2 mol eq.) were mixed thoroughly to form a clear, homogeneous, and viscous liquid. 1,8-Diazabicyclo-[5.4.0]-undec-7-ene (DBU) catalyst (3 mol%) was quickly added and mixed thoroughly. The mixture was cast on Mylar® substrate with an adjustable film applicator. Mixtures were allowed to crosslink for 24 h at room temperature and the final films were dried at reduced pressure (0.1 mmHg) at 60 °C for 24 h.

7.3.6 *In situ* FTIR reactions for model studies

In an exemplary kinetic study, a reaction mixture consisted of a 1.2:1.0 molar ratio of diacrylate to bisacetoacetate and 3mol% 1,8-diazabicyclo-[5.4.0]-undec-7-ene as the base in the presence of the *in situ* FTIR spectrometer. A 25-mL, flame-dried, round-bottomed two-necked flask contained Krasol® bisAcAc (5.0 g, 2.5 mmol). A rubber septum sealing one neck of the flask, and the DiComp probe was inserted into the second neck and sealed. The probe tip submerged below the oligomer surface, and the ReactIR spectrometer programmed a spectrum collection every 1 min for 5 h. Nitrogen purged the reaction flask for 15 min and then reaction flask submerged into 23 ^{o}C oil bath. DBU (3mol%, 511ml) was added to the round-bottomed flask, and the contents were allowed to equilibrate for 60 min. After the 60 min pre-equilibration, the reaction was monitored with the *in situ* FTIR spectrometer. Once the first scan was complete, the Krasol diacrylate was quickly added to the round-bottomed flask. Tracking the C=C vinyl vibrational frequency peaks for the Krasol diacrylate oligomer at 890 cm^{-1} generated a normalized 2D waterfall plot for absorbance vs. time (sec). Vinyl concentration disappearance over time elucidated the Michael crosslinking reaction, revealing a 1.5 h reaction time.

7.3.7 Preparing EPDM, PVC, and TPO tensile samples with Michael adhesives

Krasol® bisAcAc (2.5 g, 1.25 mmol) and Krasol diacrylate (3.0 g, 1.5 mmol, 1.2 mol eq.) were mixed thoroughly in clean reaction vial to form a clear, homogeneous, and viscous liquid. Roofing membranes were prepared in 2, 10 x 15 cm sheets and cleaned with hexanes prior to Michael adhesive coating. 1,8-Diazabicyclo-[5.4.0]-undec-7-ene (DBU) catalyst (3 mol%) was quickly added and mixed thoroughly. The mixture was pipetted on the 10 x 15 cm roofing sheets and brushed until coverage reached a 5 x 7.5 cm area for both substrate surfaces. Gelation proceeded for 1-5 min, and the roofing sheets were placed together. A 2.3 kg roller passed over

the prepared sample and crosslinking occurred for 24 h at room temperature. The final samples were dried at reduced pressure (0.1 mmHg) at 23 °C for 24 h prior to tensile experiments.

7.4 *Results and Discussion*

Scheme 7.1 depicts the synthesis of poly(hydrogenated butadiene) based Michael donors and acceptors, a facile approach involving modification of commercially available Krasol® diols. These reactive oligmeric diols offer hydrogenation levels greater than 97%, M_n of 2,000 g/mol, excellent thermal stability, good weatherability, hydrophobicity, low color, high clarity, and low glass transition temperatures (T_g = - 55 ^oC), affording their compatibility for applications involving acid and base resistance, adhesion, asphalt miscibility, electrical insulation, and low temperature flexibility. Reacting Krasol® diols with acryloyl chloride or *tert*-butyl acetoacetate produces novel diacrylate (DA) acceptors (Scheme 7.1A) and bisacetoacetate (BisAcAc) donors (Scheme 7.1B), following the literature synthetic protocols for modifying poly(propylene glycol).[21] ^1H NMR revealed a shift in -CH_2- protons upon modifying the diol to a diacrylate and bisacetoacetate, revealing quantitative functionalization as the -CH_2- protons for the diol derivative disappeared.

Scheme 7.1 General reaction scheme synthesizing Krasol® A) Michael acceptor and B) Michael donor**.**

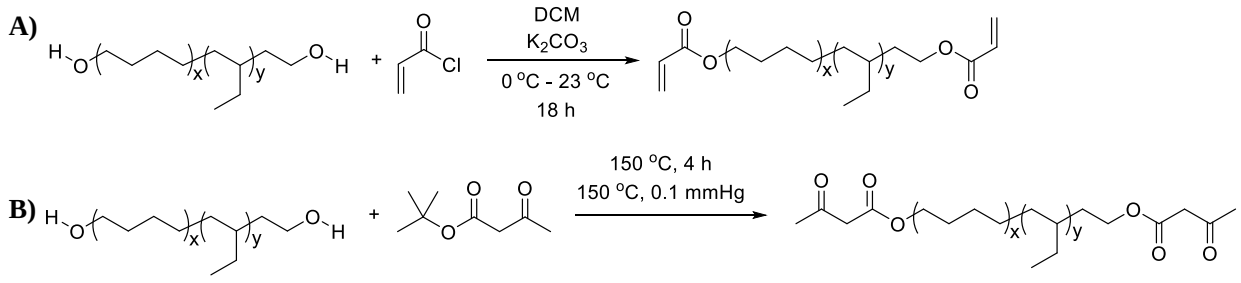

The structural change from a diol to diacrylate and bisacetoacetate also drastically influenced the viscosity of the Krasol® oligomer. Shear viscosity rheological studies generated a viscosity (Pa*s) vs. shear rate (s^{-1}) plot, comparing each functionalized Krasol® oligomer at 25 °C and 50 °C (Fig. 7.1). The Krasol diol exhibited the highest viscosity (60 Pa*s) at 25 °C, presumably due to the hydrophilic, hydroxyl- end groups aggregating from the hydrophobic hydrogenated poly(butadiene) oligomer backbone. Converting the hydrophilic, hydroxyl- end groups to a more hydrophobic diacrylate and bisacetoacetate homogenized the liquid oligomer and enabled shear viscosity properties suitable for coating applications. Viscosity values drastically reduced with end group functionality, revealing a decreasing viscosity trend in the following order: Krasol® diol > Krasol® DA > Krasol® BisAcAc. Heating the oligomers to 50 °C further reduced shear viscosities, dropping the values by an order of magnitude yet maintaining the common trend where Krasol® diol > Krasol® DA > Krasol® BisAcAc. Contact angle measurements on and ethylene propylene diene monomer (EPDM) roofing substrate corresponded to shear viscosity observations, and further elucidated the influence of end group functionality on wetting behavior (Fig. 7.2). Contact angle values decreased as the viscosity of the liquid oligomer decreased, enabling improved coating properties. The contact angle decreased with end group functionality in the following order: 60° > 45° ≥ 45°, Krasol® diol > Krasol® DA ≥ Krasol® BisAcAc. Advantageously, Krasol® DA and Krasol® BisAcAc exhibit comparable contact angle measurements and reveal consistency in wetting behavior with the EPDM substrate, ensuring homogeneous coating for Michael addition reaction mixtures.

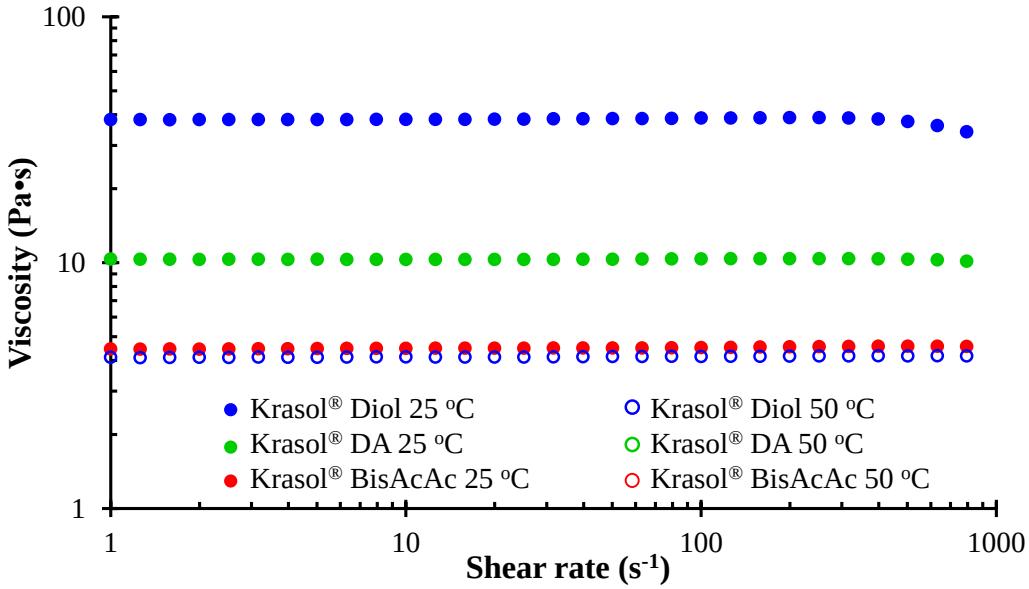

Figure 7.1. Shear viscosities for Krasol® oligomers, generated using shear sweeps at a constant 1 Hz frequency and constant temperature. Filled dots correspond to shear viscosity at 25 ºC and empty dots correspond to 50 ºC.

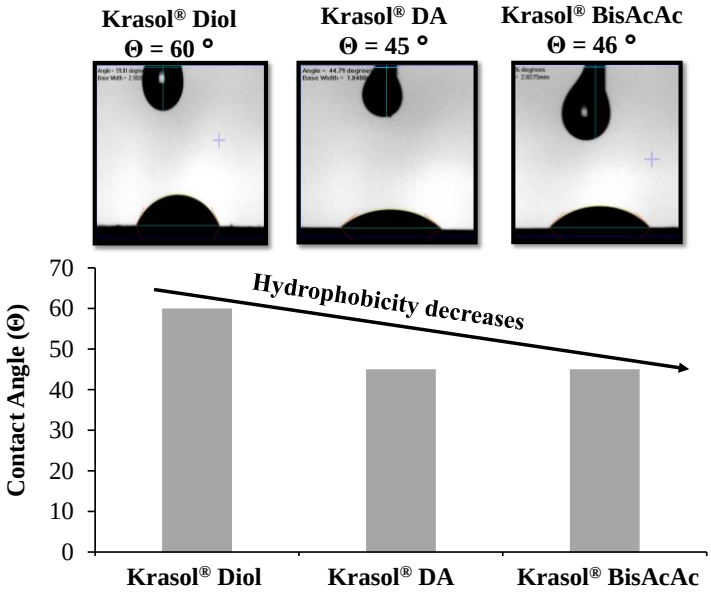

Figure 7.2. Contact angle measurements for Krasol® oligomers with variable end group functionality. Modifications from a diol to a diacrylate and bisacetoacetate influences the degree of wetting.

Mixing a 1.0:1.4 molar ratio of Krasol® BisAcAc, Michael donor to Krasol® diacrylate, Michael acceptor with catalytic DBU enables a 2-component reactive curing system and provides a crosslinked Michael network under ambient conditions. Scheme 7.2 depicts the reaction strategy. *In situ* FTIR spectroscopy monitored the Michael crosslinking reaction for kinetic analysis, tracking the C=C out-of-wag vinyl vibrational frequency for Krasol® diacrylate at 890 cm^{-1} and generating a normalized 2D waterfall plot for absorbance vs. time (sec) (Fig. 7.3). Vinyl concentration disappearance over time elucidated Michael addition, revealing a 1.5 h crosslinking reaction time for the Krasol® Michael donor and acceptor mixture. Fig. 7.5 depicts an extension of the spectral data into a pseudo-first order kinetic plot for diacrylate concentration (M/M_0) vs. time (sec) provided additional insight into the polymerization kinetics, revealing an agreeable observed rate constant, k_{obs}, for Krasol® diacrylate (2.1×10^{-3} s^{-1}) in comparison to previously reported Michael crosslinking reactions with poly(propylene glycol)-containing donors and acceptors (3.8×10^{-3} s^{-1}). The literature agreement confirmed suitable Michael addition polymerization conditions for synthesizing novel hydrogenated polybutadiene-containing Michael networks.

Scheme 7.2. Michael addition reaction for synthesis of Krasol® crosslinked Michael networks.

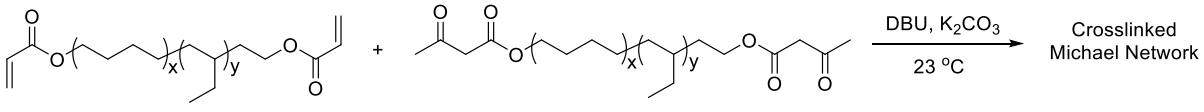

Compositional changes to the diacrylate acceptor strongly influences the crosslinking reaction time and kinetics (Scheme 7.3). *In situ* FTIR spectroscopy enabled kinetic studies with 1,4-butanediol diacrylate (1,4-BDA) (810 cm^{-1}) and trimethylolpropane triacrylate (TMPTA) (815

cm^{-1}) for comparison with the Krasol® diacrylate oligomer (Fig. 7.3 and 7.4). As expected, the small molecule 1,4-BDA and TMPTA drastically increased the crosslinking reaction times and k_{obs} values, with TMPTA exhibiting the fastest conditions (t = 5 mins, k_{obs} = 1.0 x 10^{-2} s^{-1}) due to its acrylic trifunctionality. Formulating mixtures of Michael acceptors also enables tunable reaction times and kinetics. For example, incorporating 5 mol% TMPTA into Krasol diacrylate increased the reaction time to 40 min and the k_{obs} value to 4.1 x 10^{-3} s^{-1}. Varying reaction kinetics as a function of Michael acceptor composition and formulation provided a facile method for broadening the operational windows for these novel Michael networks in roofing adhesives.

Scheme 7.3. Model reaction kinetic studies for Michael addition reactions as a function of Michael acceptor compositions: Krasol® DA, 1,4-BDA, and TMPTA.

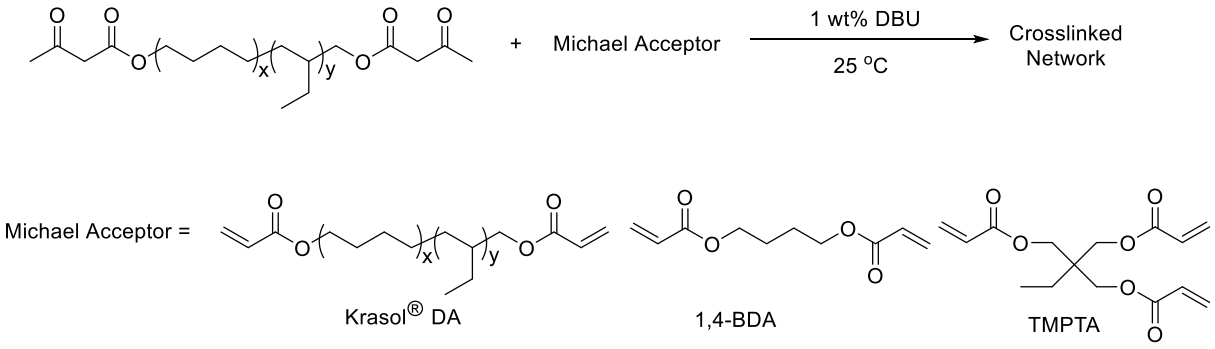

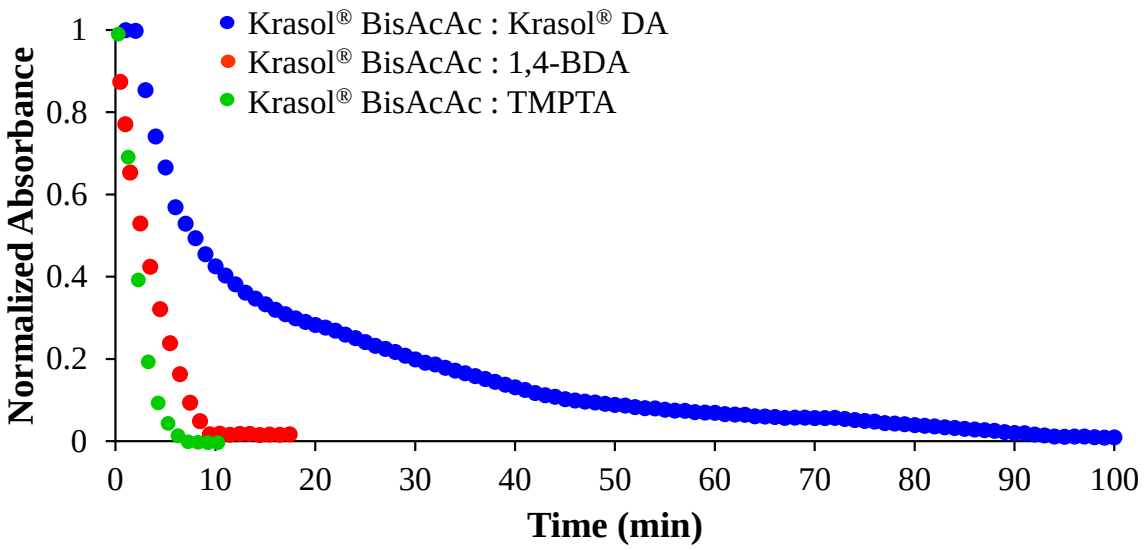

Figure 7.3. *In situ* FTIR spectroscopy monitors the Michael crosslinking reaction as a function of Michael acceptor compositions, tracking the C=C vinyl vibrational frequency peaks for each acceptor (Krasol® DA, 890 cm^{-1} ; 1,4-BDA, 0810 cm^{-1} ; and TMPTA, 815 cm^{-1}).

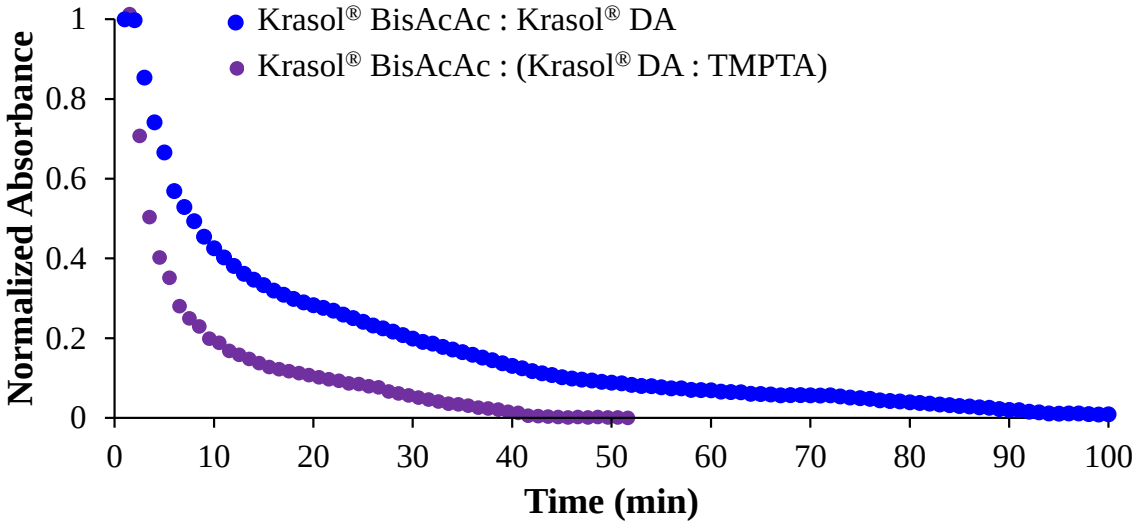

Figure 7.4. *In situ* FTIR spectroscopy monitors the Michael crosslinking reaction with 1.0:1.4 molar ratios of Krasol BisAcAc to Michael acceptor, where the Michael acceptor = Krasol DA

(Blue), or a 95:5 mol% ratio of Krasol DA: TMPTA (Purple). Tracking the C=C vinyl vibrational frequency peaks for Krasol® DA (890 cm^{-1}) generated the 2D waterfall plot.

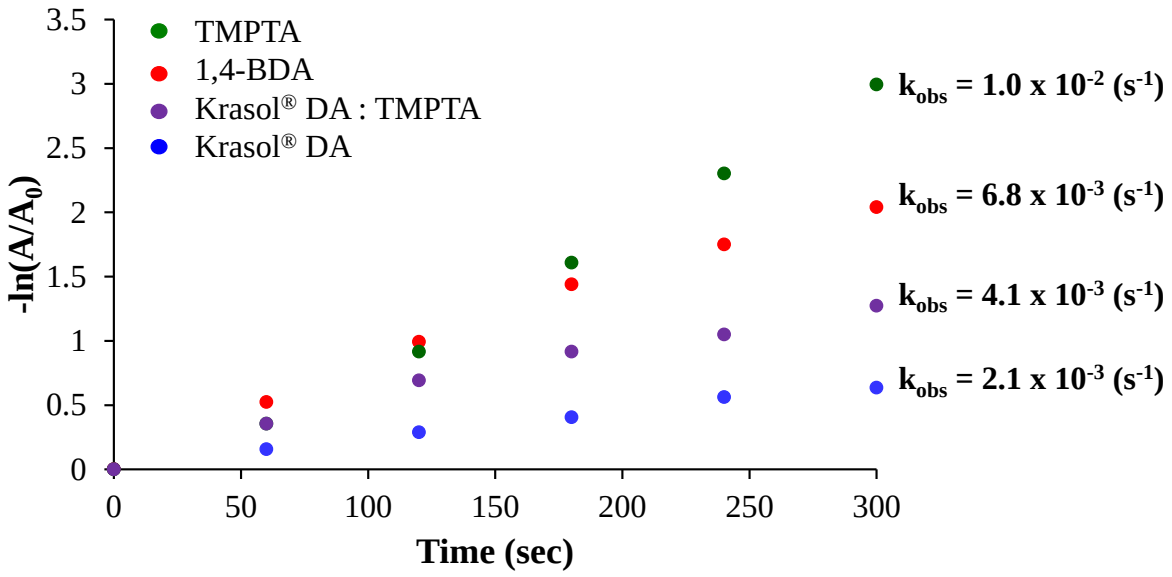

Figure 7.5. Pseudo-first-order kinetic analysis calculates the observed rates, k_{obs} (s^{-1}), of Michael crosslinking reactions as a function of Michael acceptor compositions.

Formulations with tackifiers also represent an important compositional effect on the Michael crosslinking reaction and kinetics. Scheme 7.4 reveals a modified synthetic strategy, accounting for a Krasol Michael network formation with the presence of 10 wt. % Indopole H-100 or Wingtack 10. Previous literature reports these commercially available tackifiers as common additives in thermoplastic elastomer blends and formulations, ideal for achieving enhanced viscoelastic properties required for tacky, adhesive applications.[25-28] For the case of this synthetic study, these low molecular weight oligomers with M_n values in the 500-900 g/mol range were selected as suitable tackifiers due to their comparable chemical and physical properties to the Krasol® Michael donors and acceptors.

Scheme 7.4. Model reaction kinetic studies for Michael addition reactions with the presence of 10 wt. % tackifier, Indopole H-100 or Wingtack 10.

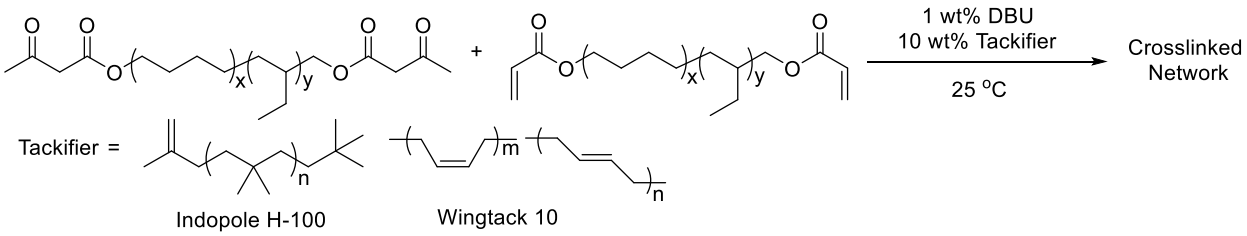

In situ FTIR spectroscopy elucidated the influence of the added tackifiers on Michael reaction kinetics, tracking the vinyl C=C vibrational frequency for the Krasol® diacrylate acceptor at 890 cm^{-1} and generating a normalized 2D waterfall plot for absorbance vs. time (sec) (Fig. 7.6). Pseudo-first-order kinetic analysis calculated k_{obs} values and elucidated the effect of incorporated tackifiers on the rates of crosslinking (Fig. 7.7). In comparison to the 90 min crosslinking reaction time for control Michael reaction and a k_{obs} = 2.1 x 10^{-3} s^{-1}, the addition of 10 wt. % tackifier afforded slightly increased reaction times and k_{obs} values. Michael networks containing Wingtack 10 afforded crosslinked compositions in 130 min with k_{obs} = 1.6 x 10^{-3} s^{-1}, and networks containing Indopole H-100 achieved complete crosslinking in 140 min with k_{obs} = 1.1 x 10^{-3} s^{-1}.

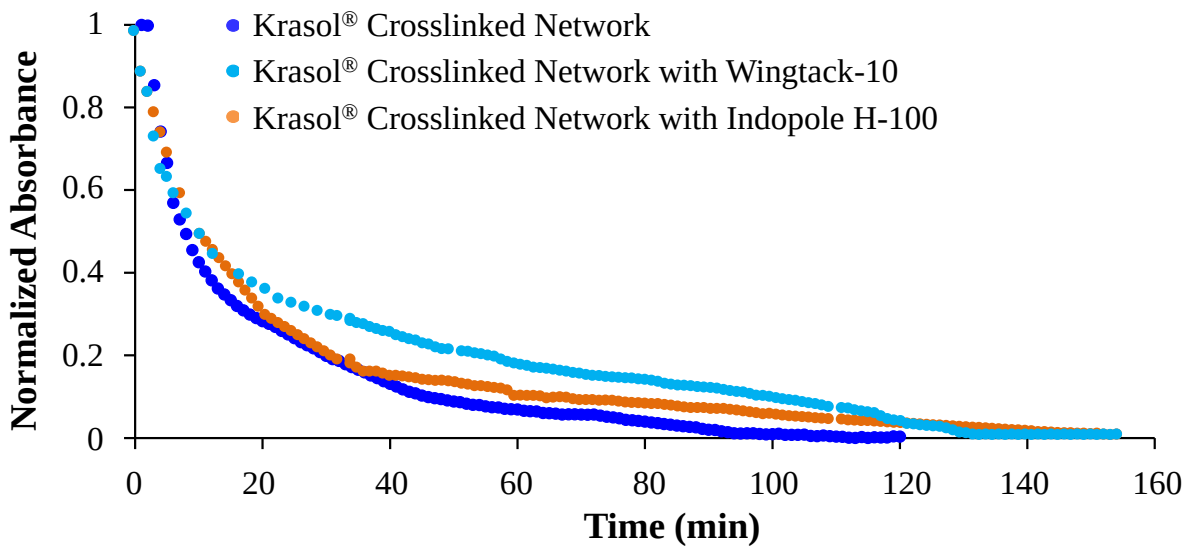

Figure 7.6. *In situ* FTIR spectroscopy monitors the Michael crosslinking with the presence of 10 wt. % tackifier, Indopole H-100 or Wingtack 10, tracking the C=C vinyl vibrational frequency peaks for Krasol® DA at 890 cm^{-1}.

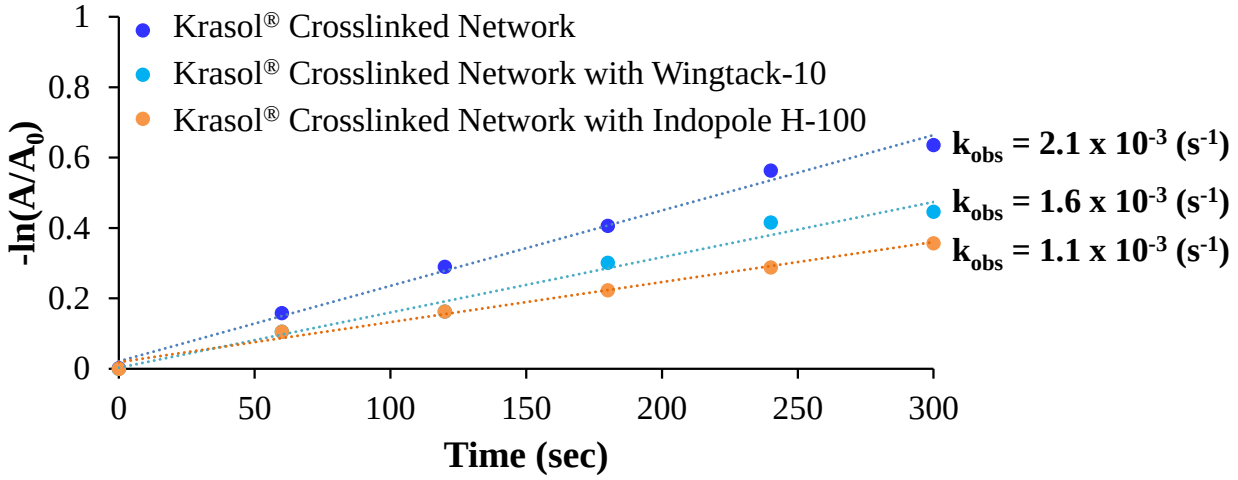

Figure 7.7. Pseudo-first-order kinetic analysis calculates the observed rates, k_{obs} (s^{-1}), of Michael crosslinking reactions with the presence of 10 wt. % tackifier, Indopole H-100 or Wingtack 10.

Rheological analysis elucidated crosslinking reaction kinetics, revealing the effects of catalyst concentration, temperature, and acceptor composition, and tackifier concentration on gelation time and storage modulus (G'). A steady-strain oscillation experiment monitored the storage and loss moduli (G', G") as the viscous, 2-component curing systems achieved crosslinked networks. The G' and G" crossover point represented the viscoelastic transition point, known as the gel point, and occurred at various times as a function of the tested variables (Fig. 7.8). In the case of catalyst concentration (Scheme 7.5)), increasing DBU concentration from 1 wt. %, 2 wt. %, and 3 wt. % afforded faster gelation in tunable time frames of 80 min, 60 min, and 15 min (Figure 1A). Figure 1B is a representative rheological plot, revealing crosslinking behavior, G' and G" (Pa) vs. time, as a function of 2 wt. % DBU and depicts the gel point at approximately 60 min and a final crosslinked modulus slightly above the Dahlquist criterion for free-standing films (1 x 10^5 Pa). Exhibiting G' near the Dahlquist enables a combination of mechanical and adhesive properties for the Krasol® Michael networks.

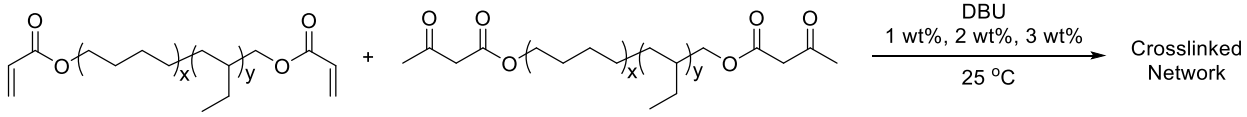

Scheme 7.5. Michael addition curing reaction of Krasol® diacrylate and bisacetoacetate as a function of DBU concentration.

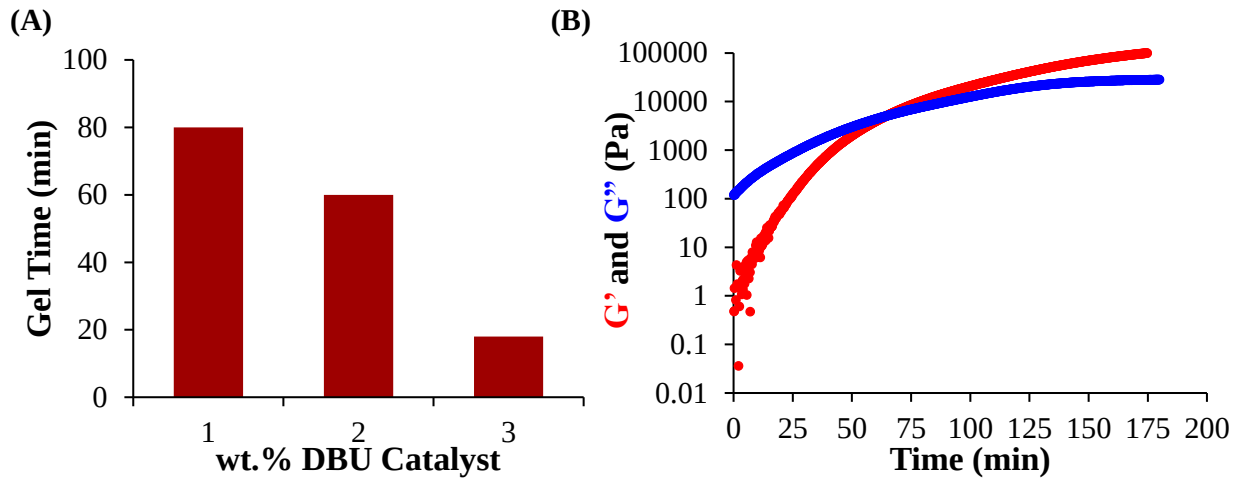

Figure 7.8. Rheological characterization of Michael network formation as function of wt. % DBU catalyst. (A) Graphical summary of gel time (min) vs. wt. % DBU. (B) Representative rheological plot of G' and G" (Pa) vs. Time (min) for network crosslinking with 2 wt. % DBU.

Rheology studies demonstrated crosslinking efficiency for Michael adhesives at temperatures ranging from -10 ^{o}C to 25 ^{o}C and 50 ^{o}C (Scheme 7.6). Steady-strain oscillation studies at these temperatures, with a constant catalyst concentration of 1 wt. % DBU, demonstrated Michael network formation and determined precise gel points (Fig. 7.9). Crosslinking behavior occurred the slowest at -10 ^{o}C, presumably corresponding to increased oligomeric chain rigidity and decreased intermolecular motion. Increasing the temperature to ambient conditions increased chain mobility and enabled crosslinking to occur within 80 min. The fastest crosslinking time (20 min) occurred at 50 ^{o}C, where intermolecular motion approached fluidic behavior and the addition reaction was kinetically favored.

Scheme 7.6. Michael addition curing reaction as a function of temperature.

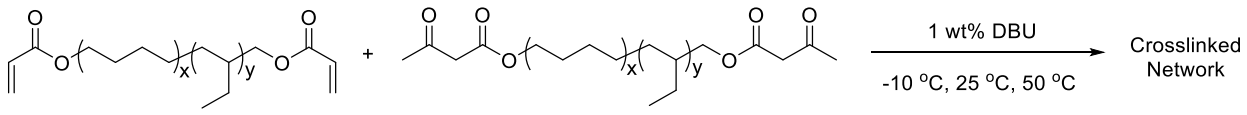

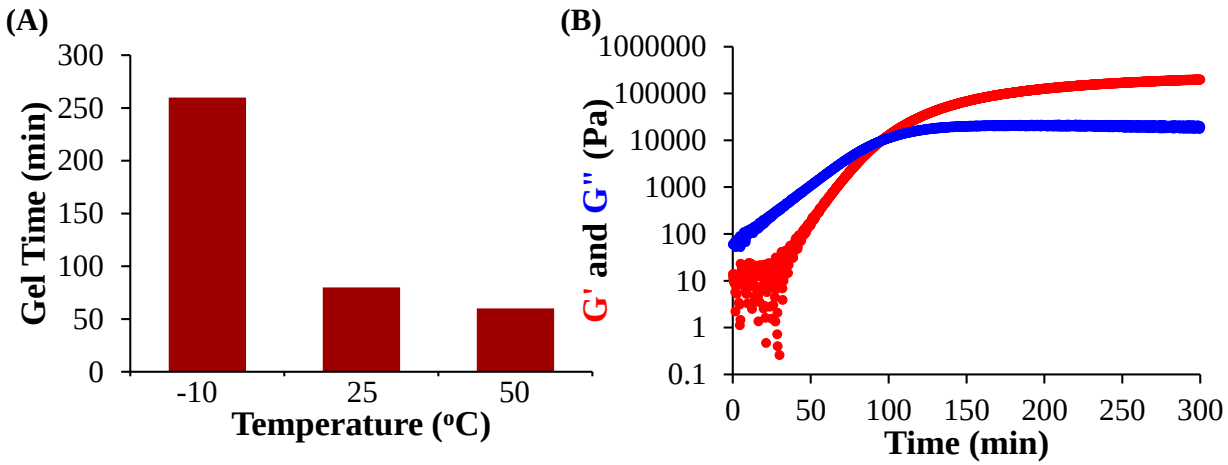

Figure 7.9 Rheological characterization of Michael network formation as function of temperature. (A) Graphical summary of gel time (min) vs. temperature (°C). (B) Representative rheological plot of G' and G" (Pa) vs. Time (min) for network crosslinking with 1 wt. % DBU at 25 °C.

Steady-strain oscillation experiments provided complimentary results to previous *in situ* FTIR spectroscopy studies, particularly in demonstrating the effect of compositional changes to the diacrylate acceptor and the addition of tackifiers on crosslinking kinetics (Scheme 7.3). Rheology probed Michael crosslinking reactions with 1,4-BDA, TMPTA, 95:5 molar ratio mixture of Krasol DA: TMPTA, revealing gel times in the increasing order: TMPTA < 1,4-BDA < Krasol DA: TMPTA < Krasol DA (Fig. 7.10). This trend agreed with the previous results from *in situ* FTIR spectroscopy. However, the steady-strain oscillation studies also provided insight into mechanical properties for the crosslinked films, revealing G' values near the Dahlquist criterion for networks formed with Krasol DA acceptors (1 x 10^5 Pa) and G' values above the Dahlquist criterion for networks formed with the small molecule acceptors, 1,4-BDA and TMPTA (1 x 10^6 Pa). As expected, 1,4-BDA and TMPTA enabled tighter crosslinked densities and afforded mechanically reinforced Michael networks.

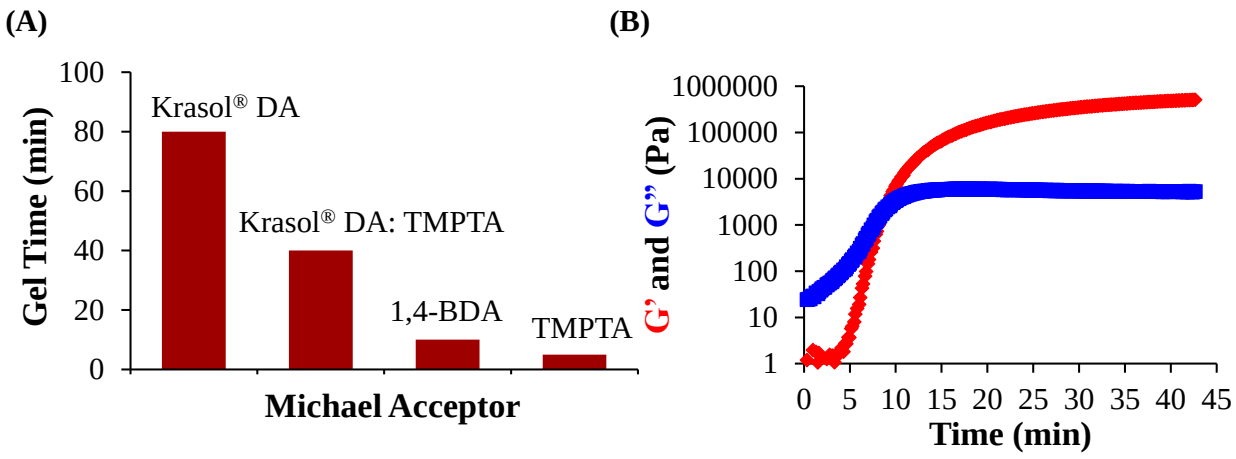

Figure 7.10. Rheological characterization of Michael network formation as function of Michael acceptor compositions: Krasol® DA, 1,4-BDA, and TMPTA. (A) Graphical summary of gel time (min) vs. temperature (°C). (B) Representative rheological plot of G' and G" (Pa) vs. Time (min) for crosslinking 1,4-BDA with 1 wt. % DBU at 25 °C.

Crosslinking reactions with 1,4-butanediol diacrylate were conducted at various temperatures for additional comparative studies with Krasol DA (Scheme 7.7 and Fig. 7.11). 1,4-BDA drastically reduced the gel times in comparison to the control Krasol networks at 25 °C and 50 °C, revealing gel times of 20 min and 10 min. At ambient and high temperature, 1,4-BDA enables kinetically favored crosslinking reactions and affords mechanically reinforced networks over the conventional Krasol DA mixture. Cooling the temperature to -10 °C, however, affords drastically increased gel times for both networks, requiring 300 min for both crosslinking reactions to complete. At low temperatures, the decreased intermolecular motion of the Krasol bisAcAc governs the crosslinking reaction and renders the Michael acceptor selection arbitrary.

Scheme 7.7. Michael addition curing reaction of 2-components involving 2000 g/mol Krasol® bisacetoacetate and the commercially available 1,4-butanediol diacrylate as function of temperature (°C).

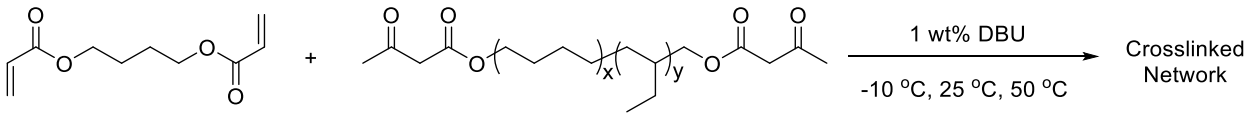

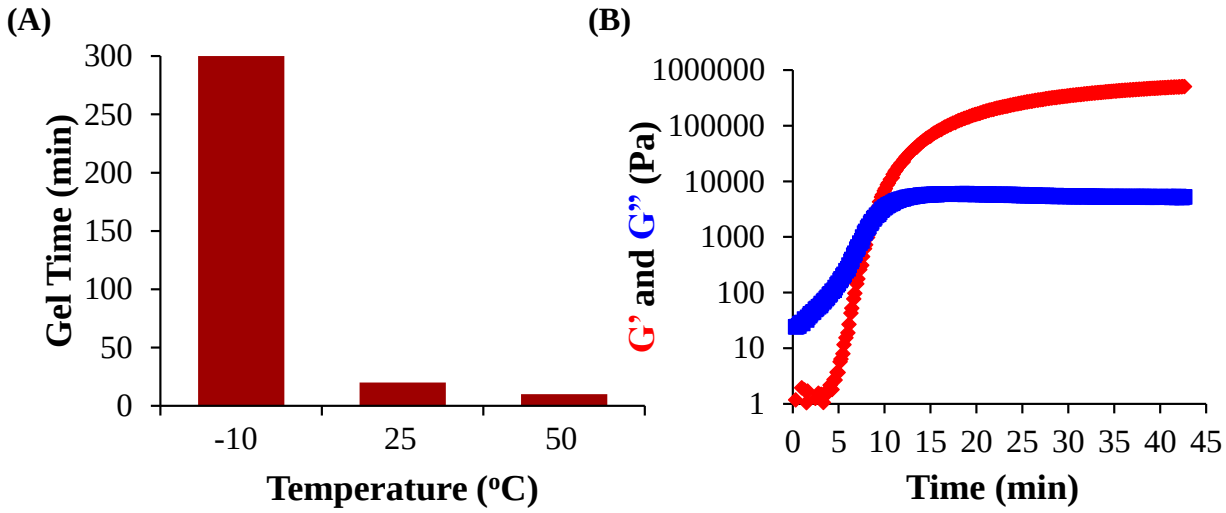

Figure 7.11. Rheological characterization of acetoacetate curing systems involving Krasol® bisAcAc and 1,4-BDA with variable temperature (°C). (A) Graphical summary of gel time (min) vs. temperature (°C). (B) Representative rheological plot of G' and G" (Pa) vs. Temperature (°C) for network crosslinking with 1 wt. % DBU at 50 °C.

Incorporating tackifier into the crosslinked Krasol® network resulted in increased gel times in the order of Krasol® crosslinked network < Krasol® crosslinked network with Wingtack 10 < Krasol® crosslinked network with Indopole H-100 (Fig. 7.12). This trend also agreed with the previous results from *in situ* FTIR spectroscopy. Steady-strain oscillation studies also revealed the mechanical properties for these crosslinked films, showing depressed G' values well below the

Dahlquist criterion by an order of magnitude (1 x 10^4 Pa). As expected, Wingtack 10 and Indopole H-100 tackifiers enabled plasticized crosslinked polymer matrices and afforded mechanical deformation for enhanced adhesive properties.

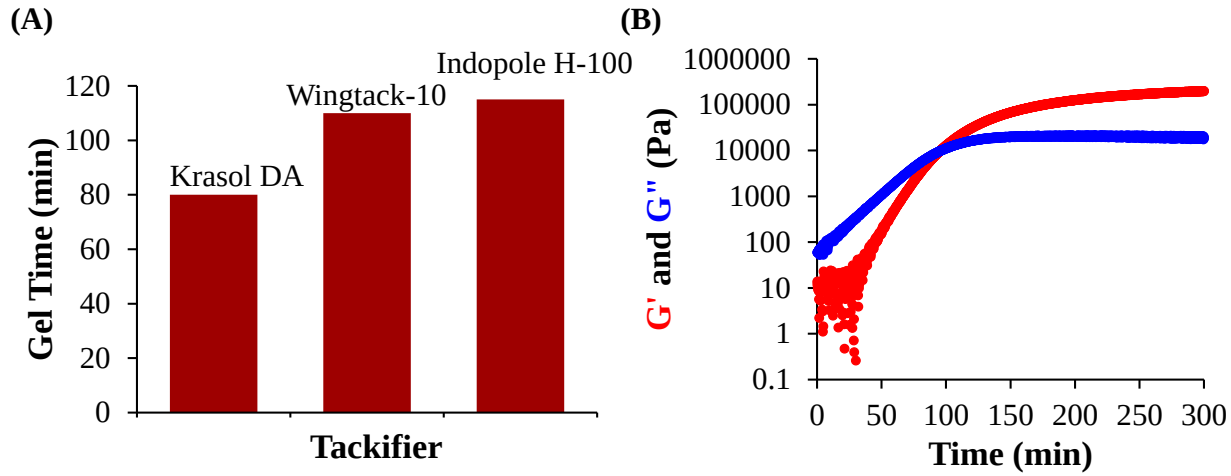

Figure 7.12. Rheological characterization of Krasol® network formation as with the presence of 10 wt. % tackifier, Indopole H-100 or Wingtack 10. (A) Graphical summary of gel time (min) vs. temperature (ºC). (B) Representative rheological plot of G' and G" (Pa) vs. Time (min) for crosslinking 1,4-BDA with 1 wt. % DBU at 25 ºC.

180º Peel tests investigated adhesion strength and failure modes for cured membrane samples including EPDM to EPDM, PVC to PVC, and TPO to TPO substrates (Fig. 7.13). These studies provided insight into adhesive compatibility with the various roofing membranes, and provided peel strength data in comparison to conventional commercial bonding adhesives. Michael adhesives involving Krasol® bisAcAc served as a universal curing system for the three different roofing membranes, revealing comparable peel strength to the highest performing, solvent-based

commercial adhesives and improved strength in comparison to low VOC adhesives. Incorporating 10 wt. % tackifiers into the crosslinking Michael network revealed enhanced peel strengths for EPDM, PVC, and TPO bonding substrates and revealed formulation opportunities to achieve tunable and predictable peel strength properties (Fig. 7.14). Table 7.1 reports average peel loads (N, and lbs.) and failure modes for all roofing samples with Michael adhesives along with suitable adhesive controls. Advantageously, all Michael adhesive samples revealed cohesive failure and suggested adhesive dependence on strength of the crosslinked networks.

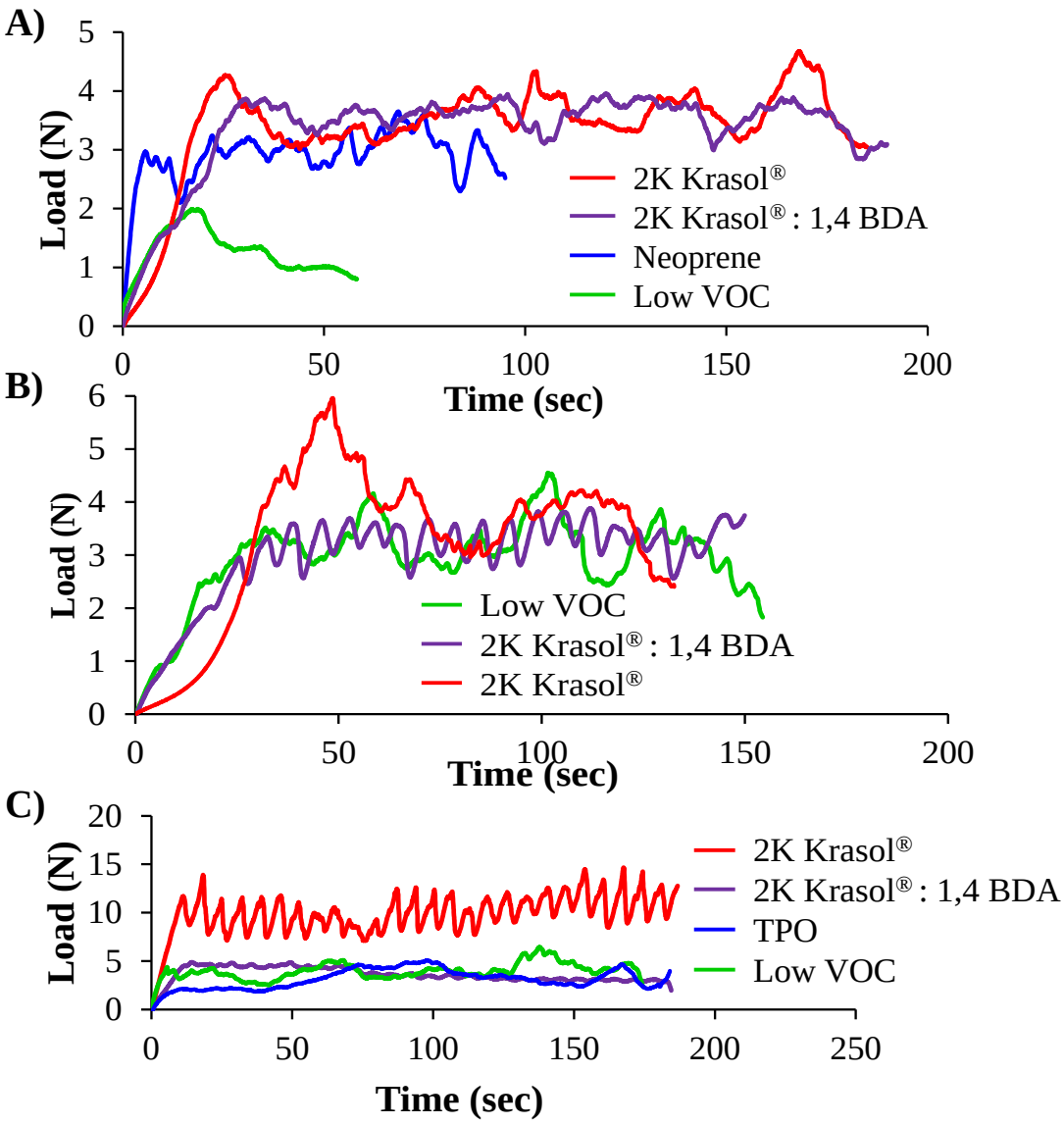

Figure 7.13. Instron 180 peel tests of acetoacetate curing systems involving 2000 g/mol Krasol® bisacetoacetate and diacrylate (2K Krasol®), 2000 g/mol Krasol® bisacetoacetate and the commercially available 1,4-butanediol diacrylate (2K Krasol®: 1,4 BDA), Neoprene and TPO based bonding adhesives, and Low VOC bonding adhesives. Representative plots of average data of 3 adhered roofing samples: (A) EPDM to EPDM, (B) PVC to PVC, and (C) TPO to TPO.

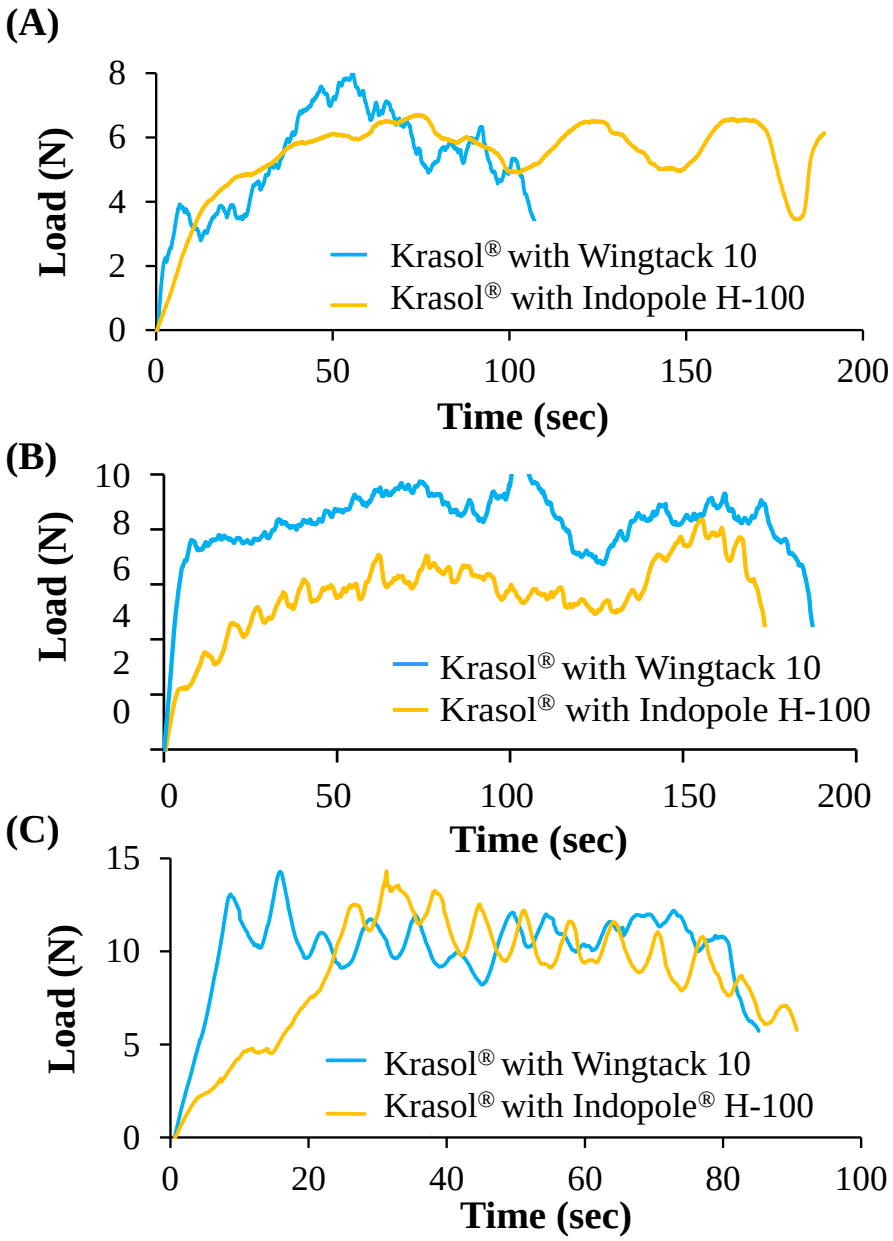

Figure 7.14. Instron 180^{o} peel tests of acetoacetate curing systems involving 2000 g/mol Krasol® bisacetoacetate and diacrylate (2K Krasol®) with 10 wt. % incorporated tackifiers wingtack-10 or indopole h-100. Representative plots of average data of 3 adhered roofing samples: (A) EPDM to EPDM, (B) PVC to PVC, and (C) TPO to TPO.

Table 7.1. Instron 180^{o} peel tests results

Substrate/adhesives	Failure Mode	Average Load (N)	Average Load (lbs.)
EPDM/ Krasol®	**Cohesive**	**4.0**	**0.9**
EPDM/ Krasol®: 1,4 BDA	**Cohesive**	**4.0**	**0.9**
EPDM/ Krasol®: Wingtack 10	**Cohesive**	**6.0**	**1.3**
EPDM/ Krasol®: Indopole H-100	**Cohesive**	**6.0**	**1.3**
EPDM/Neoprene	**Cohesive**	**3.5**	**0.8**
EPDM/Low VOC	**Adhesive**	**1.5**	**0.3**
PVC/ Krasol®	**Cohesive**	**4.0**	**0.9**
PVC/ Krasol®: 1,4 BDA	**Cohesive**	**3.5**	**0.8**
PVC/ Krasol®: Wingtack 10	**Cohesive**	**8.0**	**1.8**
PVC/ Krasol®: Indopole H-100	**Cohesive**	**6.0**	**1.3**
PVC/Low VOC	**Cohesive**	**3.5**	**0.8**
TPO/ Krasol®	**Cohesive**	**10.0**	**2.3**
TPO/ Krasol®: 1,4 BDA	**Cohesive**	**5.0**	**1.1**
TPO/ Krasol®: Wingtack 10	**Cohesive**	**12.0**	**2.7**
TPO/ Krasol®: Indopole H-100	**Cohesive**	**12.0**	**2.7**
TPO/TPO adhesive	**Cohesive**	**4.5**	**1.0**
TPO/Low VOC	**Cohesive**	**5.0**	**1.1**

7.5 *Conclusions*

Michael adhesives represent a green alternative to solvent-based roofing adhesives, and provides various reaction mixtures, with tunable catalyst concentration, temperature, acceptor composition, and tackifier additives. Encompassing the various chemistries listed previously, this technology is intended to market a catalog of adhesive compositions tunable for roofing membrane substrates. This study highlights Krasol® based Michael networks as proof-of-concept adhesives, and promotes this technology for its universal adhesive performance with EPDM, PVC, and TPO roofing substrates. Rheological studies elucidated effects of catalyst concentration, temperature, M_n, donor/acceptor compositions on gelation times, revealing tunable gel times in a 10-300 min time range. 180^{o} peel tests revealed crosslinked Michael networks as high performing adhesives for binding roofing substrates, exhibiting comparable peel strengths to traditional solvent-based

adhesives and improved strengths to Low VOC adhesives. Future studies will involve 90° peel tests with construction materials ranging from wood to polyurethane foam platforms. Research will also explore other proposed compositions (catalyst or catalyst-free) as proof-of-concept curing systems and a Michael adhesive catalog will develop.

7.6 *References*

(1) Kim, Y. B.; Kim, H. K.; Nishida, H.; Endo, T. *Macromolecular Materials and Engineering* **2004**, *289*, 923.

(2) Mather, B. D.; Miller, K. M.; Long, T. E. *Macromolecular Chemistry and Physics* **2006**, *207*, 1324.

(3) Mather, B. D.; Viswanathan, K.; Miller, K. M.; Long, T. E. *Progress in Polymer Science* **2006**, *31*, 487.

(4) Nair, D. P.; Podgórski, M.; Chatani, S.; Gong, T.; Xi, W.; Fenoli, C. R.; Bowman, C. N. *Chemistry of Materials* **2013**, *26*, 724.

(5) Rizzi, S. C.; Hubbell, J. A. *Biomacromolecules* **2005**, *6*, 1226.

(6) Rydholm, A. E.; Bowman, C. N.; Anseth, K. S. *Biomaterials* **2005**, *26*, 4495.

(7) Yamauchi, K.; Lizotte, J. R.; Long, T. E. *Macromolecules* **2002**, *35*, 8745.

(8) Richardson, S. C.; Pattrick, N. G.; Stella Man, Y.; Ferruti, P.; Duncan, R. *Biomacromolecules* **2001**, *2*, 1023.

(9) Chen, W.; Yang, H.; Wang, R.; Cheng, R.; Meng, F.; Wei, W.; Zhong, Z. *Macromolecules* **2009**, *43*, 201.

(10) Clemens, R. J.; Del Rector, F. *JCT, Journal of coatings technology* **1989**, *61*, 83.

(11) Pavlinec, J.; Moszner, N. *Journal of applied polymer science* **1997**, *65*, 165.

(12) Liu, Y.; Li, K. *International Journal of Adhesion and Adhesives* **2007**, *27*, 59.

(13) Kamimura, A.; Murakami, N.; Kawahara, F.; Yokota, K.; Omata, Y.; Matsuura, K.; Oishi, Y.; Morita, R.; Mitsudera, H.; Suzukawa, H. *Tetrahedron* **2003**, *59*, 9537.

(14) Firouzabadi, H.; Iranpoor, N.; Jafari, A. *Advanced Synthesis & Catalysis* **2005**, *347*, 655.

(15) Ferruti, P.; Marchisio, M. A.; Duncan, R. *Macromolecular Rapid Communications* **2002**, *23*, 332.

(16) Klee, J. E.; Neidhart, F.; Flammersheim, H. J.; Mülhaupt, R. *Macromolecular Chemistry and Physics* **1999**, *200*, 517.
(17) Yamamoto, K.; Higuchi, M.; Takai, H.; Nishiumi, T. *Organic letters* **2001**, *3*, 131.
(18) Cellesi, F.; Tirelli, N.; Hubbell, J. A. *Biomaterials* **2004**, *25*, 5115.
(19) Gimbert, C.; Lumbierres, M.; Marchi, C.; Moreno-Mañas, M.; Sebastián, R. M.; Vallribera, A. *Tetrahedron* **2005**, *61*, 8598.
(20) Bickel, C. L. *Journal of the American Chemical Society* **1950**, *72*, 1022.
(21) Williams, S. R.; Miller, K. M.; Long, T. E. *Prog. React. Kinet. Mech.* **2007**, *32*, 165.
(22) Ebnesajjad, S. *Handbook of adhesives and surface preparation: technology, applications and manufacturing*; William Andrew, 2010.
(23) Zysman, B.; Skelly, P. D. *Metal Finishing* **2000**, *98*, 84.
(24) Porter, M. E.; Van der Linde, C. *The journal of economic perspectives* **1995**, *9*, 97.
(25) Ardemagni, L. A.; Google Patents: 1978.
(26) Puskas, I.; Banas, E. M.; Nerheim, A. G. In *Journal of polymer science: Polymer symposia*; Wiley Online Library: 1976; Vol. 56, p 191.
(27) Marin, G.; Derail, C. *The Journal of Adhesion* **2006**, *82*, 469.
(28) EWINS JR, E.; DAVIES, G. *Handbook of Adhesives* **2012**, 239.

Chapter 8: Suggested Work

8.1 *Phosphonium-containing polyurethanes for mask projection microstereolithography*

Future directions in 3D printing phosphonium-containing ionic liquids may extend to photocurable polyurethanes, enabling future 3D structures with complex hierarchical polymeric architectures for tailored mechanical and ion-transport properties. Photo-curable polymers account for approximately 50% of all 3D printing materials sale, yet remain limited to commercially available compositions that closely resemble tough, stiff materials such as acrylonitrile butadiene styrene (ABS) and polypropylene.[1] Polyurethanes receive continued interest due to their well-defined segmented block compositions and tailored mechanical properties, suitable for diverse applications ranging from coatings[2], adhesives[3], medicine[42], biomedical and bioengineering applications[4,5], and electronic devices[6]. Implementing crosslinks within polyurethane compositions affords mechanical reinforcement, improved thermal stabilities, abrasion resistance, as well as acid and solvent resistance. Previous literature reveals photo-curable polyurethanes as promising compositions for the 3D printing market, and reports precedence for photo-curing linear, sulfonated polyurethane precursors with acrylic-functionality (hydroxyl ethyl acrylate, HEA, or 2-hydroxyl ethyl methacrylate HEMA).[7,8] These earlier efforts describe photo-polymerization as an efficient strategy for achieving crosslinked polyurethane networks with low energy, and solvent-free requirements. Concerns for thermal and charge stability due to low temperature degradation reactions poses an architectural design flaw, and enables future directions for phosphonium-containing polyurethanes.

Scheme 8.1.1 reveals a transesterification method to incorporate phosphonium functionality within the soft segment of urethane diacrylates. This reaction yields a phosphonium-

containing PTMO diol, which can react with HDMI and HEA in a 2-step process for achieving photo-curable urethanes for 3D printing (Scheme 8.1.2). Varying the concentration of hard and soft components will enable a series of phosphonium-containing photo-curable urethanes for 3D printed crosslinked networks with tunable mechanical properties. Thermal gravimetric analysis, dynamic mechanical analysis, and tensile studies will elucidate the compositional effects on thermal stability and mechanical performance. Salt permeability studies can also probe the influence of the phosphonium charge on ion-transport properties. Precedential neutral and sulfonated polyurethane compositions can serve as control analogues for comparison.

Scheme 8.1.1. Proposed transesterification reaction between dimethyl 5-benzyl trioctylphosphonium bis(trifluoromethane) sulfonamide salt and PTMO.

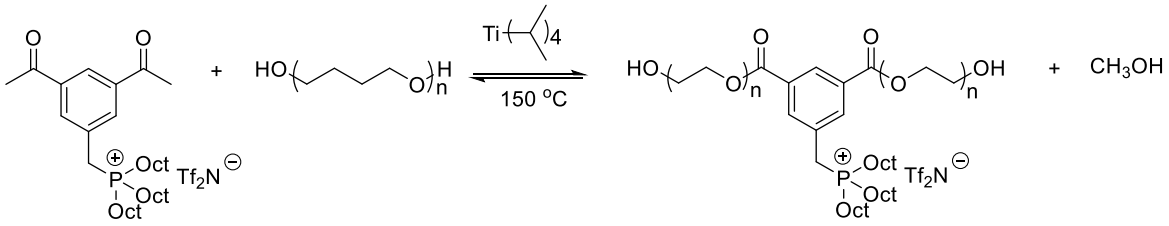

Scheme 8.1.2. Two-step synthesis of PTMO-based urethane diacrylates

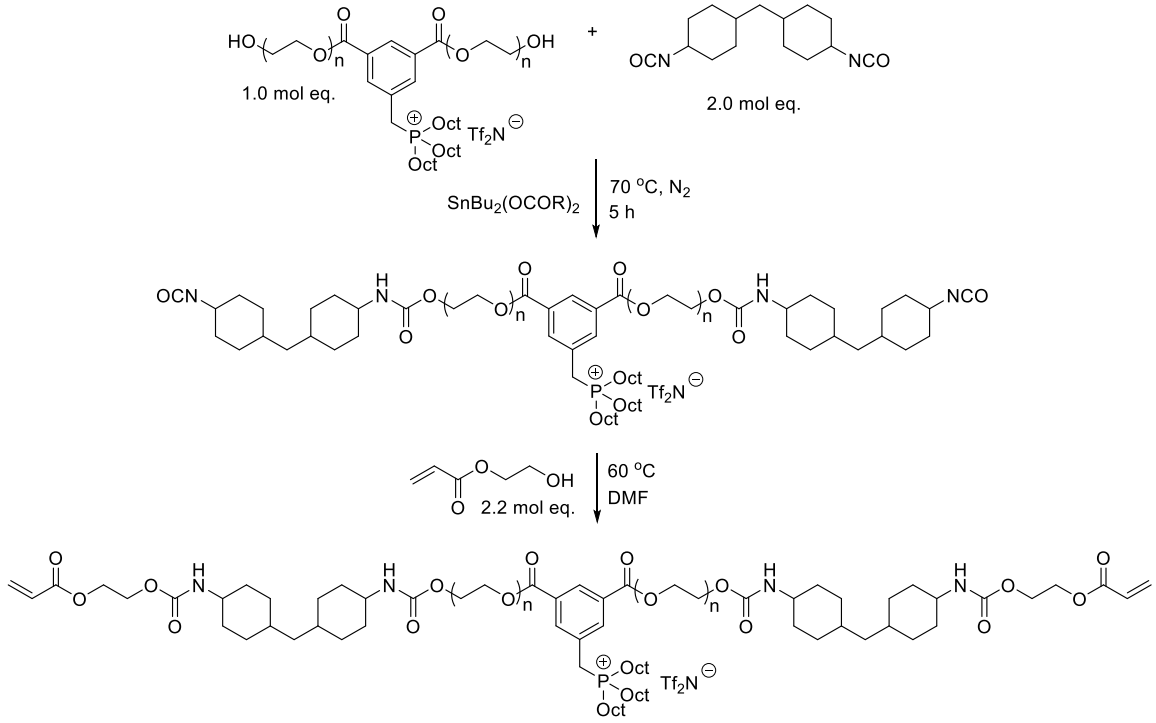

8.2 *Phosphonium-containing diblocks for 3D printing with thiol-ene "click" chemistry*

Future endeavors in 3D printing may also focus on alternative photopolymerization mechanisms aside from typical free radical photoinitiation in order to achieve photo-crosslinked, phosphonium- containing thermosets. Earlier literature describes a thiol-ene "click" chemistry approach for photocrosslinking SBS rubber, enabling photoinduced addtition of a thiol onto the olefinic double bond for rapid crosslinking of the vinyl-functionalized polymers.[9] The chain reaction proceeds by a step growth addition mechanism which is propagated by a chain transfer reaction involving thiol radicals. Alkyl radicals are also capable of abstracting hydrogen atoms from the thiol, attributing to the decreased sensitivity to air inhibition for uv-curable thiol-ene reactions in comparison to conventional radical-induced polymerization. Previous precedence for

the effiency of photo-clicking SBS rubber compositions inspires future potential for uv-curing and 3D printing phosphonium-containing styrenic rubbers (Scheme 8.2.1).

Scheme 8.2.1. Thiol-ene "click" chemistry affords efficient uv-curing of polyolefins.

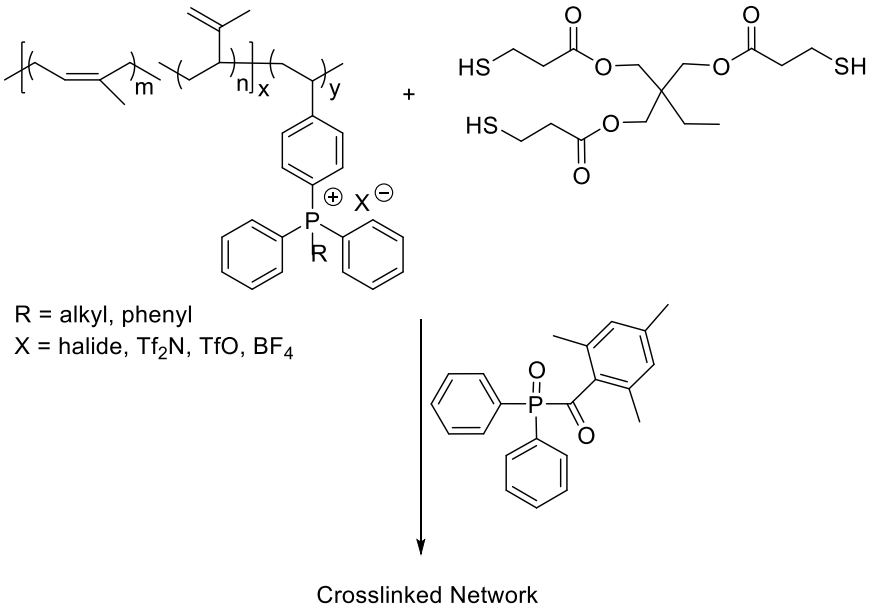

8.3 *Phosphonium-containing ABC triblock copolymers for ion-transport studies*

The versatile applications for ion-containing block copolymers continues to stimulate new synthetic opportunities for achieving well-defined compositions with tunable morphologies, mechanical performance, and ion conductivity for emerging electro-active applications ranging from high performance energy devices to water purification membranes. In previous chapters, we described the synthesis of phosphorus-containing AB and ABC block copolymers with tailored chemical compositions, high degrees of phase separation, and high degrees of alkylation for incorporating charge. Extending this research further with alkylated ABC triblock copolymers will enable unprecedented phosphonium-containing thermoplastic elastomers with tunable mechanical performance and ion-transport properties (Scheme 8.3.1). As sulfonated styrenic block copolymers

receive continued attention as ion-containing compositions, there remains an opportunity to explore these unprecedented phosphonium-containing styrenic block copolymers for enabling complementary, cation-containing polymer derivatives.

Scheme 8.3.1. Alkylating phosphorus-containing ABC triblock copolymers enable cation-containing styrenic block copolymers to complement sulfonated analogues.

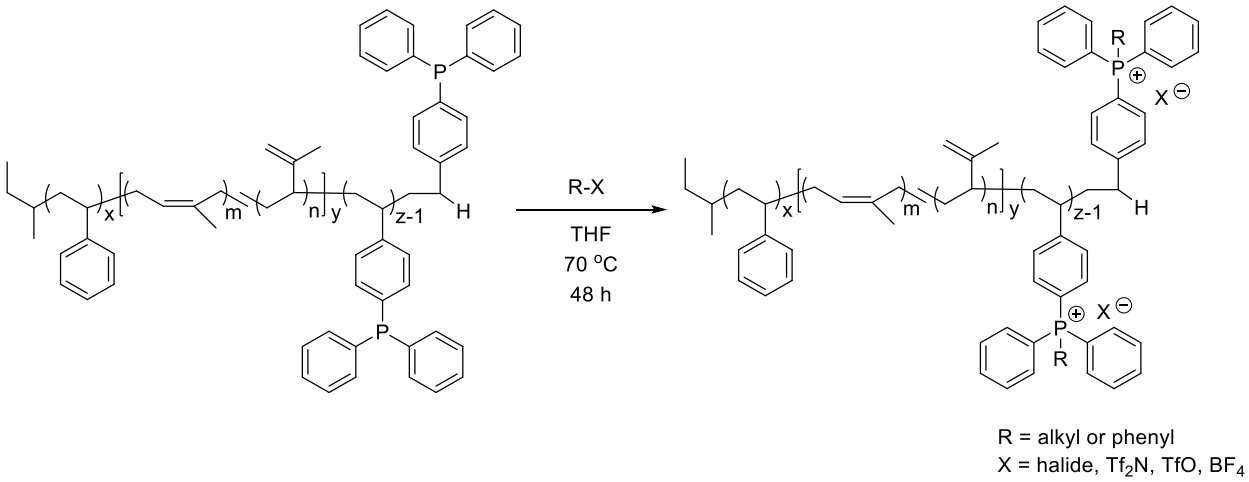

8.4. *Living anionic polymerization with a piperazine-containing dilithium initiator achieves liquid polyisoprene diols*

Liquid polyisoprenes (PIs), which typically range from 1000 to 10000 g/mol, are versatile oligomers that receive continued attention for their industrial significance in adhesives and coatings.[10,11] Low bulk and solution viscosity and high levels of unsaturation enables subsequent chemical modifications and fosters diverse applications for liquid PIs.[10,11] Earlier literature describes anionic, coordination, cationic or free radical polymerization strategies for synthesizing liquid PIs.[10] Among these various methods, anionic polymerization provides the most efficient route for achieving controlled molecular weights and well-defined microstructures. The use of an organolithium diinitiator enables post-polymerization reactions involving electrophilic agents,

providing liquid PIs with chain end difunctionality. The unprecedented piperazine-containing diinitiator highlighted in chapter 7 serves as an ideal candidate for producing difunctional liquid PIs.

Scheme 8.4.1 re-introduces the synthetic strategy for producing 1,4-bis[4-(1-phenylethenyl)benzyl] piperazine, involving a nucleophilic substitution reaction with 4-(1-phenylethenyl)benzyl bromide and piperazine. Once the diinitiator is charged with *sec*BuLi, the piperazine component serves as a polar additive to facilitate electrostatic dispersion in nonpolar solvents. This enables a homogeneous anionic polymerization of isoprene and subsequent termination with ethylene oxide to quantitatively produce liquid PI diols with tunable M_n and viscosity (**Scheme 8.4.2**). Finally, hydrogenation with a nickel (II) octanoate/ triethyl aluminum suspension catalyst will enhance the thermal and oxidative stability of the custom-designed liquid PI diols (**Scheme 8.4.2**). Achieving well-defined liquid PI diols will facilitate future synthetic strategies involving Michael crosslinking chemistry, photo-chemistry and 3D printing, and step-growth polymerization.

Scheme 8.4.1. Synthetic method for producing and initiating 1,4-bis[4-(1-phenylethenyl)benzyl] piperazine.

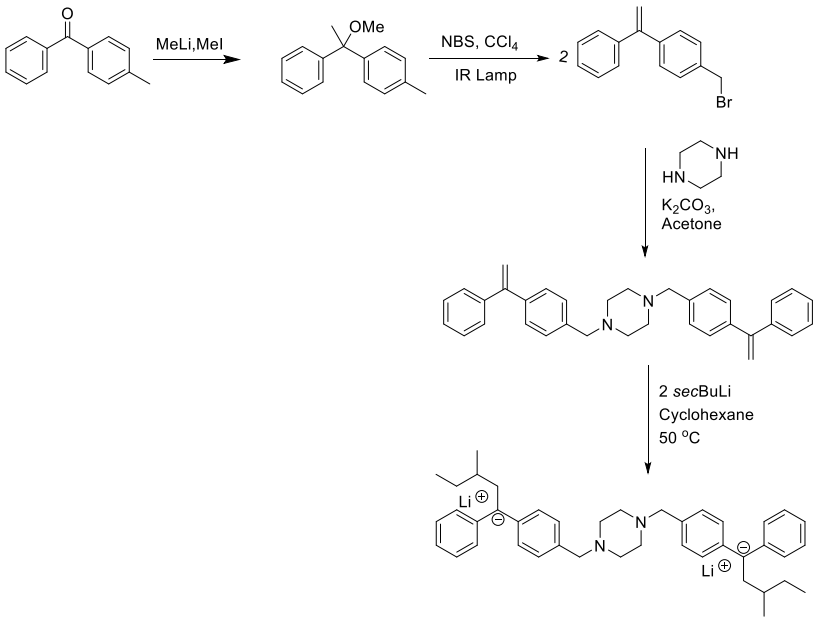

Scheme 8.4.2. Synthetic route for achieving hydrogenated polyisoprene diols.

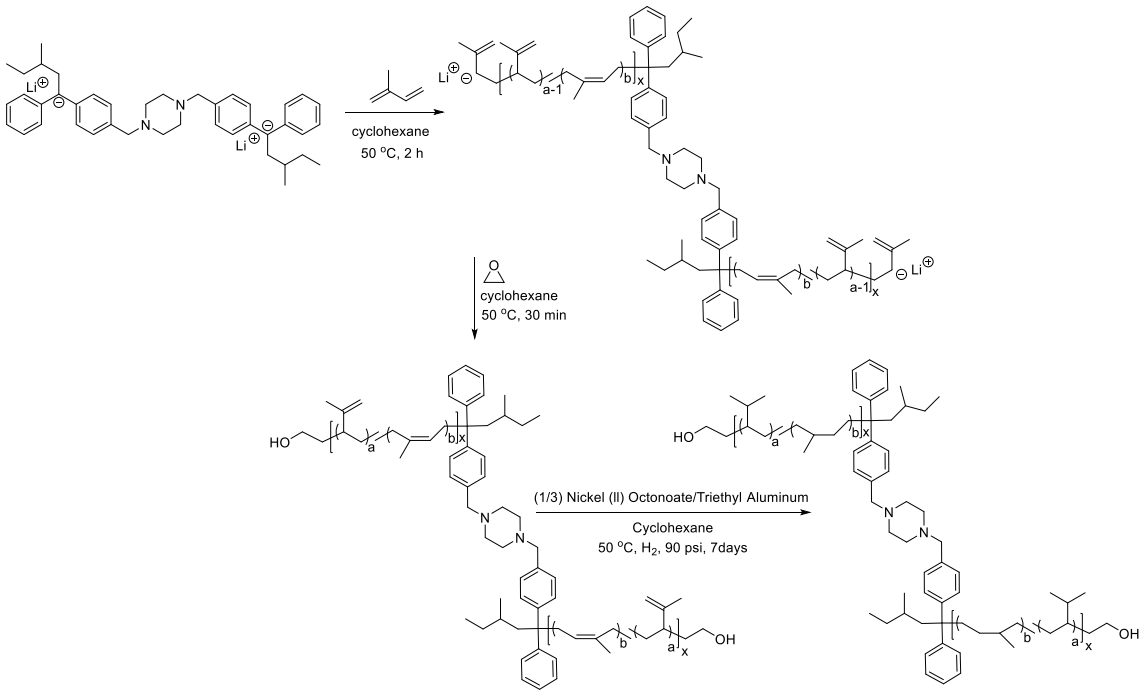

8.5. *Living anionic polymerization with a piperazine-containing dilithium initiator achieves phosphorus-containing ABA triblock copolymers*

Future research may also employ the 1,4-bis[4-(1-phenylethenyl)benzyl] piperazine dilithium initiator for the synthesis of phosphorus-containing ABA triblock copolymers. Living anionic polymerization strategies involving the sequential addition of DPPS remain limited to ABC-type compositions due to the insolubility of poly(DPPS) in the nonpolar, hydrocarbon solvent. Moreover, the addition of polar solvents or additives are prohibited during the sequential addition process in order to prevent undesirable 3,4 addition of isoprene. The ABC triblock copolymer composition enables the polymerization of isoprene with well-defined microstructure, and also establishes a polymeric solution compatible with poly(DPPS). The ABC triblock is, consequently, limited to one phosphorus-containing sequence, restricting potential charge incorporation for ion-transport applications.

The synthesis of a novel piperazine-containing dilithium initiator, as presented in chapter 7, will enable the living anionic polymerization of poly(DPPS-*b*-I-*b*-DPPS). Scheme 8.5.1 reveals the new sequential addition method involving the new dilithium initiator, isoprene, and 4-DPPS. As represented in the synthetic mechanism, isoprene undergoes polymerization first in order to achieve a rubbery midblock with precise microstructural control and sequential addition with 4-DPPS enables reinforcing, poly(DPPS) outer blocks. Future research can explore these novel thermoplastic elastomers in comparison to the ABC analogues, and post-alkylation studies will enable charged derivatives additional studies with the alkylated ABC triblocks.

Scheme 8.5.1. Anionic polymerization with a piperazine-containing dilithium initiator affords poly(DPPS-b-I-b-DPPS).

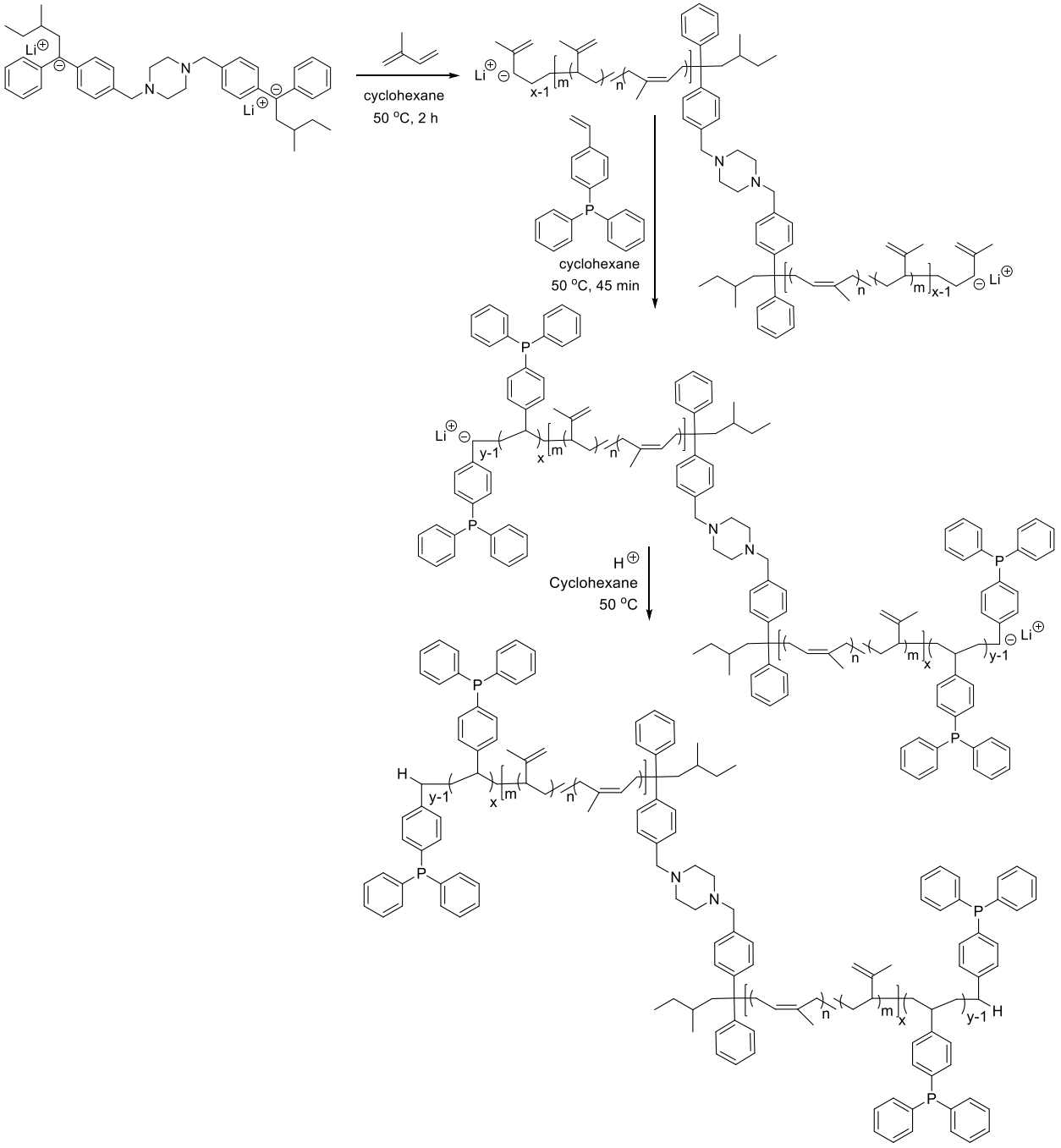

8.6 *Dichlorophosphino styrene enables the production of diverse phosphorus-containing styrenic monomers*

Previous literature extensively documents substitution reactions involving 4-vinylbenzyl chloride and nucleophilic phosphines for producing styrenic monomers bearing phosphonium functionality at the *para*-benzylic site.[12] While benzylic substitution affords facile monomer synthesis, thermal and chemical instability also results due to the acidity of benzylic hydrogens and susceptibility to undergo Hoffman elimination degradation.[12] 4-Diphenylphosphino styrene is a commercially available monomer without benzylic protons, eliminating the possibility of the Hoffman elimination mechanism. As demonstrated in previous chapters, we distinguished DPPS for its unique ability to polymerize under harsh anionic polymerization conditions and produce unprecedented phosphonium-containing diblock copolymers.[13] The enhanced thermal stability of this monomer and its compatibility with anionic polymerization conditions inspires new synthetic opportunities for phosphino styrenic monomers.

Scheme 8.6.1. Alkylation reaction with dichlorophosphino styrene affords diverse phosphino styrenic monomers with alkyl or phenyl substituents.

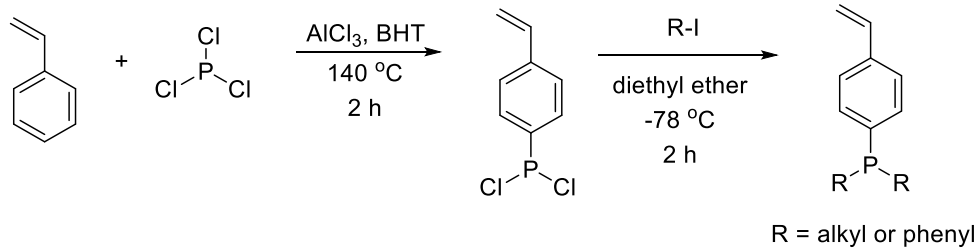

Adopting previously reported synthetic protocols for tolyl- and xylene- based phosphines will enable the production of diverse phosphino styrenic monomers with alkyl or phenyl substituents.[14,15] Scheme 8.6.1 reveals alkylation as a facile synthetic approach for achieving

phosphino styrenic monomers from a dichlorophosphino styrene precursor. Reacting styrene and phosphorus trichloride with an aluminum trichloride catalyst under reflux first achieves the dichlorophosphino styrene monomer, and subsequent post-alkylation with diverse alkylating agents affords various phosphino styrenic monomers with di-alkyl or di-phenyl substituents.

8.7 *References*

(1) Bechtold, S. *3D printing and the intellectual property system*, World Intellectual Property Organization-Economics and Statistics Division, 2015.

(2) Maganty, S.; Roma, M. P.; Meschter, S. J.; Starkey, D.; Gomez, M.; Edwards, D. G.; Ekin, A.; Elsken, K.; Cho, J. *Progress in Organic Coatings* **2016**, *90*, 243.

(3) Leitsch, E. K.; Heath, W. H.; Torkelson, J. M. *Int. J. Ad. and Ad.* **2016**, *64*, 1.

(4) Balcioglu, S.; Parlakpinar, H.; Vardi, N.; Denkbas, E. B.; Karaaslan, M. G.; Gulgen, S.; Taslidere, E.; Koytepe, S.; Ates, B. *ACS applied materials & interfaces* **2016**, *8*, 4456.

(5) Huang, J.; Sun, J.; Zhang, R.; Zou, R.; Liu, X.; Yang, Z.; Yuan, T. *Progress in Organic Coatings* **2016**, *95*, 20.

(6) Hsiao, S.-T.; Ma, C.-C. M.; Tien, H.-W.; Liao, W.-H.; Wang, Y.-S.; Li, S.-M.; Huang, Y.-C. *Carbon* **2013**, *60*, 57.

(7) Shidian, H.; Yangzhi, J. *Magnetic Recording Materiais* **2001**, *2*, 008.

(8) Ligon-Auer, S. C.; Schwentenwein, M.; Gorsche, C.; Stampfl, J.; Liska, R. *Polymer Chemistry* **2016**, *7*, 257.

(9) Decker, C.; Viet, T. N. T. *Macr. Chem. and Phys.* **1999**, *200*, 1965.

(10) Saito, T.; Harich, K. C.; Long, T. E. *Macr. Chem. and Phys.* **2008**, *209*, 1983.

(11) Luxton, A. R. *Rubber Chemistry and Technology* **1981**, *54*, 596.

(12) Ye, Y.; Elabd, Y. A. *Macromolecules* **2011**, *44*, 8494.

(13) Schultz, A. R.; Fahs, G. B.; Jangu, C.; Chen, M.; Moore, R. B.; Long, T. E. *Chemical Communications* **2016**, *52*, 950.

(14) Buchner, B.; Lockhart, L. B. *Journal of the American Chemical Society* **1951**, *73*, 755.

(15) Baldwin, R.; Smitheman, K.; Washburn, R. *The Journal of Organic Chemistry* **1961**, *26*, 3547.